Modelling of Gasoline Injection Process and its Application to the Development of a new GDI Engine

A thesis submitted for the degree of

Doctor of Philosophy

by

Mohan Raj Peethambaram

Department of Mechanical and Aerospace Engineering

College of Engineering, Design and Physical Sciences

Brunel University London

July 2021

Abstract

This thesis details an experimentally validated and simplified spray modelling approach and its application to the development of low emission, high efficiency modern GDI engines. A detailed literature review was carried out to describe the underlying process of spray atomisation. In this modelling approach, the fundamental nozzle parameters, such as nozzle diameter and static flow rate, are used as simulation inputs. The effect of modelling constants in resolving the secondary droplet breakup mechanisms was studied. A set of modelling constants was obtained for injection pressures ranging from 150 bar to 350 bar. There is a good correlation with the penetration depth and the Sauter-mean diameter (SMD) with the experimental data.

In-cylinder simulation was then carried out to evaluate and optimise the injection strategy for faster catalyst light-off during the cold-start operations. Simulation shows that earlier second injection prevents charge motion decay and fuel wall wettings. Equivalence ratio and turbulent kinetic energy around the spark plug show a qualitative agreement with the measured engine combustion stability differentiating the fuel injection timing.

Further studies were carried out to understand the benefit of air-guided piston in comparison to the wall-guided piston. The air-guided piston is shown to decrease the wall wetting of fuel by 14% in comparison to the wall-guided piston. Engine data show that the PN (#/cm^3) with air-guided strategy decreased by an order of magnitude (19 times lower) during the catalyst light-off condition. This enables to meet the emission standards over the WLTC driving cycle. Effects of injection timing and injection quantity on the charge motion were studied. The charge motion improvements achieved with the side-mounted injector were provided. Effect of spray patterns on the charge motion, wall wetting and mixing were also analysed. The outward pointing sprays benefit the charge motion/tumble ratio by 60 to 70%.

A detailed study was carried out to understand the difference in charge motion between the early inlet valve closing (EIVC) and late inlet valve closing (LIVC) approach adopted for improving thermal efficiency of engines. For the LIVC CAMs, under all operating conditions, the tumble ratio is 40 to 50% higher in comparison to the tumble ratio obtained for EIVC CAMs. This results in higher turbulent kinetic energy (TKE) for LIVC engines, which will benefit combustion and emission. However, the residual gas fraction shows to be higher for the LIVC CAMs. Based on the initial understanding of the spray on charge motion, a multiple injection strategy was adopted to improve the charge motion for EIVC CAMs for a low speed high load condition. Simulations show that the TKE and mixing could be improved significantly for faster combustion with multiple injection strategy for EIVC CAMs. The triple injection strategy increased the mixing and TKE resulting in 36% decrease in burn duration. Spray input

parameters were further improved using a simplified nozzle flow model to recalculate the effective injection velocity by considering the nozzle flow contraction for a given injection pressure, L/D and static flow rates. This improvement requires further evaluation for future work.

Acknowledgements

Firstly, my sincere thanks to Dr. Quanbao Zhou for his instant approval of my desire to pursue a PhD. He approved my review meetings in the university for the time off from work without any hesitation. Moreover, I would sincerely like to extend my gratitude to Dr. Xiaoyu Zhang, Mr. Martin Joyce, Dr. Tiegang Hu, Mr. Brent Liu, Mr. Ken Pendlebury, Ms. Kelly Lo, Mrs. Sophie Fu and Ms. Queenie Mei for the funding arrangements for all these years.

I sincerely thank Dr. Huiyu Fu for providing continuous support and learning in the in-cylinder CFD simulations carried out so far. His continuous guidance and valuable technical suggestions made it possible for me to extend my knowledge in spray and combustion. While working with him, I find that I learn every day.

I sincerely thank Professor Hua Zhao for providing this opportunity for my PhD under his supervision. Furthermore, I am thankful for him affording me access to the engines lab and spray data from the Changan-funded projects. His continuous review, guidance, comments and support have allowed me to consolidate my work on a regular basis. Despite his busy schedule, all the feedback and comments were succinct and precise, enabling me to move forward with this research. I would also like to thank my supervisor, Dr. Jun Xia, for the time and effort spent in reviewing my work during the review meetings. I am very thankful to Dr. Meghna Dhanji for sharing the spray and in-cylinder data, which proved to be useful for my validation studies. The detailed discussions were very informative and it helped me to visualise better. My sincere gratitude to the examiners, Professor Thanos Megaritis and Professor Kai Luo (UCL), for reviewing my thesis and for providing valuable suggestions.

I also thank Mr. David Hale for the CAD model support, which was an input for my simulation studies. The data shared by Changan Engine development lead, Dr. Benjamin Waters, Mr. Nicholas Jepson, Mr. Vince Mike and Dr. Mike McGhee, guided my research in the simulation understanding and improvements. Injector data were one of the main inputs for my studies. In this regard, I would like to thank Mr. Michael Putnam and Delphi support, mainly Ms. Joyce Faville and Dr. Bizhan Befrui. My sincere thanks also to Dr. Rickard Solsjö, as a Siemens technical support engineer, and Mr. Mubeen Irshad for their help during this period. I also would like to extend my thanks to Dr. Suresh Kumar Nambully for the recent support in the Converge tool. Due to my studies and extended working hours, I had given less time and attention to my family. In this regard, I should like to thank my daughter Harshika and my wife Mrs. Lavanyalatha for their understanding and sacrifices. I would also like to thank my family members, my late mother-in-law, my father-in-law, my parents and my brother (Mr. Nandakumar), for their encouragements during the studies. Lastly, I thank Dr. Ganapathi Bhat and Dr. Kamath for sharing their experiences, which kept me motivated.

Nomenclature

a	Eccentricity defining deformation of droplets
$\bar{A}$	Mean flame area
ADE	Algebraic differential equation Solver
AFR	Air fuel ratio
AI10, 50 90	10%, 50% and 90% burn location, respectively
ATDC	After piston, top dead centre
$A_{wrinkles}$	Wrinkled flame area
B_0	Model constant KH-RT model
B_1	Model constant KH-RT model
BSFC	Brake specific fuel consumption
BTDC	Before piston top dead centre
BTE	Brake thermal efficiency
C_3	KH-RT model constant
CAM	Intake and exhaust cam profile
c_{b1}	Critical Weber number for bag breakup
c_{b2}	Bag breakup time constant
CCD	Charge-coupled device
C_c	Contraction coefficient
C_{dd}	Droplet drag coefficient, dynamic
C_d	Nozzle discharge coefficient
$C_{d,s}$	Droplet drag coefficient, solid sphere

CDF	Cumulative distribution function
CFD	Computational fluid dynamics
CMC	Continuous multi-component fuel evaporation
CO_2	Carbon dioxide
COV	Coefficient of variation (100*Standard deviation/Mean)
CR	Compression ratio
c_{s1}	Critical stripping breakup constant
c_{s2}	Critical stripping breakup time constant
C_v	Specific heat at constant volume
C_τ	KH-RT model constant for time
D_d	Droplet diameter
$D_{d,\ stable}$	Stable droplet size
DISI	Direct injection spark ignition
DLM	Diffusion limit model
ECFM3Z	Extended coherent Flame model, 3 zone
ECU	Engine control unit
EGR	Exhaust gas recirculation
EIVC	Earlier intake valve closing
EOI2	End of second injection
EOI3	End of third injection
EU	European Union
FTP	Federal test procedure

GDI	Gasoline direct injection
GHG	Greenhouse gas
GPF	Gasoline particulate filters
HC	Hydrocarbon
HCC	Heat conduction in components, two-dimensional code
HCCI	Homogeneous charge compression ignition
H_{charge}	Angular moment of inertia of the charge mass
H_{spray}	Angular moment of inertia of spray
HV	Hybrid vehicle
IC	Internal combustion
ICCT	international council on clean transportation
ICE	Internal combustion engines
IMEP	Indicated mean effective pressure
KHRT	Kelvin-Helmholtz and Rayleigh-Taylor model
KIVA-3V	In-cylinder moving mesh CFD solver
L/D	Nozzle length/Nozzle diameter
La	Laplace number
LAS	Laser absorption and scattering
L_{BU}	Liquid breakup length
LES	Large eddy simulation
LIF	Laser-induced fluorescence
LIVC	Late intake valve closing

MBT	Minimum ignition advance for best torque
MCR	Miller cycle rate
MESIM	Multi-dimensional engine simulation
MMD	Mass median density
NA	Naturally aspirated
NIST	National Institute of Standards and Technology
NMEP	Net mean effective pressure
NO_x	Nitrous oxides
NVH	Noise and vibration harshness
O	Charge mass centre of rotation in cylinder
OBFCM	On-board fuel and/or energy consumption monitoring device
Oh	Ohnesorge number
P	Pressure
PAH	Polycyclic and aromatic hydrocarbons
PDF	Probability density function
PDPA	Phase Doppler particle analyser
PFI	Port fuel injection
PIV	Particle image velocimetry
PN/PM	Particulate number/Particulate matter
P_{ref}	Reference pressure for laminar flame speed calculation
Q	Cumulative distribution function
Q^*	Specific internal energy

Q_{ideal}	Ideal flow through the nozzle (calculated based on Bernoulli flow assumption)
Q_{static}	Injector static flow rate
r	Radius
$\vec{r}$	Position vector in space
R&D	Reitz-Diwakar model
r/D	Nozzle entry radius/Nozzle diameter
r_c	Volumetric compression ratio
Re	Reynolds number
r_e	Volumetric expansion ratio
RGF	Residual gas fraction
RMM	Rapid mixing model
RNG	Re-normalisation group theory
RPM	Engine speed
RR	Rosin-Rammler distribution
SI	Spark ignition
SI-CAI	Spark ignition-controlled auto-ignition
SICI	Spark-assisted compression ignition
S_{ij}	Mean strain rate tensor
S_L	Laminar flame speed
SMD	Sauter mean diameter
SOI1	Start of first injection
SOI2	Start of second injection

S_t	Turbulent flame speed
STAR-CD/ES-ICE	Siemens CFD solver
Std-NMEP	Standard deviation of NMEP
t	Time
TAB	Taylor analogy breakup
TDC	Piston top dead centre
TKE	Turbulent kinetic energy
TR	Tumble ratio
TSM	Thin Skin Model
T_u	Unburned gas temperature
u'	Turbulent velocity
$\bar{U}$	Ensemble average velocity
u', v', w'	Turbulent velocity in three directions
U_0	Droplet relative velocity(m/s)
U_d	Droplet velocity(m/s)
U_f	Gas velocity(m/s)
uHC	Unburned hydrocarbon
$\tilde{u}_i$	Favre averaged velocity vector
U_L	Liquid jet velocity from nozzle
u_{mean}	Mean nozzle flow velocity
V1/V	Volume around spark plug/Clearance volume
VOF	Volume of fluid

v'_{rms}	Turbulent root mean square velocity
We	Weber number
WLTC	Worldwide harmonized Light vehicles Test Cycles
WOT	Wide open throttle
x_i, x_j	Position vector
y'	Droplet distortion

List of Symbols

κ_{KH}	Wave number for KH instability
μ	Laminar dynamic viscosity
μ_T	Eddy viscosity
ν	Kinematic viscosity
ϕ	Equivalence ratio
Σ	Flame surface density
χ^2	Chi-Square variable for droplet distribution
Ω_{ij}	Anti-symmetric stress tensor
Δp	Pressure head across the nozzle
δ_M	Gas film constant for mass transfer
δ_{ij}	Kronecker delta tensor
δ_T	Gas film constant for heat transfer
κ-ε	Turbulent kinetic energy and dissipation
λ	Actual air fuel ratio/Stoichiometric air fuel ratio

Λ_{KH}	Wavelength for KH
Λ_{RT}	Wavelength for RT
ρ_a	Air density
ρ_d	Droplet density
ρ_l	Liquid density
σ_d	Droplet surface tension(N/m)
τ_b	Bag breakup time
ω	Angular velocity
ω_{KH}	Growth rate for KH
ω_{RT}	Growth rate for RT
γ	Specific heat ratio (c_p/c_v)

Table of Contents

List of Figures

List of Tables

Chapter 1. Introduction

1.1 Background

Greenhouse gas (GHG) and pollutant emissions are some of the major problems that government plans to mitigate against global warming and air quality. Road, aviation, rail and water transport contribute to rapid development in the global economy. These transport sectors are responsible for 23% of the total energy-related CO_2 emissions (Sims et al., 2014). In this, 74% of the GHG emission was from the road transport sector. Internal combustion (IC) engines play a major role in the road transport sector. With an ever-increasing energy use, controlling the GHG emission is becoming a challenge. China, the European Union, India, Japan, Mexico, Saudi Arabia, South Korea, United Kingdom and the United States have established emission standards (Tietge et al., 2017; 2020; Yang and Bandivadekar, 2017) for vehicles. The emission standards were established based on the amount of CO_2 released per kilometre and fuel consumption in litres per 100 km. Typical emission standards for the passenger vehicles were provided from the literature (Figure 1.1).

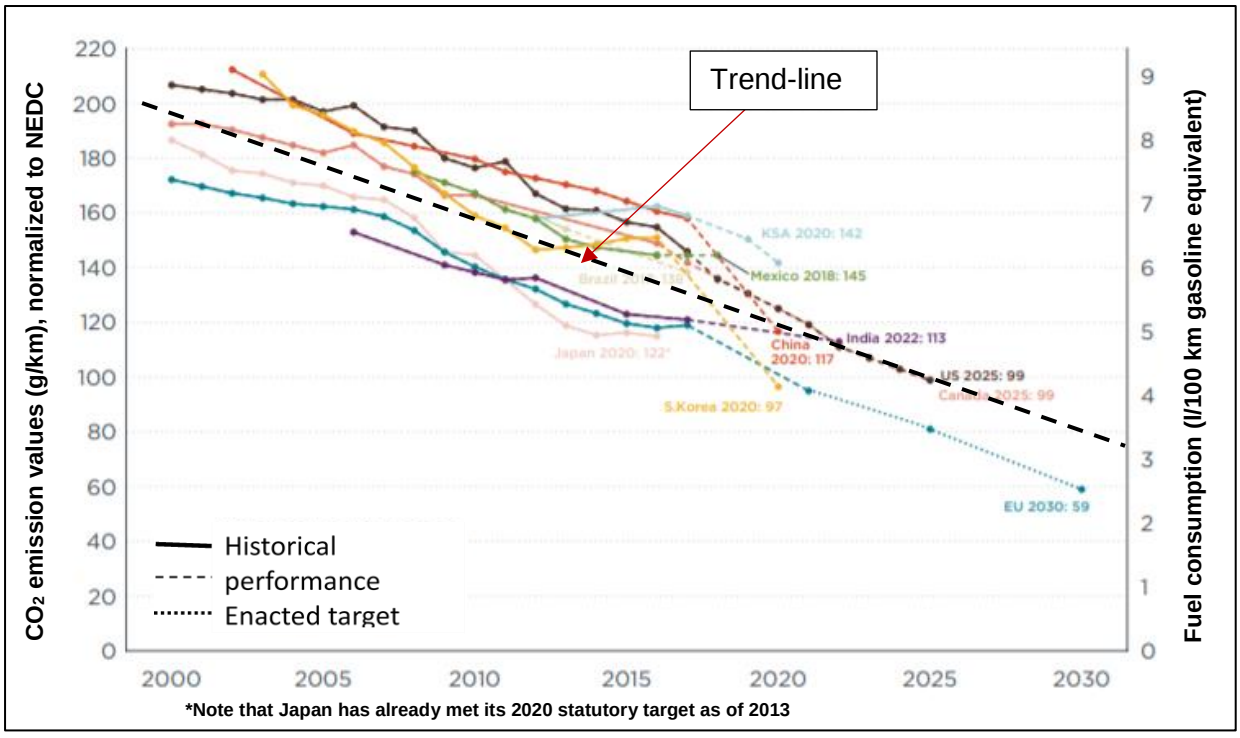

Figure 1.1: Comparison of global CO_2 regulations for new passenger cars (Yang and Bandivadekar, 2017; Mock, 2019).

An approximate trend-line from the data shows, within the last 25 years, there was 54.5% decrease in CO_2 emission. Moreover, it should also be noted that there is an ever-increasing demand in thermal efficiency, to meet future emission and due to the existence of internal combustion engines. It should also be noted that new EU car CO_2 emissions (Mock, 2019), on an average need to be reduced by 15% by 2025 and further by 37.5%by 2030, relative to 2021 baseline. For systematically monitoring CO_2 emissions under real-world driving conditions, all cars must be equipped with an on-board fuel and/or energy consumption monitoring device (OBFCM). Based on the International Council on Clean Transportation (ICCT) roadmap model, the proposed regulation is estimated to reduce 170 million tonnes of CO_2 in the period 2020 to 2030 with better air quality.

Downsized engines (Turner et al., 2014; King et al., 2016; Melaika, Mamikoglu and Dahlander, 2019) and alternative fuels (Tuner, 2016) with electrified powertrains (An, Stodolsky and Santini, 1999; An and Santini, 2004) were considered to meet the near future emission requirements. Based on data analysis by MAHLE powertrain (Cooper et al., 2020), an estimated 59 g/km fleet CO_2 emission limit is required to achieve EU 2030 CO_2 emission standard.

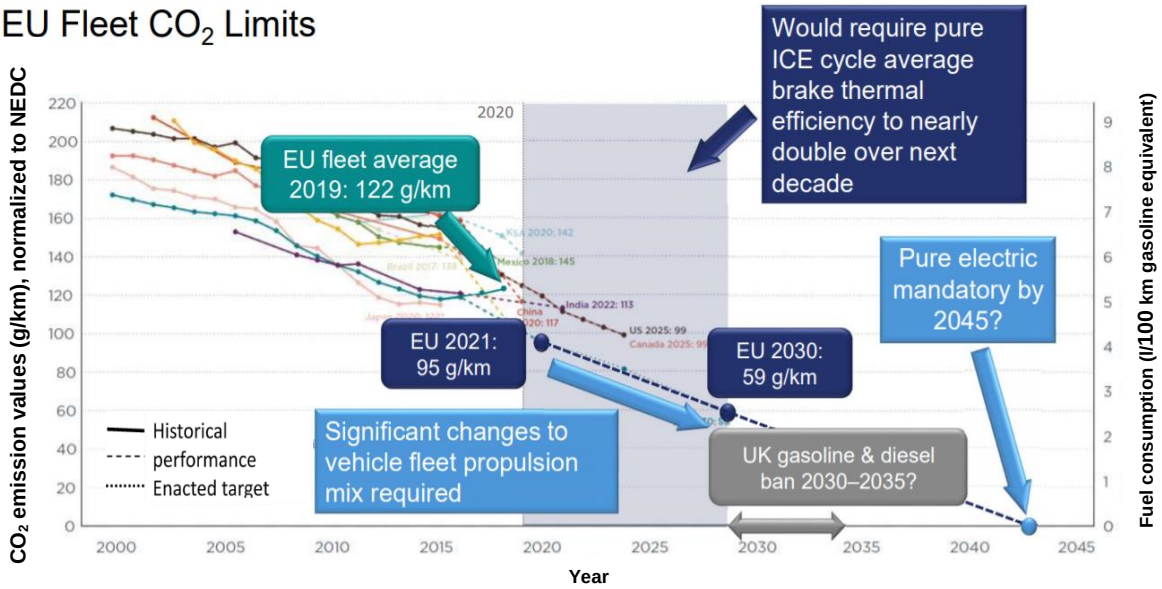

Figure 1.2: CO_2, target driving manufactures towards increased electrification (Cooper et al., 2020).

The extrapolation of the possible thermal efficiency with the available technologies, such as, lean burn and advanced ignition system (active pre-chamber) along with electrification (Mild-HV, Fully-HV and Plug-in-HV) were estimated to meet the near future emission demands. As can be seen, beyond 2040/2045, if only based on the tailpipe emission, pure electric vehicles will likely become mandatory. However, the IC engines fuelled with green hydrogen and

carbon natural fuels can meet the zero carbon emissions when such fuels have become available. Hence, in the modern gasoline engine development, the research focusing on high thermal efficiency, along with an ultra-low emission of pollutants, such as $NO_{x,}$ particulates and hydro carbon (HC), is necessary to decrease global warming.

As reported (Joshi, 2020), the transport sector is bound to adopt and meet the societal needs in reducing NO_x, particulates number/particulates mass (PN/PM) and CO_2 (greenhouse gases). Moreover, it should be noted that the major focus remains on the reduction of cold-start emission. The particulate number standards in Europe and China have enforced gasoline particulate filters (GPFs). In the future, with the introduction of further stringent particulate emission regulations, GPFs are required even for the port fuel injection vehicles (PFI). This enables the ever-increasing demands for the particulate emission reduction requirements for the existence of ICE.

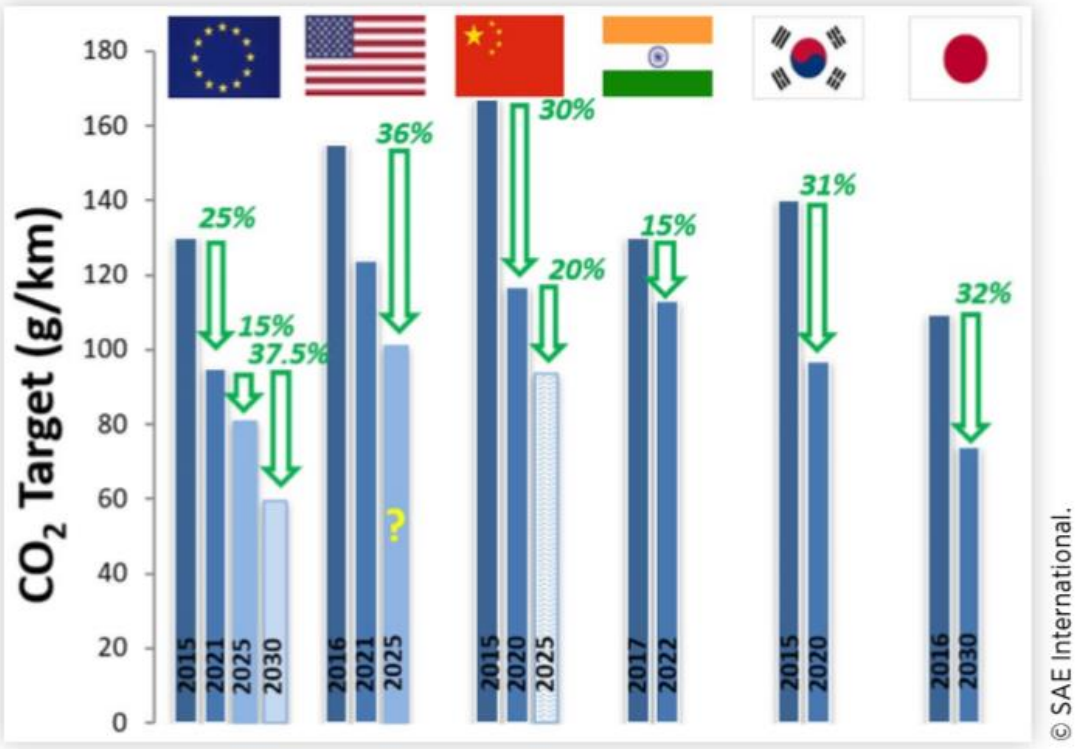

Figure 1.3: Summary of CO2 targets for light-duty passenger cars in major markets (Joshi, 2020).

Engines for hybrid vehicles with high efficiency technologies, such as Atkinson cycle, Miller cycle, lean burn, cooled EGR, variable compression ratio (CR), cylinder deactivation, spark assisted gasoline compression ignition, water injection, pre-chamber and homogeneous lean burn are of focus for the near future engine development.

This necessitates designing an optimum air intake and combustion system, resulting in lower emission with improved fuel efficiency and specific power output. There are different operational strategies adopted to increase the power output and the efficiency of the engine in-line to meet emission norms. Direct injection spark ignition (DISI) engines combine the benefit of the diesel and the spark ignition engine having a better break specific fuel consumption (BSFC) and higher specific power output along with much lower CO_2 and PN/PM emission. This leads to the increase in research towards the gasoline direct injection (GDI) engine development. In engine downsizing, the boosted GDI engine plays a key role to increase the power density of the engine and to decrease the CO_2 emissions. GDI technology enables an efficient way to run the engine with highly stratified fuel injections under both lean and rich fuel mixtures as and when required. This also helps in having difference valve train strategies to improve fuel economy, knock and auto ignition. Generally, GDI improves the fuel atomisation and mixing process so the non-homogeneity of fuel in the charge air mixing is minimised. As the fuel needs to be mixed with the air in a relatively short duration, it necessitates a strong sustaining air flow current through the intake port and the cylinder. This strong charge motion increases the mixing of the atomised fuel to evaporate and improve mixing with air. There are many factors which affects the fuel air non-homogeneity, namely, fuel blends, the droplet size, air flow mixing characterised by the tumble and swirl, injection timing, droplet wall interaction and liquid film formation. The high energised air fuel mixture available during the beginning of the spark would help in increasing the burn rate and improving combustion stability, which results in improving the efficiency along with low engine emissions. The primary feature driving the mixing is the fuel atomisation and subsequent mixing process. Atomisation (Lefebver, 1989) is the process by which a voluminous liquid lump is converted to fine droplets by energising (pressure) the liquid to redistribute into droplets kinetic energy and droplet interface surface (surface tension) energy. In the modern GDI engine with the availability of advanced manufacturing of injector nozzles (~90 µm to 200 µm) and precise control of injection quantity, different injection strategies can be adopted to improve the fuel mixing and fuel stratification. The engine combustion system is a combination of injectors, intake port, exhaust port, intake valve lift profile, exhaust valve lift profile, piston and cylinder head shape. Simulations are required to understand the interactions of the individual components to improve the design. Moreover, it helps to devise new strategies and requirements for different load conditions. In the engine development, with the availability of high performance computers/cluster, CFD simulations play a key role in predicting the in-cylinder charge motions and fuel mixing, which helps in designing a better engine. To have a reliable prediction of the in-cylinder mixing process, a good spray and moving mesh models will be required. In this part of the work, STAR-CD/ES-ICE and Converge commercial CFD

tools were used with a careful evaluation of spray methodologies implemented using Fortran routines.

1.2 Thesis outline

In Chapter 2, a detailed literature survey describing the spray atomisation process, in-cylinder spray application and high efficiency engine strategies is reported. Moreover, the current fuel stratification techniques are also described. The fundamental understanding of the turbulence modelling, spray and mixing is outlined to build the mathematical model for the simulation process. The two spray modelling techniques, namely, Reitz-Diwakar (R&D) model and Kelvin-Helmholtz and Rayleigh-Taylor (KHRT) model, are presented. The effects of modelling parameter or constants for calibrating the spray are presented. Modelling approaches, along with the experimental characterisation of the droplet breakup mechanisms, are provided. Fuel stratification during the charge preparation process and the relation to PN/PM formation are also discussed and the current research direction in understanding the mixing process and direction to build the ultra-low PN/PM emission system outlined.

The spray calibration and secondary breakup model constants sensitivity are included in Chapter 3. In the general spray calibration process, the spray model is calibrated for each injector from the supplier. In this work, a more general approach has been adopted in calibrating the spray by knowing the fundamental characteristics, such as the nozzle size, injector static flow rate and injection pressure.

In Chapter 4, catalyst heating/light-off condition and the fuel enrichment or fuel stratification setup in the engine are detailed. The developed spray model is applied to the catalyst heating application and validated for a twin injection case with two different injection timings. The fuel air mixing and the final fuel rich mixture available near the spark plug and the turbulent kinetic energy are correlated to the engine stability.

In Chapter 5, detailed study is presented to understand the air-guided and wall-guided pistons for the modern engine application. Analysis shows that the air-guided piston with the twin injection strategy can improve mixing and decrease the PN/PM (#/cm^3) emission by an order of magnitude during the catalyst light-off condition. Different piston designs were studied to understand the influence of the piston crown in building necessary fuel stratification near the spark plug with the overall lambda ~1. Different spray patterns were analysed, starting from a 6-hole injector to a five-hole injector with the simplified spray model. The benefits of the side-mounted injector on tumble ratio and mixing are demonstrated.

In the engine development, another key in-cylinder charge motion controller is the intake and exhaust CAMs. The thermal efficiency of the engines is improved using the over expansion

process, either achieved by Atkinson or Miller's engine cycle. The enabling parameter for achieving this is the intake and exhaust CAM design and timing. In Chapter 6, the charge motion benefits and disadvantages of the two different CAMs strategies are discussed for the low speed high load and medium speed low load condition. Moreover, the improvements achieved by multiple injection strategy are provided. Finally, in Chapter 7, the summary and conclusion of the research are presented along with the future work.

Chapter 2. Literature Review

2.1 Introduction

In this chapter, a detailed literature review is presented to understand the underlying focus for future engine development. There are many researches reported in the literature, starting from the mathematical model developments in defining the flow instabilities to the development of modern high efficiency GDI engines. In this chapter, some of the literatures are outlined to describe the details of the GDI spray formation and fundamentals for the in-cylinder charge air mixing processes for the motivation of this research. This is categorised into four sections. In the first section, the fundamental research carried out on droplet breakup is provided. In the second section, further developments in applying the spray modelling in engine simulations are reported. In the third section, the main technologies focused for the development of high efficiency engines are consolidated and, in the fourth section, the requirements for fuel stratifications are provided.

Lastly, based on the current research and the reported developments, the aim and objective of this work are summarised.

2.1.1 Liquid jet breakup

Atomisation regime is one of the jet breakup descriptions in the classical jet breakup mechanism (Leferbver, 1989; Baumgarten, 2006). The linear instability theories define the growth of the unstable wave induced by the perturbation. These unstable wavelengths are related to the surface tension (σ_d), relative droplet velocity (U_0), gas (ρ_a) and liquid (ρ_d) densities via linear instability theories. The non-dimensionalised numbers, such as the Weber number (We), Reynolds number (Re), Laplace number (La) and Ohnesorge number (Oh), are often used to define the competition of different forces on the liquid ligaments or droplets. The typical forces include aerodynamic, inertia, surface tension and viscous forces.

$$We = \frac{\rho_a U_0^2 D_d}{\sigma_d} \qquad (2.1)$$

$$Re = \frac{\rho_a U_0 D_d}{\mu_a} \qquad (2.2)$$

$$Re_d = \frac{\rho_d U_0 D_d}{\mu_d} \qquad (2.3)$$

$$Oh = \frac{\sqrt{We}}{\mathrm{Re}_d} \qquad (2.4)$$

$$La = \frac{\rho_d \sigma_d D_d}{\mu_d^2} \qquad (2.5)$$

$U_0 = |U_f - U_d|$

U_f = Gas Velocity(m/s)

U_d = Droplet velocity(m/s)

Experiments were carried out to categorise these forces with the resultant droplet breakup mechanism. Krezeckowski (1980) carried out an experimental study to describe the deformation mechanism and the breakup duration of liquid droplets in an air stream. The mechanism of the droplet deformation and disintegration was investigated by a photo camera and a spark splash. In this paper, the droplet deformation processes were described as bag, bag-jet transition and shear regions. The breakup time depends on the Weber number (We), Laplace number (La) and the density ratios (ρ_d / ρ_a).

Pilch and Erdman (1987) reviewed the mechanism of acceleration-induced breakup of liquid droplets. Several data on acceleration induced fragmentation of liquids were collected and summarised based on the critical Weber number, breakup time and velocity and fragment sizes. They further characterised the droplet breakup mechanisms: vibrational breakup (We <=12), bag breakup (12< We <=50), bag and stamen breakup (50<We <=100), sheet stripping (100<We <=350) and wave crest stripping followed by catastrophic breakup (We > 350). The concept of maximum stable diameter was established to estimate the largest stable fragments which are a function of the critical Weber number and inversely proportional to the droplet to gas velocity ratio.

Yang (1990) established a dispersion equation for a non-axisymmetric breakup of a liquid jet to estimate a critical Weber number above which a non-axisymmetric disturbance becomes

unstable. According to the analysis of a high-speed jet, small droplets break away from the core surface instead of rings. He also explained the different modes of instability and showed that, with higher transverse modes in the circumferential direction of the liquid jet, it leads to the ripping away of small droplets from the surface of the jet.

Hslang and Faeth (1992) studied the droplet deformation and the secondary breakup mechanism for different liquids, such as water, glycerol, n-heptane, ethyl alcohol and mercury to cover a range of Weber numbers (0.5 to 1000) and Ohnesorge (Oh, viscous force to surface tension) number (0.0006 to 4) with shock-initiated disturbances in air at normal temperature and pressure. Their measurements include shadowgraph and holograph to study and characterise the breakup regimes in terms of We and Oh numbers. The Weber number regimes were reiterated to represent the no-deformation, non-oscillatory deformation, bag breakup, multimode breakup and shear breakup. It was indicated that, for a pressure-atomised dense spray after secondary breakup, it satisfies the ratio of MMD (mass median diameter)/SMD (Sauter mean diameter) =1.2 for universal root normal distribution with Oh <0.1. In shear droplet breakup process, the secondary droplet size was related to the liquid velocity boundary layer thickness and dictated by the liquid viscosity, initial droplet relative velocity and initial droplet diameters.

Liu and Reitz (1997) studied the distortion and the breakup mechanisms of liquid droplets injected into a transverse high velocity air jet at room temperature and atmospheric pressure. They have used an ultra-high magnification, short exposure photography to study the bag, shear and catastrophic breakup regimes. In this case, diesel droplets were taken for the study. They have covered droplet diameters of 69, 121 and 198 microns with a transverse jet velocity from 68 to 331 m/s. This covers a range of Weber numbers from 56 to 463. As reported by other researchers, they found that the droplet breakup is initiated by a two-stage process. In the beginning phase, the aero-dynamical pressure force exerted on the spherical droplets deforms to flat disc and the breakup starts subsequently. The initial droplet deformation was numerically estimated with their modified dynamic drag breakup model (DDB). In this, they have derived the rate of change of the non-dimensional radius to determine the elipsoidity and

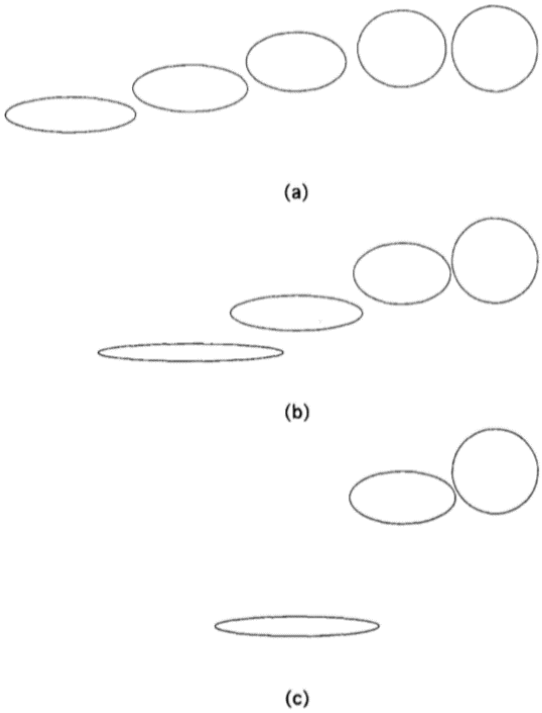

Figure 2.1: Predicted droplet trajectory and distortion as function of weber number. Distortion shows that the rate of distortion increases (a to c) with droplet velocity (Liu et al., 1997).

re-compute the droplet drag scaled linearly between discs to a sphere. The drag force was found to show a major influence in the droplet trajectory. The droplet drag coefficient is specified as a function of the droplet Reynolds number using solid-sphere correlations (Liu and Reitz, 1997)

$$C_{d,s} = \frac{24}{Re}\left(1 + \frac{1}{6}Re^{\frac{2}{3}}\right)\ Re \leq 1000\ \ C_{d,s} = 0.424\ Re > 1000$$

$$C_{dd} = C_{D,s}\left(1 + 2.632\, y^{'}\right) \qquad (2.6)$$

$$y^{'} = min\left(1, \left\{\frac{a}{r} - 1\right\}\right); a = 2r, when\ the\ droplet\ is\ fully\ distorted$$

The expression shows that the drag coefficient of the disc is about 3.6 times that of a sphere.

Senecal et al. (1999) carried out a linear instability analysis for a liquid sheet including the effects of the surrounding gas, surface tension and the liquid viscosity on the wave growth process. The resulting dispersion relation was used to predict the maximum unstable growth rate, wavelength, the sheet breakup length and the resulting droplet size for pressure-swirl

atomisers. The predicted droplet size is used as a boundary condition in a multi-dimensional spray model. The results show that the model was able to accurately predict liquid spray penetration, local Sauter mean diameter and overall spray shape.

Nauwerck et al. (2005), carried out experimental study to evaluate the injector characteristics with high injection pressure of 50 MPa. In this study, two injectors, with the same nozzle size of 120 µm(D) but different L/D of 2.5 (Type 1) and 5 (Type 2), were chosen. L, denotes the length of the nozzle hole. Both, particle image velocimetry (PIV) and phase Doppler anemometer (PDA) were used to characterise the spray. A spray plume/beam was analysed at different radial locations.

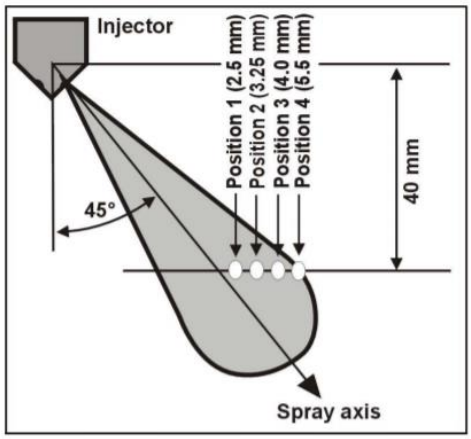

Figure 2.2: Position of PDA measurements (Taken from Nauwerck et al., 2005).

Spray measurements show high droplet velocity gradients measuring up to 30 m/s to 40 m/s per millimetre. This indicates a high velocity zone near the core axis of the spray. The droplet size measurements show that the SMD is around 6 µm with 50 MPa injection pressure (~50% reduction from 10 MPa injection pressure). However, the SMD dependency on injection pressure was not shown to be linear. They also reported (Figure 2.3) the droplet velocities to be associated with the droplet diameter.

It clearly indicates that the larger droplets are associated with higher velocity and are responsible for the spray penetration. Droplets will decrease their velocities when they move away from the spray axis, suggesting a centre core having larger droplets. It was reported that the air entrainment velocity increases with higher injection pressure. In the modern injectors, the air entrainment velocity is a feature required for improving the fuel evaporation and fuel air

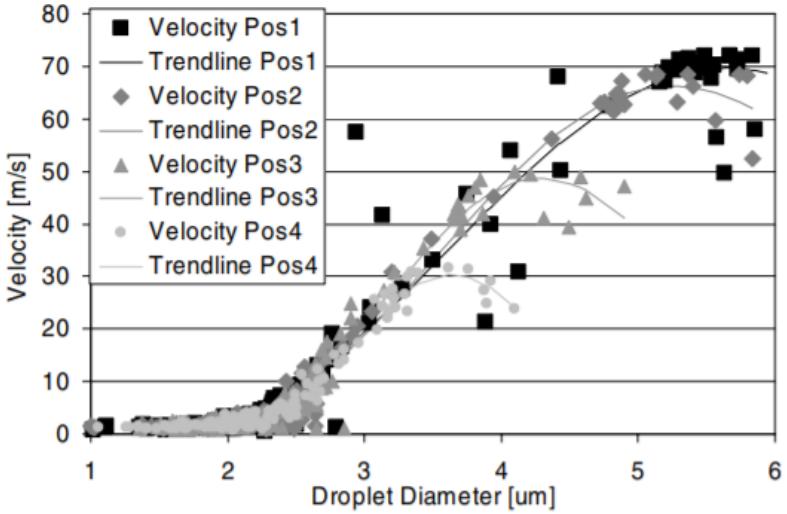

Figure 2.3: Velocity vs corresponding droplet diameter at various positions in the spray for 30 MPa, injector type 2 (Taken from Nauwerck et al., 2005).

mixing process. In the numerical simulation processes, these fundamental characteristics need to be captured for more accurate predictions during the engine development phase.

Guildenbecher, Lopez-Rivera and Sojka (2009) revised and reviewed the different secondary droplet breakup mechanisms and concluded that the viscous shear plays a small role in the breakup of liquid droplets in a gaseous environment. Details of different methods for secondary droplet breakup measurements, such as shock tube, continuous jets and droplet towers, were discussed. It was described that the secondary atomisation of R-T instabilities is typically assumed to occur either at the front or rear stagnation points, while K-H instabilities occur at the periphery where the relative velocities between the droplet and ambient are the maximum. It was reported that the catastrophic breakup is controlled by R-T instabilities.

As the perturbations might be from different sources, this results in the flow instabilities and the resultant liquid ligament breakup processes. Under higher injection pressure, the cavitation should also be considered for the primary droplet breakup mechanism. Nurick (1976) characterised the cavitation for circular and rectangular nozzles and developed a correlation for nozzle discharge coefficients as a function of L (nozzle length)/D (nozzle

diameters) and entrance radius. The contraction area was formulated based on empirical constants and the entrance radius to the nozzle diameters.

Von Kuensberg Sarre, Kong and Reitz (1999) developed a phenomenological nozzle flow model and implemented it in both FIRE and KIVA-II codes to simulate the effects of the nozzle geometry on fuel injection and spray processes. The model considers the nozzle passage inlet configuration, flow losses, cavitation, injection pressure and combustion chamber conditions and provides initial conditions for multidimensional spray modelling. The discharge coefficient of the injector, the effective injection velocity and the initial droplet of injected liquid “blob” sizes are calculated dynamically during the entire injection event. The model was coupled with the wave breakup model to simulate experiments of non-vaporising sprays under diesel conditions. Good agreement was shown in liquid penetration, spray angle and droplet size (SMD). The integrated model was also used to model combustion in a Cummins single-cylinder optical engine with good agreement. They have shown the different cavitation regimes in the nozzle flows, such as turbulent flow, onset of cavitation, super cavitation, hydraulic flip and partly reattached flow. In this model, the exit droplet/blob velocity and diameter were calculated from the effective exit area from the nozzle. Their previous study demonstrated how easily the mass flow rates are changed due to small imperfections and asymmetries caused by variations in the inlet radius. It was also reported that different turbulence models give different time and length scales for the turbulent eddies, thus the drag forces due to the turbulent flow and, consequently, the droplet transport will also be different. Semi-cone angle predicted by the Huh and Gossman (1991) model was also provided. In this case, the semi-cone angle is proportional to the turbulent velocity fluctuation to the effective nozzle velocity ratio. It was also reported that, to eliminate the non-representative penetration by a single leading droplet, the spray penetration was defined by the farthest droplet position of the 99% of the injected mass for their spray calibration work. To avoid some spurious droplet collision and coalescence, an arbitrary model constant was used. Their injector model was used in the in-cylinder simulation, which shows an improvement in the in-cylinder pressure trace predictions.

Daif et al. (1999) studied the droplet evaporation experimentally in a thermal wind tunnel. In this, a single droplet was suspended in the hot air stream and the evaporation was recorded with a video recording system and infra-red camera. Experiments were carried out with n-heptane and decane fuel droplets with different composition. The transient surface temperature and the diameters were interpreted from the infra-red thermal imaging and image processing from video recordings. In this, the droplets were subjected to both natural and forced convection environment. A numerical model was also developed with Abramzon and

Sirignano's (1989) approach using the “film theory” for predicting the evaporation rates. The numerical results were reported to match well with their experimental data.

Abramzon and Sirignano (1989) built a simplified droplet evaporation model considering the variable thermos-physical properties, non-unitary Lewis number in the gas film, the effect of the Stefan flow on heat and mass transfer between the droplet and the gas, and the effect of internal circulation and transient liquid heating. A general zero-dimensional algorithm was presented to account for the heat and mass transfer corrections to account for blowdown effects. The film theory assumes that the resistance to heat or mass exchange between a surface and a gas flow may be modelled by introducing the concept of gas films of constant thicknesses (δ_T and δ_M). However, the presence of the Stefan flow will influence the values of δ_T and δ_M, since a surface blowing results in the thickening of the laminar boundary layer (Schlichting, 1979).

2.1.2 In-cylinder GDI spray

Liu and Reitz (1998) developed a two-dimensional (axis-symmetric) transient heat conduction in components (HCC) computer code for predicting engine combustion chamber wall temperatures. Special treatments for the head gasket, the piston-liner air gap, the piston movement and a grid transformation for describing the piston bowl shape were designed and utilised. The results were compared with a finite element method and verified to be accurate for simplified test problems. In addition, the method was applied to realistic problems of heat transfer in an Isuzu engine and a Caterpillar diesel engine, and showed agreement with experimental measurements. It was discussed that the cooling of the cylinder head, block and piston is desired to avoid problems such as thermal stresses in regions of high heat flux, deterioration of the lubricating oil film, and knock and pre-ignition in spark ignition engines. However, excessive heat transfer is directly linked to the overall efficiency of the engines. It was reported that, in a conventional diesel engine, about 30% of the fuel energy was lost as heat. In this, 50% of the energy is lost through the piston and 30% through the cylinder head. The importance of the heat transfer model was discussed in this paper. It was reported that the chamber wall temperature is a vital parameter for determining magnitude of heat flux. If an accurate wall temperature distribution is unavailable, it is impossible to obtain accurate heat flux results. In general, the combustion chamber of an internal combustion engine is formed by the cylinder wall, head and piston, each with different surface temperature distributions. The constant temperature assumption on each surface is not consistent with the actual situation occurring on these surfaces of the combustion chamber. In this study, an asymmetric heat conduction model was solved numerically using ADE solver. Additionally, a more realist piston geometry was considered. In the simulation, a coordinate transformation was adopted to incorporate the moving piston. The computed heat transfer was compared

with the motored and the fired case. It was shown to have a quantitative matching with the actual engine data.

Cheng et al. (1993) provided an overview of spark-ignition engine unburned hydrocarbon emissions mechanisms, and used this framework to relate measured engine-out hydrocarbon emission levels to the processes within the engine. It was cited that spark-ignition engine-out HC levels are 1.5 to 2% of the gasoline fuel flow into the engine; about half this amount is unburned fuel and half is partially reacted fuel components. HC emissions and performance losses occur during starting and warm-up. Moreover, the HC emissions were shown to be significant in both warmed-up and cold engine. Their experiments indicate that, with liquid gasoline present on the walls of the intake and flowing into the cylinder in significant amounts, hydrocarbon emissions may be about 50% higher than HC emissions with gasoline with more sophisticated injection systems which prevent liquid film build-up.

Shin, Cheng and Heywood (1994) observed the liquid entry into the cylinder and its subsequent behaviour through the combustion cycle was observed by a high-speed CCD camera in a transparent engine. Strip-atomisation of the fuel film by the intake flow, squeezing of fuel film between the intake valve and valve seat at valve closing to form large droplets and deposition of liquid fuel as films distributed on the intake valve and head region were captured. It was shown that some of the liquid fuel survives combustion into the next cycle. The time evolution of the in-cylinder liquid film is influenced by the injection geometry, injection timing, injected air-to-fuel ratio and port surface temperature. Photographs showing the liquid fuel features and an explanation of the observed phenomena are given in the paper.

Nagaoka, Kawazoe and Nomura (1994) developed a new spray/wall impingement model for gasoline engines. The model is based on experimental analysis of impinging spray droplets using a phase Doppler particle analyser (PDPA). Three new equations were obtained in terms of droplet size, Weber number and the angle from a wall for droplets which were splashed after impinging or created by the impact of a droplet on the liquid film layer on the wall. The model is also applied to the fuel mixture formation process in a lean-burn gasoline engine.

O'Rourke and Amsden (1996) detailed the dynamics of the wall film are influenced by interactions with the impinging spray, the wall and the gas flow near the wall. The coupled nature of the gas flow, wall film and the solid wall were introduced. The spray influences the wall film mass, tangential momentum and energy addition. The wall affects the film through the no-slip boundary condition and heat transfer and the gas alters film dynamics through tangential stresses and heat and mass transfer in the gas boundary layers above the films. New wall functions are given to predict transport in the boundary layers above the vaporising

films. The unsteady heating of the film was considered as the liquid Prandtl numbers are typically about higher (~10).

O'Rourke and Amsden (2000) reported the extensions of a three-dimensional computational model for the liquid wall films formed in port fuel injected engines. The extensions incorporate effects associated with spray/wall interactions-including droplet splash, film spreading due to impingement forces, and motion due to film inertia. It also includes a sub-model for the effects of liquid expelled from valve seat areas when valves close. Implementation of the extensions in the KIVA-3V computer program was described, and results of KIVA calculations of open and closed valve injection in a realistic four-valve engine geometry presented. Computed film locations agree qualitatively with laser-induced fluorescence measurements. Stevens and Steeper (2001) studied the piston-wetting effects in an optical direct injection spark ignited (DISI) engine. Fuel spray impingement on the piston leads to the formation of fuel films, which are visualised with a laser-induced fluorescence (LIF) imaging technique. Oxygen quenching was found to reduce the fluorescence yield from liquid gasoline. Fuel films that exist during combustion of the premixed charge ignite to create piston-top pool fires. It was characterised using direct flame imaging. Soot produced by the pool fires is imaged using laser elastic scattering and is found to persist throughout the exhaust stroke, implying that piston-top pool fires are a likely source of engine-out particulate emissions for DISI engines.

Sandquist, Lindgren and Denbratt (2000) detailed the influence of fuel properties on exhaust hydrocarbon (HC) emission and investigated the sources of HC emission in GDI engine. In this case, Ricardo Hydra MK III single cylinder engine was used to understand the emissions. It was reported that the overmixing (quenching) at the boundaries of the air fuel mixture cloud, and undermixing of both in the spray centre and on the surface of the piston bowl are the dominating mechanism of HC emission formation. The injection timing and the flow structure determines the fuel and air mixing timescales. Also, the undermixing increases the fuel air mixture non-homogeneity and results in carbon monoxide and soot emissions. The main sources of hydrocarbon emissions from SI engines were listed as:

a. Filling of crevices resulting in unburned mixture escaping combustion.
b. Absorption of fuel by lubricating oil during the intake and compression strokes
c. Quenching of flame at the cylinder walls
d. Quenching of flame in the bulk gas due to local mixture inhomogeneities
e. Deposit absorption and desorption of fuel
f. Valve leakage.

Their literature review suggests that the 90% of unburned HC from homogeneous charge SI engines results from crevices and the fuel absorption and desorption by cylinder lubricating oil. The volatility of the fuels shows higher influence on HC emissions. It was also reported that a more realistic fuel was recommended when developing DISI engines.

Han, Yi and Trigui (2002) studied the combustion of a stratified-charge DISI combustion system at Ford. This paper presents the multidimensional engine CFD modelling analysis of mixture formation and piston surface wetting under the stratified-charge conditions. The effect of various design and operating parameters, including piston shape, spray cone angle, swirl ratio, injection timing, engine speed and load on charge stratification and piston-wetting due to spray impingement, were studied. The model was shown to be capable to predict piston surface wetting and a qualitative correlation was found between the amount of the remaining liquid fuel on the piston surface and the engine-out smoke number.

Drake et al. (2003) detailed the effects of wall films of liquid fuel on the piston surface in DISI engines. It was reported that these fuel films can result in pool fires that lead to deposit formation and increased HC and smoke emissions. High-speed refractive-index-matching imaging technique was used for quantitative time and space-resolved measurements of fuel-film mass on a quartz piston window of an optically-accessible direct-injection engine operating over a range of fully-warmed up stratified-charge conditions with both a high-pressure hollow-cone swirl-type injector and with a high-pressure multi-hole injector. Most of the piston fuel-film mass evaporates during the cycle and burns as a pool fire. The fuel-film data are also correlated with engine-out HC and smoke emissions measurements from a conventional all-metal single-cylinder engine of the same design. Smoke emissions from the engine with a high-pressure swirl injector increase linearly with the measured fuel-film mass. Swirl atomiser reported higher smoke emission in comparison to high pressure multi-hole injector. Fuel film alone was not the only cause of HC emission at all engine operating conditions. Soot or particulate emission is one of the major challenges in the future engine development.

Smith (1981) discussed experimental evidence obtained on a wide variety of different combustion systems (premixed and diffusion flames, perfectly stirred reactors, etc.) and with wide variety of different fuels indicating that chemical kinetics is the dominant rate process governing the emission of soot from the system. Even well-mixed systems are observed to emit soot when the local carbon to oxygen ratio in the fuel-oxidiser mixture exceeds 0.5. The mechanism of soot formation formed from the vapour phase flames was detailed. In this, the pyrolysis or the oxidative pyrolysis initiates the inception of the soot and subsequently followed by nucleation. Pyrolysis reactions are generally endothermic, with the result that their rates are often highly temperature dependent. In parallel, the process of surface growth and

coagulation results in the growth of the soot particles, followed by coalescences. Coagulation and aggregation may be minimised by use of additives which act to promote particle charging by lowering the ionisation potential of the particulate material. In soot oxidation kinetics, particle oxidation will be enhanced by long residence times under conditions of high temperature (T > 2000K) and large partial pressure of oxygen. Radiation has shown to result in significant heat losses in such systems, which reduces the particulate oxidation. Final soot emission is the result of competition between the coagulation-aggregation and surface oxidation rates. This study further necessitates the importance of the local carbon to oxygen ratio. As the commercial fuel is a mixture of a finite number of surrogate components with different thermochemical properties and evaporation characteristics, a proper representation is required in the simulation process.

Yang and Reitz (2009) developed a continuous multi-component (CMC) fuel evaporation model which has been integrated with an improved G-equation combustion and detailed chemical kinetics model. The integrated code has been successfully used to simulate a gasoline direct injection engine. Ra and Reitz (2009) developed a discrete multi-component (DMC) fuel approach used to model the properties and composition of gasoline and diesel model fuels. The gasoline was represented as seven components (iC_5H_{12}, iC_6H_{14}, iC_7H_{16}, iC_8H_{18}, C_9H_{20}, $C_{10}H_{22}$ and $C_{12}H_{26}$). Unsteady vaporisation of single and multi-component fuel droplets and sprays was considered for both normal and flash-boiling evaporation conditions. An unsteady internal heat flux model and a model for the determination of the droplet surface temperature were formulated. An approximate solution to the quasi-steady energy equation was used to derive an explicit expression for the heat flux from the surrounding gas to the droplet–gas interface, with inter-diffusion of fuel vapour and the surrounding gas. The density change of the droplet as a function of temperature was also considered. The vaporisation models were implemented into a multi-dimensional CFD code and applied to calculate evaporation processes of single and multi-component fuel droplets and sprays for various ambient temperatures and droplet temperatures. Differences between representing model fuels using the single and multi-component fuel descriptions were discussed. The variation of ambient temperature is also very influential. The rate of decrease of drop lifetime with respect to increases in the ambient temperature decreases with increasing ambient temperature. The initial droplet temperature mainly affects the early stages of evaporation of single multi-component droplets. Preferential evaporation of the light-end components of multi-component fuels increases the number of light-end components upstream of the spray plume. The heavy-end components are found predominantly in the region near the tip of the spray. Flash-boiling enhances the evaporation rate of multi-component fuel sprays such that the fuel vapour

distribution in the near-nozzle region becomes wider and the vapour penetration distance is shortened.

Xu et al. (2009) developed a CFD model to account for the multicomponent droplets to address design challenges in GDI engine combustion system development. In-house. Ford developed CFD code MESIM (Multi-dimensional Engine Simulation) which was applied to the study. The effect of the multi-component droplet model on the fuel air mixture preparations under different engine conditions was discussed and the modelling approach was applied to guide the GDI engine piston designs. Effects of piston designs on the fuel air mixture preparation were presented. It was found that the multi-component fuel model was critical to the accuracy of the model prediction under cold start conditions. The gasoline was considered as a blend n-pentane (0.22), iso-octane (0.58) and n-decane (0.2). It is concluded that, under engine warm up conditions, single component fuel modelling could produce similar fuel vaporisation characteristics as that of multi-component fuel modelling.

Therefore, the single component fuel could be used to simulate the air-fuel mixing process and evaluate the effect of designs on this process with little sacrifice in accuracy. However, under engine cold start conditions, both n-hexane fuel and iso-octane fuel significantly over predict fuel vaporisation at certain temperatures, while significantly under-predicting at other temperatures in comparison with the three-component fuel.

Wang and Lee (2005) developed a multicomponent fuel film vaporisation model using continuous thermodynamics for multidimensional spray and wall film. The vaporisation rate at the film surface was evaluated using the turbulent boundary-layer assumption and a quasi-steady approximation. Third-order polynomials were used to model the fuel composition profiles and the temperature within the liquid phase to predict accurate surface properties that are important for evaluating the mass and moment vaporisation rates and heat flux. By this approach, the governing equations for the film are reduced to a set of ordinary differential equations resulting in a significant reduction in computational cost while maintaining adequate accuracy compared to solving the governing equations for the film. The fuel mixture is described by a continuous distribution function (Cotterman et al., 1985) as a function of their molecular weights of each component.

Rotondi and Bella (2005) carried out a numerical study of a hollow cone fuel spray generated by a high-pressure swirl injector for a gasoline engine. The spray characterisation was carried out with a quiescent air chamber at ambient temperature and pressure. The modelling methodologies to predict the initial breakup length were discussed in Han et al. (1997) and Nagaoka and Kawamura's (2001) primary breakup model for hollow cone sprays. The measured transient initial cone angles were used in their simulation tool. They could predict the penetration depth less than 2% with that of the experiments. The different secondary

breakup occurrences for vibrational and bag were resolved over time. These two mechanisms were found to oppose each other. These models were used in the multidimensional in-cylinder CFD simulations to predict the charge air fuel distribution for both homogeneous and stratified mode.

Torres et al. (2006) provided the fundamental framework for the single component and multicomponent droplet evaporation using a single droplet approach. This was implemented in KIVA 3V. In this code, the internal conduction and species diffusion in the droplet and liquid film were solved by discretising the energy and species conservation equation. As the computational time is very expensive on top of the general flow and fuel mixing, a very coarse approach was adopted to resolve the droplets and the liquid film. In this, a simple one dimensional finite volume code with a TDMA solver were used for droplets. The single droplet surface temperature and the droplet diameter were validated with the experimental data from Daif et al. (1999).

Huu et al. (2007) described the numerical implementation and validation of a newly developed hybrid T-blob/T-TAB model into their existing CFD code. This model extends the two widely used Kelvin-Helmholtz (KH) instability model of Reitz (1987) for primary breakup and Taylor analogy breakup (TAB) secondary droplet breakup model of O'Rourke and Amsden (1987) to include the liquid turbulence effects. The secondary droplet breakup mechanisms were modified to account for the additional turbulence forces acting on the primary droplets. They reported to predict the product droplet size better in comparison to the earlier methods.

Abianeh and Chen (2011) incorporated the liquid turbulence effect in modelling the multi-component droplet liquid jet evaporation. The finite conductivity model is based on a newly developed two-temperature two-layer film theory where the turbulence characteristics of the droplet are used to estimate the effective thermal conductivity. In this paper, effective mass transfer diffusivity within the droplet was considered. In this model, the individual droplets are considered as four regions, interior, surface of the droplet, the liquid gas interface and the surrounding gas phase. An approximate solution to the quasi-steady energy equation was used to derive explicit expression for the heat flux from the surrounding gas to the droplet–gas interface, with inter-diffusion of fuel vapour and the surrounding gas considered. The thermo-transport properties, including their dependence on temperature were considered. Validation studies were carried out by comparison with the experimental results. They have also the necessity of the multicomponent treatment of the gasoline or the diesel fuel. Multi-component fuel models are classified into two types, discrete multi-component model (computationally expensive) and continuous multi-component model. Droplet discretisation is

characterised as rapid mixing model (RMM), thin skin model (TSM) and diffusion limit model (DLM).

Reitz (2011) developed reduced chemical kinetic mechanisms for the oxidation of representative surrogate components of a typical multi-component automotive fuel and applied to model internal combustion engines. They also developed a combustion model to simulate engine combustion with multi-component fuels using the MultiChem mechanism, and the model was applied to simulate HCCI and DI engine combustion. The results show that the present multi-component combustion model gives reliable performance for combustion predictions, as well as computational efficiency improvements using reduced mechanism for multi-dimensional CFD simulations.

Tongroon and Zhao (2013) studied the possibility of direct fuel injection into hot residual gases to promote and control the auto ignition timings during controlled auto-ignition combustion of gasoline engines. To understand the underlying physical and chemical processes involved, a systematic experimental study was carried out on a single-cylinder engine with optical access by means of thermodynamic analysis, high-speed chemiluminescence imaging and in-cylinder sampling-based gas chromatography and mass spectroscopy measurements. The calculations illustrate that the charge cooling effect dominates over the volumetric expansion effect and leads to lower in-cylinder temperature. Methanol blend and ethanol blend show the least ignition delay in comparison to gasoline. The exothermic reactions enhance the ignitability more than that of pyrolysis reactions by increasing the temperature. Thermal effect of alcohol fuels dominates over the chemical effect of gasoline case. This also shows the necessity of considering the multicomponent fuel representation in the simulation procedure. This could represent the complexity of the competitive reaction kinetics of different gasoline blends found in the market fuels.

Sprays are normally modelled using stochastic approach for in-cylinder simulation application. Treatment of using multi-phase assumptions is computationally expensive. Befrui et al. (2011) modelled multi-phase flow using large eddy simulation (LES) with the actual multi-hole nozzle and the associated geometry. The simulation predicts the flow through nozzle along with the flow contraction. In Figure 2.4, the flow separation at the nozzle entrance and the two fluid zones is clearly highlighted.

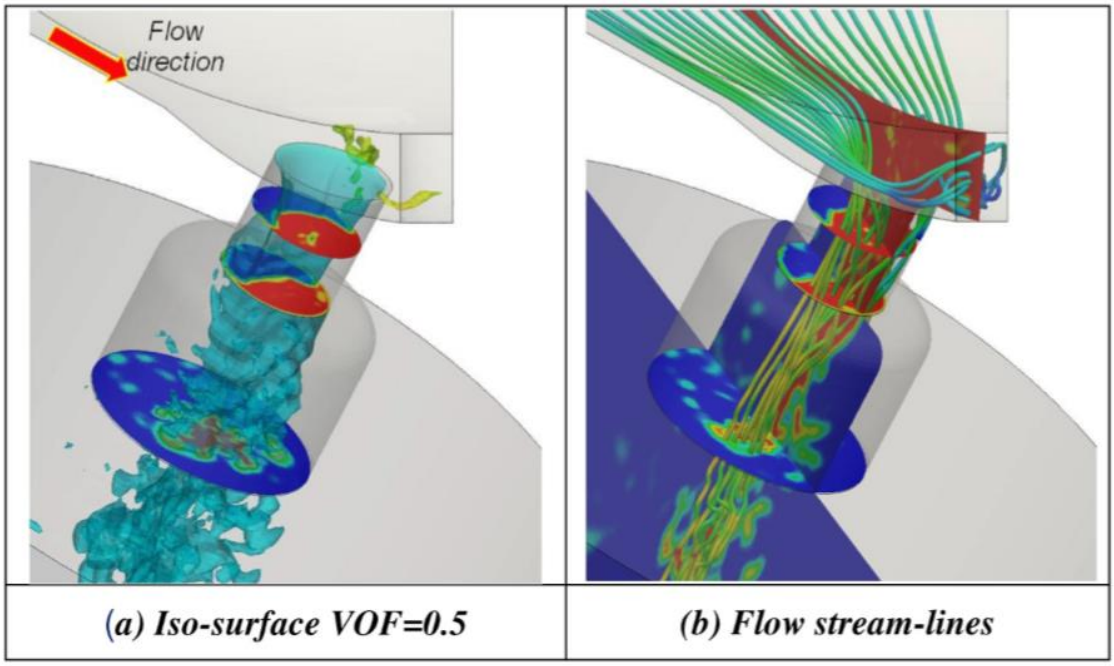

Figure 2.4: VOF-LES simulation results, showing isosurfaces of n-heptane VOF and flow-lines at 200 bar injection pressure (Picture taken from Befrui et al., 2011).

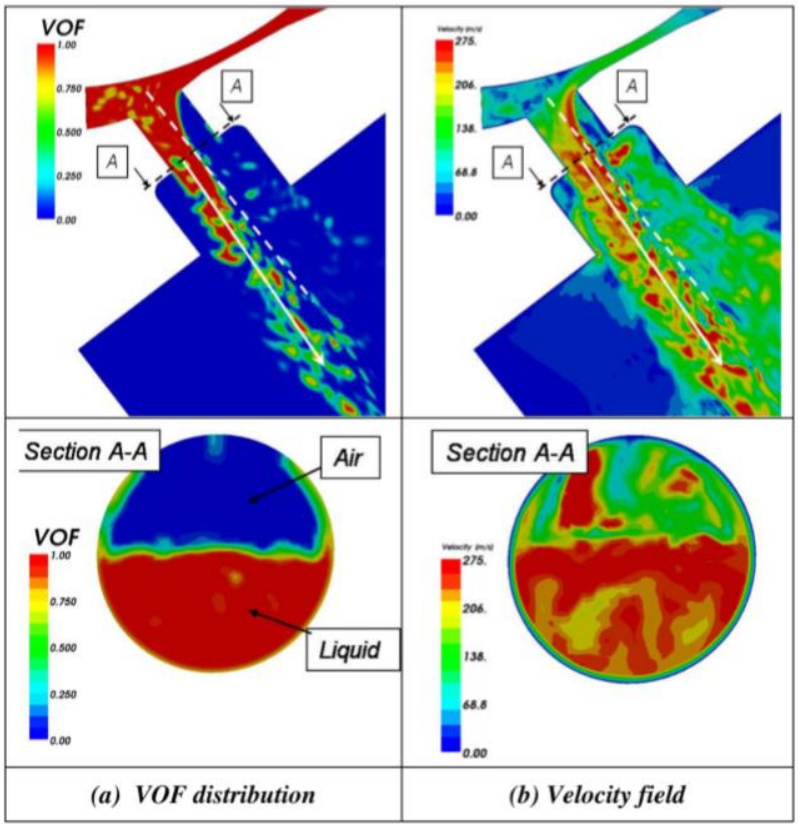

Figure 2.5: VOF-LES simulation results, showing VOF of n-heptane and velocity distribution at 200 bar injection pressure (Picture taken from Befrui et al., 2011).

It should be noted that the flow contraction at the nozzle entrance (Figure 2.5), accelerates the flow significantly. The effective flow area was significantly lower than the actual flow area of the nozzle. This was shown to be responsible for the pressure loss and low discharge coefficient of the nozzle. However, this is promoting the liquid jet breakup. Kelvin-Helmholtz instabilities are shown to be originating at the nozzle exit region and ensuring the jet primary breakup in and close vicinity to the counterbore region. They show the potential for coupling the injector valve-group geometry VOF methodology with the in-cylinder mixture formation simulation.

Wang et al. (2015) carried out CFD simulations to investigate the effect of in-cylinder flow motion on the in-cylinder conditions and spark ignition–controlled auto-ignition hybrid combustion. In this, a developed SI-CAI hybrid combustion code was integrated into ECFM3Z STAR-CD solver. It was indicated that the asymmetric intake valve events could be used to generate the swirl-dominated flow motion. Their investigation indicates that the in-cylinder turbulent kinetic energy level and the mean flow velocity around the spark plug would directly affect the early flame propagation process, which, in turn, affects the subsequent auto-ignition process through changing the heat transfer between central burned gas and end-gas. In addition, the increased temperature inhomogeneity of the spherical zones caused by the in-cylinder flow motion would prolong the auto-ignition combustion. The structures of the flame front and auto-ignition sites also demonstrate the significant impact of in-cylinder motion on the combustion process. They reviewed that the in-cylinder temperature is one of the most important factors to control the spark-assisted compression ignition (SICI). It was reported that the increase in swirl ratio would increase the flame propagation and autoignition; however, any further increase decreases the auto-ignition due to excessive heat loss by interaction of unburned gas with the autoignition sites.

Jiao and Reitz (2015) detailed the CFD model technique to represent surrogate multicomponent gasoline fuel. Initially, chemistry mechanisms for the soot formation were carried out with n-heptane, iso-octane, toluene polycyclic and aromatic hydrocarbons (PAH). This model was validated with combustion data. They introduced a grid independent wall film model for predicting wall films. It was further confirmed that the vaporisation of the wall film is one of the significant causes of the soot formation in the spark ignition engines. Simulation comparisons were shown for the late injection cases. In this, more than 89 species and 506 reactions were considered. Detailed HC oxidation chemical kinetic mechanisms were applied to simulate the post-flame reactions and heat release. In summary, they shown the mature

modelling technique to account for multicomponent droplet modelling (evaporation, boiling), wall-film, turbulence, chemical kinetics, spark modelling and soot predictions.

The soot formation mechanism was briefly described in this paper. It was depicted that, when a flame propagates towards a liquid film on the piston, all the regions swept by the flame surface become burnt regions that include some free radicals at high temperature, and these high temperature regions approaching the liquid film enhance the liquid film vaporisation and form fuel-rich zones. However, fuel oxidation in the vapour phase above the liquid film was limited due to the lack of oxygen in the burnt regions. Since combustion in rich regions near fuel wall films is of interest, fuel pyrolysis was also considered in the chemistry mechanism. Pyrolysis is the process whereby organic compounds, that is, fuels, break down into simpler molecules at high temperature in the absence of oxygen. This is considered to be the fundamental process of soot inception. They also introduced a grid-independent wall film vaporisation model for practical mesh sizes with a definite wall film thickness which was tested with backward facing step 3D model. The in-cylinder simulation showed that high soot levels are more likely to be formed in the rich regions near the wall films. The present models allow to study the influence of fuel composition and other strategies on soot emissions in DISI engines.

In the experimental investigation available from the literature, the spray atomisation is inherently stochastic in nature. These are characterised by some of the fundamental non-dimensional numbers (We, Re_d). In the GDI engine application the complexities further amplify due to the presence of air jets interacting with the atomisation process. An accurate numerical prediction of spray behaviour for the application is difficult. As described by Von Kuensberg Sarre, Kong and Reitz (1999), a phenomenological model simplifies the complexities for representing the multi-hole injector spray behaviour. The modelling constants reported in this literature are found to be a function of injection pressure. Moreover, the gasoline fuel is a blend of light and heavier components (Ra and Reitz, 2011), the differential evaporation during the mixture formation and the resultant combustion adds complexity. However, Xu et al. (2009) reported an equivalent thermo-physical property can be applied for an engine warm up conditions. A high-fidelity simulation, as applied by Jiao and Reitz (2015) considering a discrete multi-component model (DCM) with detailed chemistry to predict the particulate emission, is difficult in the engine design iteration stage. Similarly, numerical modelling using LES for the multi-hole nozzle as used by Befrui et al. (2011) in an engine application is computationally expensive. The flow contraction captured in the simulation at the vena contracta contributes to a significant change in the injection velocity for a low L/D injector nozzles, which is the case for the modern high pressure GDI injectors. It should also be noted that the spray impingement on the engine wall and the resultant combustion are responsible

for the HC and PN/PM emission. The liquid film thickness depends on the size of the droplets and the impinging wall conditions. Hence, a good spray atomisation model is required to predict the droplet size and velocity after the breakup. This is required to predict the mixture formation and the resultant combustion processes. Moreover, the injector model requires a more simplistic phenomenological model accounting for an equivalent representation to apply it for the in-cylinder application.

2.1.3 Modelling of in-cylinder flow

In this section, a short review on the existing numerical simulation methods applicable to turbulent flow with a focus on a spark ignited GDI engine is provided. In the turbulence model description, the species transport and chemical reaction details are not included in the discussion.

Gas exchange between the engine cylinder with the intake and exhausts, dilution, fuel injection, surface heat transfer and spark energy governs the combustion process. Generally, the charge motion in the cylinder develops during the intake stroke from the transient air jet entering through the intake port and the valve passages. The local flow instabilities originated from the relative scale of inertial and viscous forces result in turbulence. In comparison to laminar flow, the turbulent flow transport happens in a chaotic manner, resulting in enhanced mixing of fluid layers. This increases the mass, momentum and energy transfer along with enhanced reaction rates. Turbulence is a continuum phenomenon governed by general fluid mechanics. The equations of motion are non-linear and unique in terms of characteristics which are associated with the initial and boundary conditions.

2.1.3.1 General transport equation

The governing equations for a compressible Newtonian fluid (continuity, momentum and energy), in the absence of source terms are given in tensor form as below,

Continuity:

$$\frac{\partial \rho}{\partial t} + \frac{\partial}{\partial x_i}(\rho v_i) = 0 \qquad (2.7)$$

Momentum (Navier-Stokes):

$$\frac{\partial}{\partial t}(\rho v_i) + \frac{\partial}{\partial x_j}\left(\rho v_j v_i\right) = -\frac{\partial p}{\partial x_i} + \frac{\partial \tau_{ij}}{\partial x_j} \qquad (2.8)$$

The component of viscous stress tensor, τ_{ij} in Equation 2.8 and 2.9 are defined as

$$\tau_{ij} = 2\mu S_{ij} + \lambda \frac{\partial v_k}{\partial x_k} \delta_{ij} = 2\mu S_{ij} - \left(\frac{2\mu}{3}\right) \frac{\partial v_k}{\partial x_k} \delta_{ij} \qquad (2.9)$$

where,

v_i is the components of velocity

$\mu \ is$ the absolute/dynamic viscosity

$p \ is$ the static pressure

λ is called the second viscosity and defined by the stokes hypothesis as below

$$\lambda = -\frac{2}{3}\mu$$

The components of symmetric strain-rate (S_{ij}) tensor is given by

$$S_{ij} = \frac{1}{2}\left(\frac{\partial v_i}{\partial x_j} + \frac{\partial v_j}{\partial x_i}\right) \qquad (2.10)$$

The anti-symmetric rotation-rate (Ω_{ij}) tensor is given by

$$\Omega_{ij} = \frac{1}{2}\left(\frac{\partial v_i}{\partial x_j} - \frac{\partial v_j}{\partial x_i}\right) \qquad (2.11)$$

Energy:

$$\frac{\partial}{\partial t}(\rho E) + \frac{\partial}{\partial x_j}(\rho v_j H) = \frac{\partial}{\partial x_j}(v_i \tau_{ij}) + \frac{\partial}{\partial x_j}\left(k \frac{\partial T}{\partial x_j}\right) \qquad (2.12)$$

The total energy E and the total enthalpy H in Equation 2.12, are given by

$$E = e + \frac{1}{2} v_i v_i$$

$$H = h + \frac{1}{2} v_i v_i = E + \frac{p}{\rho}$$

where,

e and h are the internal energy and specific enthalpy, respectively

As defined earlier, the fundamental Equations 2.7, 2.8, 2.9 and 2.12 are in general form and applicable for all Newtonian compressible flows (either laminar or turbulent flow). These governing partial differential equations can be solved numerically with higher order difference scheme (Liu and Liu,1993; Cook and Riley, 1996). However, due to the complexity of the flow structure, length and time scales, capturing the resulting non-linearity requires higher order

discretisation along with higher resolution in space and time. This is referred to as Direct Numerical Simulation (DNS).

2.1.3.2 Scales of turbulent motion

In turbulence theories (Tennekes and Lumley, 1972), the randomness in the flow structure is associated with different scales of fluid structure present on a mean flow which are referred as “Eddies”. The randomness indicates that there is a wide range of eddy length scales (wave number space) present in the turbulent flow structure. The largest eddies scale is referred as “Outer or Integral” scale and the smallest as “Inner or Kolmogorov” scale. Fluid continuum is valid, i.e., even the smallest scale is much larger than the molecular lengths scale. In the turbulent flow scaling analysis, the length, velocity and time scales associated with the integral scales are defined by, $\ell_I, u_I \text{ and } \tau_I$, respectively. Similarly, for Kolmogorov scale, the length, velocity and time scales are defined by $\ell_k, u_k \text{ and } \tau_k$, respectively. It is assumed that the rate at which large-scale eddies supply energy to the small-scale eddies is inversely proportional to the time scale of the largest eddies, τ_I,

where,

$$\tau_I = \frac{\ell_I}{u_I} \qquad (2.13)$$

The energy content of the eddies is defined by its kinetic energy. The amount of kinetic energy per unit mass of the eddies associated in the integral length scale is proportional to the square of the integral velocity scale (u_I^2). Thus, the rate of energy supplied by the integral eddies is given by

$$\frac{u_I^2}{\tau_I} = \frac{u_I^3}{\ell_I} \qquad (2.14)$$

By Kolmogorov’s universal equilibrium theory of small-scale structure, the net rate of energy dissipated in molecular scale, ϵ, is equal to the rate at which the is energy supplied (Equation 2.14) by the large-scale eddy motion.

Kolmogorov length, time and velocity scales are given by

$$\ell_k \equiv \left(\frac{\nu^3}{\epsilon}\right)^{1/4} \qquad (2.15)$$

$$\tau_k \equiv \left(\frac{\nu}{\epsilon}\right)^{1/2} \qquad (2.16)$$

$$u_k \equiv (\nu\epsilon)^{1/4} \qquad (2.17)$$

where,

ν and ϵ are kinematic viscosity and dissipation, respectively. It should be noted that the Reynolds number based on the smallest eddy motion scales is $Re_k \sim 1$ ($i.e.\ Re_k = \frac{u_k \ell_k}{\nu} = \frac{(\nu\epsilon)^{1/4}\left(\frac{\nu^3}{\epsilon}\right)^{1/4}}{\nu} = 1$). It indicates that the small-scale motions are highly viscous and, hence, the small scales are viscosity-controlled.

Using the above scaling forms, the length, time and velocity scales of the smallest and largest eddies present in a turbulent flow structure can be related based on the integral Reynolds number ($Re_I = \frac{u_I \ell_I}{\nu}$). The final forms of the relative scale are given below,

$$\frac{\ell_k}{\ell_I} \sim (Re_I)^{-3/4} \qquad (2.18)$$

$$\frac{\tau_k}{\tau_I} \sim (Re_I)^{-1/2} \qquad (2.19)$$

$$\frac{u_k}{u_I} \sim (Re_I)^{-1/4} \qquad (2.20)$$

$u_I \sim u' \sim (\frac{2}{3}k)^{1/2}$ (Pope, 2000, p. 183)

A schematic of a typical engine condition taken for understanding the relative scales for resolving space and time of a typical numerical simulation is shown in Figure 2.6.

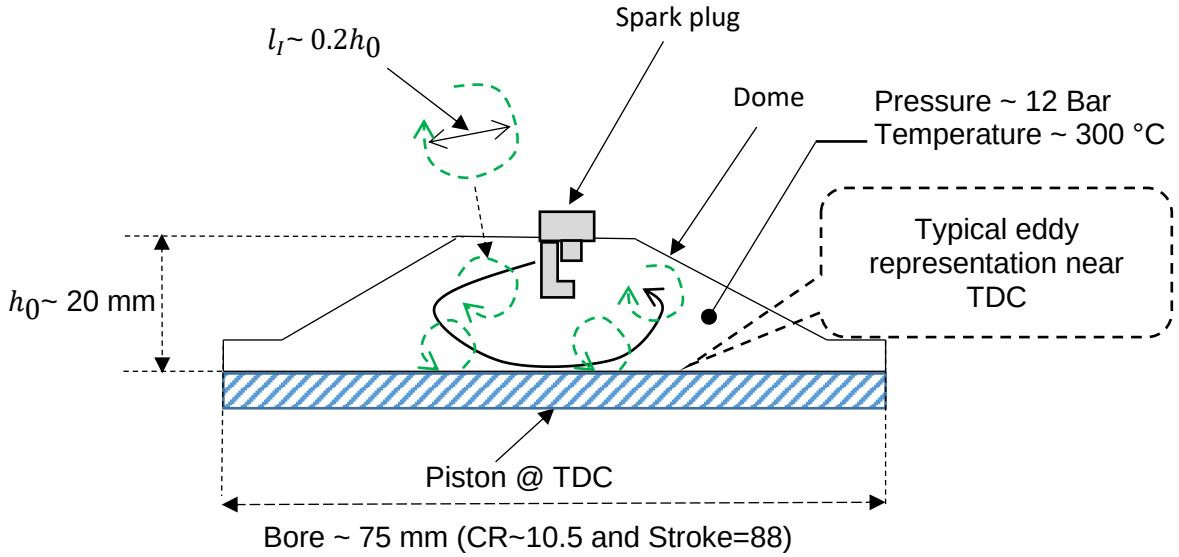

Figure 2.6: A Schematic of a typical engine parameters taken for the simple scaling analysis for evaluating the space and time resolution. This is equivalent to a condition with the piston at compression top dead centre of the cylinder.

In this case, $\ell_I \sim 0.2\ h_0$ and $u_I \sim u' = 0.5\ \bar{V}_P$ (Heywood, 1989, p. 341) are taken. The engine parameters used for the calculation are listed in Table 2.1.

Table 2.1 Typical in-cylinder condition taken for scaling analysis

Engine speed	1200	RPM
Bore size (B)	73.5	mm
Stroke (S)	81.8	mm
Compression ratio(CR)	10.5	
Clearance height (h_0)	20	mm
Pressure at TDC	12	Bar
Temperature	573.15	K
Dynamic viscosity (μ)	2.93E-05	Ns/m^2
Density (ρ)	7.28	kg/m^3
Mean piston speed ($\bar{V}_p$)	3.272	m/s
Stroke volume (S_V)	347070.63	mm^3
Clearance volume (V_c)	36533.75	mm^3

Using Equations 2.18, 2.19 and 2.20, the calculated scales of turbulent motion are shown in Table 2.2. The calculated turbulent Reynolds number from the integral scale is ($Re_I = \frac{u_I \ell_I}{\nu}$) ~ 1600. It should be noted that, lower the kinematic viscosity, higher the Reynolds number of the largest eddies for the same velocity and length scale.

Table 2.2: Typical in-cylinder condition noticed near TDC.

Integral length scale (ℓ_I) ~ 0.2 h_0	4	mm
Integral velocity scale ($u_I \sim u' = 0.5\ \bar{V}_P$)	1.636	m/s
Integral time scale ($\tau_I = \ell_I / u_I$)	0.002445	s
Kinematic viscosity (ν= μ/ρ)	4.02E-06	m^2/s
Integral scale Reynolds number ($Re_I = u_I\ \ell_I$ / ν)	1629.5	
$\ell_k/\ell_I = (Re_I)^{-(3/4)}$	3.90E-03	
$\tau_k/\tau_I = (Re_I)^{-(1/2)}$	2.48E-02	
$u_k/u_I = (Re_I)^{-(1/4)}$	1.57E-01	
Kolmogorov length scale (l_k)	1.56E-02	mm
Kolmogorov time scale ($\tau_k = (Re_I)^{-(1/2)}\ \tau_I$)	6.06E-05	s
Size of eddy resolution ~ (ℓ_k x ℓ_k x ℓ_k)	3.79E-06	mm^3
Number of cells (Clearance volume / Size for eddy resolution)	9.6E+09	#

It is evident that for the chosen condition illustrated in Figure 2.6, the ratio of Kolmogorov length scale to the integral length scale is small (i.e., ℓ_k , is $4\mathrm{e}^{-3}$ times smaller than ℓ_I). This is equivalent to a Kolmogorov length scale (ℓ_k) of $1.6\mathrm{e}^{-2}\mathrm{mm}$. Thus, to capture one smallest length scale contained in a cell, a volume equivalent of $3.8\mathrm{e}^{-6}$ mm^3 is required. In an engine simulation with a clearance volume of 36533.75 mm^3, at least $9.6\mathrm{e}^{9}$ cells may be required. The cell number needs to be further scaled up for resolving the smallest eddy. Hence, DNS is computationally expensive and difficult to be carried out for a normal engine simulation even with an extremely powerful computing facility. The complexity adds up in the time scales, if reactions and other scalar transports are considered.

Instead of a fully resolved DNS simulation approach, statistical methods are considered to represent the equivalent randomness in flow, fuel mixing, chemical reactions and the resultant flame propagations (Heywood, 1989; Turns, 2000).

2.1.3.3 Reynolds decomposition of instantaneous velocity and scalar components

The first approach for the approximate treatment of turbulent flows was presented by Reynolds (1895). Wherein, the instantaneous velocity is split into mean velocity ($\bar{v}_i$) and fluctuating/turbulent velocity (v'_i). This is given by Equation 2.21. A similar definition holds for the pressure (P) and density (ρ) term which are given by Equation 2.22 and 2.23, respectively.

$$v_i = \bar{v}_i + v'_i \qquad (2.21)$$

$$P = \bar{P} + p' \qquad (2.22)$$

$$\rho = \bar{\rho} + \rho' \qquad (2.23)$$

where, $\bar{P}$ and $\bar{\rho}$ are the Reynolds averaged mean pressure and density, respectively. Similarly, p' and ρ' are the fluctuating pressure and density, respectively.

The mean component is calculated using one of the three forms of the Reynolds averaging procedure, namely, time averaging, spatial averaging and ensembled averaging. The mathematical descriptions for time averaging, spatial averaging and ensembled averaging for velocity (v_i) are given in Equation 2.24, 2.25 and 2.26, respectively

$$\bar{v}_i = \lim_{\tau\to\infty} \frac{1}{\tau} \int_t^{t+\tau} v_i \, dt \qquad (2.24)$$

where,

τ is typical time larger than the turbulence velocity time scale

$$\bar{v}_i = \lim_{\Omega \to \infty} \frac{1}{\Omega} \int_{\Omega} v_i d\Omega \qquad (2.25)$$

where,

Ω is control volume in space

$$\bar{v}_i = \lim_{N \to \infty} \frac{1}{N} \sum_{i=1}^{N} v_i \qquad (2.26)$$

where,

N is the number of experiments for a specific spatial location and time

In all the three-averaging process, the below statistical assumptions are made,

$\overline{v'_i} = 0;\ \overline{v'_i v'_i} \neq 0;\ \overline{v'_i v'_j} \neq 0$

A schematic representation of turbulent flow velocity component at a sample point for an engine cylinder application is shown in Figure 2.7. In this description, the three velocity representations, namely instantaneous velocity (v_i), Reynolds average velocity ($\bar{v}_i$) and fluctuating velocity (v'_i) are shown. In statistically non-stationary turbulence, for any fixed spatial coordinates, $\bar{v}_i$ is a function of time. Hence, the ensembled form of Reynolds averaging is adopted. In this case, at each spatial location and time, the velocity components and the scalar quantities are averaged by superimposing several repeated experiments starting with the same initial and boundary conditions.

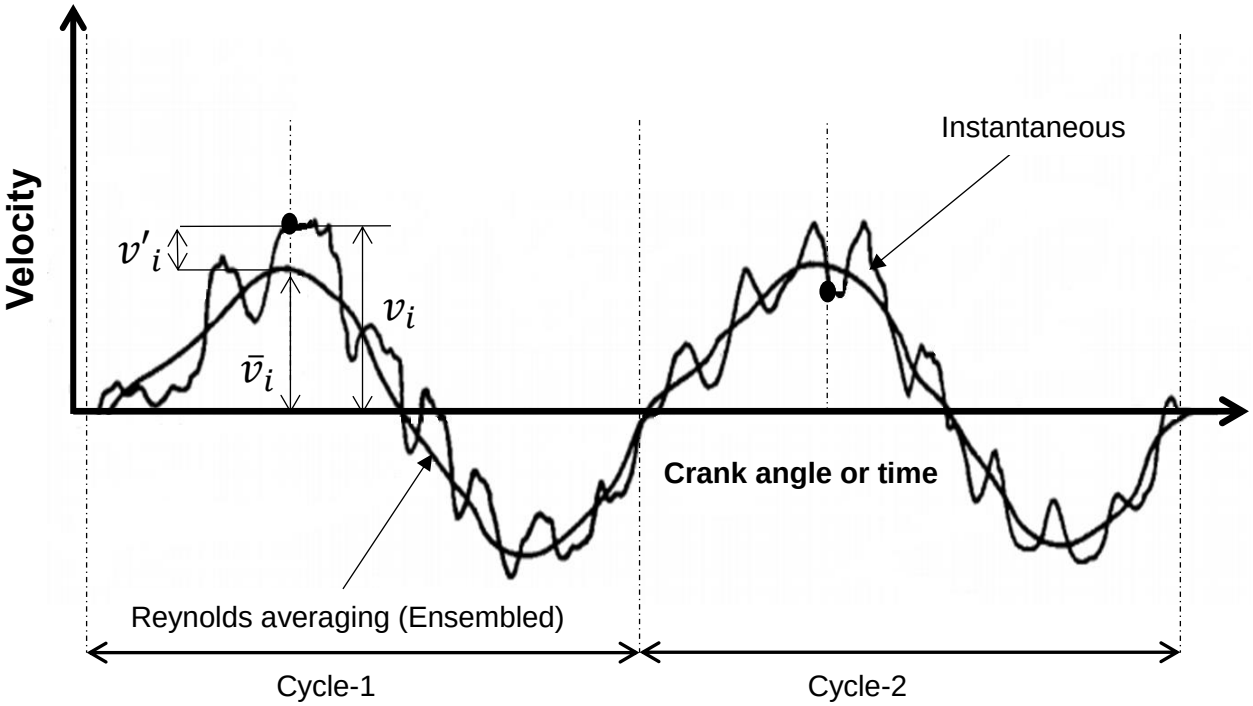

Figure 2.7: Schematic of i[th] velocity component variation with crank angle or time at a fixed location of the engine cylinder for two consecutive engine cycles are shown for numerical simulation considerations. Dots indicate instantaneous i[th] velocity component for the two-adjacent engine cycle.

2.1.3.3.1 Compressibility corrections

In compressible turbulent flows (Wilcox, 2006, pp. 239-296), Morkovin's hypothesis is commonly used to assume that the turbulent structure is less affected by the density fluctuation (ρ'). However, in a flow with significant heat transfer or with combustion, the density fluctuation is significant (i.e. $\rho'/\bar{\rho}$ is not small). In this case, density/mass weighted or Favre decomposition (Favre,1965) is adopted for velocity and other scalars (internal energy, enthalpy and temperatures) in the transport equation. Favre averaged velocity decomposition is given by Equation 2.27.

$$v_i = \tilde{v}_i + v''_i \qquad (2.27)$$

where,

$$\tilde{v}_i = \frac{1}{\rho}\lim_{\tau\to\infty}\frac{1}{\tau}\int_t^{t+\tau}\rho \mathrm{v}_i\, dt = \frac{\overline{\rho v_i}}{\bar{\rho}} \qquad (2.28)$$

$$\bar{\rho}\tilde{v}_i = \overline{\rho v_i} \qquad (2.29)$$

$\tilde{v}_i$ is Favre averaged velocity. Substituting, $v_i = \bar{v}_i + v'_i$ in Equation 2.28 and averaging yields

$$\bar{\rho}\tilde{v}_i = \bar{\rho}u_i + \overline{\rho' u'_i} \qquad (2.30)$$

$\overline{v''_i}$, is fluctuating velocity component originated from Favre averaging ($\widetilde{v''_i} = \frac{\overline{\rho v''_i}}{\bar{\rho}} \sim 0$ and $\overline{v''_i} \neq 0$) with compressible flow assumption.

The primitive-variable form of the compressible continuity equation (Equation 2.31) is obtained by substituting Equation 2.21 and 2.23 in Equation 2.7.

$$\frac{\partial \bar{\rho}}{\partial t} + \frac{\partial}{\partial x_i}\left(\bar{\rho}u_i + \overline{\rho' u'_i}\right) = 0 \qquad (2.31)$$

A form defined by Equation 2.28 is applicable for Favre decomposition of other scalars, such as, temperature, enthalpy and internal energy. This can be given by, $T = \tilde{T} + T''$, $h = \tilde{h} + h''$, $e = \tilde{e} + e''$, for temperature, enthalpy and internal energy, respectively. The local heat flux vector is given by the sum of the laminar heat flux and turbulent heat flux which is given by $q_j = q_{L_j} + q'_j$. Where, q_j, q_{L_j} and q'_j are the total heat flux, laminar heat flux and turbulent heat flux, respectively. However, a standard ensembled form of Reynolds averaging (Equation 2.24) is adopted for density and pressure.

The governing equation for continuity, momentum and energy for turbulent compressible flows (Blazek, 2001; Wilcox, 2006) are given below,

Continuity:

$$\frac{\partial \bar{\rho}}{\partial t} + \frac{\partial}{\partial x_i}(\bar{\rho}\,\tilde{v}_i) = 0 \qquad (2.32)$$

It could be noticed in Equation 2.32 that the primitive-variable form of velocity description in Equation 2.31 is replaced by Equation 2.30. This simplifies the continuity equation mathematically for accounting the density fluctuations in turbulent compressible flows.

Momentum:

$$\frac{\partial}{\partial t}(\bar{\rho}\tilde{v}_i) + \frac{\partial}{\partial x_j}\left(\bar{\rho}\tilde{v}_j\tilde{v}_i\right) = -\frac{\partial \bar{P}}{\partial x_i} + \frac{\partial}{\partial x_j}\left(\tau^F_{ji} - \overline{\rho v''_j v''_i}\right) \qquad (2.33)$$

where,

$\bar{P} = \bar{\rho} R \tilde{T}$; R, Gas constant; $\tilde{T}$, Favre averaged gas temperature.

τ_{ji}^{F} , the viscous stress tensor, calculated from the Favre-averaged velocity components.

Equation 2.33 is referred to as Favre Reynolds-Averaged Navier-Stokes equation (Favre-RANS). In comparison to the general compressible flow, Navier-Stokes Equation 2.8, the mathematical simplification with the velocity decomposition using Favre averaging (Equation 2.31) approximates the enhanced momentum transfer from eddies/fluctuating velocity scales with an additional gradient of second order tensor $-\overline{\rho v''_j v''_i}$. The term, $-\overline{\rho v''_i v''_j}$, in Equation 2.33, is referred as Favre-averaged Reynolds-stress. This simplification enables to solve the turbulent momentum transfer with Favre averaged velocity, without having to resolve different scales of eddy motion on the mean velocity flow field. However, to solve the Favre-RANS equation, the second order Reynolds stress needs a closure/assumption/model.

The second order Reynold stress tensor could be expanded into nine components in 3-D, as given below:

$$-\overline{\rho v''_j v''_i} = \begin{bmatrix} \overline{\rho v''_1 v''_1} & \overline{\rho v''_1 v''_2} & \overline{\rho v''_1 v''_3} \\ \overline{\rho v''_2 v''_1} & \overline{\rho v''_2 v''_2} & \overline{\rho v''_2 v''_3} \\ \overline{\rho v''_3 v''_1} & \overline{\rho v''_3 v''_2} & \overline{\rho v''_3 v''_3} \end{bmatrix} \qquad (2.34)$$

In Equation 2.34, the fluctuating velocity components, v''_i and v''_j in $\overline{\rho v''_i v''_j}$ are interchangeable. It means $\overline{\rho v''_1 v''_2} = \overline{\rho v''_2 v''_1}$; $\overline{\rho v''_1 v''_3} = \overline{\rho v''_3 v''_1}$; and $\overline{\rho v''_2 v''_3} = \overline{\rho v''_3 v''_2}$. This simplifies the nine variables defined in Equation 2.34 to six variables. The diagonal terms in Reynolds stress Equation 2.34 represent the normal components. The sum of the diagonal terms in Equation 2.34 is used to compute the density weighted turbulent kinetic energy, which can be given as

$$\bar{\rho} k = \frac{1}{2} \overline{\rho v''_\iota v''_\iota} = \frac{1}{2} \left(\overline{\rho v''_1 v''_1} + \overline{\rho v''_2 v''_2} + \overline{\rho v''_3 v''_3} \right) \qquad (2.35)$$

k, Turbulent kinetic energy

Favre-averaged turbulent kinetic energy transport equation is arrived at by averaging each term of the equation formed by the dot product of instantaneous momentum equation (Equation 2.8) and fluctuating velocity vector (v''_i). The final form of turbulent kinetic energy is given by Equation 2.36.

$$\frac{\partial}{\partial t}(\bar{\rho}k) + \frac{\partial}{\partial x_j}(\bar{\rho}\tilde{v}_j k) = -\overline{\rho v''_j v''_i}\frac{\partial \tilde{v}_i}{\partial x_j} - \bar{\rho}\epsilon + \frac{\partial}{\partial x_j}\left[\left(\overline{\tau^F_{ji} v''_i} - \overline{\rho v''_j \frac{1}{2} v''_i v''_i} - \overline{\mathrm{p}' v''_j}\right)\right] - \overline{v''_i}\frac{\partial \bar{\mathrm{p}}}{\partial x_i} + \overline{\mathrm{p}'\frac{\partial v''_i}{\partial x_i}} \quad (2.36)$$

where,

ϵ , the rate of dissipation of kinetic energy

Energy:

$$\frac{\partial}{\partial t}(\bar{\rho}E) + \frac{\partial}{\partial x_j}(\bar{\rho}\tilde{v}_j H) = \frac{\partial}{\partial x_j}\left(k\frac{\partial \tilde{T}}{\partial x_j} - \overline{\rho v''_j h''} + \overline{\tau^F_{ji} v''_i} - \overline{\rho v''_j \frac{1}{2} v''_i v''_i}\right) + \frac{\partial}{\partial x_j}\left[\tilde{v}_i\left(\tau^F_{ij} - \overline{\rho v''_i v''_j}\right)\right] \quad (2.37)$$

where,

$E = \tilde{e} + \frac{1}{2}\widetilde{v_i}\widetilde{v_i} + k$,

$\tilde{e}$, Favre averaged internal energy

$H = \tilde{h} + \frac{1}{2}\widetilde{v_i}\widetilde{v_i} + k$

H, total enthalpy

$\widetilde{h}$, Favre averaged specific enthalpy

Similarly, in comparison to the general form of energy equation (Equation 2.12), the Favre averaged Reynolds decomposition on energy equation yields Equation 2.35 with the additional averaged terms containing the fluctuating velocity (v''_i) and fluctuating enthalpy (h''). This accounts for the additional transport of heat transfer due to the eddy motion which was isolated during the Favre averaged Reynolds decomposition. In Equation 2.37, the term. $-\overline{\rho v''_j h''}$, is referred to as turbulent heat flux vector. This is an additional local fluid transport variable which needs to be closed in the solution procedure.

2.1.3.3.2 Turbulence closure models

In general, the "Closure" in turbulence modelling is referred to as the additional assumptions or approximations which are used to close the turbulent Reynolds stress tensor Equation 2.34 and the turbulent heat flux vector in Equation 2.37.

The commonly employed Reynolds stress tensor approximation was first presented by Boussinesq (1877; 1896). His approximation is based on the observation that, in turbulent flows, the mixing caused by the larger energetic eddies contributes to the major momentum

exchange. Boussinesq's hypothesis assumes (equilibrium between turbulence and mean strain rate) that the turbulent shear stress tensor is linearly proportional to the mean strain rate as in laminar flows and is given by Equation 2.38.

$$-\overline{\rho v''_i v''_j} = 2\mu_T\left(\tilde{S}_{ij} - \frac{1}{3}\frac{\partial \tilde{v}_k}{\partial x_k}\delta_{ij}\right) - \frac{2}{3}\bar{\rho}k\,\delta_{ij} \quad (2.38)$$

where,

μ_T is the turbulent or eddy viscosity

$\tilde{S}_{ij}$ the symmetric strain rate stress tensor calculated based on the Favre averaged components of velocity ($\tilde{v}_i$), given by Equation 2.39.

$$\tilde{S}_{ij} = \frac{1}{2}\left(\frac{\partial \tilde{v}_i}{\partial x_j} + \frac{\partial \tilde{v}_j}{\partial x_i}\right) \quad (2.39)$$

In Equation 2.38, it can be noticed that additional equations are required to solve for μ_T and turbulent kinetic energy (k).

Turbulent heat-flux vector closure:

The commonly employed closure for turbulent heat-flux vector (q'_j) is from the Reynolds analogy (Reynolds, 1874) between the momentum and heat transfer. It is assumed that the turbulent heat flux vector is proportional to the mean temperature gradients. The proportionality constant is derived by scaling the eddy viscosity (μ_T) with the turbulent Prandtl number (Pr_T)

$$q'_j = \overline{\rho v''_j h''} = -\frac{\mu_T C_p}{Pr_T}\frac{\partial \tilde{T}}{\partial x_j} = -\frac{\mu_T}{Pr_T}\frac{\partial \tilde{h}}{\partial x_j} \quad (2.40)$$

where, C_p is the specific heat at constant pressure for the gas

Pr_T is assumed to be a constant a value of 0.89 or 0.9 in the case a boundary layer flows. At the edge of the boundary layer and in free shear layer, a value in the order of 0.5 was recommended (Wilcox, 2006).

In order to consider the non-linearity of turbulent stress tensor with the mean strain rates, Lumley (1970; 1978) extended the linear Boussinesq equation (Equation 2.38) with higher order products of strain and rotation tensor. In comparison to the linear Boussinesq approximation, the non-linear models are computationally expensive. However, it offers substantial improved predictions for complex turbulent swirling flows.

The general first order closure models are listed in Table 2.3. This list covers a few of the variants that are widely referred to in the literature. This includes the one equation and the two equation models (turbulent kinetic energy[k] and dissipation[ε]/specific dissipation rate[ω]) for closing the turbulent eddy viscosity.

Dissipation equation for the two-equation model is given by Equation 2.41.

$$\frac{\partial}{\partial t}(\bar{\rho}\,\epsilon) + \frac{\partial}{\partial x_i}(\bar{\rho}\tilde{v}_i\epsilon) = \frac{\partial}{\partial x_j}\left[\left(\mu + \frac{\mu_T}{\sigma_\epsilon}\right)\frac{\partial \epsilon}{\partial x_j}\right] + C_{\epsilon 1}\frac{\epsilon}{k}\left[\mu_T P - \frac{2}{3}\left(\mu_T \frac{\partial \tilde{v}_i}{\partial x_i} + \rho k\right)\frac{\partial \tilde{v}_i}{\partial x_i}\right] + C_{\epsilon 3}\frac{\epsilon}{k}\mu_T P_B - C_{\epsilon 2}\rho\frac{\epsilon^2}{k} + C_{\epsilon 4}\rho\epsilon\frac{\partial \tilde{v}_i}{\partial x_i} + C_{\epsilon 1}\frac{\epsilon}{k}\mu_T P_{NL} \qquad (2.41)$$

The model constants defined by Equation 2.41 could be referred from Star-CD (2018).

Table 2.3: First order closure models and the eddy/turbulent viscosity (μ_T) assumptions are listed.

Turbulent viscosity (μ_T)	**First order closure models**	**Number of equation**
$l_m^2 S_{ij}$	Algebraic mixing length model (Prandtl, 1925)	Zero
$\bar{\rho}\tilde{\vartheta} f_{\vartheta 1}$	Spalart-Allmaras (Spalart and Allmaras, 1992)	One
$\bar{\rho} C_\mu \frac{k^2}{\epsilon}$	Standard k-ε (Launder and Spalding, 1974)	Two
$\alpha^* \frac{\bar{\rho} k}{\omega}$	k-ω (Wilcox, 1988)	Two

It should be emphasised that there are many variants of $k-\epsilon$ turbulence model used in engine flow simulations. They are Standard $k-\epsilon$, Realisable $k-\epsilon$ and RNG- $k-\epsilon$ (Yakhot and Orszag, 1986). It is reported that the accuracy of the standard $k-\epsilon$ model degrades for flows with adverse pressure gradient (Wilcox, 2006, p.192). The transport equations k and ϵ are derived considering the core turbulent flow far from the wall or high Reynolds number (i.e. the momentum or the local heat transport is dictated only by eddy viscosity and not by the molecular viscosity). However, very close to the wall (viscous sublayer), the molecular viscosity dominates in damping down the turbulent kinetic energy to zero. Hence, damping function is required for limiting the turbulent kinetic energy by scaling the dissipation near the wall (turbulent kinetic energy, $k \sim y^2$, where, y is the normal distance from the wall; Dissipation, $\epsilon \sim 2\nu$). It corrects the calculated turbulent kinetic energy through excess dissipation by the addition of explicit wall terms in dissipation transport equation. This approach is referred as Low-Reynolds number treatment, which requires a very fine grid resolution near the solid walls. The Low-Reynolds-number $k-\omega$ turbulence model (Wilcox, 2006, p. 267) is shown to correlate the measured near wall velocity profiles for compressible flat plate in comparison to the Low-Reynolds-number $k-\epsilon$ turbulence model.

Shih et al. (1994) modified the standard $k-\epsilon$ turbulence model with a new dissipation rate equation based on mean-square vorticity fluctuation along with a new eddy viscosity formulation based on the realisability constraints for maintaining positive normal Reynolds stress. This is generally referred to as Realisable $k-\epsilon$ model. There is a wide range of turbulent flows, such as (i) rotating homogeneous shear flows, (ii) boundary free shear flows, including a mixing layer, planar and round jets, (iii) channel flow, and flat plate boundary layers with and without pressure gradient; and (iv) backward facing step separated flows. This new model is shown to have significant improvement over the standard $k-\epsilon$ turbulence model.

As detailed earlier, the engine in-cylinder consists of a complex turbulent compressible flow structure. The $k-\epsilon$ turbulence model was originally developed (Launder and Spalding, 1974; Launder, 1991) and validated for incompressible flows. Watkins (1977) implemented the $k-\epsilon$ turbulence model for predicting turbulent flow and heat transfer in reciprocating engines. In his model, the compressible form of governing equations with Reynolds averaged flow variables was solved by ignoring the density fluctuations. A similar approach was widely adopted in engine flow simulation tools (Amsden et al., 1989) accounting variable-density and eddy diffusivities.

Yakhot and Orszag (1986) derived the RNG $k-\epsilon$ turbulence model for incompressible flows. RNG, refers to the Renormalisation Group method, which as originally developed in the

context of quantum field theory. The modelling constants were mathematically derived for the dissipation equation (ϵ). However, Smith and Reynolds (1992) reported a numerical error in the initial RNG κ-ε turbulence model derivation.

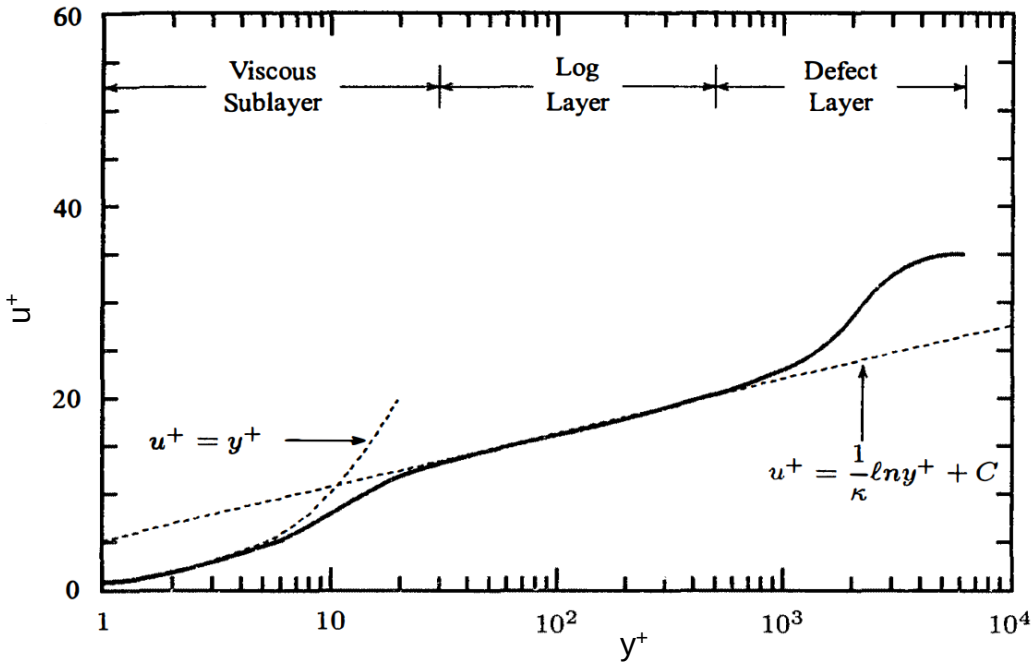

Figure 2.8: Typical velocity profile representing a turbulent boundary layer (Picture taken from Wilcox, 2006).

Han and Reitz (1995) modified the corrected RNG $k-\epsilon$ turbulence model and applied it to variable-density engine flows. The modified model was applied to diesel spray combustion computations. It was shown that the choice of the RNG $k-\epsilon$ turbulence model enabled to capture the high strain rates associated with spray and combustion. Large-scale flow structures were predicted, which were affected by the spray and the squish. These were consistent with endoscope combustion images. The effects of flow compressibility on both non-reacting compressing/expanding flows and reacting flows were discussed. They concluded that predicted combustion parameters, particularly, soot emissions are significantly influenced by compressibility. Due to the coupled nature of the in-cylinder flows, the heat (wall film, solid conduction, droplet heat transfer, spark, chemical reaction), mass (species diffusion, evaporation) and momentum transfer (intake turbulent flow, droplet and flow interactions) need to be captured simultaneously. Hence, individual models need to be accounted accurately to study the coupled behaviour.

The law of the wall:

The law of the wall is the empirical relation observed in turbulent flows defining the streamwise velocity profile from the solid wall. Measurements show that, for both internal and external flows, the streamwise velocity varies logarithmically with the distance from wall. This logarithmic relation defined by the non-dimensional wall distance (y^+) and velocity (u^+) is defined as wall function.

$$y^+ = \frac{u_\tau y}{\nu} \qquad (2.42)$$

where, u_τ is scaled friction velocity representing the near wall region and is given by Equation 2.43.

$$u_\tau = \sqrt{\frac{\tau_w}{\rho}} \qquad (2.43)$$

$$u^+ = \frac{U}{u_\tau} \qquad (2.44)$$

where, U is the streamwise velocity near the wall and τ_w is the wall surface shear stress.

As defined earlier, it is inevitable that low Reynolds number models require a very fine mesh near the solid walls. This enables to fix the first node near the wall at a non-dimensional wall distance, $y^+ \leq 1$. In order to decrease the number of grids, a coarser mesh is used with $10 \leq y^+ \leq 100$. It avoids the viscous sublayer region (Figure 2.8) in the computation domain, and, hence, the damping functions may not be required. In this case, wall functions can be used in the first near-wall-cell centre to bridge no-slip wall and the log-layer. Numerically, the wall functions can be used to determine the friction velocity (u_τ) to evaluate the k and ϵ in the first cell. Hence, the turbulence kinetic energy ($k \sim u_\tau^2$) and dissipation ($\epsilon \sim \frac{k^{3/2}}{y}$) equations may not be required to solve at the solid walls and in the first cell. The wall functions are defined by assuming the flow is attached with the solid wall boundary. Therefore, the application of wall function for highly separated near wall flow is questionable.

Reynolds stress transport model (RSM):

The exact form of the Reynolds stress transport equations are derived by taking the time average of the second-order moment with the Navier-Stokes operator. This is also referred to as second-order closure.

The general form of Reynolds stress transport equation is given by

$$\frac{\partial}{\partial t}\left(\rho\overline{v_i''v_j''}\right)+\frac{\partial \tilde{v}_k\,\rho\overline{v_i''v_j''}}{\partial x_k}-\frac{\partial}{\partial x_k}\left[\left(-\rho\overline{v_i''v_j''v_k''}-\delta_{ik}\,\overline{\mathrm{p}'v_j''}-\delta_{jk}\,\overline{\mathrm{p}'v_i''}+\mu\,\delta_{kl}\,\frac{\partial}{\partial x_l}\left(\overline{v_i''v_j''}\right)\right)\right]=$$

$$-\rho\left(\overline{v_i''v_k''}\frac{\partial\,\tilde{v}_j}{\partial x_k}+\overline{v_j''v_k''}\frac{\partial\,\tilde{v}_i}{\partial x_k}\right)+\overline{\mathrm{p}'\left(\frac{\partial v_i''}{\partial x_j}+\frac{\partial v_j''}{\partial x_i}\right)}-\rho\frac{2}{3}\delta_{ij}\varepsilon \quad (2.45)$$

$$\mu_T=\rho C_\mu\frac{k^2}{\epsilon} \quad (2.46)$$

In this constitutive equation for eddy viscosity, ϵ can be obtained by solving the dissipation equation (Equation 2.41) as obtained for the two-equation model. The turbulent kinetic energy can be calculated from summing the normal components of the Reynold stress as in Equation 2.35. The Reynolds stress equation contains an additional third order tensor term, $-\rho\overline{v_i''v_j''v_k''}$. Thus, an additional empirical relation is needed to close this equation.

Reynolds stress transport model is computationally expensive as there is a need to solve six additional equations along with a dissipation equation. More detail on this model can be found in Pope (2000) and Star-CD (2018). However, application of Reynolds stress transport model is rarely reported for an engine application.

Large eddy simulations:

The large eddy simulation (LES) methodology was first employed in the field of atmospheric sciences by Smagorinsky (1963). LES, is based on the theory that the small-scale turbulent structures are more universal than the larger high energy content eddies. Due to the more universal character of the small scales, a much simpler subgrid-scale model is adopted. This significantly decreases the number of grid requirements. Given the availability of low cost and high speed computing facilities with reasonable flow geometries, LES, is employed.

LES is three dimensional and transient by its definition. In comparison to RSM turbulence modelling, LES requires high-grid resolution in both streamwise ($50 \leq x^+ \leq 150$) and cross-streamwise ($15 \leq z^+ \leq 40$) direction. However, LES is computationally less expensive in comparison to DNS. It is reported (Balzek, 2001) that the total grid requirement with DNS is proportional to $Re^{9/4}$, against $Re^{1.8}$ for LES simulations.

In compressible LES, an approach similar to the Favre averaged Reynolds decomposition, defined by Equation 2.27 is applied to the governing equations (2.7, 2.8, 2.9 and 2.12). However, the Favre averaging is on the spatially filtered velocity components, energy and temperature. The velocity component decomposition at a location ($\vec{r}_0$) and time (t) in this approach is given by Equation 2.47.

$$U_i = \widetilde{U}_i + U''_i \quad (2.47)$$

where,

$\widetilde{U}_i$ is the filtered velocity component

U_i'' is fluctuating velocity component in the subgrid-scale

$$\widetilde{U}_i(\vec{r}_0, t) = \frac{\overline{\rho U_i}}{\rho} = \frac{1}{\rho} \int_D \rho(\vec{r}_0, t)\, U_i(\vec{r}_0, t)\, G(\vec{r}_0, \vec{r}, \Delta) d\vec{r} \quad (2.48)$$

where,

$G(\vec{r}_0, \vec{r}, \Delta)$ is the filter function (top-hat, cut-off or Gaussian type of filter) and Δ is the filter width

The main functionality of the subgrid-scale model is to account for the energy transfer from the large scale to the small scale. In some instances, the energy can also flow from the small scale to the large scale, and this process is called 'backscatter'.

A detailed mathematical description and theory is provided in Pope (2000, p. 558). Some of the fundamental differences between Reynolds-averaged Navier-Stoke (RANS) and LES combustion models for non-premixed and premixed turbulent combustion are provided in Pitsch (2006). The results from the simulation are compared with the available simulation and experimental data (Sandia flame experiments). It is reported that LES offers more advantage towards accurate and predictive simulations of turbulent combustion.

A comparative study of LES with spark ignition models with flame surface density (FSD) transport combustion model in a downsized GDI engine configuration was provided in d'Adamo et al. (2015). This paper reports the cycle-to-cycle variability of engine performance with the spark-ignition process. In this work, Imposed Stretch Spark-Ignition Model (ISSIM) and Arc Kernel Tracking Ignition Model (AKTIM) spark ignition models are used in the large eddy simulation using Star-CD-ES-ICE, 2018, code. The simulation is reported to be underpredicting the experimental cycle-to-cycle variation of pressure. In this simulation, 10 engine cycles were carried out.

There are more researches focused on LES in the engine applications (Patil et al., 2018) for predicting the cycle-to-cycle variation of dilution and combustion variability. In this, 20 engine cycles were considered in the simulation. The instantaneous flow field shows to have a good correlation with the PIV data. Most recently, Ritter et al. (2021) showed the workflow for the assessment and validation of LES for the in-cylinder mixture preparation process using CONVERGE™ CFD (Converge, © 2020) tool. In this work, the velocity fields obtained from the simulation were compared with the PIV measurements. Later, the cycle-to-cycle flow variability was reported. Lagrangian spray modelling approach for LES was also reported. The

mixture distribution results from the LES simulation are compared with the Laser Induced Fluorescence (LIF) measurements. A qualitative prediction of the overall mixing process was reported. Similar to the earlier literature (Patil et al., 2018), the cycle-to-cycle variability in the mixing is reported to be underestimated. Even though LES is reportedly used for in-cylinder flow simulations, due to the overall simulation time comparison to the engine development design iteration time and the computational cost, it still is largely considered in academic studies for detailed understanding. This could be used for further fundamental model in-cylinder development.

In summary, a detailed literature review describing the physical and numerical modelling methodology for RANS, LES and DNS is provided in this section. It includes the turbulence model assumptions, computational costs and feasibility in application to the in-cylinder engine flow simulations. From the above review, the two-equation Realisable $k-\epsilon$ and RNG $k-\epsilon$ models are the most preferred directions for the in-cylinder engine simulation. These are considered to provide computational turnaround time without the loss of simulation accuracy.

2.1.4 High efficiency GDI engine

Apart from the droplet breakup and fuel mixing requirement, different engine technologies are adopted to improve the efficiency of the modern GDI engines. Technologies include, low friction, over-expanded cycles (Atkinson cycle or Miller's cycle), lean burn, cooled EGR (exhaust gas recirculation) and advanced ignition systems. Such high efficiency engines are also well-suited for the hybrid vehicles.

Yamada et al. (2014) described the layout of the different technologies contributing to the high efficiency engines. It has been shown that the low temperature combustion decreased the cooling heat loss and improved the overall thermal efficiency. Moreover, a choice of high compression ratio and Atkinson's cycle were adopted to achieve a brake thermal efficiency close to 38%.

Piock et al. (2015) studied the influence of fuel system pressure, intake tumble charge motion and injector seat specification (static flow and plume pattern) on GDI engine particulate emissions under homogeneous combustion operation. In this study, Delphi Multec® 14 GDi multi-hole fuel injector, capable of 40 MPa fuel system pressure was used. Figure 2.9 shows the future market trend moving towards the high-pressure injector, reported in the year 2015. High pressure injector means that the nozzle sizes were decreased to improve the fuel atomisation and to improve the mixture formation. Figure 2.10 shows the probability density function (PDF) of volume fraction for the range of droplet sizes. It is evident that, for the same injected quantity, higher injection pressure tends to decrease the peak droplet size. However,

beyond 30 MPa to 40 MPa, the droplet size change was expected to be low. It also suggests that there is limit in the atomisation improvement.

In Piock et al.'s (2015) study, three different injector spray patterns with a 6-hole and 5-hole nozzle (high and low static flow rates) were used. However, the details of the spray pattern were not specified. The combination of the injectors was used on a standard intake port, medium tumble and a high tumble intake port. Consistently, the high tumble intake port was found to show lowest PN emission.

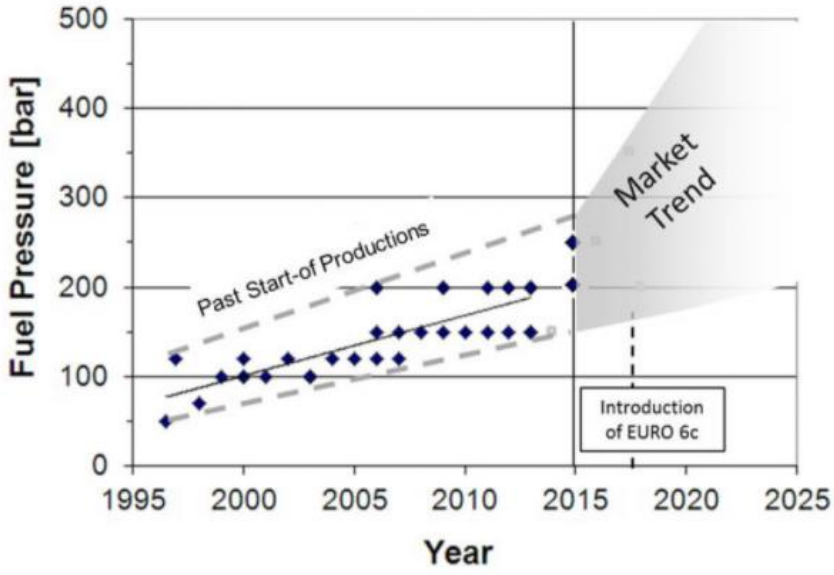

Figure 2.9: Market trends on fuel injection pressure (Taken from Piock et al., 2015).

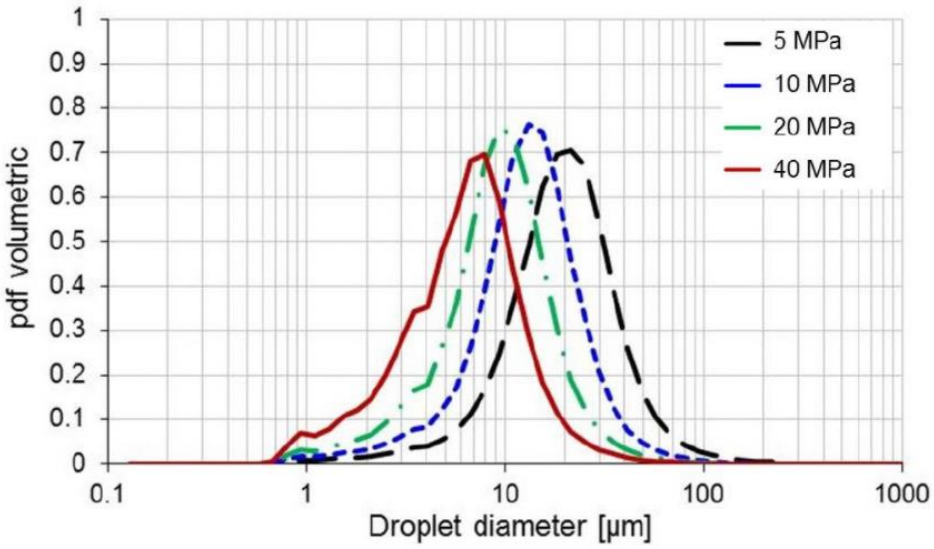

Figure 2.10: Effect of injection pressure on droplet size distribution at 50 mm from injector tip (Taken from Piock et al., 2015).

On the other side, the case with 6-hole low static flow injector showed lowest PN in comparison to other injectors. It should also be noted that all the injectors show a similar level of PN number density at 40 MPa fuel pressure. The benefit of PN, moving from an injection pressure of 30 MPa to 40 MPa, was not clear.

Takahashi et al. (2015) detailed the effect of EGR in decreasing the heat loss with low temperature combustion and improving the thermal efficiency of the engine. It was shown that high tumble ratio intake port is required to improve the EGR tolerance and help increasing the thermal efficiency to 40%. It was also shown that the new cylindrical piston crown helped retaining the tumble and increased the turbulent kinetic energy (TKE) near the compression TDC. A similar direction was shown in Tagishi et al. (2015). In this study, a single cylinder engine development was reported. A choice of high EGR (35%) combined with high compression ratio (15 to 17) was used to achieve a thermal efficiency of 45%. They also reported the fundamental piston design parameters to ensure high TKE near the TDC. A parameter defining the volume around the spark plug (V1) to the clearance volume (V) was reported. It was shown that V1/V ~ 3% or higher was required to help improve the EGR tolerance of the engine (Figure 2.11).

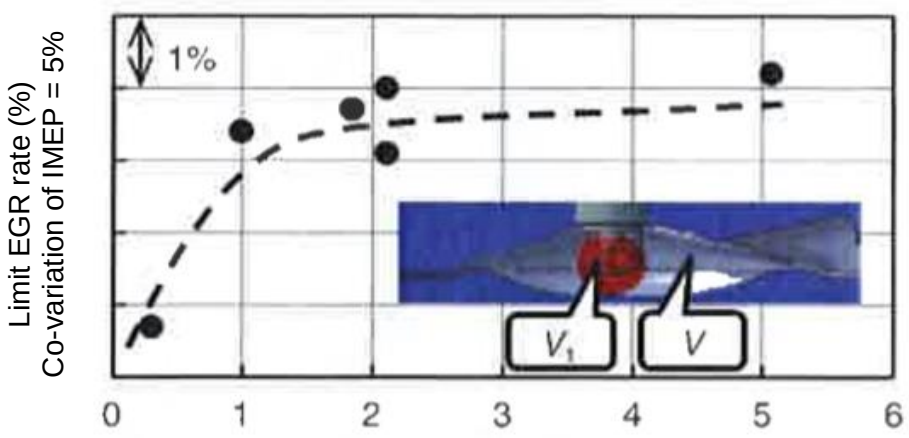

V: Combustion chamber volume at TDC
V1: Volume when virtual sphere centring on ignition plug electrode touches piston or cylinder head

Figure 2.11: Effect of V1/V on EGR rate for a fixed engine co-variance of IMEP (Tagishi et al., 2015).

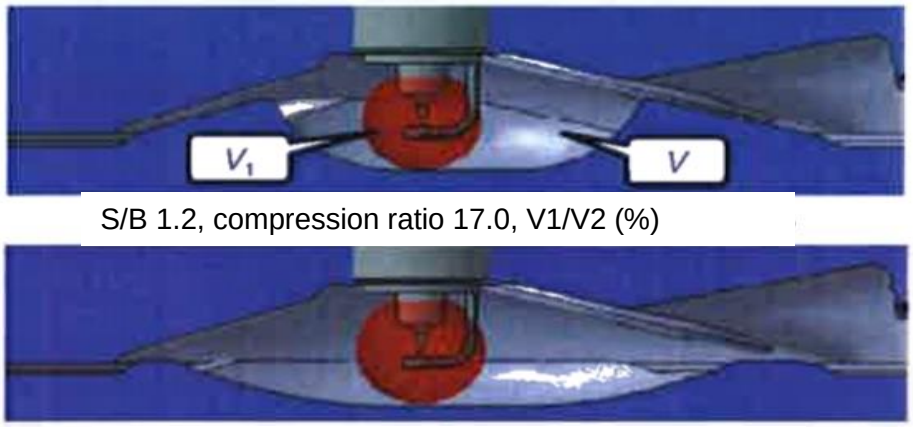

S/B 1.2, compression ratio 17.0, V1/V2 (%)

S/B 1.2, compression ratio 17.0, V1/V2 (%)

Figure 2.12: Combustion chamber shape and vicinity with increase in stroke to bore (S/B) ratio (Tagishi et al., 2015).

Moreover, they showed that the stroke to bore ratio increases the combustion efficiency for a high compression ratio engines (clearance volume increase). This indicates the three-dimensional constraints are related to the increase in compression ratio. However, with the increase in stroke to bore ratio, there is a degree of improvement achieved.

Effect of spark energy on EGR tolerance for combustion stability was reported. It indicated that higher spark energy is required to tolerate higher level of EGR. In this engine development, Atkinson type CAMs were used to mitigate knock at the part load condition.

Similarly, Nakata et al. (2016) reported that, with Atkinson cycle, cooler EGR and low friction technologies (Yamada et al., 2014), a thermal efficiency of 40% can be achieved. Moreover, a new prototype 2.5L I4 engine with long stroke and high tumble configuration were adopted with the lean boosted concept with cooled EGR, which achieved 45% engine thermal efficiency. Simulated charge motion comparison with the longer and shorter stroke engine was shown. The measured turbulence intensity (m/s) is shown to increase with the increase in engine stroke. This is considered to increase the burn rate and, thereby, the combustion phasing. Hwang et al. (2016), of Hyundai and Kia Corp., introduced the production of new Kappa 1.6L GDI dedicated hybrid vehicle with a peak thermal efficiency of 40%. Simulation showed the comparison of the intake port, intake CAMs, combustion chamber and piston developments. To meet the SULEV emission regulations, the spray pattern of the laser drilled-injector was optimised with the high tumble port and piston configuration. Li et al. (2015) carried out an experimental study on a single cylinder DISI engine to investigate the fuel economy benefit with Miller's cycles with EIVC and LIVC CAMs. The fuel economy benefits were compared with standard Otto CAM. The effect of Miller cycle was quantified by Miller cycle rate (MCR), defined by the below equation:

$$MCR = 100 \text{ X } \frac{Geometric\ CR - Effective\ CR}{Geometric\ CR} \quad -(7)$$

The higher the value of MCR, the lower the effective compression ratio. In the CAM timing setup, 7.5%, 32% and 40% MCR were achieved for standard Otto, LIVC and EIVC CAMs, respectively. It should be noted that a low level of MCR can be achieved using the standard Otto CAM. At higher load, MBT was achievable with higher level of MCR and, hence, both EIVC and LIVC show a good improvement in fuel economy. Combustion stability was reported with EIVC CAMs at low load conditions. LIVC CAM was found to show lower level of pumping

loss. The advantages and disadvantages of EIVC and LIVC CAMs were provided. The LIVC CAM was shown to have less scavenging in comparison to EIVC CAM due to lower level of overlap for a similar % of MCR. Exhaust back pressure influence was higher with EIVC CAM as against LIVC CAM. In general, it was noticed that CA50 for EIVC was later than LIVC CAM. Another aspect of this study was related to the effect of fuel burn rate with the injection strategy on EIVC configuration.

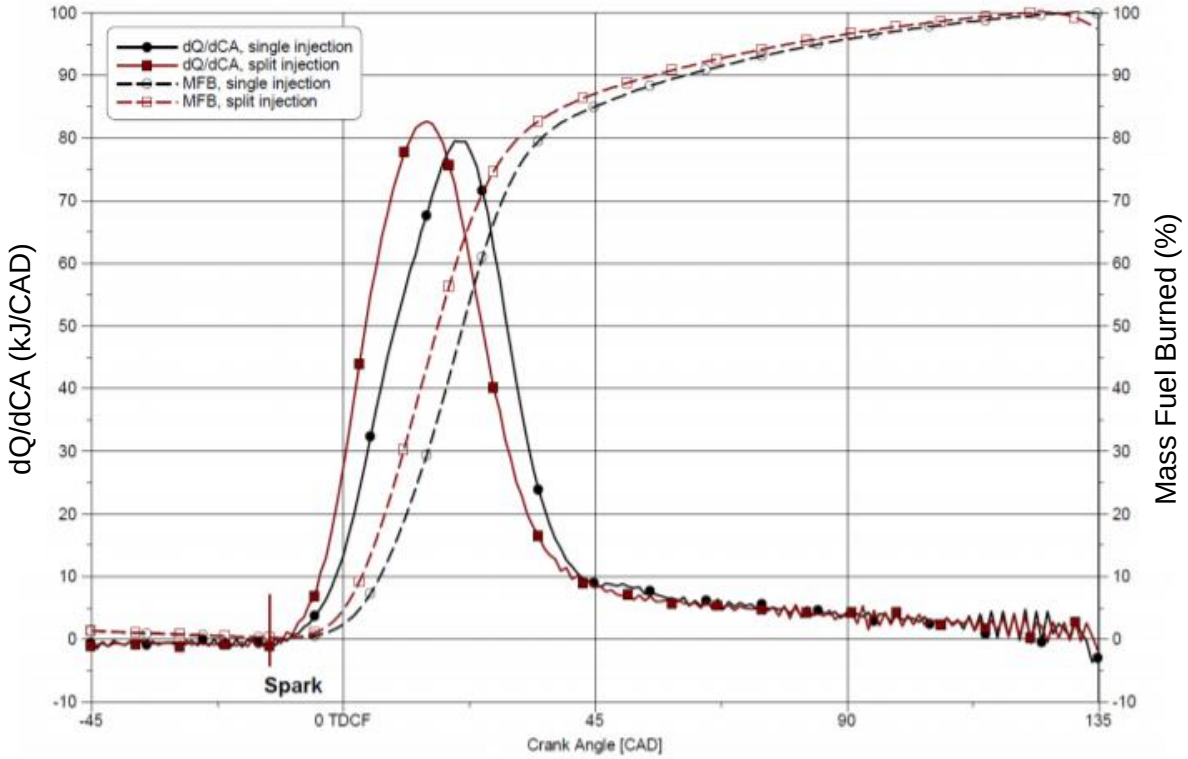

Figure 2.13: Heat release and mass fuel burned vs crank angle at 2000RPM 25.6 bar (Li et al., 2015). Split injection strategy was included in this engine cycle diagram.

Figure 2.13 shows the comparison of the burn rate with single and split injection strategy. The delayed second injection is shown to improve the burn rate significantly. It should also be noted that an outward opening hollow cone injector was used in the engine setup. This highlights the importance of the injection timing and benefit on burn rate. In summary, the Miller cycle with the EIVC cam timing was shown to be promising technology for further improvements of boosted gasoline engines. As emphasised in this work, the burn rate was estimated to be lower with EIVC CAM and there is a possibility of improvements with suitable injection timing taken into consideration.

Hakariya et al. (2017), in the Toyota Motor Co. Ltd., developed a 40% efficiency natural aspirated engine with multi-hole DI and PFI fuel system with a modified high tumble and high flow intake port. In this case, a cladded intake valve seat was developed to increase the flow coefficient. The cavity piston bowl was modified with a hemispherical to increase the in-cylinder turbulent kinetic energy. However, the effect of emission and the mixture stratification with the piston bowl were not highlighted. In this engine, Atkinson cycle CAMs were adopted with an optimum timing to balance the engine stability and pumping loss.

Osborne et al. (2017), in Ricardo UK Ltd., developed a single cylinder high efficiency engine (Magma engine concept) characterised by a high compression ratio and central injector combustion system using Miller cycle. The key findings reported were the earlier intake valve closing (EIVC) approach used to mitigate knock as against the Atkinson cycle or the late intake valve closing (LIVC) in the competitor engines. This was shown to improve fuel economy significantly. It was reported that the comparison of the weighted key point cycle predictions from the single cylinder engine predicted fuel consumption savings over the WLTC and FTP-75 of 12.5% and 16.4%, respectively. It was reported that the increased air motion is required to preserve acceptable combustion parameters with an EIVC strategy. In the engine development, different Miller's cycle concepts (either EIVC or LIVC) were adopted by carefully studying their combustion system and strategies. However, there is a need to understand the details of the charge motion numerically with a few EIVC and LIVC CAMs.

Lee et al. (2017), for the Hyundai Motor Company, achieved 40% thermal efficiency with higher compression ratio, higher level of cooled EGR and long stroke engine with Atkinson cycle engine operation. In this development, further enhancement in thermal efficiency to 42% was targeted. The focus was to improve the tumble ratio, optimise the compression ratio, EGR enhancement and choice of having twin spark plug. It was reported that any compression ratio more than 14 CR was found to limit MBT point due to knock at 2000 RPM higher load conditions (> 8 bar BMEP). Twin spark plug was expected to increase the fuel mass fraction burn and to decrease the cycle to cycle combustion variability. Test data showed that, at 2000 RPM low load condition, both ignition delay and burn duration decreased by nearly 50%. This enabled to increase the EGR to maximum of 35% to improve the thermal efficiency to 42.2% for the naturally aspirated (NA) engine application (2L, I4 proto-type engine).

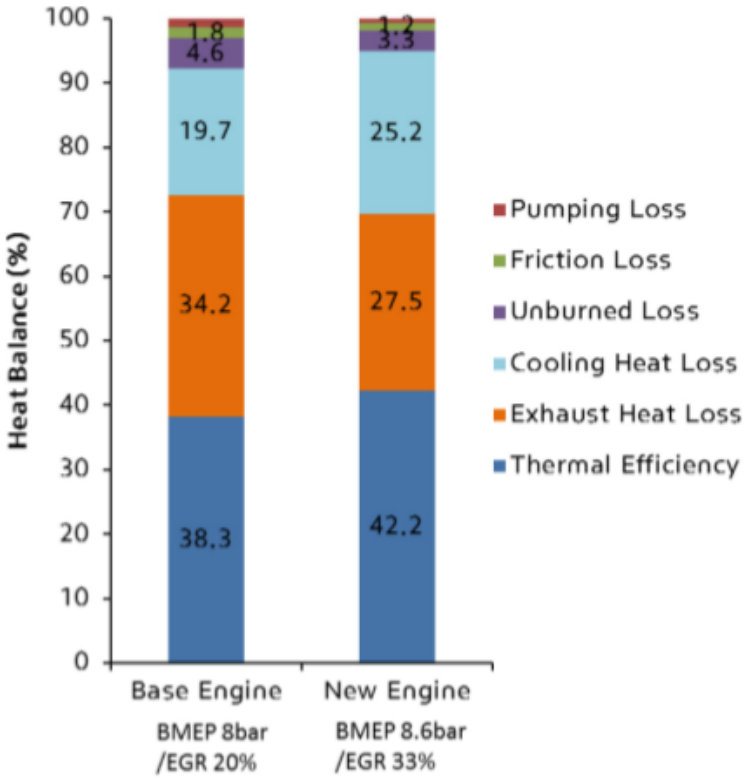

Figure 2.14: Comparison of energy balance for the new engine with the base engine (Taken from Lee et al., 2017).

It is very evident from Figure 2.14 that lower exhaust/cooling heat loss due to low temperature combustion with higher level of EGR and the improvement in combustion efficiency are the main contributors for the thermal efficiency improvements. It should be noted that, for the NA application, Atkinson cycle (LIVC) approach was adopted. In the modern engine development, very high injection pressure injector (500 to 1000 bar), lean burn, cooled EGR and advance ignition system such as high energy coil, Corona discharge ignition (Cimarello et al., 2017), active and passive pre-chamber were used (Toulson et al., 2010). Serrano et al. (2019) introduced an innovative optimised combustion system for ultra-lean operation and very high efficiency. In this, a centrally located active pre-chamber design was adopted which allows to control the air/fuel ratio independently to that of the main combustion chamber. A single cylinder engine was developed to demonstrate the capability. Here, a maximum indicated thermal efficiency of 47% was achieved at λ =2 with optimised injection settings in the pre-chamber and the main combustion chamber. With a very high combustion speed, a knock free combustion was demonstrated. It should be noted that the charge motion requirement is less important. This also showed to have 1/17th of NO_x and the particulate emissions were halved. 3D CFD simulation was performed using the Converge CFD software. In this case, both gas (CH_4) injection and gasoline injection in the pre-chamber were evaluated. Control of minimum fuel quantity of fuel injected was reported to be a challenge. Gasoline injection in the pre-

chamber allowed to run the engine with relatively higher AFR (>2). It was also reported a maximum indicated efficiency of 50% with an electrical boosting of 900m bar differential pressure (intake to exhaust) with a pumping benefit of +0.8 bar. However, higher HC emission was noticed with higher level of scavenging.

In summary, the focus of the vehicle manufactures is towards a high thermal efficiency engine using the over-expanded cycles, such as Atkinson or Miller's (Miller, 1956; 1957). Moreover, the low temperature combustion along with high compression ratio is reported to improve the thermal efficiency of the engine to 38%. Using advanced manufacturing processes such as laser drilling, the nozzle sizes are decreased significantly to improve fuel atomisation. This results in high injection pressure for the same injection static flow. The droplet size distribution decreases with injection pressure and benefits the PN/PM emission.

Higher level of cooled EGR (~35%) and over-expanded cycles were used to improve thermal efficiency of the engine further. The engine stability with high EGR was reported to be challenging. The burn duration was investigated with the parameters relating to the turbulent velocity scales and mixing. Higher turbulent velocities (u') during combustion are reported to improve the burn rate. Effect of combustion chamber clearance volume and volume around the spark plug defined is shown to be influential in preserving the turbulent flow characteristics. Increase in engine stroke length increases the mean piston speed and helps in building a stronger charge motion during the intake stroke. Moreover, for the same compression ratio, longer stroke engine allocates more clearance volume, which increases the aspect ratio and helps in preventing the charge motion decay during the end of compression stroke. During the high EGR operating condition, high energy ignition coils are required to improve engine stability. Different over-expanded cycle strategies such as LIVC and EIVC were reported. In comparison to LIVC engine, EIVC CAMs are shown to have longer burn duration. Multiple injection strategy is reported to improve the burn rate for the EIVC engines. Moreover, a very high boost pressure is required for the EIVC operation. Electrical boosting device is reported to improve the overall thermal efficiency of the engine.

Another main direction for high efficiency engine is the lean burn operation with advanced ignition system (Serrano et al.,2019). An active pre-chamber with ultra-lean operation improves the thermal efficiency of the engine to 47%. This decreased the NO_x emission by an order of magnitude and PN/PM emission by half. It should be noted that the HC emissions were reported to be in higher level. In this case, EIVC CAMs are used. More understanding is required in terms of charge motion and mixture formation to quantify the difference between the EIVC and LIVC strategy.

2.1.5 Fuel stratification

Fuel stratification is a process by which the fuel air mixture distribution (equivalence ratio, ϕ) in the engine cylinder is controlled in GDI/PFI engine before the start of combustion. Kuwahara, Ueda and Ando (1998) elucidated the mixture preparation and the resulting combustion processes in Mitsubishi GDI engine. They demonstrated the effects of in-cylinder flow (reverse tumble) on the charge stratification using a spherical cavity piston and injection timing. The mixture strength at the spark plug at the spark timing (Figure 2.15) was controlled by injection timing. A “two-stage mixing” concept was first reported. The various benefits include, the control of fuel rich mixture near the spark plug to improve combustion stability, burning up of the generated soot from rich combustion and followed by lean combustion assisted by CO and soot itself. A new knock suppression technique with the “two-stage mixing” was also reported. This paper demonstrates the key benefits of charge motion, fuel stratification and the following combustion control.

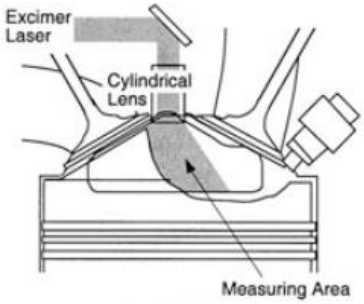

(a) Gasoline LIF Measuring Area

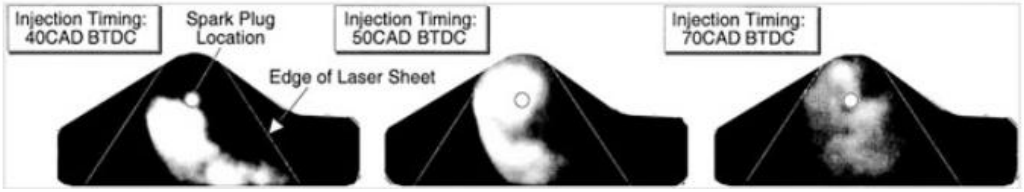

(b) Comparison of Gasoline LIF Distributions in the Cases of Different Injection Start Timings (With Reverse Tumble, Imaging Timing: 15CAD BTDC.

Figure 2.15: Measurement of gasoline LIF distribution in cylindrical chamber (Taken from Kuwahara, Ueda and Ando, 1998) (b) Comparison of Gasoline LIF Distributions in the Cases of Different Injection Start Timings (With Reverse Tumble, Imaging Timing: 15CAD BTDC.

Li et al. (2003) investigated the effect of split injections on mixture formation process in direct injection gasoline engine sprays using laser absorption and scattering (LAS) technique. It was reported that the high concentration liquid spray accumulation at the leading edge of the spray can be avoided by double injections with enough dwell time and appropriate mass ratio.

Penetration of liquid phase and vapour phase were analysed. At 35 mm, downstream from the injector tip, the range of higher vapour phase equivalence ratio (ϕ_v=0.7 to 1.3) increases with split injection. It was also reported that too small dwell or too small percentage of fuel mass injected in first injection shows an adverse effect in mixing performance.

Li et al. (2004) further extended the study combined with the laser-sheet imaging, LIF-PIV and the LAS technique. It was reported that the spray-induced ambient air motion can help the formation of more combustible mixture. As shown in Figure (2.16), the single injection case shows an “over lean” mixture in comparison to the split injection case. A wall-guided type DI gasoline engine was demonstrated with an application to the split injection. They reported to decrease the engine out emissions, such as smoke and $NO_{x,}$ significantly. However, the HC emission increased with the split injection strategy (delayed, second injection) due to spray-wall impingement on piston cavity, resulting in local rich fuel mixture formation.

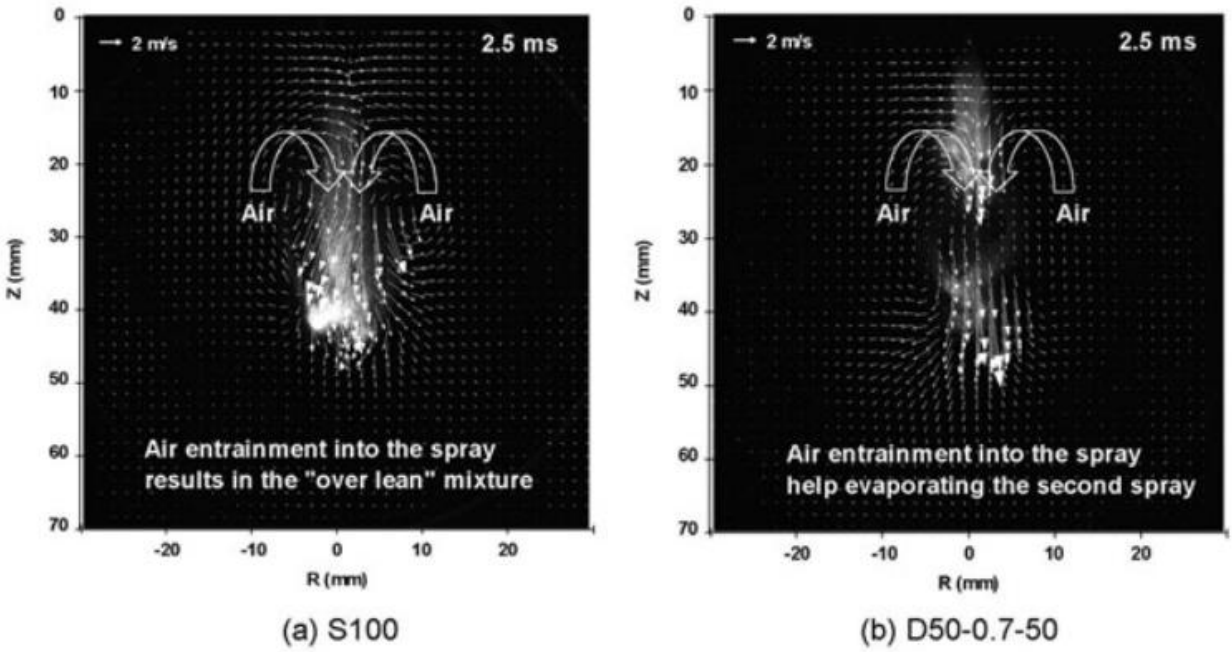

Figure 2.16: Effect of ambient air entrainment on mixture formations of single injection and split injections (Taken from Li et al., 2004). S100 and D50-0.7-50 refer to the single and twin injection, respectively.

Moriyoshi et al. (2018) demonstrated the fuel stratification benefit for an ultra-lean burn configuration with an excess air ratio of 1.8. The limiting parameter for this operation was the cycle to cycle combustion variation. It was reported that a bulk quenching of the lean mixture during the early part of the expansion stroke is one of the causes of engine combustion variability (COV of IMEP). A parallel fuel stratification approach was used to decrease the combustion variability. In this case, the stratification was achieved by using a port fuel injection with an asymmetric number of holes (6:4), biasing the fuel entry through individual intake port

legs. The intake port leg, targeted with higher number of holes, receives more fuel in comparison to the other port leg. Moreover, a differential tumble was setup using a velocity differential generated between the two intake port legs. The weakly, parallel stratification extended the ultra-lean limit, thereby increasing the indicated efficiency by 0.3% compared to homogeneous condition. The details of the charge motion and the flow structure were not detailed in this paper.

A “two-stage” mixing process is detailed, using a twin injection strategy with a side- mounted injector. A bowl-shaped piston crown helps prepare the parallel stratification to improve combustion and to decrease the particulate emission. This can be categorised to be wall-guided fuel stratification. However, during the engine warm up with relatively lower engine coolant temperature, the fuel evaporation from the liquid film and mixing is expected to be poor. Li et al. (2004) reported a lower smoke and NO_x with twin injection but with, however, higher HC emission due to spray-wall impingement and local rich fuel mixture formation. The optical measurements showed a significant air entrainment during multiple or split injection. A controlled parallel fuel stratification improved the combustion stability. The PIV measurements also showed the local charge velocity improvement due to the momentum exchange from the high velocity droplets (drag force). This advantage needs to be utilised effectively with an appropriate spray pattern to support the charge motion. During the intake stroke, the charge motion builds up from the piston speed and the boost pressure in the intake port and the intake valve opening events. As the piston starts moving towards the TDC during the compression stroke, the aspect ratio decreases, and the charge motion is found to decay. As reported in the earlier section, the turbulent velocity decreases significantly during the end of compression stroke. Splitting the injection quantity with multiple injection strategy with a more precise control of fuel quantity the charge motion benefits could be explored when the charge motion is weak. Hence, a detailed study is required to assess the different spray patterns, injection timing, injection quantity and the injection mounting (central or side-mounted injectors). Moreover, the benefits of the piston crown shape to decrease the liquid film formation need to be explored. With the advent of high-pressure injectors and engine control unit (ECU), the benefits need to be assessed for the modern engine development to meet the high efficiency and ultra-low emission targets. Any fractional improvement in the efficiency of the engine is an advantage.

2.2 Aim and objectives

2.2.1 Challenges in the modelling gasoline injection process and its application to the development of a new GDI engine

Based on the literature review, several major challenges and areas of additional works have been identified in the development and application of gasoline injection to the development of a high efficiency and ultra-low emission GDI engine, as listed below.

1. Complete representation of the spray using numerical simulation is very difficult and computationally expensive. The model simplification for the engineering design application is essential, with the confidentiality of the injector internal details from the supplier. A more general approach for spray tuning methodology is required. This could be readily used for new injectors with fundamental parameters such as Q_{stat}, nozzle diameter(D), L/D and nozzle manufacturing process. As discussed, the modern GDI injectors are designed for high rate of atomisation to meet future emission requirements. Hence, a high-pressure injector with a very low L/D multi-hole nozzles, designed using the laser drilled manufacturing process. This results in significant flow contraction as reported in Befrui et al. (2011). Thereby, the droplet or ligaments obtained at the end of the primary breakup considering the flow contraction is essential to evaluate the injection velocity and effective diameter. Thus, a phenomenological model needs to be built to represent the primary droplets originating from the exit of the nozzle. This should include the fundamental nozzle parameters and requires no further tuning and could be readily applied to represent injectors for a range of injection pressures and nozzle sizes.

2. In the spray tuning process, a more reasonable representation of penetration depth is required to validate the experimental spray rig data having shot-to-shot variability in penetration depth (Dhanji et al., 2019; 2020). The validation parameters, such as penetration depth and droplet SMD at different stations, need to be compared with the available spray rig data. The effect of modelling constants to represent the phenomenological droplet breakup mechanism in the Reitz Diwakar (R&D) and Kelvin Helmholtz and Rayleigh Taylor (KH-RT) models is required. This helps to arrive at a single set of model constants for representing a spray.

3. As summarised by Joshi (2020), in the modern engine development, cold start and catalyst light-off, are still important conditions contributing to the total engine PN and PM emission in the real driving emission or WLTP cycle. Under cold engine condition, understanding the mixture formation process and the contributing factors for HC, PN

and PM emissions, as reported in Sandquist, Lindgren and Denbratt (2000), is essential. In the engine development, the parameter required for faster catalyst light-off is the heat flux density (kW/L) available to warm up the catalyst for better NO_x conversion efficiency. Retarded combustion strategy is employed to maximise exhaust gas enthalpy and improve combustion efficiency. Combustion stability during this operation results in NVH issues which are addressed using the cycle-to-cycle coefficient of variation (COV) of indicated mean effective pressure (IMEP). The development of new piston crown shapes and better injection strategies are required to decrease the engine pollutant emission.

4. As detailed in the literature review, fuel stratification plays an important role in maintaining the engine COV and decreasing the pollutant emissions. A detailed understanding of the fuel stratification process starting from, the fuel injection, the air entrainment, wall-impingement, liquid film formation and liquid film vaporisation and fuel mixture distribution at the time of spark is required.

5. The piston and the spray pattern are considered as the main controlling parameters for the fuel stratification process. Considering the effect of injection on air motion, the benefits that can be derived from the spray pattern designs and controlled injection as and when required, need to be assessed in detail. The controlling parameters, such as injection quantity, injection timing, spray pattern (number of plumes, spray angle relative to cylinder volume centre) and piston bowl/crown, need more understanding.

6. As reported in Takahashi et al. (2015) regarding the TKE requirements for the development of high efficiency engines, there is a need to explore the possibility of improving the TKE with the modern high pressure injectors. With the increasing demand on the high efficiency engines to decrease CO_2 emissions, several technologies are discussed in the literature review. Over-expanded cycle (LIVC and EIVC), high EGR and ultra-lean burn combustion are used. The fundamental technologies described are LIVC and EIVC (Heywood, 1989), wherein, the intake valve closing was controlled during intake or compression stroke to decrease the effective start of compression. Charge motion with LIVC or EIVC cycles has a fundamental difference for the same MCR (Li et al., 2015) due to the CAM profiles (duration and lift profile). In general, the valve lifts and duration for LIVC CAMs are higher than the EIVC CAMs. The charge motion and composition differences setup during the start of combustion with LIVC and EIVC requires more understanding to reveal the advantages and disadvantages of the CAMs. The parameters considered for

evaluation are charge velocity, temperature, TKE, RGFs, heat loss, boost pressure and scavenging for a typical engine condition.

7. The effect of multiple injection needs to be realised to improve some of the disadvantages of low lift and short duration EIVC CAMs as reported in the literature (Li et al., 2015). Simulations are required to understand the underlying process during the start of combustion.

2.2.2 Objectives

The aim of the PhD work is to identify ways to improve the accuracy of a simplified gasoline spray model through parametric and experimental validation and to investigate how the performance of a turbocharged GDI engine can be improved and emissions reduced by CFD studies with improved spray models.

The specific objectives are listed below.

1. Spray model simplification with diameter and static flow of the nozzle to be used as a fundamental input to estimate the probability density function (PDF) of droplet distribution from the primary breakup mechanism. This phenomenological modelling assumption is to be used for the engineering application representing multi-hole nozzles, wherein the injector nozzle geometry is proprietary.
2. Simple robust discrete Lagrangian multiphase approximation with phenomenological models such as R&D and KH-RT to be used to understand the secondary droplet mechanism along with the effect of modelling constants. A single set of modelling constants needs to be tuned for the chosen primary droplet, PDF distribution.
3. The transient evolution of penetration depth and droplet SMD needs to be compared with the available spray rig data. For the reliable evaluation of penetration depth, a new method of evaluation using the volume/void fraction will be adopted for reliable comparison of the experimental spray image.
4. Simplified spray model needs to be compared with different injection pressure and from different nozzle sizes.
5. Detailed understanding of fuel stratification during catalyst heating and correlation with PN and HC emission.
6. Mixture formation process with air-guided and wall-guided piston and the development to ultra-low PN emission engine.

7. Development of spray pattern design and synchronisation with in-cylinder port flow and minimised wall wetting.
8. Evaluate different sets of LIVC and EIVC CAMs and identify the advantages and disadvantages considering, tumble ratio, TKE and RGFs.
9. With the detailed understanding on the mixture formation process, the underlying details of combustion improvement with multiple injections needs to be revealed. A suitable injection strategy needs to be evaluated to improve the charge motion and resulting combustion for EIVC CAMs at low speed high load condition.
10. Nozzle velocity correction with 0-D model simplification for the modern high-pressure injector to consider flow contraction and resulting cavitation.

Chapter 3. Spray Modelling and Validation

In this chapter, the details of modelling approach for spray characterisation based on two of the widely used phenomenological models, namely, Reitz and Diwakar (R&D) and Kelvin Helmholtz-Rayleigh Taylor (KH-RT) models, are presented and discussed. The updated spray model with the nozzle geometry and its validation are provided.

3.1 Spray modelling

Fuel spray and charge motion in the engine cylinder plays a key role in mixture formation for combustion process, while injector nozzle geometry and injection strategy determine the fuel atomisation and mixing. Typical atomisation process in an injector is shown in Figure 3.1. It is essential for the spray model to capture the underlining process of air-fuel mixing and wall film dynamics. The droplet breakup mechanism (Leferbver, 1989; Baumgarten, 2006) is characterised in two stages, namely, primary and secondary breakup.

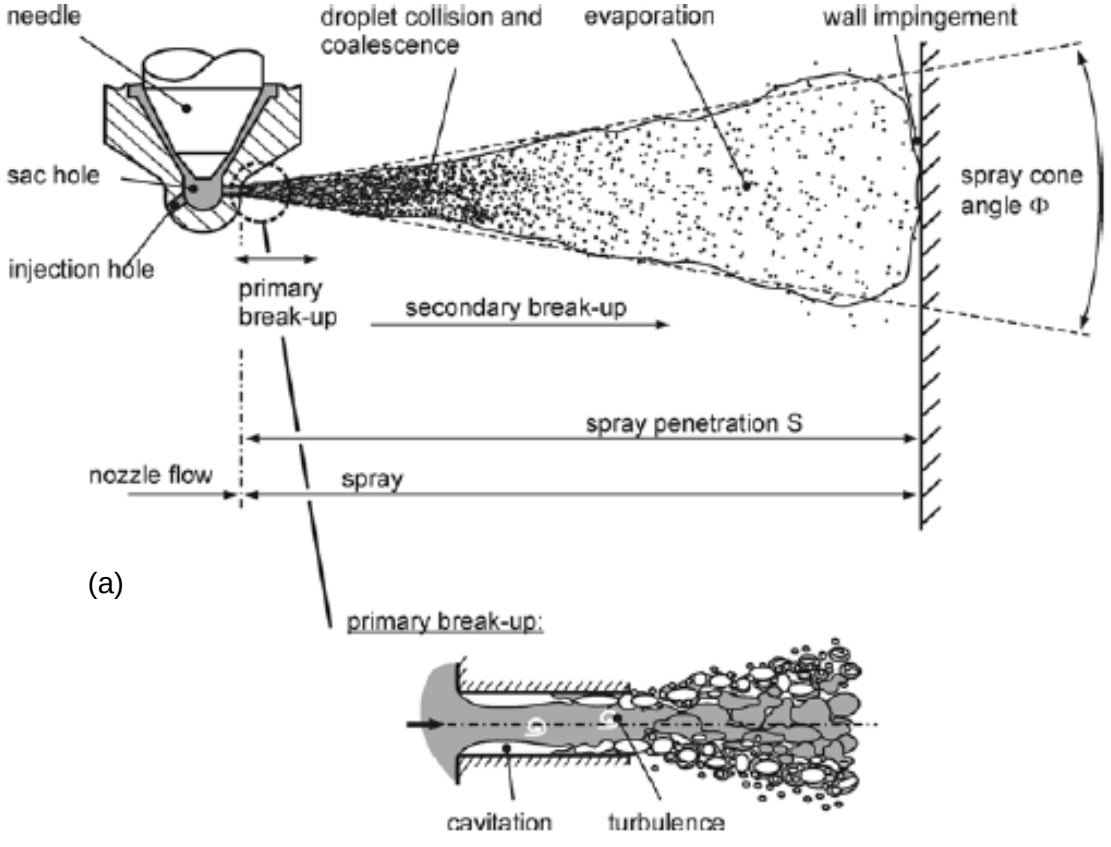

Figure 3.1: Typical spray atomisation description near the nozzle (Baumgarten, 2006).

As shown in Figure 3.1b, the high pressure continuous liquid enters the nozzle with many disturbances and is subjected to further surface and internal forces (cavitation bubble and turbulence) before leaving the nozzle. Flow instabilities, resulted from perturbation on the liquid, propagate and lead to the primary droplet breakup. Hence, primary droplet breakup depends on the nozzle geometry(L/D), nose radius (manufacturing process, laser drilled/spark eroded), sac volume, needle motion, static flow rate, liquid properties, turbulence intensity and the cavitation mechanism induced at different injection pressures. The primary droplet breakup is numerically captured with a multiphase model by resolving the liquid phase in both space and time (~10^{-9} to 10^{-6} m and ~10^{-13} s). It is computationally expensive to integrate with the full in-cylinder simulation. However, due to confidentiality of the injector supplier, it is also difficult to obtain the detailed injector geometry in the design and development stages.

The dense liquid ligaments originating from the nozzle exit are probabilistic in nature. There are several exit droplet representations reported in the literature (Hiroyasu and Kadota, 1974). In the most simplistic approach, “Blob” model, the initial droplet size is the nozzle exit diameter which is used in KIVA (Amsden et al., 1985). In this model, it is assumed that the atomisation and drop breakup are indistinguishable processes within the dense spray near the nozzle exit. This is later modified by redefining the nozzle exit droplets by SMD, which is calculated from correlation to injection velocity, surface tension and density (Reitz and Diwakar, 1987). The two mainly used droplet distributions are Rosin-Rammler (RR) and Chi-Square (χ^2) (Leferbver, 1989; Heywood, 1989; Baumgarten, 2006). In both cases, the cumulative volume fraction of the droplet sizes can be defined based on the SMD.

The primary droplets originated from the continuous liquid ligament further break down into multiple droplets, which are referred to as the secondary droplet breakup. Depending on the atomisation, millions of droplets can be generated from a single injection, which interacts and disintegrates continuously. Capturing secondary droplet breakup through a multiphase modelling representation is extremely difficult. This has resulted in a phenomenological model for describing the secondary droplet breakup mechanism built, based on the experimental observations.

In general, depending on fluid properties and on the relative velocity of the liquid ligament and the surrounding gases, breakup of liquid jet from the nozzle follows different breakup mechanisms. This is characterised by the liquid breakup length and droplet sizes. The general description of the primary and secondary droplet breakup is provided in the below section based on experimental observations reported in the literature.

3.1.1 Primary breakup

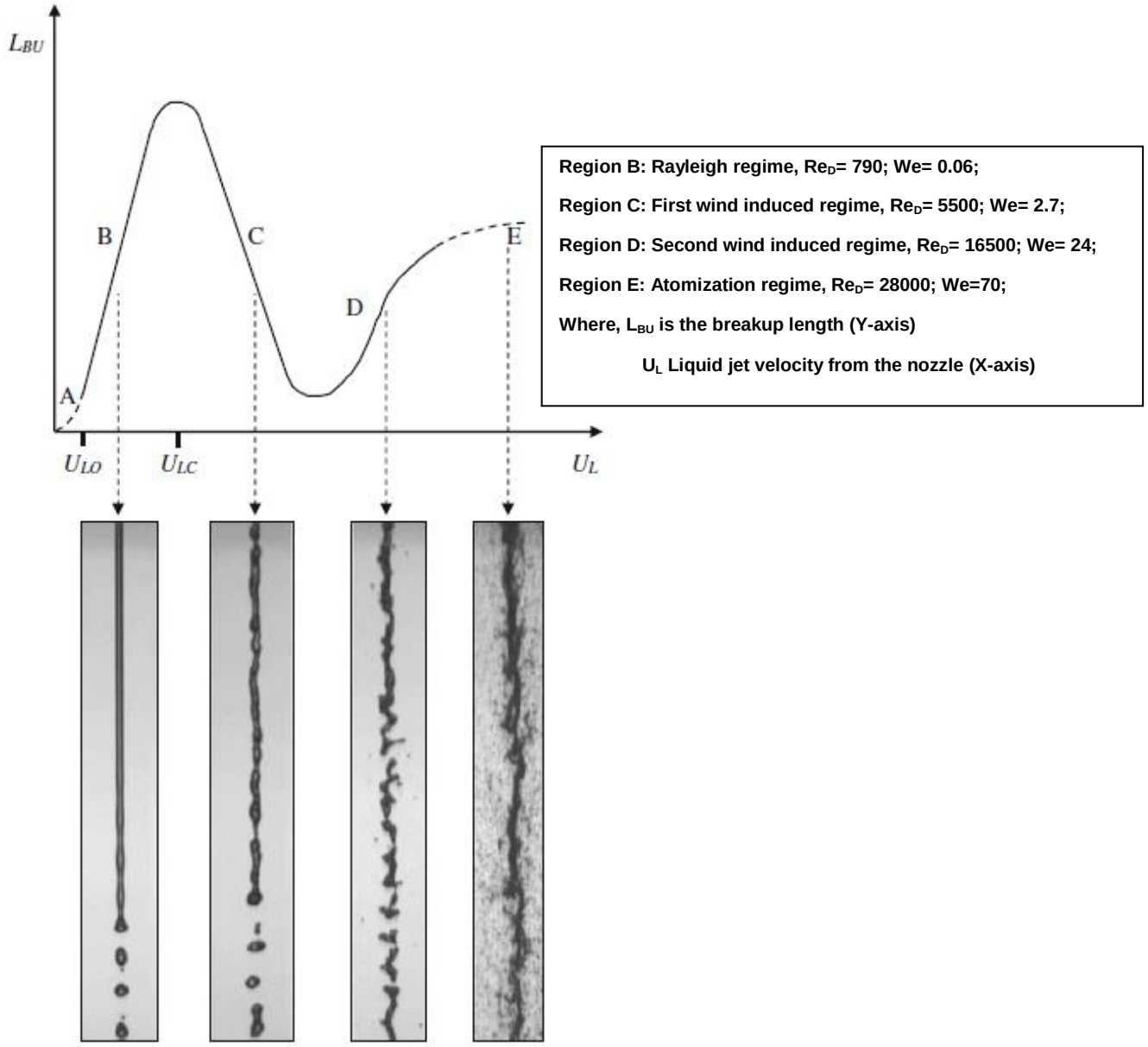

Figure 3.2: Cylindrical jet behaviour (Taken from Dumouchel, 2008). Top, stability curve and bottom, example of visualisation (from left to right).

Figure 3.2 depicts the different regimes covering the early liquid deformation before forming the first isolated droplets from the continuous liquid jet. This initial disintegration process is referred to as primary breakup mechanism. It is characterised by regimes defined by liquid jet velocity and the continuous liquid length. The different regimes shown in the figure are Rayleigh, first-wind breakdown, second-wind breakdown and atomisation regimes. In Rayleigh regime, the instability is from the liquid inertia and the surface tension. During this mechanism, the size of the droplet is larger than the nozzle diameter (~1.89D). In the first

wind-induced regime, liquid breakdown is induced by the aerodynamic forces from the surrounding gases. The droplet diameter is in the order of nozzle size. In the second wind-induced regime, the liquid breaks up due to the turbulence induced in the nozzle and the aerodynamic forces around liquid jet. It is in mixed zone wherein smaller primary droplets arise by shearing/peeling from the main liquid jet and the rest from the main liquid ligament itself. Atomisation regime is wherein there is a rapid liquid ligament disintegration near the nozzle exit due to the instability induced by turbulence, cavitation and near gas shear. As a result, a wide range of droplet diameters could be found. This regime is normally noticed in the modern high pressure multi-hole injectors. As detailed earlier in the modelling approach, a probabilistic representation is required to represent the outcome of the primary droplets/ligaments.

A reasonable primary droplet distribution assumption (Von Kuensberg Sarre, Kong and Reitz, 1999; Abani, Bakshi and Ravikrishna, 2001) is required to predict the penetration depth and end droplet distribution in the real engine scenarios. Droplet distortion (Liu and Reitz, 1997) would be significant near the injector tip as the droplet is more as a ligament than spheroids. In the initial injector model, the initial primary droplets are assumed to be in spherical shape and the cavitation-induced breakdown is ignored.

In the modern high-pressure injectors (150 to 350 bar), the typical Re_D is in the range 27000 to 40000. The Weber number (Equation 2.1) is normally larger than 70 (n-heptane or gasoline, assuming initial droplet size to be in the order of nozzle diameter ~140μm). Hence, during the main injection event, the breakup mechanism falls in the atomisation regime. This results in a rapid liquid ligament disintegration near the nozzle exit due to the instability induced by turbulence, cavitation and near gas shear. A wide range of dense droplet diameters are found at the nozzle exit. This can be reasonably represented by a droplet size distribution, such as Chi-square (χ^2) and Rosin-Rammler (RR).

3.1.1.1 Primary droplet SMD and nozzle exit velocity

Commercial CFD code STAR-CD/ES-ICE (STAR-CD methodology manual, 2018) is used in this work. The SMD and velocity of droplets at nozzle exit together with droplet size distribution are part of input data for spray modelling. It is assumed that the fuel is fully atomised at nozzle exit and the droplet sizes can be described by the RR distribution as shown in Equation 3.1:

$$Q(D) = 1 - e^{-\left(\frac{D}{\bar{D}}\right)^q} \qquad (3.1)$$

Q is the cumulative distribution function (CDF), i.e., the volume fraction of the droplets whose diameters are less than diameter, D, as shown in Figure 3.3. This is considered as the simplest assumption with the available nozzle data from the injector supplier.

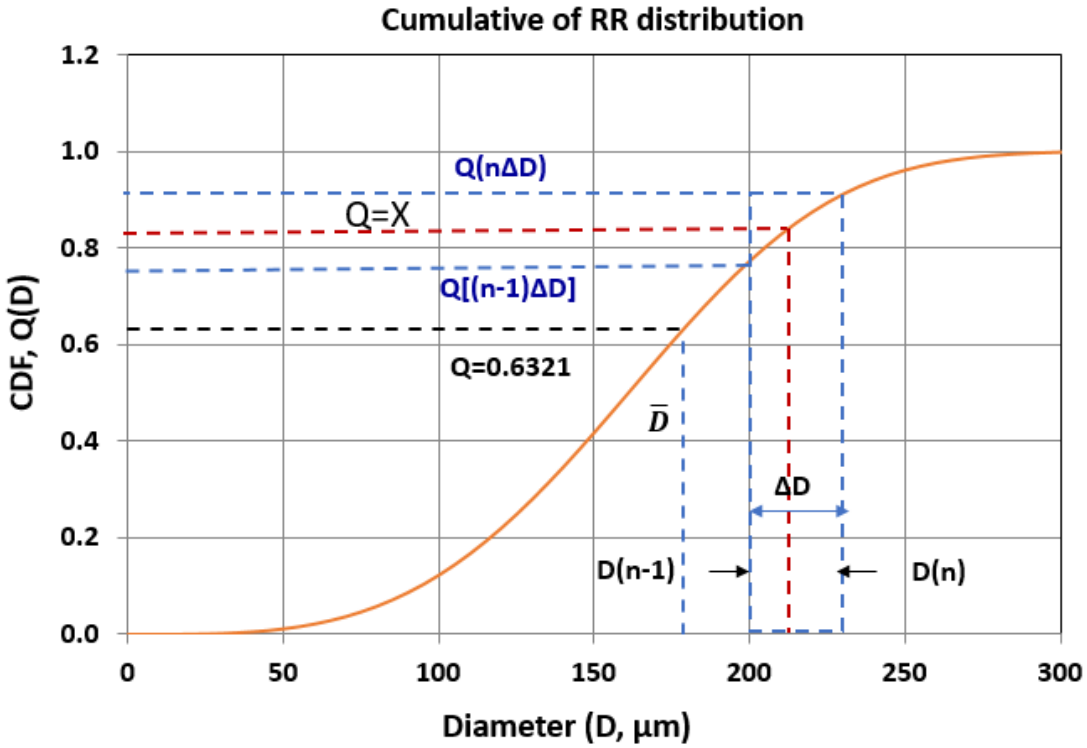

Figure 3.3: Cumulative distribution function of Rosin-Rammler distribution.

The derivative of the cumulative distribution ($\frac{dQ}{dD}$) function represents the probability density function(PDF). PDF function derived from the chosen RR distribution defined by Equation 3.1 is given in Equation 3.2:

$$\frac{dQ}{dD} = \frac{q}{\bar{D}}\left(\frac{D}{\bar{D}}\right)^{q-1} e^{-\left(\frac{D}{\bar{D}}\right)^{q}} \quad (3.2)$$

where

$$\bar{D} = SMD\left[\Gamma\left(1-\frac{1}{q}\right)\right] \quad (3.3)$$

$$\Gamma(x) = \int_0^{\infty} e^{-t}\, t^{x-1} dt \quad (3.4)$$

Figure 3.4 shows the PDF function plotted for the chosen droplet diameters. In Equation 3.1 and 3.2, q=3.5 is used (Abani et al., 1999). $\bar{D}$ can be calculated from SMD and Gamma function as shown in Equation 3.4. For q=3.5, Γ(1-1/q) =1.276 which is the ratio of $\bar{D}$/SMD.

For D=$\overline{D}$, $Q = 1 - e^{-1} = 0.6321$, irrespective of q, as shown in Figure 3.3. This is a distinct feature of Rosin-Rammler distribution.

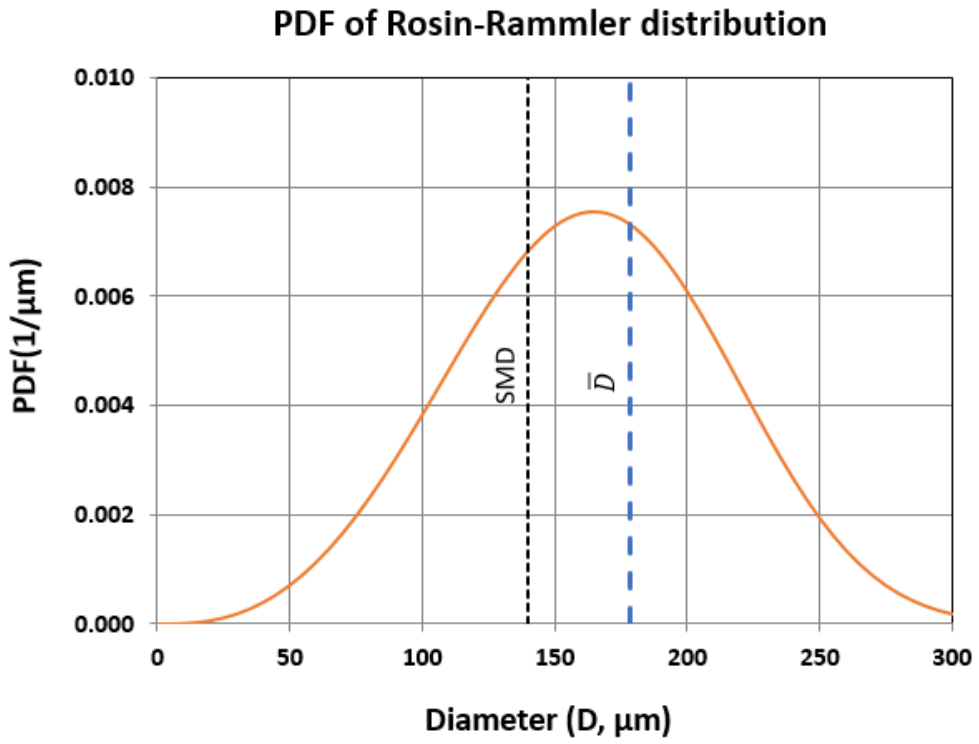

Figure 3.4: Probability density function of RR distribution.

Values of Q(D) in increments of ΔD= 0.025*SMD between D=0 and D=2.5*SMD are stored. The value of Q(2.5*SMD) is taken to be unity. This involves only a slight inaccuracy, since Q(2.5*SMD) is greater than 0.999. If X, as shown in Figure 3.3, is a random number in the interval (0,1), we find that value of "n" for which

$$Q[\Delta D(n-1)] < X < Q[\Delta D(n)] \quad (3.5)$$

Then, the corresponding droplet diameter is

$$D = \Delta D(n) = 0.025(SMD)(n) \quad (3.6)$$

A user subroutine is made to implement the Rosin-Rammler distribution. Numerically, these droplets are packed as parcels during each time step of the simulation. Sufficient time resolution is chosen to have a more representative statistical distribution of the droplets.

Droplet exit velocity is calculated based on a uniform flow through the nozzle hole diameter (u_{mean}) and static flow rate (Q_{static}) provided by the injector supplier. Static flow rate of injector Q_{static}, i.e., the flow rate at 10 MPa fuel pressure is known and the discharge coefficient of injector, C_d, can be calculated using Equation 3.7:

$$C_d = \frac{Q_{static}}{Q_{ideal}} = \frac{Q_{static}}{\rho_l A_{hole}\sqrt{\frac{2\Delta p}{\rho_l}}} = \frac{Q_{static}}{A_{hole}\sqrt{2\rho_l \Delta p}} \qquad (3.7)$$

where

ρ_l is the density of liquid fuel

Δp is the static pressure 10 MPa

A_{hole} is the total area of nozzle holes.

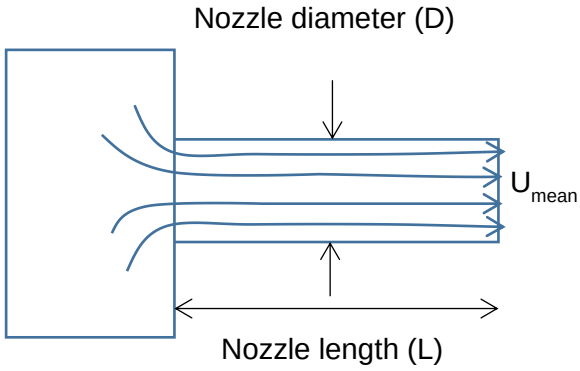

Figure 3.5: Typical nozzle flow showing the path lines covering total cross-section.

At a given engine operating condition, mean velocity in nozzle hole u_{mean}, can be calculated from C_d and the pressure difference between fuel rail and combustion chamber.

$$u_{mean} = C_d\sqrt{\frac{2\Delta P}{\rho_l}} \qquad (3.8)$$

ΔP is the pressure difference between fuel rail and combustion chamber at the given engine operating condition. Thus, the mean velocity calculated based on the nozzle total area and the static flow rate will be used as the initial droplet velocity. Numerically, once the initial diameter is stripped from the RR distribution (Figure 3.3) an equal velocity and temperature are assigned for each droplet parcels.

3.1.2 Secondary breakup

The droplet breakup after the first initial liquid ligament broken-up from the main liquid length connecting the nozzle exit is characterised as secondary breakup. As detailed in the literature

review section, several researchers experimentally observed the droplet disintegration process under different droplet initial conditions and environment (Pressure and Temperature). The breakup mechanisms (Pilch and Erdman, 1987; Hsiang and Faeth, 1992; Guildenbecher et al., 2009) are characterised by non-dimensional numbers such as Weber number ($We = \frac{\rho_a U_0^2 D_d}{\sigma_d}$), Ohnesorge number ($Oh = \frac{\sqrt{We}}{\mathrm{Re}_d}$) and Reynolds number ($Re = \frac{\rho_a U_0 D_d}{\mu_a}$). Some of the secondary droplet breakup modes described are vibrational, bag, multimode, sheet-thinning and catastrophic. The pictorial representation of the different modes of droplet breakup is shown in Figure 3.6.

Vibrational: We < 11

Bag: 11<We < 35

Multimode: 35 < We < 80

Sheet-thinning: 80 < We < 350

Catastrophic: We > 350

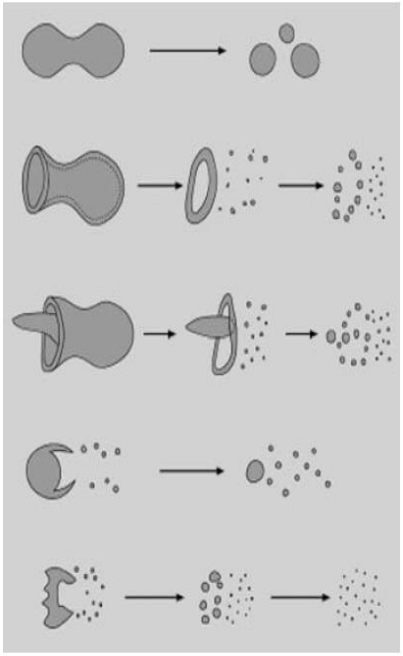

Figure 3.6: Breakup mechanism: @Oh<0.1 (Guildenbecher, Lopez-Rivera and Sojka, 2009).

It could be seen that the parent single droplet undergoes different deformation, which are dictated by the relative forces of the inertia and surface tension. It is very evident that a wide range of length and timescales associated during this breakup mechanism. Hence, capturing the detailed characteristics are extremely difficult. However, the droplet breakup characteristics are categorised by several researchers using non-dimensional numbers (We and Oh) in the form of regime map. The regime map categorised by Hsiang and Faeth, 1992, is shown in Figure 3.7.

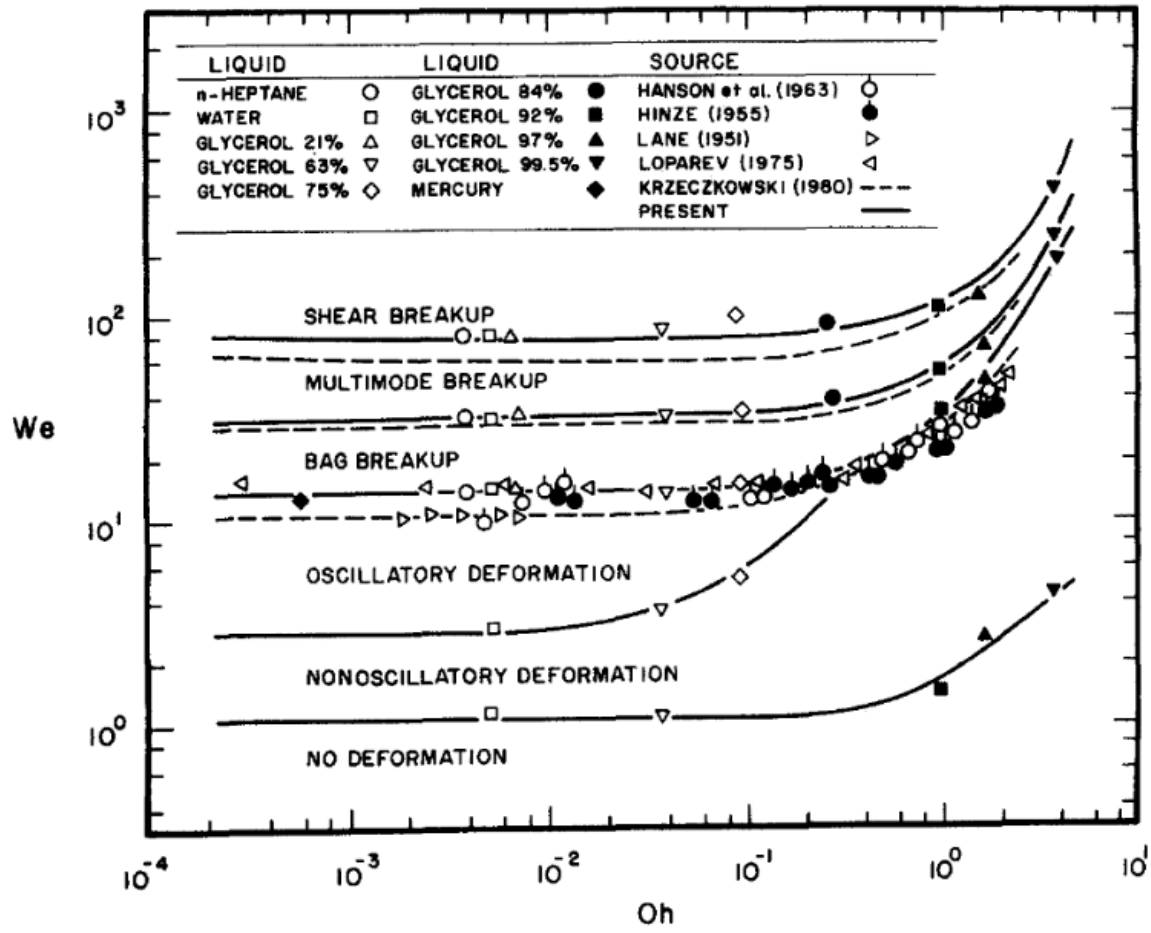

Figure 3.7: Droplet deformation and breakup regime map (Taken from Hsiang and Faeth, 1992).

The fundamental observation from this chart is that for the fixed Oh number, the droplet mechanism changes with increase or decrease in We number. Similarly, for the fixed We number, there is a dependency in the changes in droplet mechanism. This indicates that for the same We number, different fluid can undergo different breakup mechanism. These are used as the basis for the phenomenological representation of the secondary droplet breakup mechanism.

As mentioned in Section 3.1.1, a typical droplet Weber number $(We = \frac{\rho_a U_0^2 D_d}{\sigma_d})$ for the modern high pressure fuel injector with a nozzle size of 140 μm at an injection pressure of 150 bar for n-heptane fuel is shown in Table 3.1. In the calculation, a minimum primary droplet diameter (50 μm) at the nozzle exit is chosen from the RR distribution shown in Figure 3.3. The mean velocity is calculated based on Equation 3.8 with a discharge coefficient (C_d) of 0.67.

Table 3.1: List of parameters used for droplet Weber number calculation.

n-heptane at 150 bar injection pressure		
Density air (ρ_a)	1.16	kg/m^3
Droplet diameter (D_d)	50	µm
Initial droplet velocity (U_0)	138	m/s
Surface tension (σ_d)	0.02	N/m
Density droplet (ρ_l)	693	kg/m^3
Weber number (We)	70.80	

The Weber number calculated with this assumption is 70.8. In the regime chart shown in Figure 3.7, the most noticeable droplet breakup mechanism at a Weber number of 70 is the shear breakup. Moreover, as reported in Guildenbecher, Lopez-Rivera and Sojka (2009), the droplet size outcome from shear breakup is extremely small. During the normal engine operation of the modern GDI engines, an injection pressure of 300 to 350 bar is commonly used. This should result in a much higher Weber number. Hence, it is expected that the most dominant droplet mechanism is shear/stripping breakup. Both Reitz-Diwakar and KH-RT models consider shear/stripping and bag breakup explicitly. These models also account for bag breakup. Moreover, these models are widely used, and are recommended as a part of the best practices in STAR-CD/ES-ICE (2018) for engine flow simulation. Hence, in this work these two models are taken for the study. Brief descriptions of the two secondary droplet models and adjustable parameters are provided in the section below.

3.1.2.1 Reitz-Diwakar model

In this model, bag breakup and stripping/sheet-thinning breakup regimes are considered.

The rate of change of droplet diameter due to instability is given by the Equation 3.9:

$$\frac{dD_d}{dt} = -\frac{(D_d - D_{d,stable})}{\tau_b} \qquad (3.9)$$

where

$D_{d,stable}$ = Stable droplet size

τ_b = Breakup time scale

The stable droplet size ($D_{d,\,stable}$) is obtained from Equation 3.10:

$$\frac{\rho_a U_0^2 D_d}{2\sigma} \geq C_{b1} \qquad (3.10)$$

where

c_{b1} = Critical Weber number for bag breakup

$U_0 = |U_f - U_d|$

U_f = Gas velocity (m/s)

U_d = Droplet velocity (m/s)

The bag breakup time constant evaluated using Equation 3.11:

$$\tau_b = \frac{C_{b2}}{2}\left(\frac{\rho_d}{\rho}\right)^{1/2}\frac{D_d^{3/2}}{4\sigma_d^{1/2}} \quad (3.11)$$

where

c_{b2} = Bag breakup time constant

ρ_d = Droplet density (kg/m^3)

σ = Droplet surface tension

ρ = Gas density (kg/m^3)

The stripping breakup criteria is given by Equation 3.12:

$$\frac{We}{\sqrt{\mathrm{Re}_d}} \geq C_{s1} \quad (3.12)$$

where

C_{s1} = Critical stripping breakup criteria

We = Weber number

Re_d = Droplet Reynolds number

The timescale for the stripping breakup regime is given by Equation 3.13:

$$\tau_b = \frac{C_{s2}}{2}\left(\frac{\rho_d}{\rho}\right)^{1/2}\frac{D_d}{U_0} \quad (3.13)$$

where

C_{s2} = Stripping breakup time constant

In the spray model calibration process, the evolution of droplet penetration depth and the

droplet sizes at predefined station are compared with the experimental data. The model constants namely, C_{b1}, C_{b2}, C_{s1} and C_{s2} are mainly adjusted to correlate with the experimental data. The final model constants are used for the actual in-cylinder simulation. In STAR-CD, model constants C_{b2} and C_{s1} are set to the default values of π and 0.5, respectively. In this work, the default values of bag breakup constant, C_{b1}(6) and stripping breakup time constant, C_{s2}(20) are adjusted to correlate the available test data. The effect of the modelling constants was studied in this work and will be presented later.

3.1.2.2 KH-RT model

In this model (Patterson and Reitz, 1998), instability growth induced by Kelvin-Helmholtz (surface growth normal to the liquid inertial direction) and Rayleigh-Taylor (surface instability due to the droplet drag or acceleration) waves are considered. The dispersion ($\omega_{KH}[\Lambda_{KH}]$, $\omega_{RT}[\Lambda_{RT}]$) equation solved to evaluate the wavelength (Λ_{KH} and Λ_{RT}) associated to the fastest growth rate (ω_{KH} and ω_{RT}) evaluated to determine the droplet cut-off diameter and timescales.

The stable droplets(D_s) of the individual modes were scaled based on the fastest growing wavelengths as against the critical Weber number as in the case of R&D model. Droplet breakdown and timescale for KH instabilities are given in Equation 3.14 and Equation 3.15, respectively:

$$\frac{dD_d}{dt} = -\frac{(D_d - D_s)}{\tau_{KH}} \qquad (3.14)$$

where

$$D_s = B_0 \Lambda_{KH}$$

$$\tau_{KH} = \frac{3.726 B_1 D}{2 \Lambda_{KH} \Omega_{KH}} \qquad (3.15)$$

$$\Omega_{KH} = \text{Growth rate of fastest growing wave in KH instability}$$

Similarly, for RT instabilities, if the scaled wavelength ($C_3\Lambda_{RT}$) calculated from the wavenumber(K_{RT}) corresponding to the maximum growth rate (Ω_{RT}) is smaller than the droplet diameter, then the wave is bound to grow. If the wave grows for a sufficient time (C_τ/Ω_{RT}) dictated by the growth rate, then the droplet break down occurs. Where, C_τ it the model time constant. The droplet size is given by the scaled wavelength. More details could be referred

from Senecal et al. (2007) and Star-CD methodology manual, (2018). Figure 3.8, shows the description of KH and RT wave growth and the resulting child droplet diameter scales.

In this study, model constants B_1 (KH-Model) and C_3 (RT-Model) were used to tune the sprays. Increasing the value of the C_3, decreases the droplet breakup leading to have a larger droplet size.

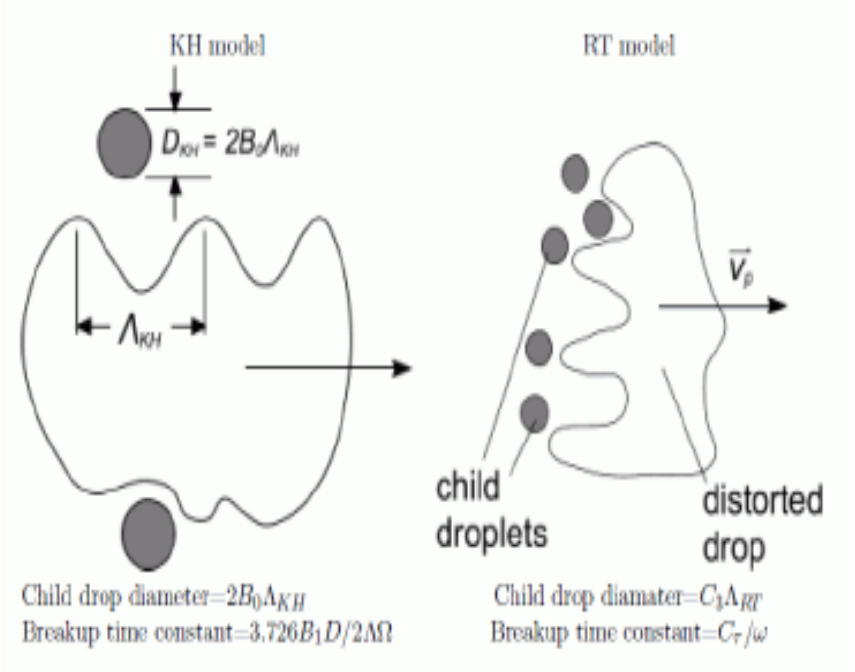

Figure 3.8: Depiction of the KH and RT wave breakup mechanism (Star-CD, 2018).

3.1.3 GDI Spray simulation and validation

In the simulation process, Lagrangian multi-phase approach is adopted using Star-CD CFD solver. Wherein, the continuous gas phase energy, momentum and species transports are solved, simultaneously. However, the discrete droplets evolved from the primary droplet breakup are tracked in the Lagrangian frame along with the phenomenological secondary droplet breakup calculated based on the droplet properties and local gas phase conditions. The resultant exchanges of species, momentum (Dukowicz, 1980) and energy with the droplets are considered as a corresponding source/sink terms in the governing equations. The detailed solver algorithm and governing equations are provided in the Star-CD CFD methodology manual (Star-CD version 4.30, Siemens, 2018). The spray rig model, boundary and initial conditions used for the simulation are provided in the following section.

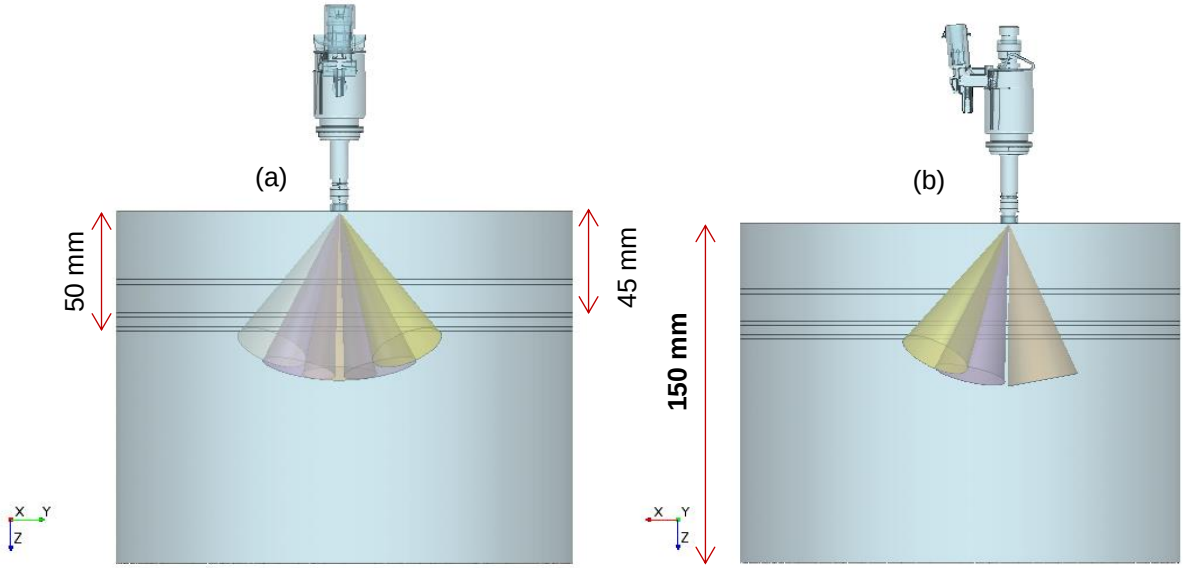

Figure 3.9: Spray rig, CFD model with front (a) and side view (b) shown.

3.1.3.1 Spray rig model setup

A reference injector model is attached to the spray rig geometry for detailing the front and side view of the spray pattern. The spray rig model is a simple cylindrical geometry, covering the extent of the possible spray penetration to avoid any influence of the boundary conditions on the droplet behaviour. In general, the SMD measurements for injectors from the suppliers are available at 45 mm to 50 mm distance from the injector axis. Hence, computational cells of 1 mm thickness are grouped at 45 and 50 mm distance (shown in Figure 3.9) from the injector axis for monitoring the droplet SMD.

3.1.3.2 Spray rig model boundary condition

The boundary condition used in the simulation were provided in Figure 3.10. The injector tip wall surface is captured with 4X4 mm patch, to capture the near air entrainment at the nozzle exit. All other surfaces of the spray rig are fixed with ambient pressure boundary conditions of 1.01325 bar and 298K.

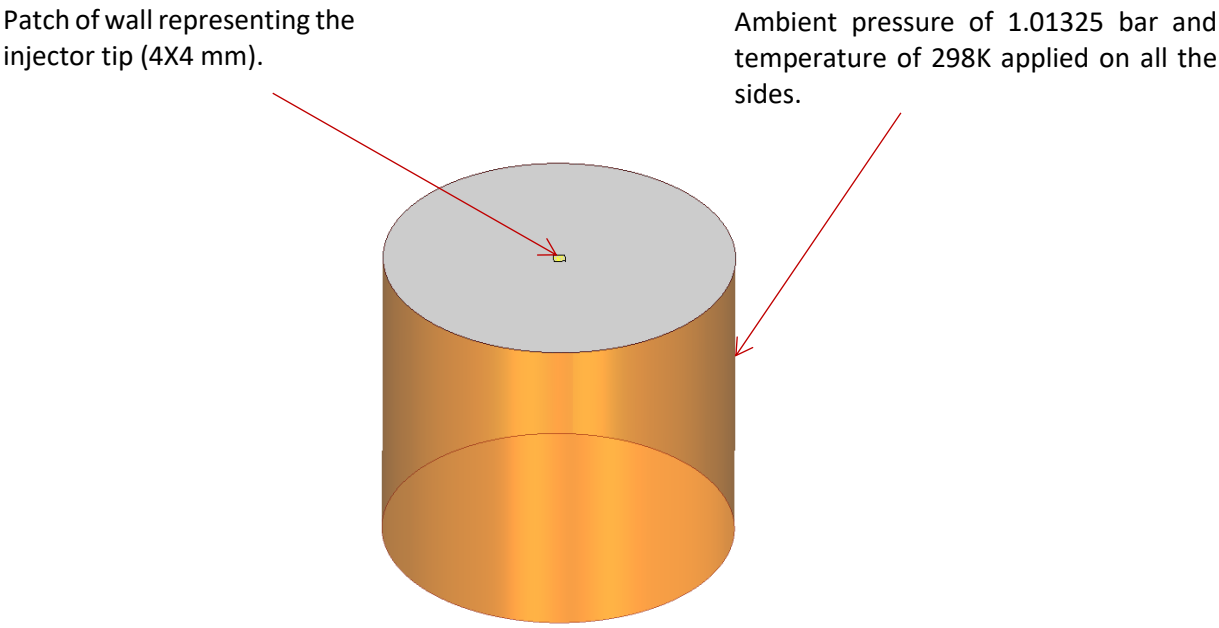

Figure 3.10: Spray rig, CFD model boundary conditions.

3.1.3.3 Spray rig mesh model

The geometry shown in Figure 3.10 is meshed with a hexahedral cell. The typical mesh obtained for the simulation is shown in Figure 3.11. Mesh refinements are provided near the injector tip to capture the air entrainment and to capture the complete evolution of the plume for the whole injection event. The total mesh size model contains a hexahedral cell count of 3.8 million.

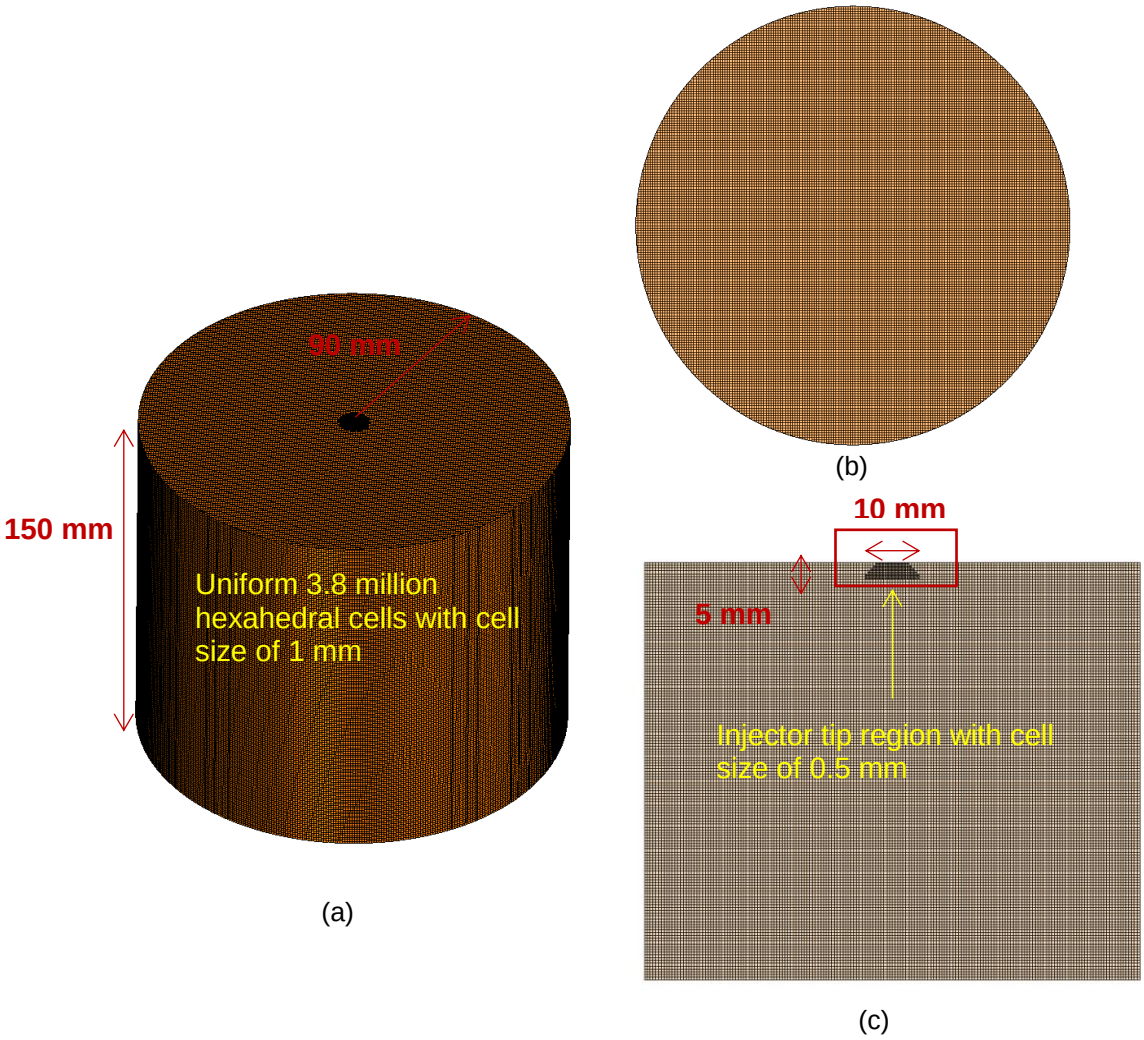

Figure 3.11: Spray rig CFD mesh model. (a). External view, (b) bottom view and (c) sectional view.

3.1.3.4 Injector conditions

In the calibration study, two injectors are used in the simulation. The injectors are referred as injector-A and B. Injector-A has a 5-hole nozzle configuration with an equivalent diameter of 140µm. The static flow rate(Q_{stat}) of the injector at 100 bar injection pressure is 8.69 cm^3/s. Injector-B has a 6-hole nozzle with an equivalent diameter of 182 µm. The Q_{stat}, for this injector is 17.5 cm^3/s at 100 bar injection pressure. In both the cases, n-heptane fuel properties are used.

Primary droplet considerations:

Cumulative distribution and probability density functions calculated as in Section 3.1.1.1 for Injector-A is shown in Figure 3.12.

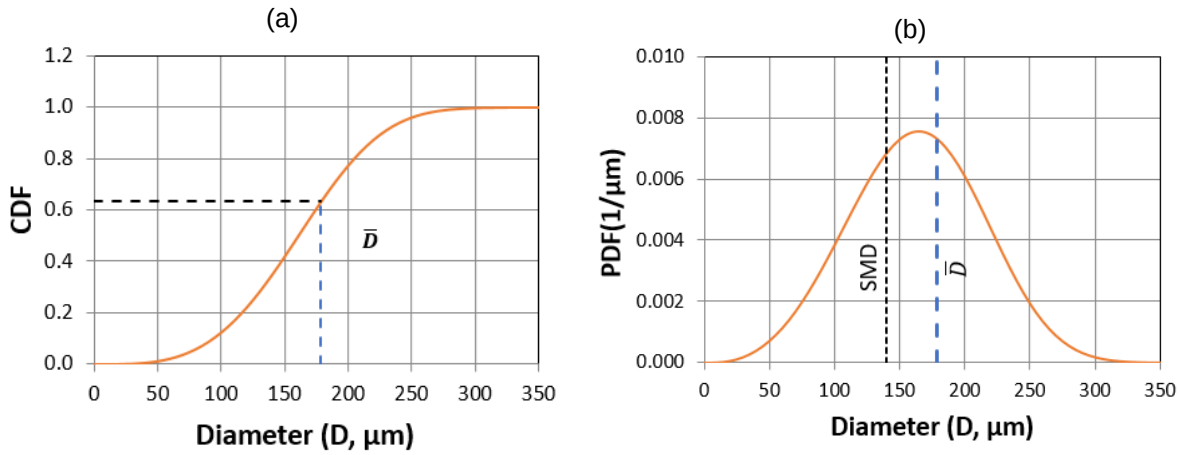

Figure 3.12: (a) Cumulative distribution and (b) probability density function for Injector-A, nozzle size of 140 µm.

The primary droplet parameters for defining Injector-A nozzles are shown in Table 3.2. It should be noted that all the nozzle is assumed to have the same primary droplet characteristics.

Table 3.2: Calculated primary droplet parameters for Injector-A.

Nozzle parameters		
SMD	140	µm
ΔD	4	µm
Dmax	350	µm
$\bar{D}$	179	µm
Cone angle	20˚	Deg.

Similarly, the cumulative distribution and probability density functions calculated as in Section 3.1.1.1 for Injector-B is shown in Figure 3.13. The primary droplet parameters for defining Injector-B nozzles are shown in Table 3.3.

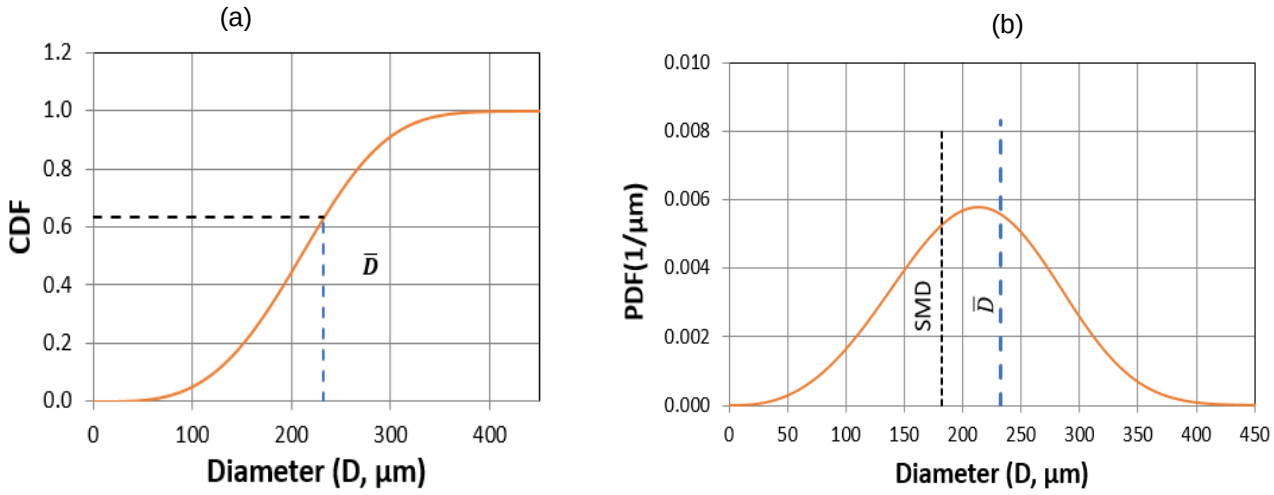

Figure 3.13: (a) Cumulative distribution and (b) probability density function for Injector-B, nozzle size of 182 µm.

Table 3.3: Calculated primary droplet parameters for Injector-B.

Nozzle parameters		
SMD	182	µm
ΔD	5	µm
Dmax	455	µm
$\bar{D}$	232	µm
Cone angle	20˚	Deg.

Primary droplet initial velocity:

The initial velocity and pulse width used for the Injector-A and B simulation are given in Table 3.4 and Table 3.5, respectively. Initial velocities are calculated from the C_d valve from Q_{stat} provided at 100 bar injection pressure. A constant discharge coefficient (C_d) value is assumed that for the high-pressure injector, with high Reynolds number (Re_D~36500).

Table 3.4: Calculated primary droplet velocity for Injector-A.

Injector-A (5-Hole nozzle; Diameter=140µm)				
Injection pressure, ΔP (Bar)	Total volume flow, Q_{stat} (cm^3/s)	Mean droplet velocity, U_{mean} (m/s)	Discharge coefficient (C_d)	Pulse width (ms)
150	10.66	138.48	0.67	1.5
300	15.10	196.17	0.67	1.5
350	16.31	211.94	0.67	1.5

Table 3.5: Calculated primary droplet velocity for Injector-B.

Injector-B (6-Hole nozzle; Diameter=182µm)				
Injection pressure, ΔP (Bar)	Total volume flow, Q_{stat} (cm^3/s)	Mean droplet velocity, U_{mean} (m/s)	Discharge coefficient (C_d)	Pulse width (ms)
150	21.43	137.32	0.66	2
200	24.75	158.58	0.66	1.5

3.1.3.5 Simulation setup

In Star-CD solver, Realisable k-ε turbulence model is chosen for the simulation. A very fine time step of $1e^{-5}$s is used in the simulation. A customised Fortran user-routine used for initialising the spray parameter such as number of parcels, diameter of the droplets, injection directions and velocity within in the cone angle and random injection location in the specified nozzle exit location. Also, for a better representation of the RR distribution, significantly larger number parcels are used (~$1e^7$-$1e^8$ parcel/s).

3.1.4 Results and discussion

Simulations are carried out for both R&D and KH-RT model for Injector-A and B, respectively. In the results section, the droplet penetration depth and the SMD predicted are compared with the available experimental data from the injector supplier. As detailed in Section 3.2.1.1 and 3.2.1.2, the chosen modelling constants, C_{b1}, C_{s2} for R&D model and B_1 and C_3 for KH-RT are modified to match the available experimental data. It is expected that, for the chosen model constants, the spray simulation should estimate both the penetration depth and droplet sizes comparable to the available experimental data. It should be noted that, unless otherwise stated, a default model constants are used for other model parameters.

3.1.4.1 Penetration depth evaluation with Injector-A

In the numerical simulation results, research (Patterson and Reitz, 1998; von Kuensberg Sarre, Kong and Reitz, 1999) has reported to estimate the liquid penetration based on the liquid mass by the farthest parcel position of 90 to 99% of the liquid mass from the injector in

the normal injector axis direction. However, experimentally, the liquid penetration depth reported are the high-speed shadow graphs/contrasts and by further image processing (Hung et al., 2009). Moreover, the penetration depths reported are through ensemble averaging of instantaneous liquid penetration for several injection events (typically, 10 to 30 or more images). As reported in Dhanji and Zhao, (2019), the instantaneous penetration depth is found to show a band and it is higher (~5 mm, which is 5 to 6% of the total penetration depth) at higher injection pressures (250 to 350 bar injection pressures). Hence, in this work, importance of penetration depth estimation and experimental comparison are reported. As the penetration depth is the vertical distance measured from the spray origin, in most of the multi-hole solid cone sprays, the penetration depth is mainly dictated by the most vertical spray plume/nozzle

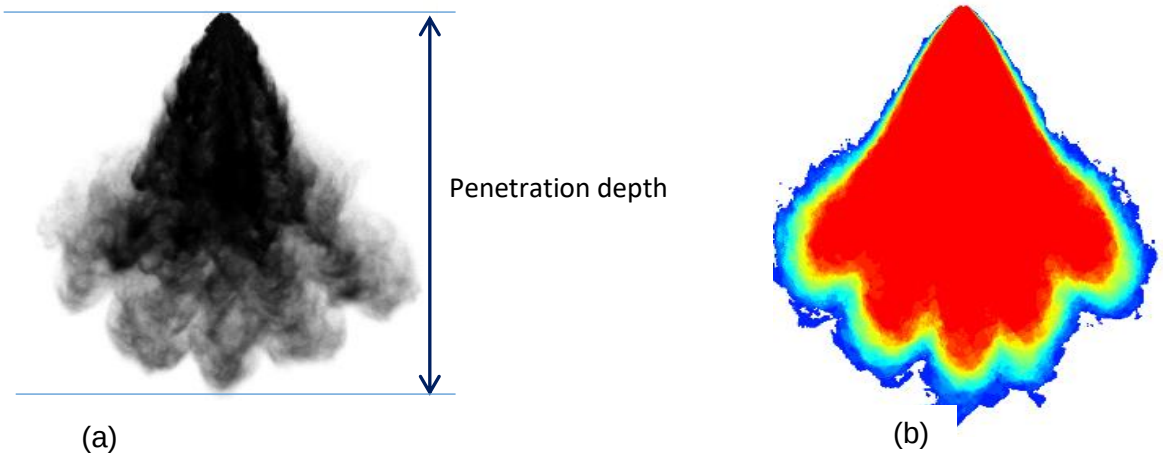

Figure 3.14: Injector-A, experimental data (a) High speed image, showing the spray structure. (b) Processed spray image differentiated by the colour contrasts. Experimental data provided by Faville and Moore (2015) (Delphi Technologies).

(assuming an equal nozzle hole configuration). Figure 3.14 shows the experimental data for Injector-A at 1.5 ms after the start of first liquid from the nozzle exit (aSOL) during the injection event that was measured by Changan UK supplier (Delphi Technologies, 2015). The penetration depth definition is also shown in the Figure 3.14a.

In the commercial CFD post processing tools, the parcels simulated from the simulation can be plotted either as “dots” or “spheres”. Based on the number of parcels displayed, the contrasts can be used for estimating the spray shape and for the penetration depth predictions. The typical comparisons between the two approaches are shown in Figure 3.15 and 3.16 for R&D and KH-RT, respectively, for Injector-A at 300 bar, injection pressure. It is evident that the simulated parcel display based on the droplet size as relative “spheres” is similar to the high-speed shadow graph images. The parcels displayed as “dots” are similar to the

processed contrast image, as shown in Figure 3.14b. This displays that the variable diameter parcel size visualisation shows a closer representation to compare the spray shadowgraphs.

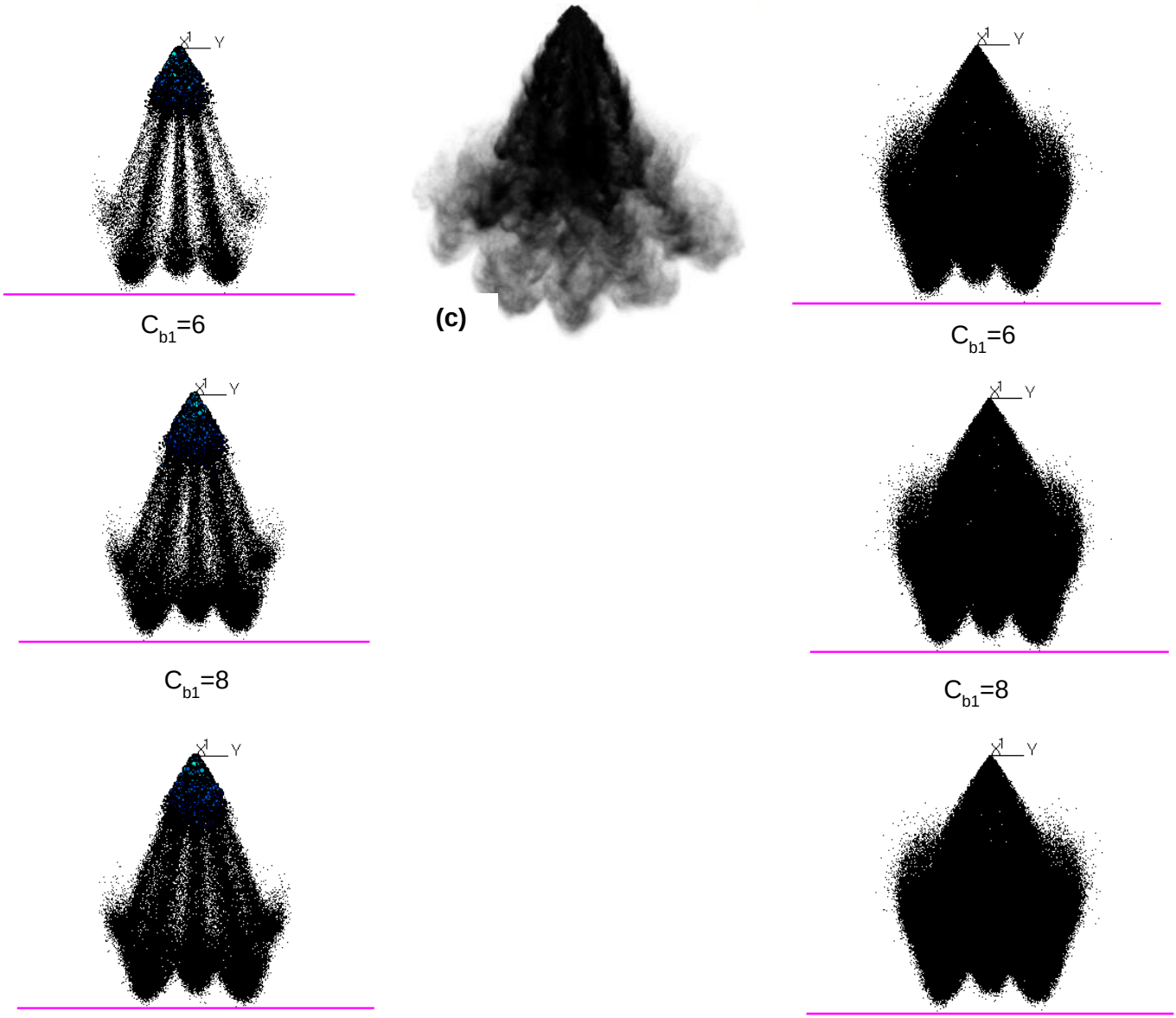

C_{b1}=6 **(c)** C_{b1}=6

C_{b1}=8 C_{b1}=8

(a) C_{s2}=25 **(b)** C_{s2}=25

Figure 3.15: (a) Results of R&D model simulation with the model constants for bag (critical Weber number, C_{b1}) and stripping breakup (time constants, C_{s2}). (a) showing the spray image displayed based on “spheres”, (b) showing the spray image display based on “dots” and (c) showing the experimental high-speed image corresponding to the same instant.

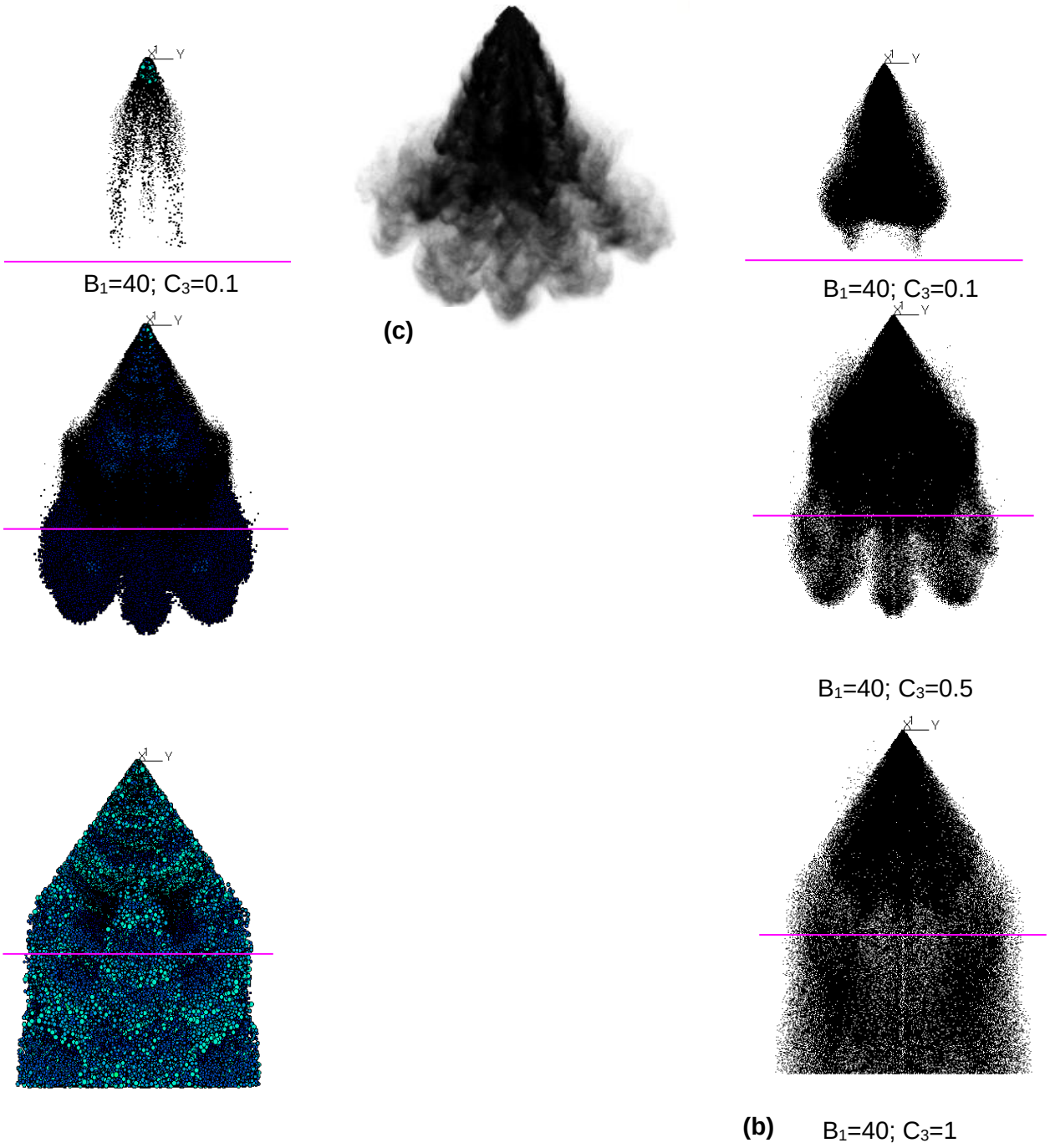

Figure 3.16: (a) Results of KH-RT model simulation with the KH droplet breakup time constant B_1 and RT breakup length constant C_3. (a) showing the spray image displayed based on "spheres", (b) showing the spray image display based on "dots" and (c) showing the experimental high-speed image corresponding to the same instant.

It should also be noted that the different nozzle sizes are expected to generate different droplet sizes distribution across the spray rig. However, a more simplified droplet visualisation with "dots" or through "spheres" may not show a consistent penetration depth estimation. In this

regard, the spray penetration estimation based on liquid fraction or void fraction are analysed after the initial model constants are estimated for R&D model.

3.1.4.2 R&D and KH-RT model constants sensitivity study with Injector-A

Figure 3.15 shows the effect of bag and stripping breakup model constants. Following bag breakup, critical Weber number (C_{b1}) increased from 6 to 8 and the secondary droplet breakup decreased significantly. This is mainly due to the increase in stable droplet size calculated from C_{b1} from Equation 3.10. Phenomenologically, it indicates that, the larger the bag breakup critical Weber number, the droplets are more stable. Similarly, when the stripping time constant C_{s2}, is increased from the default value of 20 to 25, the droplets become more stable as the rate of breakup decreases (Equation-9 and11). It means that an increase in stripping time constant increases the breakup timescale, which decreases the rate of secondary droplet breakup and, thereby, increases the droplet SMD. However, it could be seen that the tuning model constants has a linear relation with the droplet size, which benefits the spray calibration processes. In similar way, the effect of model constants was studied using the KH-RT model for the same injection parameters. In this case, the breakup time constant for KH droplet breakup, B_1 and the child droplet diameter characteristics of RT breakup constant, C_3, as detailed earlier, were chosen as a tuning parameter. Figure 3.16 shows the results of the spray characteristics with the effect of the chosen model constants. It can be seen that the effect of C_3 is very sensitive. As the model constant for RT breakup C_3 increased from 0.1 to 0.5 by fixing other constants, the droplet breakup decreased significantly. However, the effect of B_1 was found to be less significant. This shows the sensitivity of the KH-RT model for characterisation of the spray behaviour. Figure 3.17 shows the transients of the total droplet SMD with R&D and KH-RT model constants. In all cases, it is seen that the initial droplet breakup is very rapid, which happens in a timescale less than 0.25 to 0.5ms. After 0.25 to 0.5ms, the droplets are stable and the evaporation dominates the atomisation process. In the KH-RT model, a fastest break down is noticed with B_1=40 and C_3=0.1. Comparing the two approaches in the simulated total SMD the values from different models constant and sensitivity of the breakup are characterised. It was reported that the model constants in KH-RT model are also a function of injection pressure (Von Kuensberg Sarre, Kong and Reitz, 1999; Brulatout et al., 2015). This shows that the model constants for KH-RT model are sensitive. As discussed earlier, the phenomenological model of R&D uses the bag breakup and stripping breakup cut-off criteria, which is similar, as reported in the regime chart (Figure 3.7). This agrees well with many of the reported liquids and is more quantifiable in determining the model constants. Hence, in this study, the spray calibration simulation process is carried out with R&D model.

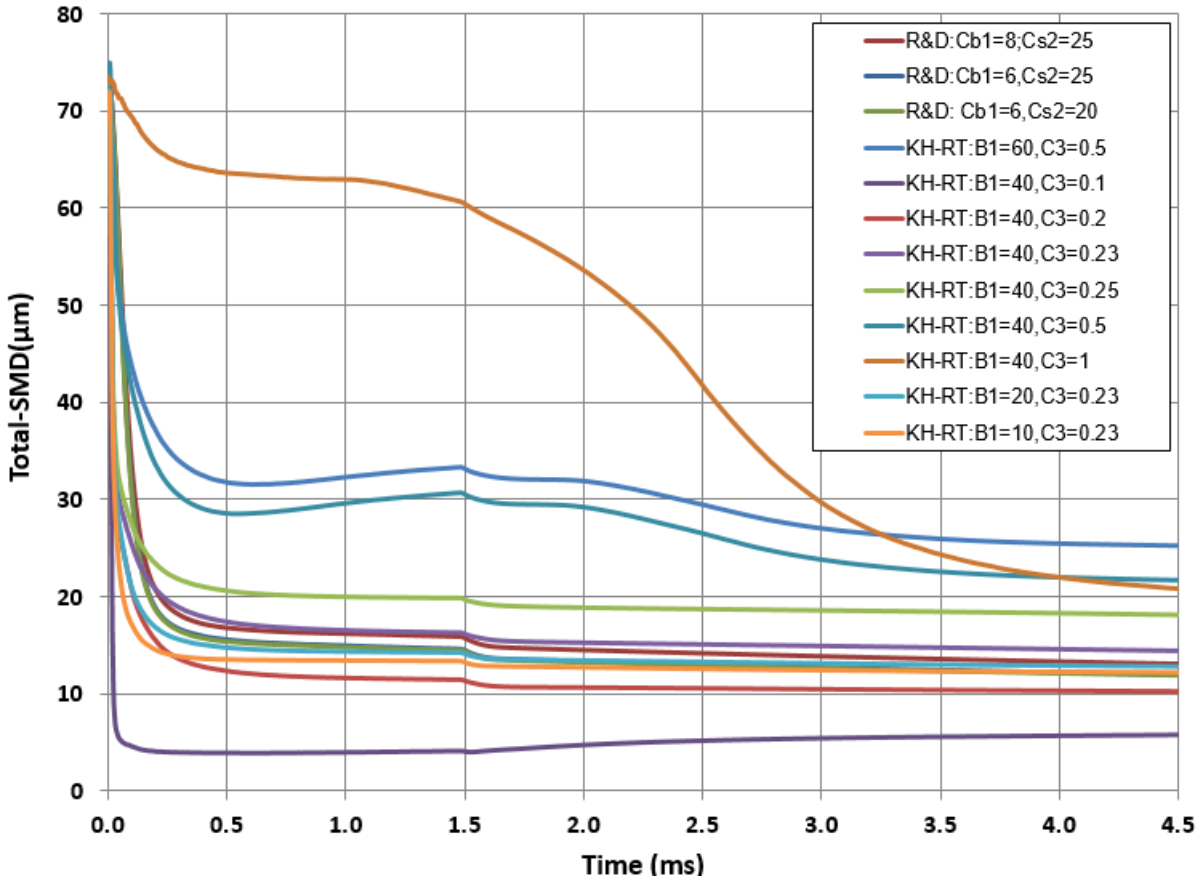

Figure 3.17: Transient total droplet SMD in the domain for R&D and KH-RT model with the different model constants are shown, where B_1 and C_3 are KH-RT model constants; C_{b1} and C_{s2} are R&D model constants.

3.1.4.3 Injector-A and Injector-B simulation correlation:

In this section, penetration depth estimation using liquid fraction or the void fraction approach is discussed. After several simulation trials using R&D model for Injector-A, bag breakup constant C_{b1} = 5 and stripping breakup time constant C_{s2}=5 are chosen to match both penetration depth and the SMD data at 45 mm from the injector tip (station shown in Figure 3.9). The comparison of the different spray images from the simulation and the experimental high-speed imaging is shown in Figure 3.18. A good correlation is observed between the experimental measurements and the numerical simulation, validating this approach.

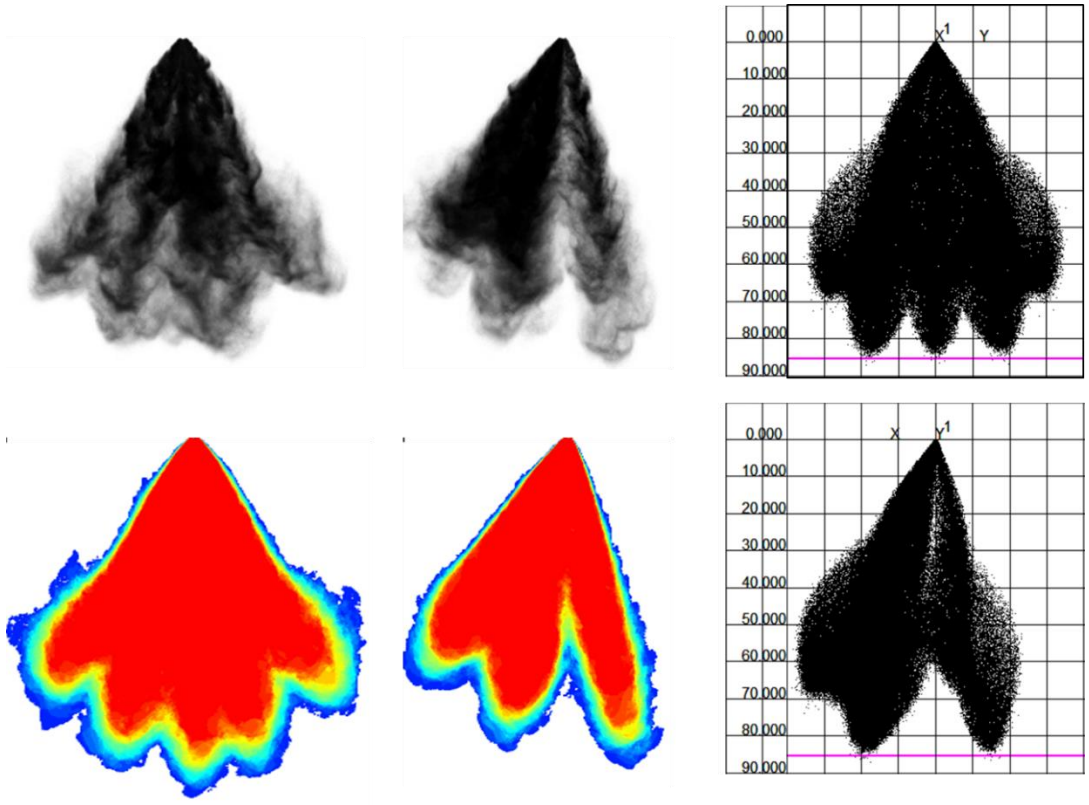

(a) **(b)** **(c)**

Figure 3.18: Spray image from Injector-A (300 bar) comparing with the experimental data and the simulation for R&D model (C_{b1}=5 and C_{s2}=5). In this (a) and (b) are the experimental data and (c) is the simulation with the droplet parcels displayed as “dots”, the magenta colour line is the experimentally measured penetration depth. Experimental data provided by Faville and Moore (2015) (Delphi Technologies).

In Figure 3.19, the discrepancies in the penetration depth definition are shown. In this case, the magenta coloured line in the numerical simulation (Figure3.19b) plot is the experimentally observed penetration depth. There is around 5 to 8 mm difference based on the farthest droplet parcel location. Hence, there could be a difference in the numerically reported values from the simulation and the experimentally observed penetration depth data.

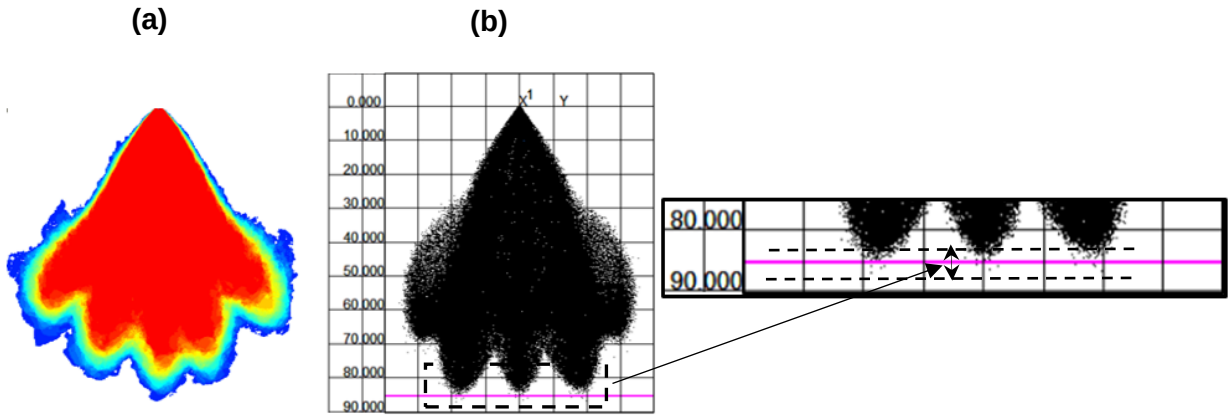

Figure 3.19: Injector-A (300 bar), spray image comparing penetration depth definition based from the simulation and the experimental image processing. (a) Processed high-speed image from experiment. (b) Parcel locations plotted from the simulation as “dots”.

To avoid this discrepancy in penetration, a liquid/void fraction boundary is proposed for reporting the penetration depth obtained from the simulation. The simulation results obtained from Injector-A at 300 bar injection pressure are shown in Figure 3.20. Typical volume fraction contour plot obtained from the simulation is overlapped with the penetration depth data and shown in Figure 3.21. In this contour plot, a volume fraction range of $2e^{-4}$ to $1e^{-3}$ is chosen as the boundary. The most vertical spray plume is chosen for the volume fraction contour plot as it shows the maximum penetration depth (Figure 3.18) in comparison to other four spray plumes in this case. Similarly, the penetration depths predicted from the R&D model are compared with the available experimental data for injection pressure 350 bar and 150 bar and shown in Figure 3.22 and 3.23, respectively. A good experimental correlation is obtained with the chosen model constants for the R&D secondary droplet breakup model. It should be noted that, for a lower injection pressure of 150 bar validation, the bag breakup model constant C_{b1} is modified from 5 to 3. This model constant is adjusted for better correlation of the SMD comparison at 150 bar injection pressure at the station 45 mm from tip of the injector axis. The corresponding SMD comparisons are shown in Figure 3.24.

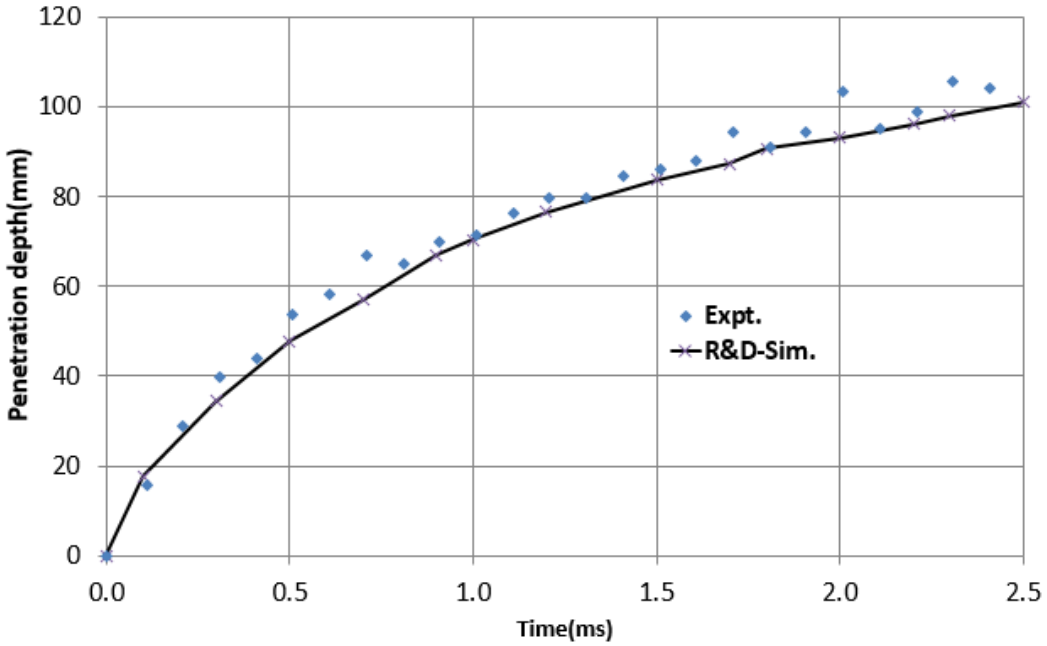

Figure 3.20: Injector-A (300 bar), penetration depth data comparing the simulation and experiments, where Expt. and R&D-Sim. refer to experiment and R&D model (prediction based on volume fraction) predicted data, respectively.

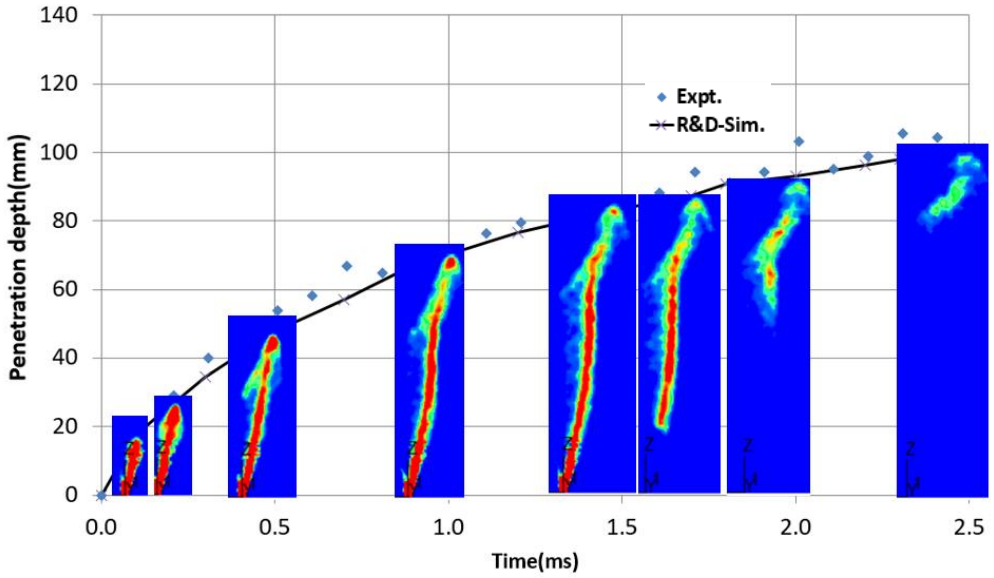

Figure 3.21: Injector-A (300 bar), penetration depth captured by the volume fraction contour comparing the experimental data are shown, where Expt. and R&D-Sim. refer to experiment and R&D model (prediction based on volume fraction) predicted data, respectively.

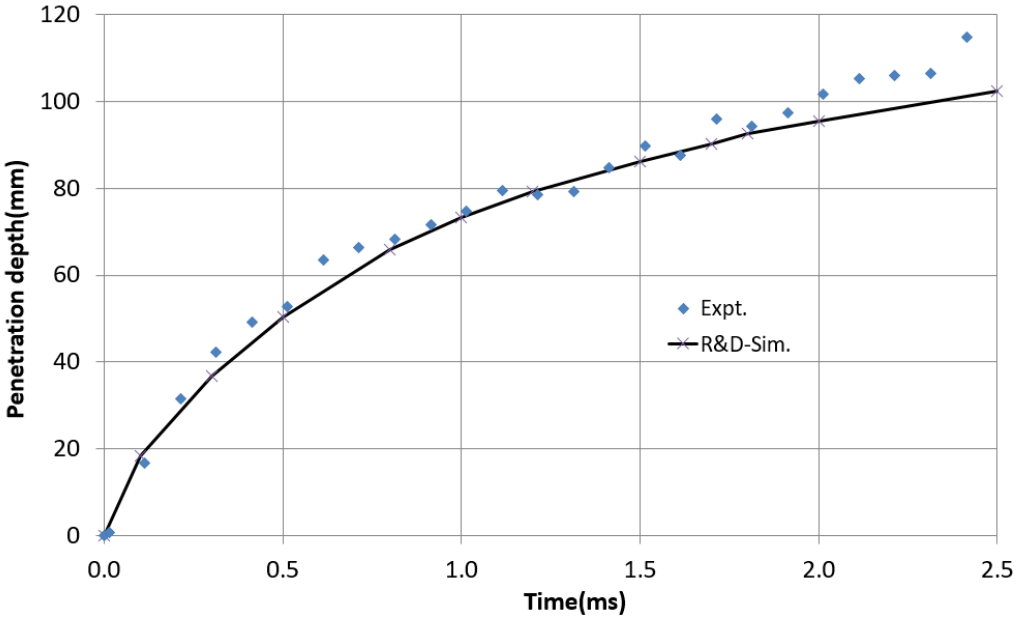

Figure 3.22: Injector-A (350 bar), penetration depth data comparing the simulation and experiments where Expt. and R&D-Sim. refer to experiment and R&D model (prediction based on volume fraction) predicted data, respectively.

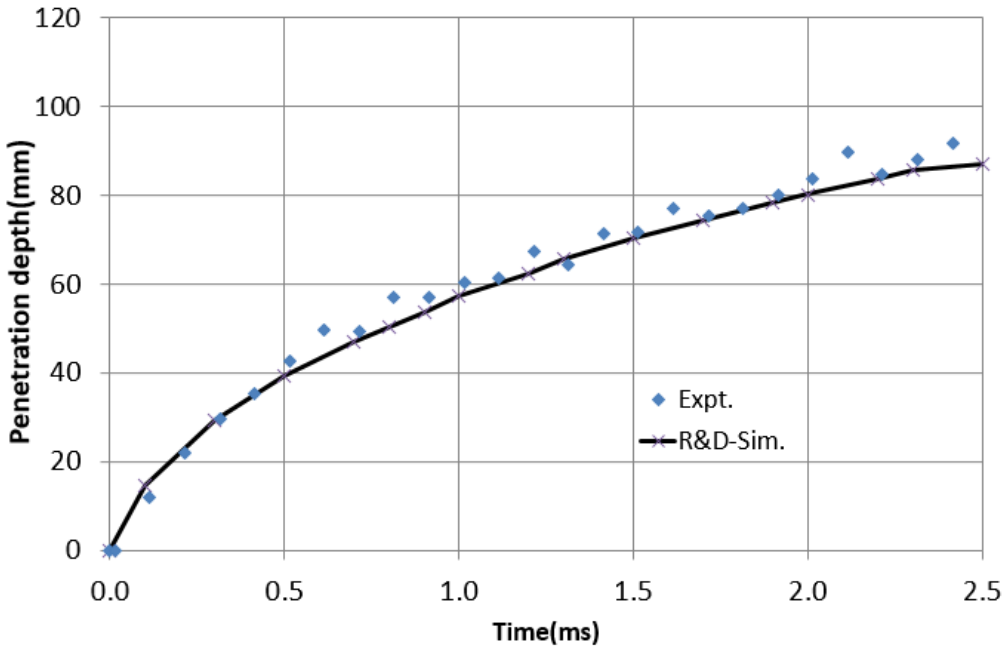

Figure 3.23: Injector-A (150 bar), penetration depth data comparing the simulation and experiments where Expt. and R&D-Sim. refer to experiment and R&D model (prediction based on volume fraction) predicted data, respectively.

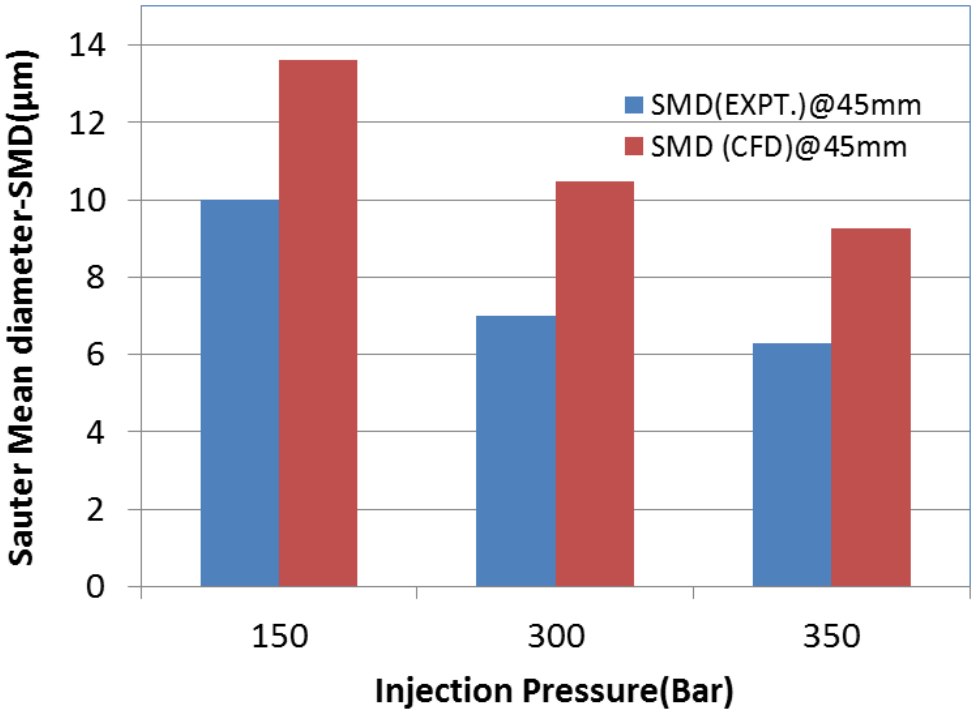

Figure 3.24: SMD data comparison of experiment with the CFD predictions at 45 mm from the injector tip is shown for Injector-A.

The validation study is carried out with the same process for Injector-B, for injection pressure 150 bar and 200 bar. Simulation comparisons for penetration depths are shown in Figure 3.25 and 3.26 for injection pressure, 150 bar and 200 bar, respectively.

Similarly, the SMD data predicted at 50 mm from the injector tip are shown in Figure 3.27. A qualitative agreement is noticed in comparison to the experimental data.

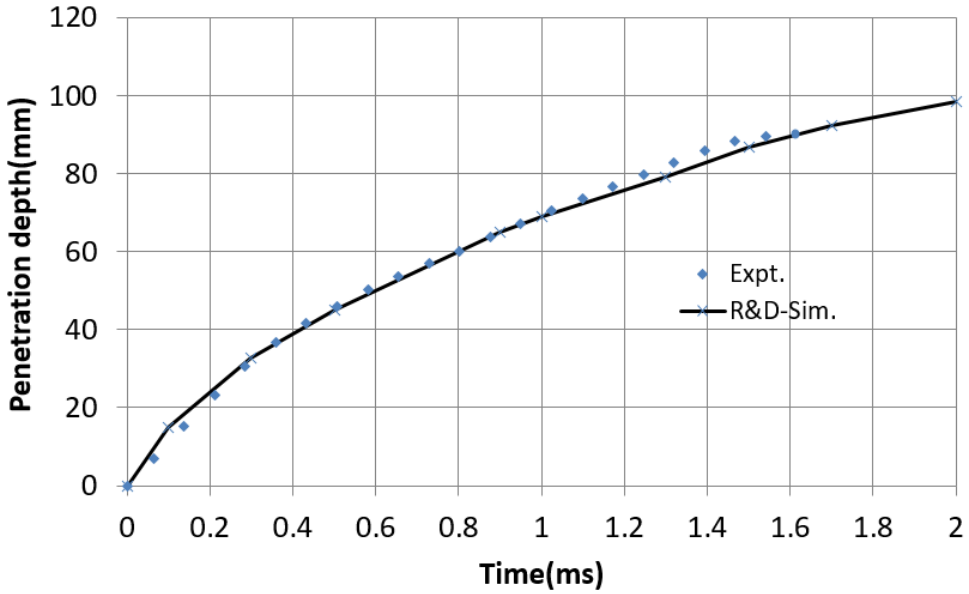

Figure 3.25: Injector-B (200 bar), penetration depth data comparing the simulation and experiments where Expt. and R&D-Sim. refer to experiment and R&D model (prediction based on volume fraction) predicted data, respectively.

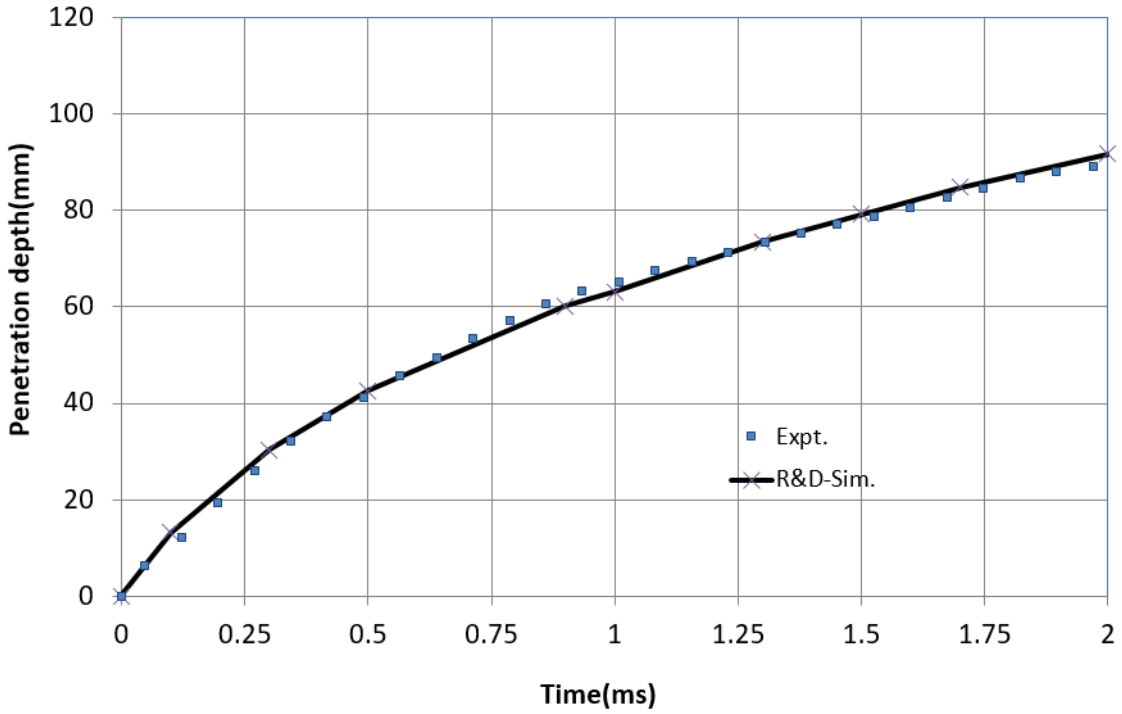

Figure 3.26: Injector-B (150 bar), penetration depth data comparing the simulation and experiments where Expt. and R&D-Sim. refer to experiment and R&D model (prediction based on volume fraction) predicted data, respectively.

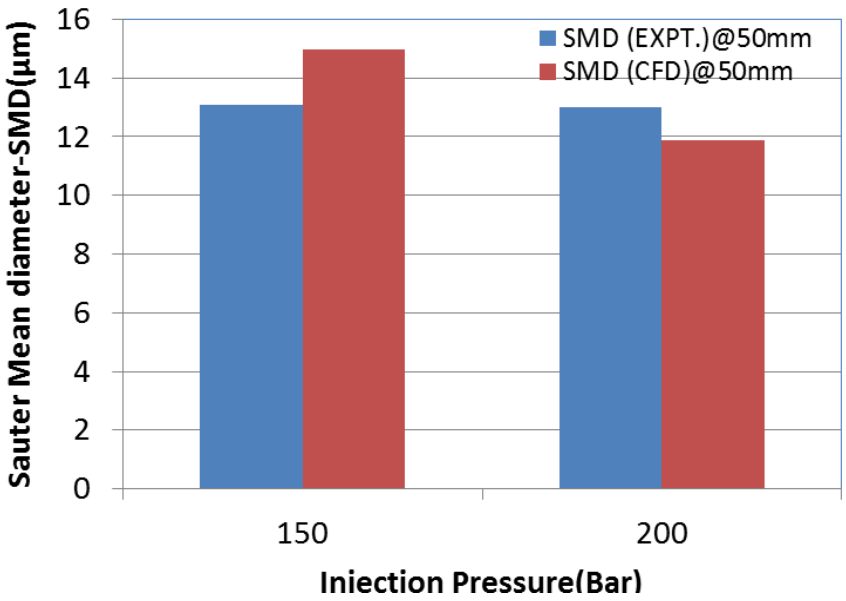

Figure 3.27: SMD data comparison of experiment with the CFD predictions at 50 mm from the injector tip is shown for Injector-B.

3.1.4.4 Summary and conclusions

In summary, an extensive spray model evaluation was carried out and the spray model adopted was then used to predict the penetration depth and SMD data for two injectors, using a simplified phenomenological primary droplet assumption. The primary droplet SMD with RR distribution assumption defined by the injector nozzle along with the R&D secondary breakup model correlates experimental penetration depth and the droplet sizes. However, the bag breakup model constant C_{b1} needs to be marginally changed from 5 to 3 to match the SMD at the downstream of the nozzle for lower injection pressure (<200 bar). The volume fraction of $2e^{-4}$ to $1e^{-3}$ for the penetration depth definition in the numerical simulation was found to show a reliable correlation with the available experimental data.

In conclusion, Reitz-Diwakar (R&D) secondary droplet breakup model with the model constants of C_{b1}=3 (<= 150-200 bar) and 5 (> 200 bar) along with a stripping model constant of C_{s2}=5 shows a good correlation with the test data. The developed Fortran routines ensure sufficient number of parcels, the droplet distribution, injection velocities and pulse width to simplify and get a better control on the droplet initial conditions.

In the current spray model, the changes in the effective flow area due to flow contraction are not considered. This is expected to over-predict the SMD, due to the under estimation of droplet breakup resulting from underestimation of droplet initial velocities.

Chapter 4. Optimisation of Mixture Formation for Engine Cold-start Operation

4.1 Introduction

4.1.1 Catalyst light-off

One of the engine operating conditions which is crucial for meeting emission regulations is the catalyst heating immediately after a cold start so that the 3-way catalyst can reach its minimum operating temperature (light-off) for effective conversion of uHC, CO and NO_x. The main requirements for the operation are maximising heat flux into catalyst, minimising engine out emissions and sustaining combustion stability for idle noise, vibration and harshness (NVH). The combustion stability is often the limiting factor for meeting the requirements. In the modern, low emission engine development, understanding the direct injection process, i.e., atomisation, fuel evaporation, air-fuel mixing, wall wetting, etc., becomes increasingly important during this operation. To meet increasingly stringent emission regulations (Joshi, 2020), fast catalyst light-off has become an essential requirement in engine combustion and exhaust systems development for increasing the NO_x conversion efficiency.

4.1.2 Faster catalyst light-off by retarded combustion

Typical engine cylinder pressure trace for the catalyst light-off condition is shown in Figure 4.1. The area under the P-V diagram represents the total indicated work available from the gas exchange and combustion process. Burn duration is defined as the time taken to combust the fuel available from the start of ignition (spark). In the normal engine operation, the ignition process is started before compression TDC (BTDC) which is referred to as spark advancement. More advanced spark initiates the earlier start of the combustion process. This requires more work from the piston to complete the compression stroke. Retarding the spark closer to TDC delays the combustion and the maximum cylinder pressure moves towards the later part of the expansion stroke. This decreases the peak engine cylinder pressure, resulting in the loss of engine torque and increase in cylinder gas temperature. There is an optimum ignition timing with minimum spark advance generating maximum engine torque. This is commonly referred to as maximum brake torque (MBT) combustion phasing (Heywood, 1989, p. 375). During the catalyst light-off phase, higher exhaust gas heat flux is required for faster exhaust catalyst warmup. However, some P-V work is required to sustain the engine operation. Hence, a retarded combustion phasing strategy is chosen to enable faster light-off without sacrificing the engine stability. Spark retard (~15 to 20 CAD after TDC) with split injection is commonly employed to achieve high exhaust heat flux for faster catalyst light-off

in GDI engines. The retarded spark timing and the resulting retarded combustion pressure rise in an engine are shown in Figure 4.1.

However, the cycle-to-cycle variation or the combustion stability is worsened due to the spark retard, which results in NVH issues. The combustion stability is quantified by the standard deviation of net indicated mean effective pressure, i.e., Std-NMEP. A design target of ≤0.3 bar std-NMEP at catalyst heating phase (1200 RPM 3 bar NMEP) is required to avoid having combustion instability and NVH issues.

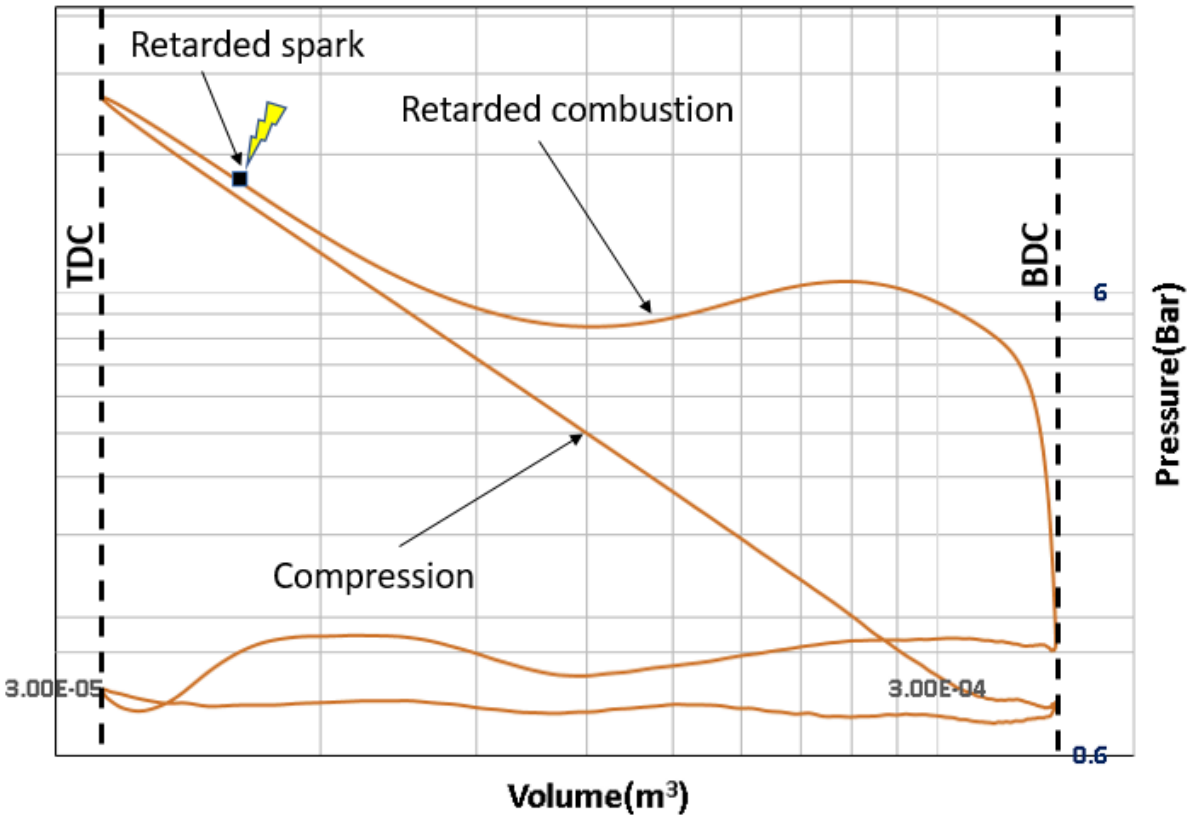

Figure 4.1: Typical Log P – Log V diagram of catalyst heating process, showing retarded spark and combustion (Waters and McGhee, 2019).

4.1.3 Factors affecting the retarded combustion

The equivalence ratio distribution, turbulent kinetic energy (TKE) and charge motion in the cylinder at the time of spark determine the combustion characteristics. It is reported that the measured laminar flame speed (Metghalchi and Keck, 1982) is a function of the equivalence ratio, unburned gas temperature and pressure. This is given by Equation 4.1:

$$S_L^0 = S_{L,ref}^0 \left(\frac{T_u}{T_{u,ref}}\right)^{\alpha} \left(\frac{P}{P_{ref}}\right)^{\beta} . F_{dil} \qquad (4.1)$$

where the subscript “ref “, refers to the reference condition of 298K and 1 atm.

F_{dil}, is a factor accounting for the diluent’s effect.

Fuel-type independent exponents “α”and “β” were functions of equivalence ratio(ϕ).

$$\alpha = 2.18 - 0.8(\phi - 1) \qquad (4.2)$$
$$\beta = -0.16 + 0.22(\phi - 1) \qquad (4.3)$$
$$S_{L,ref}^0 = B_M + B_2(\emptyset - \emptyset_M)^2 \qquad (4.4)$$

Table 4.1: Values for $\boldsymbol{B_M}$, and $\boldsymbol{B_2}$ used in Equation 4.4 (Liang and Reitz, 2006).

Fuel	B_M (cm/s)	B_2 (cm/s)	ϕ_M
Propane	34.22	-138.65	1.08
Isooctane	26.32	-84.72	1.13

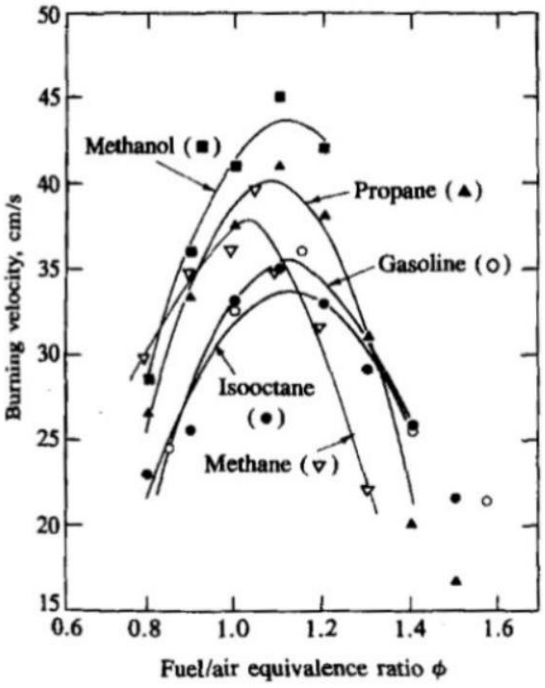

Figure 4.2: Dependence on the burning velocity of methanol, methane, propane, gasoline and iso-octane with different equivalence ratios determined from the vapour pressure of the fuel is shown (Taken from Metghalchi and Keck, 1982).

Figure 4.2 shows the laminar flame speed data obtained for different fuel air mixtures defined by the equivalence ratio of the respective fuels. It is shown that, for fuels, the burning velocity reaches maximum at ϕ ~ 1 to 1.1 and falls off, for rich and lean mixtures. Methanol, propane, gasoline and iso-octane show a maximum laminar burn speed in the range ϕ= 1-1.1. This recommends that, for a stable combustion, the fuel rich cloud around the spark plug should have an equivalence ratio in the range of 1 to 1.2.

In turbulent flows (Turns, 2000), the instantaneous velocity is defined as the sum of mean (ensemble averaged) velocity ($\overline{U}$) and fluctuating or turbulent velocity (u'). Inherently, turbulence flows are three dimensional in nature, having three-dimensional velocity fluctuations (u', v' and w'). The intensity of turbulent velocity fluctuation is represented as root mean square turbulent velocity (v'_{rms}). The kinetic energy associated with the turbulence velocity scale is given as $\sim\frac{3}{2}v'^2_{rms}$. It can be seen from Equation 4.1 that the laminar flame speed depends on the thermal and chemical properties of the mixture. However, the turbulent flame speed depends on the flow characteristics as well as the mixture properties. Many theories have been developed to relate the turbulent flame speeds to the flow properties. The simplest form given by Damköhler for a wrinkled flame assumption is shown in Equation 4.5:

$$\frac{A_{wrinkles}}{\bar{A}} = \frac{v'_{rms}}{S_L} \qquad (4.5)$$

Where, $A_{wrinkles}$ is defined as the area in excess of the time-mean flame area ($\bar{A}$). This leads to the relation of turbulent flame speed to the laminar flame speed, which is given by Equation 4.6:

$$\frac{S_t}{S_L} = 1 + {v'_{rms}}/{S_L} \qquad (4.6)$$

where S_t and S_L are the turbulent and laminar flame speed, respectively.

Another widely reported turbulent flame speed relation is the one proposed by Klimov (Abraham, Williams and Bracco, 1985; Turns, 2000) as shown in Equation 4.7:

$$\frac{S_t}{S_L} = 3.5\left({v'_{rms}}/{S_L}\right)^{0.7} \qquad (4.7)$$

In this equation, the constants are derived based on the experimental data and, hence, reported to have good correlation. This shows that an increase in the intensity of turbulence velocity fluctuation increases the wrinkled flame area for the given thermal and chemical properties of the mixture. For a low engine speed, low load ~1200 RPM, the typical TKE in the simulation near engine top dead centre (TDC) is ~ 6 J/kg. $v'_{rms}(\sim\sqrt{\frac{2}{3}TKE}$) calculated from

TKE is in the order of 2 m/s. Assuming the thermal and mixture conditions, ($S_L \sim constant;\ s_t \sim 3.5\ v'^{0.7}_{rms}$) are the same for the two design conditions and the chemical timescale is sufficiently small to take forward the reaction, then, in this case, if turbulence kinetic energy is increased by 50% in the new design, then the turbulent flame speed calculated from the new design from Equation 4.7 shows an improvement of 15.25%. This is the fundamental dependency of the turbulent kinetic energy or the turbulence intensity on the effective flame speed for the engine design. This is one of the metrics used for improving the combustion stability.

In order to achieve stable retarded combustion, a near-stoichiometric or slightly fuel rich mixture and high turbulence are desirable to increase the turbulent flame speed. The former can be realised by the stratified charge combustion in the cylinder, which results in faster and stable flame propagation in the slightly fuel rich mixture. However, stratified combustion demands appropriate fuel distribution around the spark plug by optimising the fuel injection process and combustion chamber design to avoid the formation and emission of soot particles in the very fuel rich region.

4.1.4 Outline of the chapter

In this chapter, the in-cylinder turbulent flow methodologies discussed in Section 2.1.3 and the characterised spray methodology demonstrated in Chapter 3 are applied to the analysis of the in-cylinder mixture formation for improved catalyst light-off. In particular, the underlying process of mixture formation with split injections to improve combustion stability is investigated. In the CFD simulation, the combustion and the detailed chemistry are not modelled. Instead, the simulation is carried out as a cold flow, wherein, the engine cycle, starting from intake stroke, fuel injection, compression stroke until the retarded spark timing, is considered. The local thermal and equivalence ratio, ϕ, of the mixture along with the intensity of turbulent velocity around the spark plug are used to assess the combustion stability.

4.2 Engine condition

Injector-A, detailed in Chapter 3, is used in a three-cylinder engine development. The catalyst light-off condition with two of the injection scenarios tested during the engine development are used for the validation purpose. The details of the engine operating condition are shown in Table 4.2.

Table 4.2: Engine condition for catalyst heating operation.

Engine-1: Test condition (1200 RPM, 3 bar IMEP)	**Split Injection**		
	Case-1	**Case-2**	
Port	P6	P6	
Piston type	Ski Ramp	Ski Ramp	
Bore	73.5	73.5	mm
Stroke	81.8	81.8	mm
Compression ratio	10.5	10.5	-
Crank radius	40.9	40.9	mm
Crank shaft offset	-7.2	-7.2	mm
Connecting rod length	137	137	mm
Engine speed	1200	1200	rpm
Intake port pressure	0.67	0.67	bar
Intake port temperature	302.10	302.10	K
Exhaust backpressure	1.09	1.09	bar
Exhaust temperature	879.22	879.22	K
Liner temp.	300	300	K
Head temp.	300	300	K
Piston temp.	300	300	K
Intake valve T	302	302	K
Exhaust valve T	302	302	K
Residual gas T	881.96	881.96	K
Start of first injection (SOI 1)	300.0	300.0	deg. BTDC (firing)
End of second injection (EOI 2)	45.0	90.0	BTDC
Pulse width 1	7.947	7.325	c.a. deg.
Pulse width 2	2.792	2.848	c.a. deg.
Pulse width 1	1.104	1.017	ms
Pulse width 2	0.39	0.396	ms
Total fuel mass measured	16.50	15.63	mg/cyl/cycle
ECU estimated split ratio in second injection	26	28	%
Fuel pressure	280	280	bar
Fuel temperature	300	300	K

Coolant temp	303	303	K
AFR	14.6	14.6	
Average fuel flow	1.58	1.58	kg/hr
Intake cam phase shift	15.0	15.0	CAD
Exhaust cam phase shift	-15.0	-15.0	CAD
IMOP	119.5	119.5	ATDC
EMOP	103.625	103.625	BTDC
Spark timing	-15	-15	BTDC

Table 4.3: Injection settings (fuel pressure =280 bar, engine speed =1200 RPM).

Injector-A (P_{inj}=280 bar, Q_{stat}= 15.03 cm^3/s and U_{mean}=195.22 m/s)				
	SOI 1	**EOI 2**	**Fuel split ratio**	**Total fuel injected**
Case 1	300° BTDC	45° BTDC	74% : 26%	16.50 mg
Case 2	300° BTDC	90° BTDC	72% : 28%	15.63 mg

In Table 4.3, the two injection timings used are referred to as Case-1 and Case-2. It can be seen that Case-1 has a delayed second injection with an EOI2 of 45°CAD before TDC. Case-2 has the second injection with an EOI2 at 90°CAD before TDC. In both cases, the first injection starts at 300°CAD before TDC (during the intake stroke). An injection pressure of 280 bar is used in the engine test condition. It is assumed that the injection Q_{stat} and injection velocity are kept constant during the entire pulse width. The calculated Q_{stat} and the injection velocity (U_{mean}) at 280 bar injection pressure, P_{inj} (using Equations 3.7 and 3.8) for Injector-A, are shown in Table 4.3. In the engine simulation, “Gasoline-1 NIST” fuel properties are used.

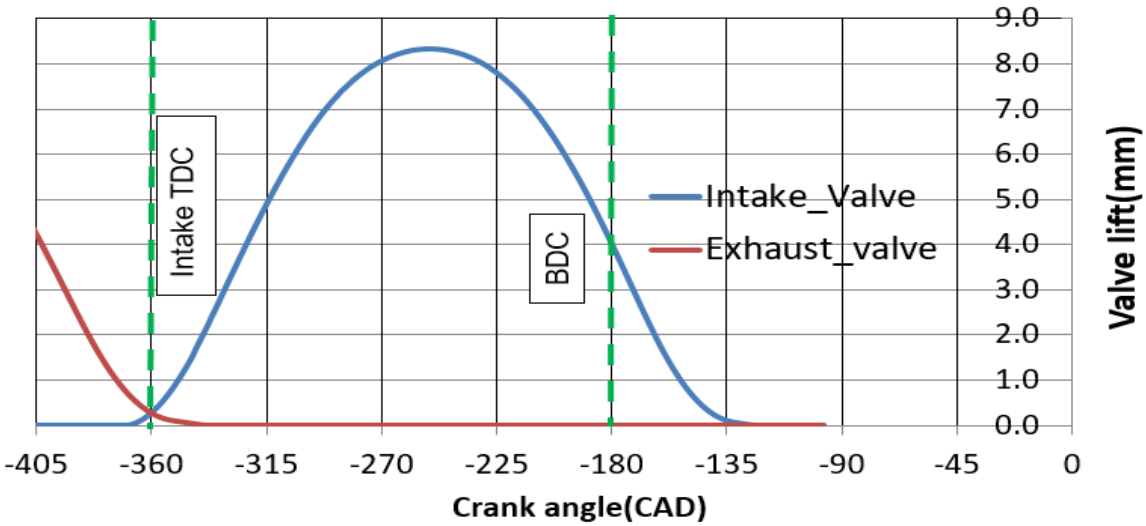

Figure 4.3: Intake and exhaust valve timing used in the engine test. The TDC and BDC reference position are also provided.

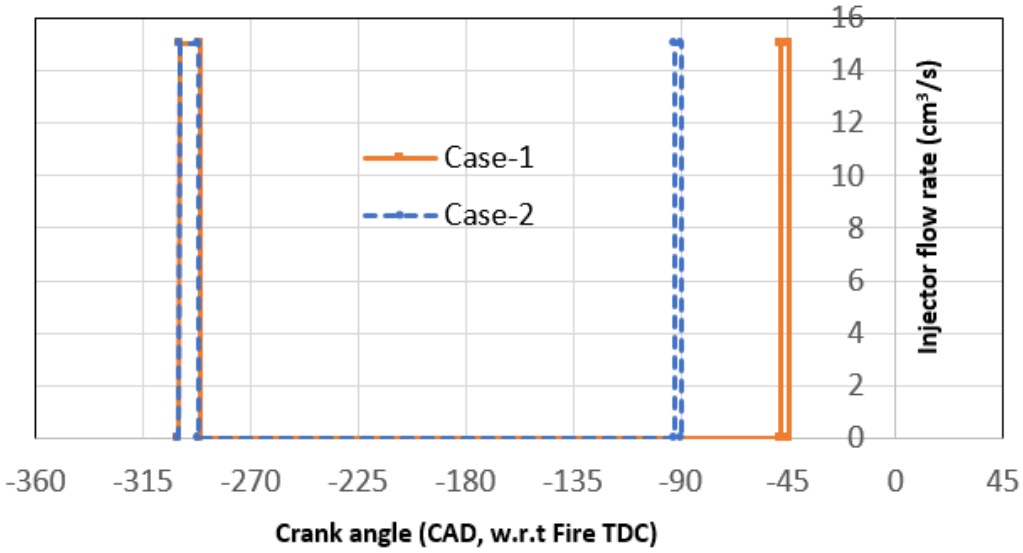

Figure 4.4: Injection rate shape for twin injection with 280 bar injection pressure is shown for Case-1 and Case-2, respectively.

The intake and the exhaust valve timing used in the engine test are shown in Figure 4.3. Similarly, the injection rate shapes used for Case-1 and Case-2 are shown in Figure 4.4. The SOI1, for both Case-1 and Case-2 is 300˚ CAD, before firing TDC. The second injection timing for Case-2 is nearly 45˚ CAD advanced in comparison to Case-1. It should be noted that, in the actual engine test, the quantity of the fuel injected in Case-2 is 5.5% lower than Case-1 due to the cycle to cycle variability in the real engine conditions.

4.3 Simulation setup

The simplified single cylinder engine geometry and mesh (Trimmed mesh with a total mesh size of 1.4 million cells) used to setup the catalyst light-off condition is shown in Figure 4.5.

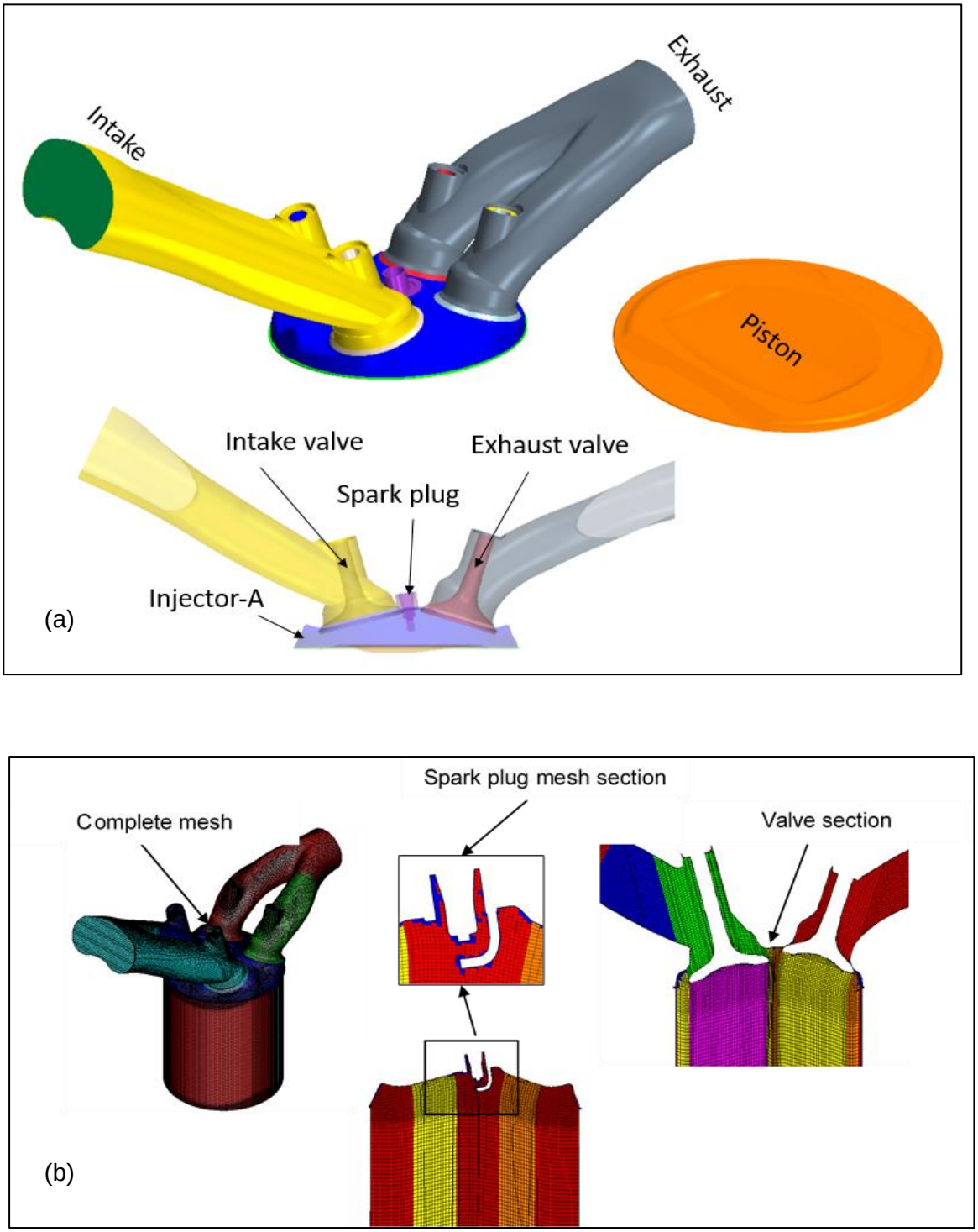

Figure 4.5: Typical in-cylinder engine geometry (a) and mesh (b) model used in the simulation.

A uniform prism layer of 0.1mm is provided at all the in-cylinder surface. Two layers of mesh extrusion are provided at intake inlet and exhaust outlet boundary faces. The piston geometry labelled in Figure 4.5 is referred as ski-ramp piston. Star-CD-ES-ICE is used to setup the moving mesh geometry with the crank dimensions specified in Table 4.2. Star-CD solver is used to solve the governing equations with the moving mesh boundary.

RNG k-ε turbulence model with Angleberger wall function (Angleberger, Poinsot and Delhay, 1997) were chosen for the simulation. Lagrangian multiphase model was used to account for the in-cylinder spray. The same R&D modelling constants along with the primary droplet representation, as recommended in Chapter 3, was used in the in-cylinder simulation. A very fine crank angle resolution (0.1 CAD) was used to resolve the in-cylinder flow development and during the injection event (0.005 CAD). Bai-ONERA wall impingement model was selected to evaluate the droplet wall interaction regime. A liquid film model was chosen to account for the liquid-film formation, stripping and evaporation and constant intake and exhaust total pressure conditions were used in the simulation. All the in-cylinder walls were fixed at constant temperature, as detailed in Table 4.2. This simulation setup was arrived at after several iterations of turbulence model, fuel properties, wall impingement model and time step choices. Tables 4.4, 4.5 and 4.6 respectively show simulation parameters for the solution methods, solver parameters and discretisation schemes used in the simulation. The theoretical details of the model setup are referred from Star-CD (2018) (Methodology document)

Table 4.4: List of solution methods setup.

Solution Algorithm	PISO
Maximum Residual Tolerance	0.0001
Maximum Number of Corrector Stages	40
Reduction in Residual for Corrector Stages	0.25
Under Relaxation for Pressure Correction	0.3

Table 4.5: List of solver parameters setup.

Variables	Number of sweeps	Residual tolerance
U-Momentum	200	1.00E-04
V-Momentum	200	1.00E-04
W-Momentum	200	1.00E-04

Pressure	1200	1.00E-05
Temperature	200	1.00E-12
Turbulence KE	200	1.00E-04
Turbulence Dissipation	200	1.00E-04

Table 4.6: List of differencing schemes (MARS- Monotone advection and reconstruction scheme, CD-Central differencing scheme and UD-First order upwind).

Variables	Convective flux formulation	Blending Factor	Blending Method
U-Momentum	MARS	5.00E-01	Fixed
V-Momentum	MARS	5.00E-01	Fixed
W-Momentum	MARS	5.00E-01	Fixed
Density	CD	1.00E-02	Fixed
Temperature	UD	-	-
Turbulence KE	MARS	5.00E-01	Fixed
Turbulence Dissipation	MARS	5.00E-01	Fixed

It should be noted that, in this simulation process, the simplified single component fuel represented as $C_{7.4}$ $H_{13.2}$ (Gasoline1, NIST properties) was used. The actual gasoline fuel is a blend of heavier and lighter hydrocarbons. It is reported that the heavier hydrocarbon fuel (n-decane) evaporates slowly and the lighter hydrocarbon (pentane, n-heptane and iso-octane) evaporates faster. In reality, this results in a differential evaporation which affects the final distribution of equivalence at the time of spark event. However, as reported in Xu et al. (2009), the equivalent fuel property as that of “Gasoline1-NIST”, was found to capture the underlying process of spray atomisation, wall wetting, fuel evaporation and mixing process.

4.4 Results and discussion

As detailed in Section 4.2, the fuel injection is carried out as two injection events. The start of first injection event for Case-1 and Case-2 are at 300 CAD before compression TDC. However, the second injection for Case-1 and Case-2 are at 45˚ CAD and 90˚ CAD before the compression TDC, respectively. In both the cases the total quantity of injected fuel is maintained nearly the same.

In the engine test, the Std-NMEP during the catalyst light-off condition was reported for two of the cases (Engine operating conditions referred in Table 4.2), Case-1 and Case-2,

respectively. As detailed earlier, the Std-NMEP is a measure of engine stability. The lower the value, the higher is the engine stability, and vice versa. This is mainly related to the combustion flame speed resulting from the local equivalence ratio and the turbulent kinetic energy of the

fuel cloud surrounding the spark plug. If the local equivalence ratio (ϕ) near the spark plug resulting from better atomisation and charge motion are in the range of ~1, a faster combustion is expected. This results in better combustion stability (i.e., low Std-NMEP). To capture this detail qualitatively, the intake charge motion, turbulence, fuel atomisation, fuel evaporation, wall impingement, liquid film formation, wall film liquid evaporation and fuel air mixture formation need to be captured simultaneously. In the simulation, analysis was carried out by computing the equivalence ratio distribution in the cylinder at the time of spark. During the cold engine start up, the combustion gas side wall and charge air were kept at ambient temperature. Each simulation takes nearly, 18 to 20 hours run time with 64 CPU's. The simulation results are discussed in the sections below.

4.4.1 Spray interaction in charge motion

The flow field obtained from the simulation for Case-1 and Case-2 are shown in Figure 4.6 and Figure 4.7. respectively. The evolutions of the flow field from the intake stroke, compression stroke and later near the spark timing of 15˚ CAD after compression TDC (Piston top dead centre) shown. The sky-ramp piston supports building charge motion in the cylinder. Spray interaction with the charge air during the split injection can be seen in the flow field. distribution. The earlier first injection (300 SOI1) shows the spray interaction with the charge motion.

The cylinder charge is displaced towards the liner. However, the delayed second injection (-45˚ CAD), as in Case-1, shows a significant interaction with the charge air due to the relative velocity gain through exchange of momentum from the atomised droplets. However, this momentum exchange is very localised and short-lived in Case-1. In Case-2, the second injection is 45˚ CAD earlier than Case-1. In this case. during the earlier second injection, the spray aligns with the initial charge motion and retains the charge motion further till the compression stroke. This shows an advantage with the side-mounted injectors.

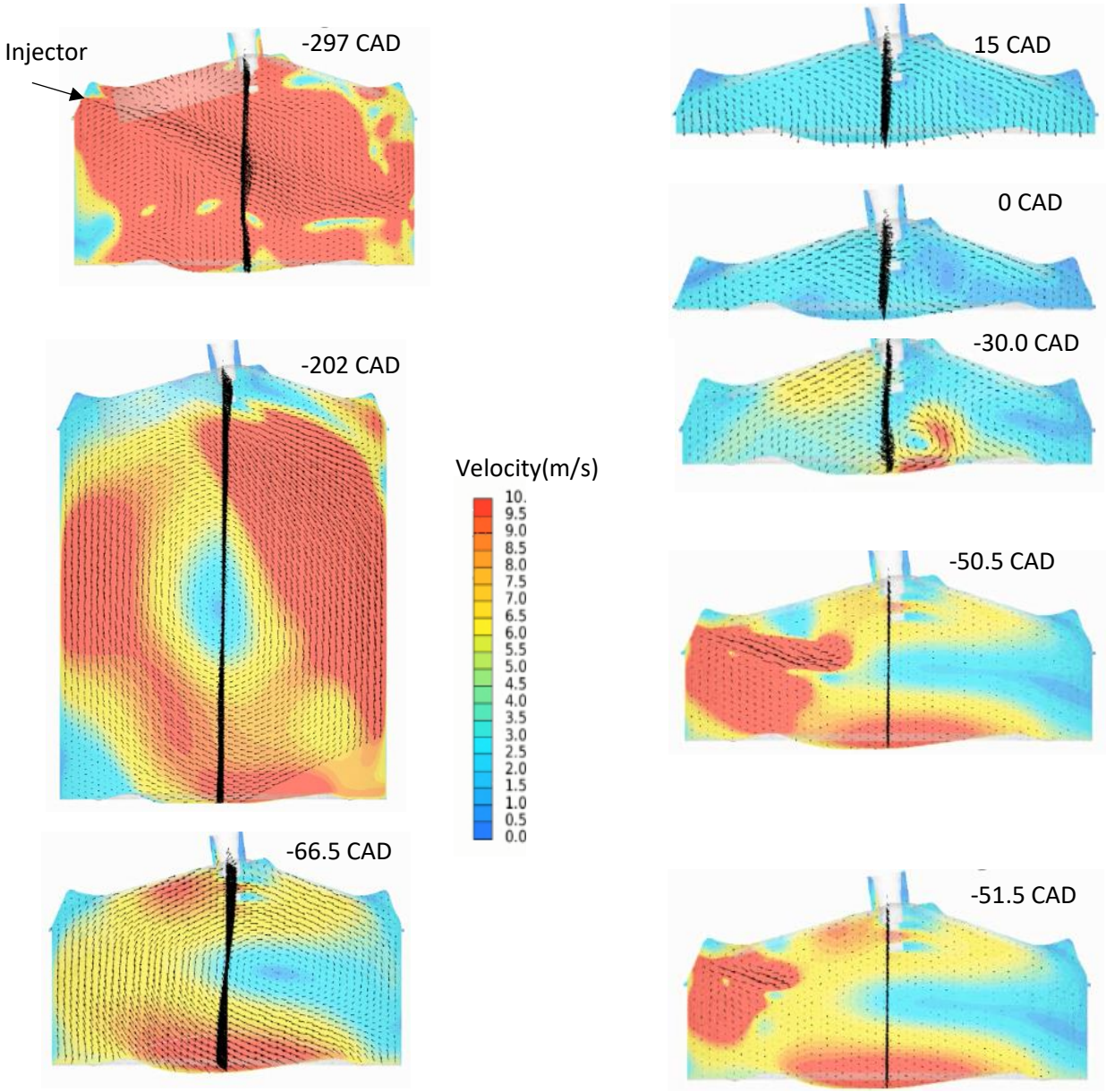

Figure 4.6: Flow field evolutions (velocity vector marked on the velocity magnitude contour) at the cylinder mid-section in the tumble plane are shown for Case-1. The crank angle (CAD) is referenced w.r.t. piston TDC.

The charge air built up in the cylinder for Case-1 and Case-2 simulation is shown in Figure 4.8. The charge mass in the cylinder accounts for the total gaseous mass trapped inside the cylinder including the evaporated fuel. As the intake pressure and the CAM, timings are the same for the two cases, there was no significant change in the in-cylinder charge air build up.

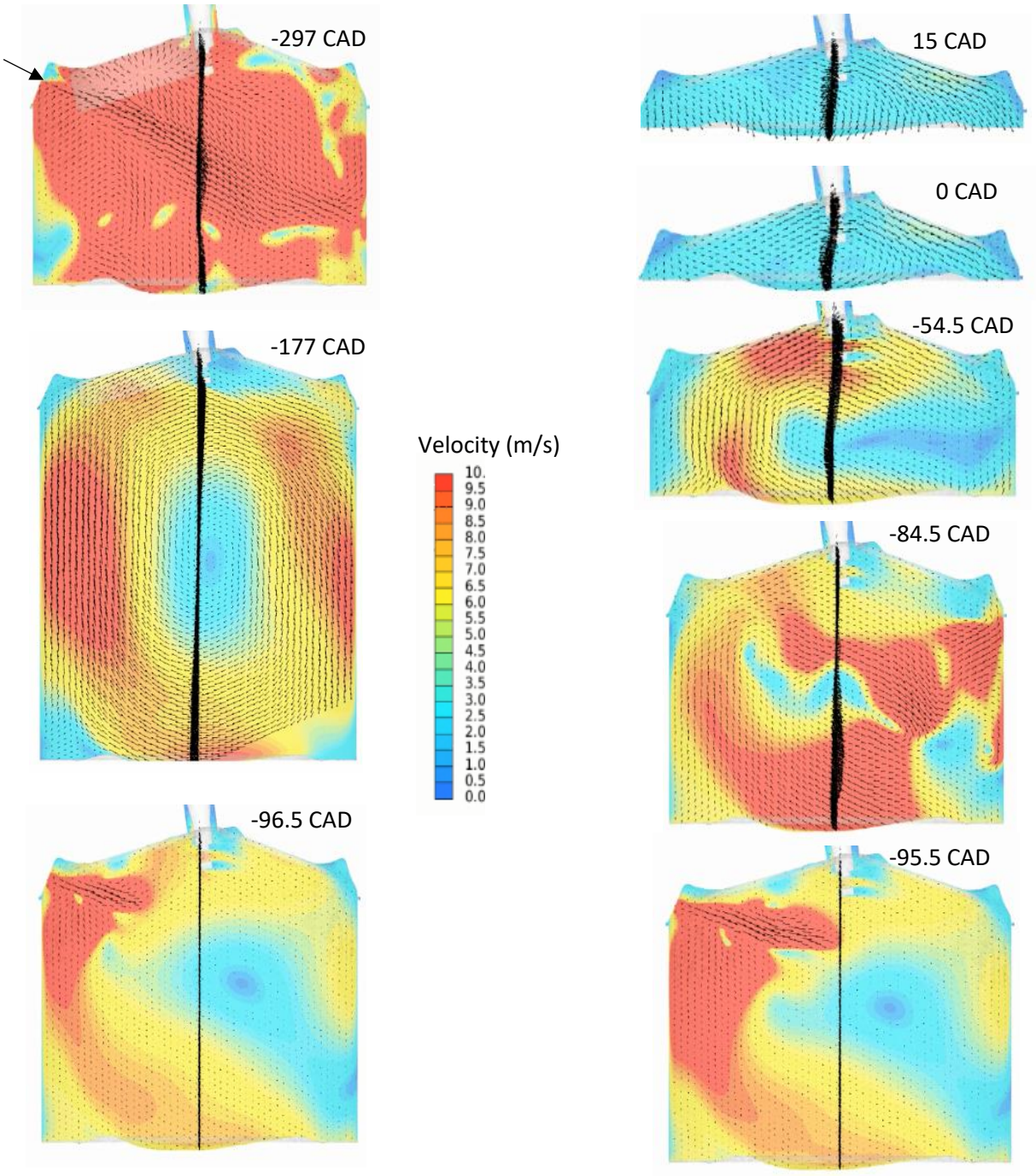

Figure 4.7: Evolutions of flow field (velocity vector marked on the velocity magnitude contour) at the cylinder mid-section in the tumble plane are shown for Case-2. The crank angle (CAD) is referenced w.r.t. piston TDC.

There is a significant charge mass “push back” (dotted circle shown in Figure 4.8 into the intake system, due to the chosen intake CAM timing (Figure 4.3). It can be seen that the intake valve closes 30˚ CAD after BDC. This allows the charge mass to leave the system while the piston is moving up during the compression stroke.

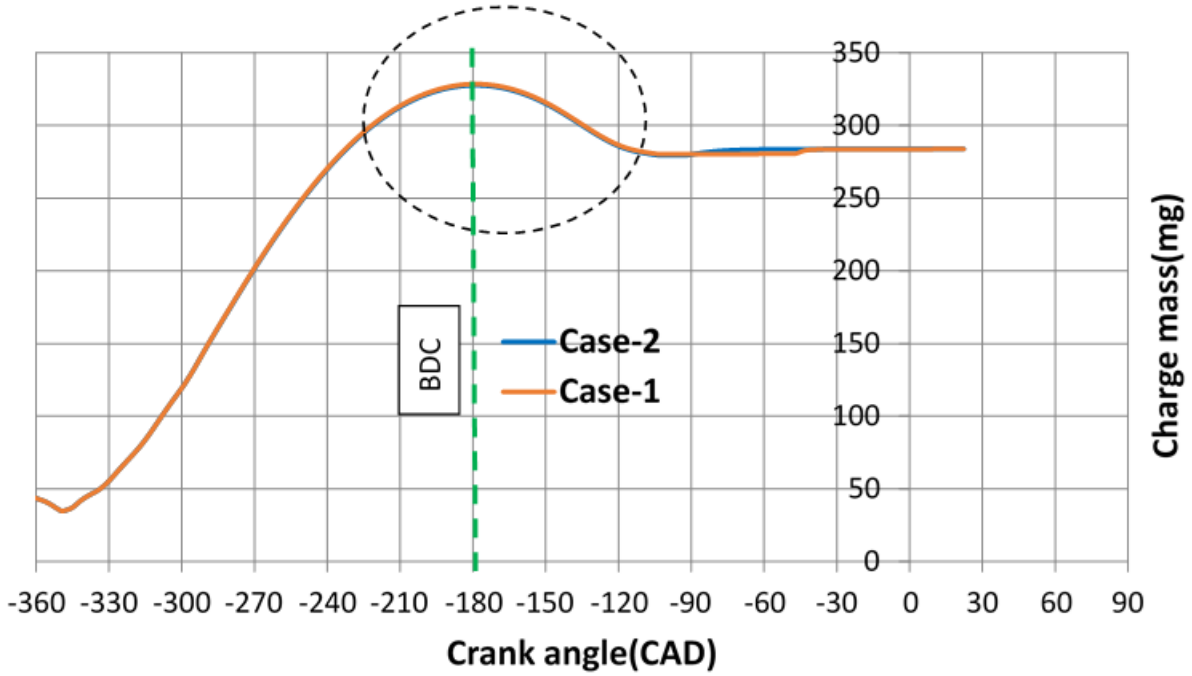

Figure 4.8: Computed in-cylinder charge mass for Case-1 and Case-2.

The in-cylinder charge motion and the spray interaction are further studied using the calculated crank angle resolved tumble ratio (TR). Tumble ratio is defined as the ratio of the angular speed of the charge motion generated by its angular momentum about the volume centre of the cylinder to the crank shaft/engine speed. Omega tumble and swirl are not considered in this discussion. The higher the tumble ratio, the better is the sustained charge motion within the cylinder. The TR obtained from Case-1 and Case-2 simulations are shown in Figure 4.9. In general, in in-cylinder air flow development, there are two tumble ratio peaks. One will normally be seen during the intake stroke and the other during the compression stroke. However, during the split injection strategy, depending on the injection timing, angular momentum discontinuity can be seen in Figure 4.9. The regions of discontinuity align with the injection timing of the split injections for Case-1 and Case-2, respectively. It is very evident that the delayed second injection, as in Case-1, decays the charge motion faster than the advanced second injection case. The advanced second injection during the compression stroke shows higher residual charge motion near the piston TDC.

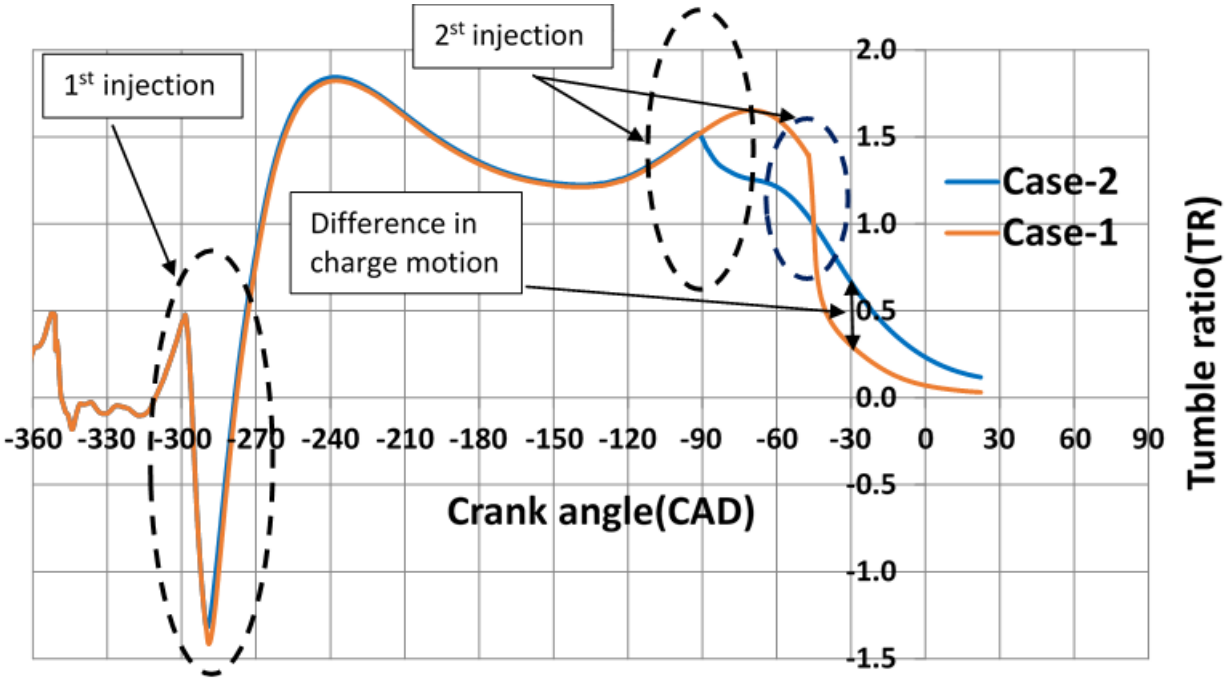

Figure 4.9: Computed in-cylinder tumble ratio with volume centre for Case-1 and Case-2.

Figure 4.10 shows the total in-cylinder turbulent kinetic energy (TKE) generated and transported during intake and the compression cycle. The spikes in the TKE plot are due to the interaction of the spray on the charge motion. This reflects the injection timing as used in Case-1 and Case-2. The delayed second injection brings in higher TKE; however, it decays

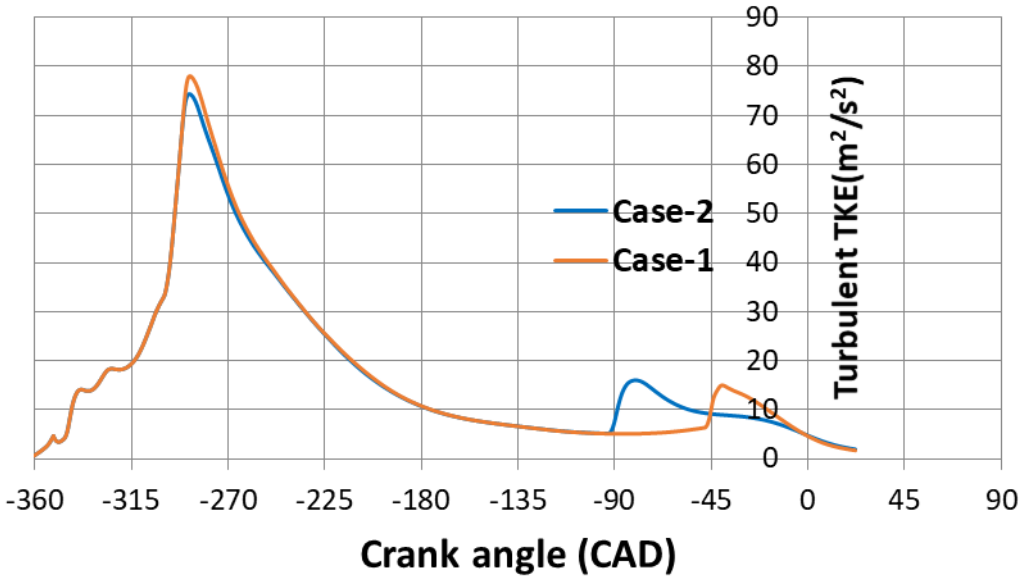

Figure 4.10: Computed in-cylinder turbulent kinetic energy for Case-1 and Case-2.

much faster than Case-1. Figure 4.11 shows the TKE at 3 mm radius around the spark plug. This signifies the amount of active charge motion around the spark plug. As defined in

Equation 4.6, high TKE along with fuel rich mixture (ϕ ~ 1.1) near the spark plug provided better ignition due to higher turbulent flame speed.

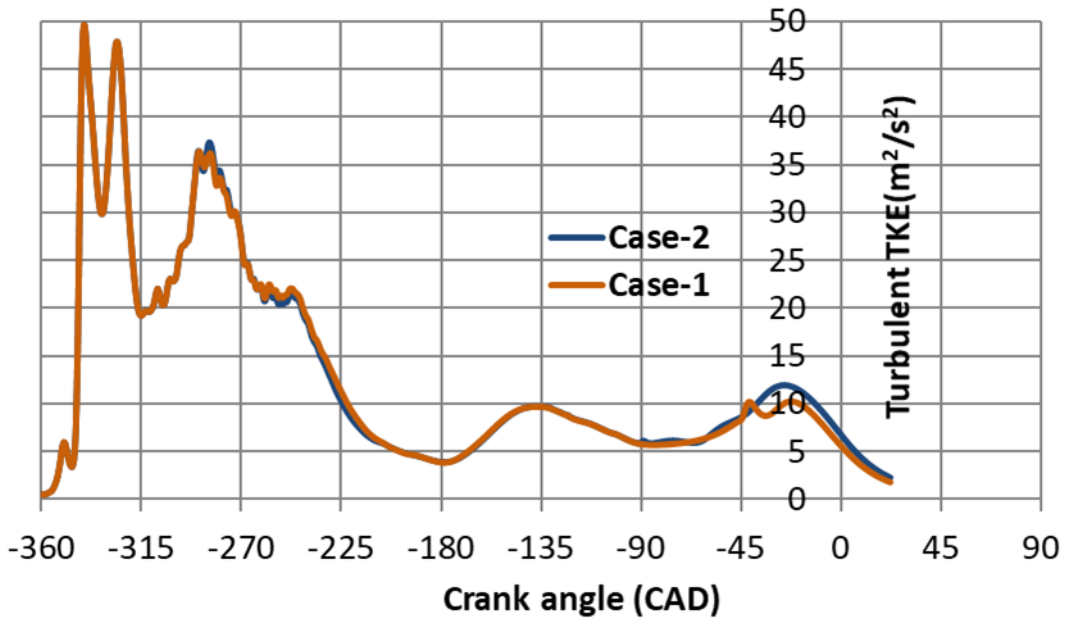

Figure 4.11: Computed in-cylinder turbulent kinetic roughly 3 mm around the spark plug for Case-1 and Case-2.

4.4.2 Spray wall interaction

Figure 4.12 shows the spray impingement on cylinder walls and the resulting liquid film formation. In this, the liquid film thickness contour is shown along with the spray evolution coloured by droplet diameter in the parcel at instants during the intake and compression stroke. It can be seen that the first injection impinges directly onto the piston, bringing a larger zone of liquid film. This film is found to evaporate with the presence of charge motion. However, the liquid film formed on the piston from the first injection did not evaporate completely. Due to the injection timing of the first injection and the spray pattern, the liner wetting during the first injection was found to be less significant.

Figure 4.13 shows the crank angle of resolved total liquid film on piston and liner. As in Case-1, the delayed second injection results in larger liquid film on the piston. The deposited film does not evaporate and remains flat during the compression stroke due to the increase in in-cylinder pressure. However, the earlier second injection, as in Case-2, shows lower piston

wetting. Hence, during the flame propagation, when the flame consumes the fuel rich mixture on the piston surface, Case-2 is expected to generate less PN/PM emission. in comparison to the Case-1.

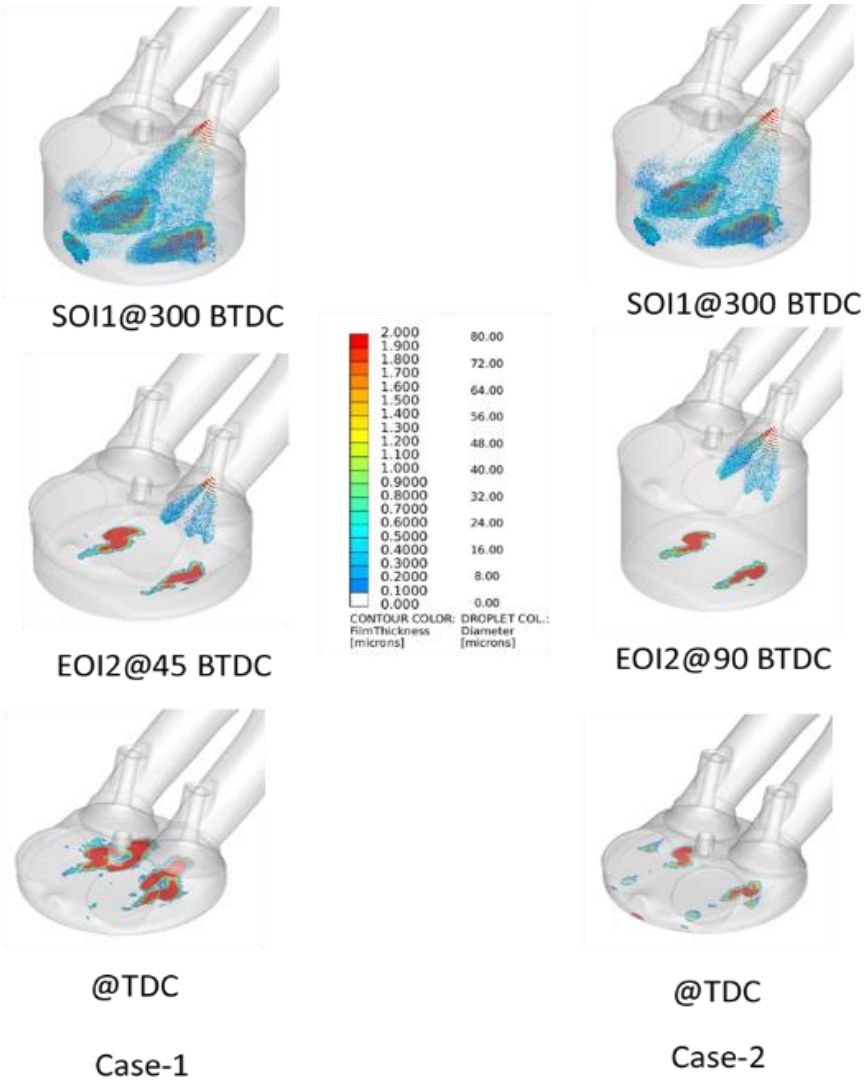

Figure 4.12: Liquid film formation due to spray wall impingement for Case-1 (-45°CAD) and Case-2 (-90°CAD).

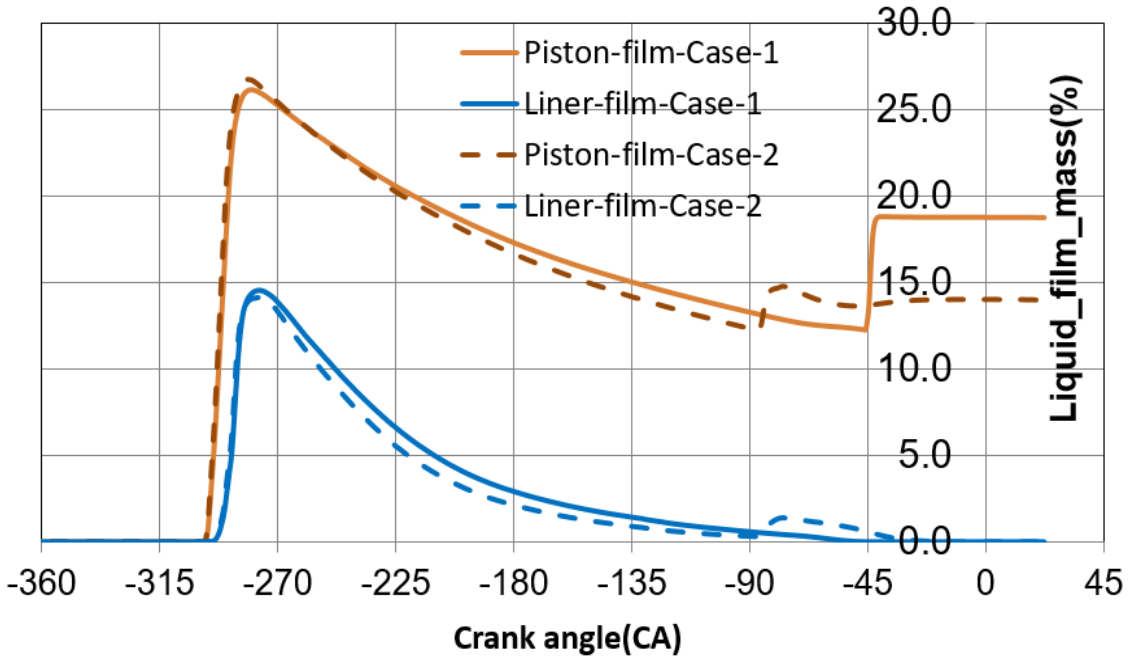

Figure 4.13: Liquid film estimate on piston and liner for Case-1 (-45°CAD) and Case-2 (-90°CAD).

4.4.3 Fuel stratification

Figure 4.14 shows the evolution of equivalence ratio distribution around the spark plug at the time of spark event. This determines the combustion stability and the resultant cycle-to-cycle variation of NIMEP. It is very evident that Case-2 was found to show more favourable AFR/equivalence ratio distribution around the spark plug. This suggests that the combustion stability is expected to be better with Case-2 than in Case-1. It should be noted that, in this simulation, the fuel quantity is not corrected to account for fuel push out as detailed in the charge mass study (Figure 4.7). Figure 4.15 shows the measured combustion stability quantified by the standard deviation of indicated mean effective pressure. The lower the number, the higher the combustion stability. As noticed in the simulation, Case-2, having a better equivalence ratio and higher turbulent kinetic energy, correlates with the engine test data. This shows an initial validation for the developed methodology to simulate the air fuel mixing under the influence of droplet atomisation and fuel evaporation from the cylinder walls and correlates with the engine behaviour.

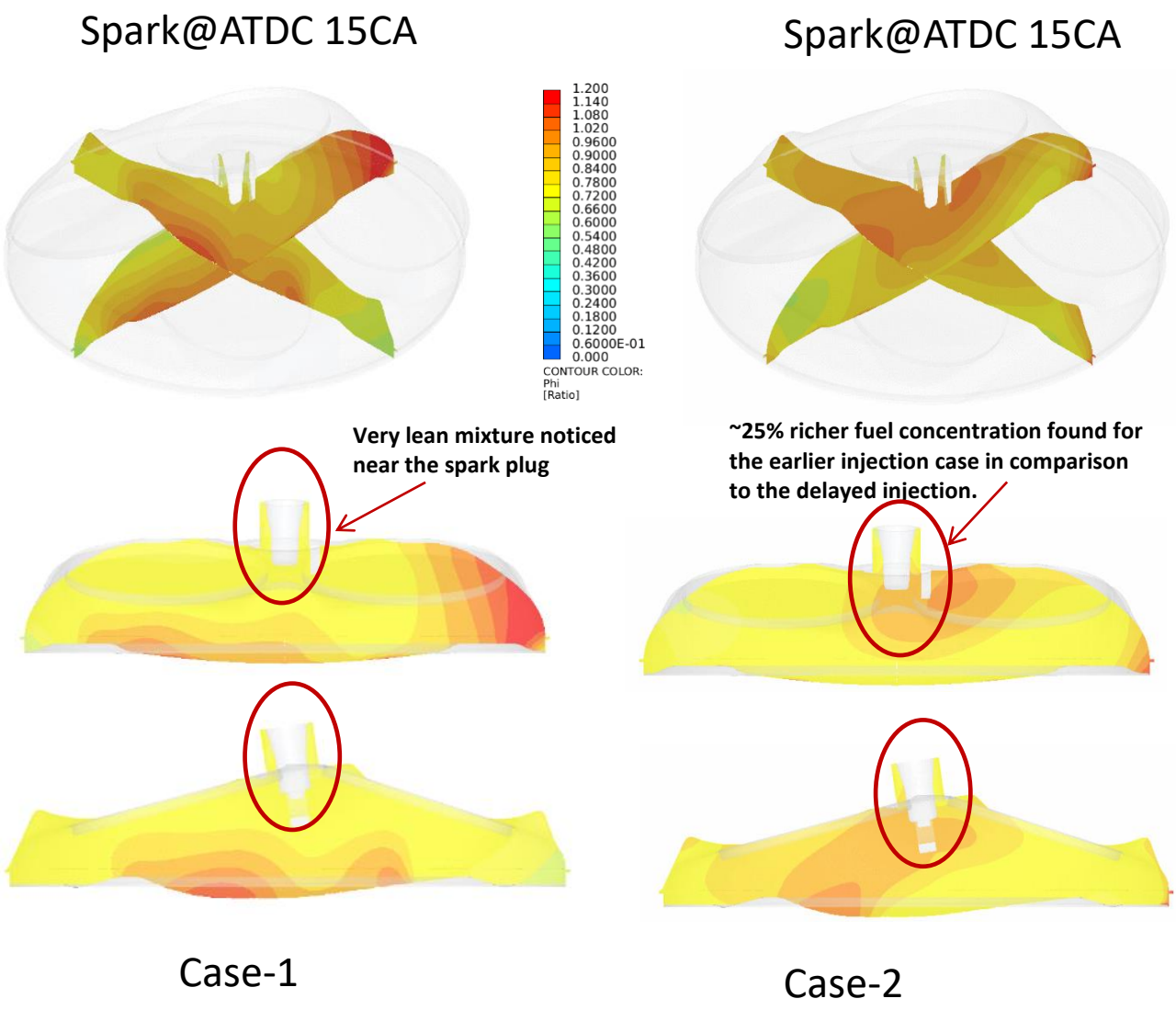

Figure 4.14: Equivalence ratio distribution around the spark plug at the time of spark for Case-1 and Case-2.

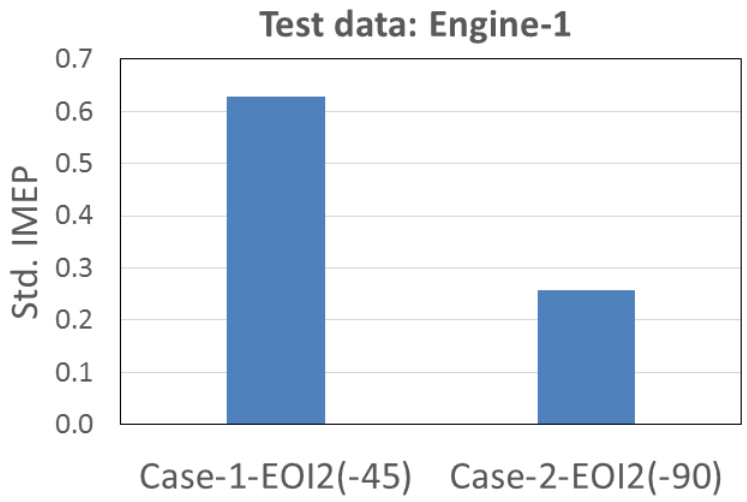

Figure 4.15: Measured combustion stability from the engine for Case-1 and Case-2 conditions (Changan UK, engine development data, 2016).

4.5 Summary and conclusions

In summary, the simplified spray model methodology has been applied to a catalyst light-off engine simulation to assess the engine stability, based on the equivalence ratio distribution, turbulent kinetic energy and charge motion at the time of spark. The side-mounted injector shows a significant influence on the charge motion by the split injection strategy. The engine Std. NIMEP data correlate well with the fuel stratification results with different injection strategies.

The tumble ratio plot shows that the delayed second injection disrupts the charge motion significantly. In the earlier second injection strategy, both the liner and piston wetting could be decreased along with better fuel stratification. This decreases PN/PM emission significantly. Due to the stringent emission regulations, and for the environmental aspects, any improvement in the injection strategy and the supporting piston design needs to be explored in more detail.

This spray model and the in-cylinder simulation setup along with the identified injection strategy, spray pattern and piston design improvement results are discussed in Chapter 5. A detailed understanding on the wall-guided and new air-guided system to develop build a low PN/PM emission engine is also provided.

Chapter 5. Investigation of Wall-guided and Air-guided System for Meeting Emission Regulations

5.1 Introduction

During catalyst light-off operation, the engine walls are normally cold. Moreover, the charge air or manifold air temperature is also close to the ambient air temperature. Liquid fuel evaporation is a function of atomisation (SMD), charge air and cylinder wall temperatures. The higher the temperature, the faster the fuel evaporation and the more fuel vapour available during the start of ignition. As detailed in Section 4.1.2, for faster light-off (catalyst heating), more heat needs to be delivered as catalyst through exhaust gas. A retarded combustion strategy is adopted for achieving higher exhaust gas temperatures. Combustion stability needs to be maintained during the retarded ignition to avoid NVH issues. Combustion stability is a function of equivalence ratio (ϕ) and turbulence intensity in the air fuel mixture. The engine load demand during the catalyst light-off is relatively low (1200 RPM, 3 bar NMEP) with the combustion stability criteria <0.3 bar standard deviation of NMEP, to meet NVH requirement. During this operating point, the manifold pressure is below atmospheric pressure (~0.6 to 0.7 bar, absolute). High pressure fuel injection during the intake stroke with a lower in-cylinder pressure results in higher liquid penetration, resulting in higher liner and piston wetting. As the wall temperatures are lower during the initial start of the engine, the evaporation of fuel from the cylinder walls is further hindered. This results in a very lean fuel-air mixture available during the start of ignition, even though a fuel equivalent of stoichiometric condition based on the trapped air is injected. Additionally, the charge air motion inside the cylinder makes the fuel-air mixture leaner. This results in unfavourable combustion condition and poor combustion stability due to misfire and cycle-to-cycle variability in NMEP. Thus, it is necessary to provide a fuel rich cloud of air-fuel mixture near the spark plug region during the cold start for faster catalyst light-off to enable a stable and complete combustion during the expansion stroke.

In the engine design, an understanding of the charge motion development during the intake stroke and synchronising the charge motion with piston and spray pattern is essential to achieve the stratified charge combustion, as well as the fuel injection process.

In this chapter, analyses of the flow and mixture formation through wall-guided, spray-guided and air-guided systems are presented. Detailed studies with a multi-hole injector using the air-guided system for the development of ultra-low PN/PM emission engine are shown and analysed. in particular, the advantages and charge motion enhancement possibilities using the side-mounted high pressure GDI injectors are detailed using the newly validated in-cylinder spray model proposed in Chapter 4.

5.2 Spray-guided, wall-guided and air-guided systems

The fuel stratification can be achieved by using spray-guided, wall-guided or air-guided systems (Ortmann et al., 2001). DISI engines with central injector arrangement can improve catalyst heating performance in terms of combustion stability when operated in spray-guided or wall-guided strategy with twin injections. In both strategies, the first injection occurs during the intake stroke and is aimed at forming a relatively well-mixed but lean air-fuel mixture. In the spray-guided strategy, the second injection takes place after firing TDC and creates a fuel rich mixture and high turbulence in the central part of the combustion chamber, which increases burning velocity and consequently improves combustion stability (Chen et al., 2009). The second injection only needs a small amount of fuel, e.g., 20% of total fuel. As a result, the corresponding piston wetting is relatively low. The optimal SOI of the second injection was found to be slightly after the spark timing, which was set to be much retarded from minimum ignition advance for best torque (MBT) spark timing and typically after firing TDC. The retarded spark leads to high exhaust heat flux for fast catalyst light-off. As the rich mixture is created by the spray plumes without interaction with combustion chamber walls, there is no specific requirement for piston crown geometry. However, the spray pattern of the injector should be designed in such a way that the spark plug is sufficiently adjacent to, or, inside the fuel clouds of spray. Modelling results show that there are high gradients in equivalence ratio in the fuel rich region (Fu, 2017). The volume of the rich region depends on the envelope of spray plumes. Presence of spray during the combustion period, high PN emission (~1e8) is observed due to the airborne droplets burning. The combustion stability is influenced by the fuel quantity of the second injection.

For the wall guide strategy, a piston bowl is required to guide the fuel rich air cloud flow created by the spray impingement of the second injection to the central region of the combustion chamber. The EOI of the second injection is in the late stage of compression stroke, e.g., 35˚ BTDC. More fuel is needed for the second injection than the spray-guided strategy, e.g., 40% of total, which leads to sufficiently rich mixture on the one hand, and high piston wetting on the other. Despite the high piston wetting with the wall-guided strategy, the PN emission is reported to be much lower than that of the spray-guided due to the absence of airborne droplets burning and overly rich gaseous mixture. However, HC emission with the wall-guided approach is much higher than the spray-guided approach.

It may be summarised that, for the DISI engines, either spray-guided or wall-guided strategy can be applied to improve combustion stability with similar levels of exhaust heat flux and NOx emission. However, there are significant differences in PN and HC emissions between the two

strategies. Although the wall-guided strategy has shown advantage over spray-guided strategy in terms of PN emission, it is still a challenge to meet the increasingly stringent emission regulations. In order to reduce PN emission further, an air-guided strategy for the side-mounted injector is proposed. In the air-guided system, the second injection takes place much earlier than that of the wall-guided strategy. The piston crown is designed in such a way that the rich mixture formed from the second injection can be guided to the spark plug region by utilising the tumble motion generated in the intake stroke.

Figure 5.1 shows the illustration of charge air motion relative to the piston shape, differentiating the air-guided and wall-guided pistons in the side-mounted injector configuration. In this figure, the dotted line indicates the general air motion direction relative to the intake port and fuel injection direction. It the wall-guided piston configuration, the curved piston wall acts as a backward facing step showing a possible stagnant zone. However, with the air-guided piston bowl shape, it aligns the flow and helps in preserving the tumble air motion. In the wall-guided approach, the curved piston wall guides the spray towards the spark plug during the late injection in the compression stroke providing the fuel rich mixture at the time of spark. In the air-guided approach, the strong tumble air motion is required during the compression stroke to retain the fuel rich mixture and guide it towards the spark plug at the time of ignition. An understanding of charge motion development, spray interaction and injection timing is essential in designing these systems. In order to understand the physics of the mixture formation process in engine catalyst heating operation, simulations of two-phase in-cylinder flow are carried out for both wall and air-guided strategies. The engine specification and operating conditions are shown in Tables 5.1 and 5.2, respectively.

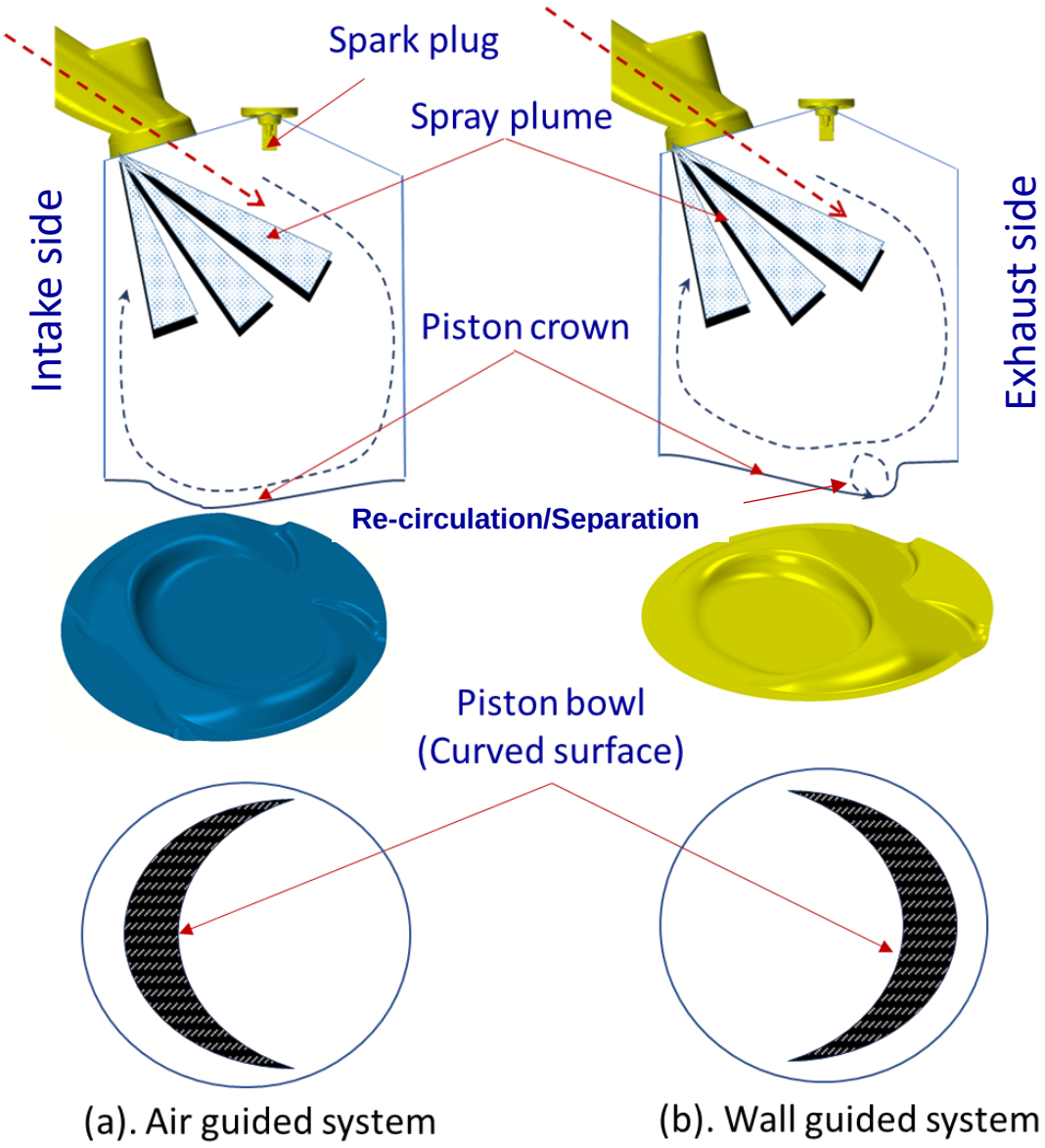

Figure 5.1: Description of air-guided (a) and wall-guided system(b) are shown. Piston arrangement relative to the injector position, intake port and exhaust port is shown. The "dotted" lines indicate the charge motion build-up direction.

Table 5.1: Engine specification-A.

Engine displacement	1.6 L
Bore	76
Stroke	88
Compression ratio	10.5
Number of cylinders	4
Injection system	DI
Injector-C	6-hole
Injector position	Side-mounted

Table 5.2: Catalyst heating operation-A.

Strategy	**Wall-guided**	**Air-guided**
Engine speed	1200 RPM	1200 RPM
IMEP	3 bar	3 Bar
Intake pressure	0.723 bar	0.723 bar
Intake temperature	28˚C	28˚C
Fuel split ratio	74% : 26%	76% : 24%
Total fuel injected/cycle/cylinder	15.8 mg	15.8 mg
SOI1	300˚ BTDC	260˚ BTDC
EOI2	45˚ BTDC	90˚ BTDC
Fuel pressure	280 bar	280 bar
wall temperature	25˚ C	25˚ C
Lambda (λ)	1	1

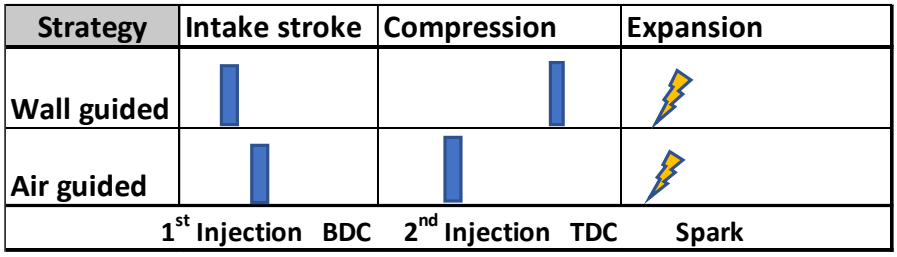

Figure 5.2: Injection and spark timings.

Figure 5.2 illustrates the injection and ignition strategies for the catalyst heating operation. A twin injection strategy is adopted, i.e., SOI1=300° and EOI2=45° C.A. BTDC, for the wall-guided system. For the air-guided system, an injection strategy of SOI1=260° and EOI2=110° C.A. BTDC is used. The first injection occurs during intake stroke and is aimed at forming a relatively well-mixed lean air-fuel mixture. The second injection takes place in the compression stroke to create a rich mixture to be guided to the spark plug region. The ignition timing is set much retarded from MBT spark and typically after compression TDC, which leads to high temperature and heat flux of exhaust gases. The cold flow simulation setup as adopted in Chapter 4 (Section 4.3) is used.

5.2.1 Results of air-guided and wall-guided cold flow simulation

The strength of the in-cylinder charge motion is assessed using the tumble ratio (TR). Figure 5.2.1 shows the calculated in-cylinder tumble ratios of the air-guided and wall-guided systems. The timing of injection has a significant effect on tumble ratios. It is observed that there is a drop of tumble ratio associated with injection.

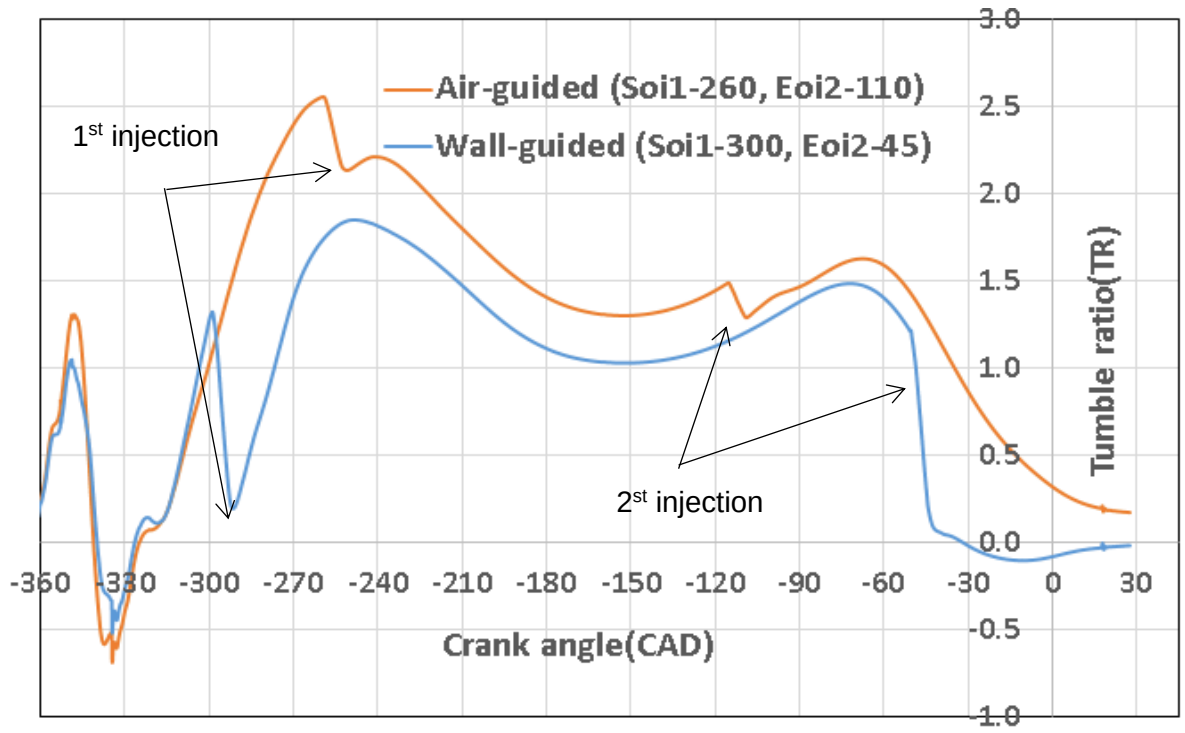

Figure 5.2.1: Tumble ratio comparison of air-guided and wall-guided system.

The injected fuel has an angular momentum about the mass centre of cylinder gas, which can offset the tumble motion in the cylinder. The angular momentum is a function of the position of mass centre during the time of injection. Therefore, the offset against the tumble motion

decreases with injection moving towards BDC and reaches its minimum when injection takes place at BDC. As a result, the tumble ratio increases with injection moving towards BDC. Since SOI1 of the air-guided is 40° more retarded than that of the wall-guided, the tumble ratio of the air-guided is higher than the wall-guided (Figure 5.2.1). As the angular momentum of cylinder gas increases with engine speed and the angular momentum of spray is independent of engine speed, therefore, the effect of injection on tumble ratio decreases with increasing engine speed. At high speed, high load condition the boost pressure is significantly higher, which results in lower fuel penetration and the charge motion influence is affected. Figure 5.2.2 shows the comparison of velocity fields near BDC. A strong charge motion in the air-guided setup is observed. The colours represent the velocity magnitude and the vectors represent the velocity direction. It is noticed that the piston surface of the air-guided system is aligned with the tumble flow direction, causing no obstruction. However, the piston surface of the wall-guided system presents an obstruction to the tumble flow and causes flow separation (Figure 5.2.2), which reduces the tumble motion.

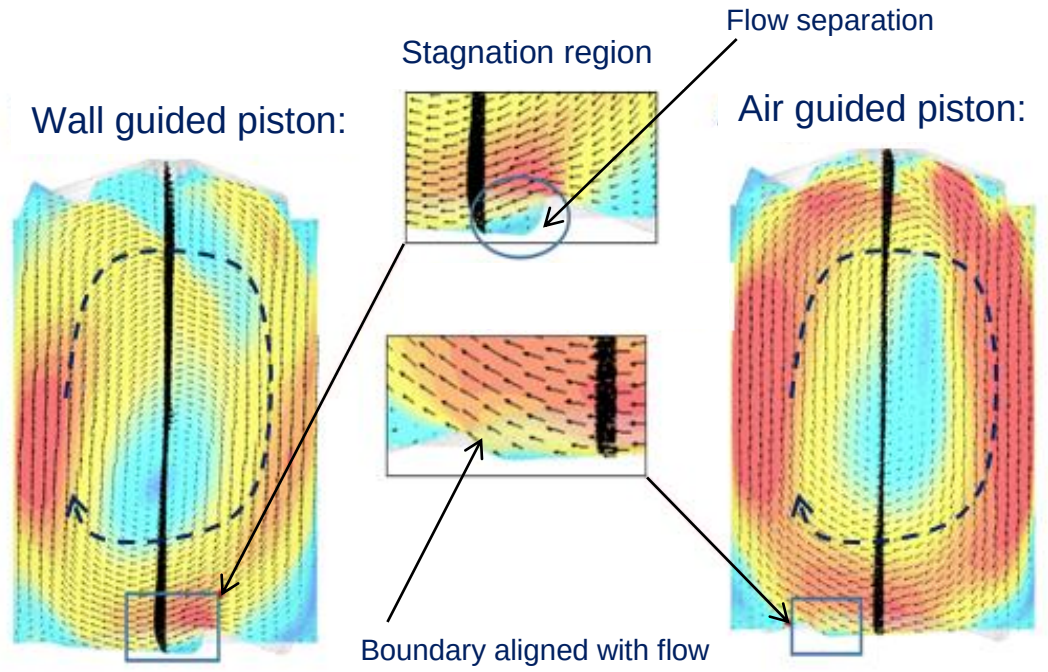

Figure 5.2.2: Charge motions near BDC in the air-guided and wall-guided system.

The second injection occurs in the compression stroke. The offset against tumble motion increases with retarded injection, as shown in Figure 5.2.1, the tumble ratio then drops sharply during the second injection of the wall-guided system.

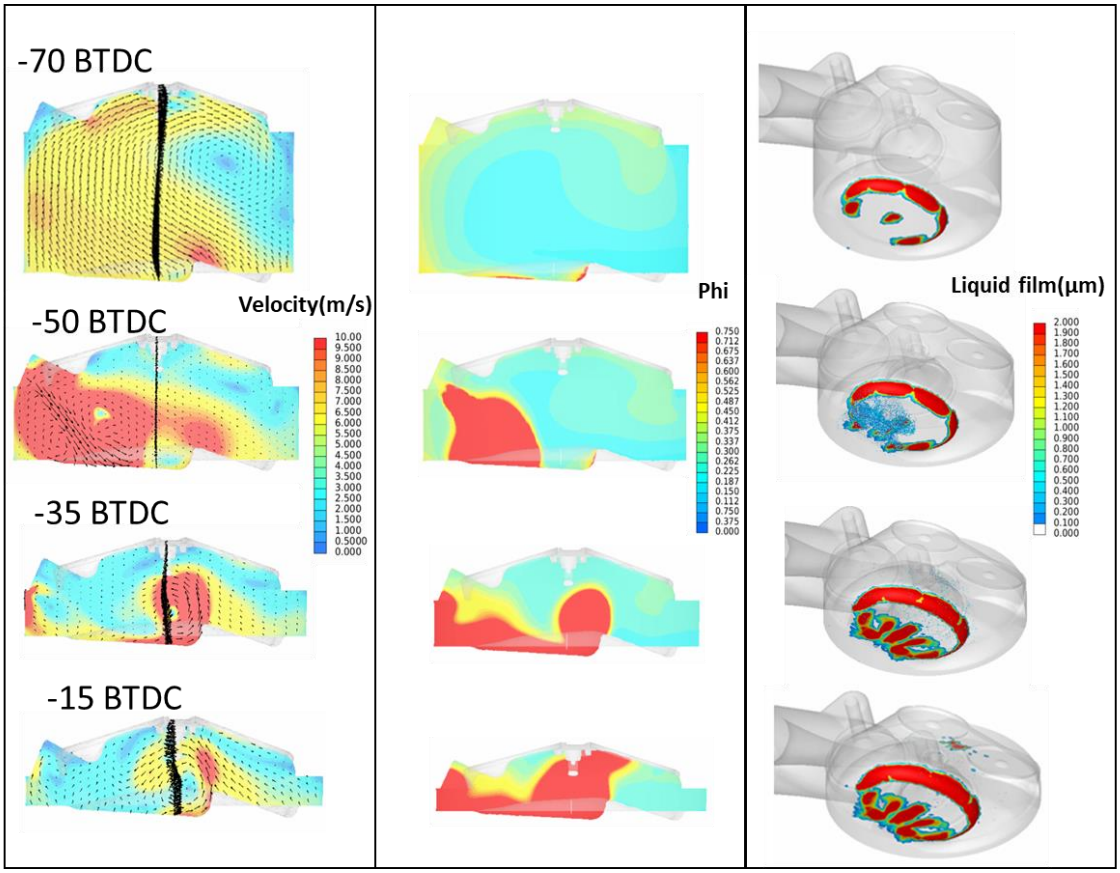

Figure 5.2.3: Velocity, equivalence ratio and wall wetting in the wall-guided system.

Figure 5.2.3 illustrates the distributions of gas velocity, equivalence ratio and liquid film thickness on piston in the wall-guided system. The spray of the second injection impinges on the piston, resulting in piston wetting and wall-guided flow. Liquid film is formed on the locations of jet impingement and the rim of piston bowl. The rich mixture created by the second injection is brought to the spark plug region by the wall-guided flow. The split injection strategy is found to improve combustion stability significantly over the strategy with a single injection during induction stroke. It is believed that the rich mixture created by the second injection is largely responsible for the combustion stability improvement.

There are two features associated with the wall-guided system, i.e., strong stratification of mixture and high piston wetting. The first feature improves combustion stability and allows more retarded spark timing, which gives high heat flux of exhaust gas. The second feature has negative effects on combustion and the resulting emission.

Figure 5.2.4 shows the velocity, equivalence ratio and wall film in the air-guided system. A stronger tumble motion due to the more retarded first injection is evident compared with that of the wall-guided. Rich mixture from the second injection is transported by the tumble flow to the spark plug region to form weak mixture stratification compared with that of the wall-guided case. This results in less spark retard and lower heat flux of exhaust gas. A distinct advantage with the air-guided system is the very low piston wetting due to the retarded first injection and the advanced second injection when the piston is further away from the injector. This reduces PN emission substantially during the cold-start operation, which is critical to meeting the emission regulations.

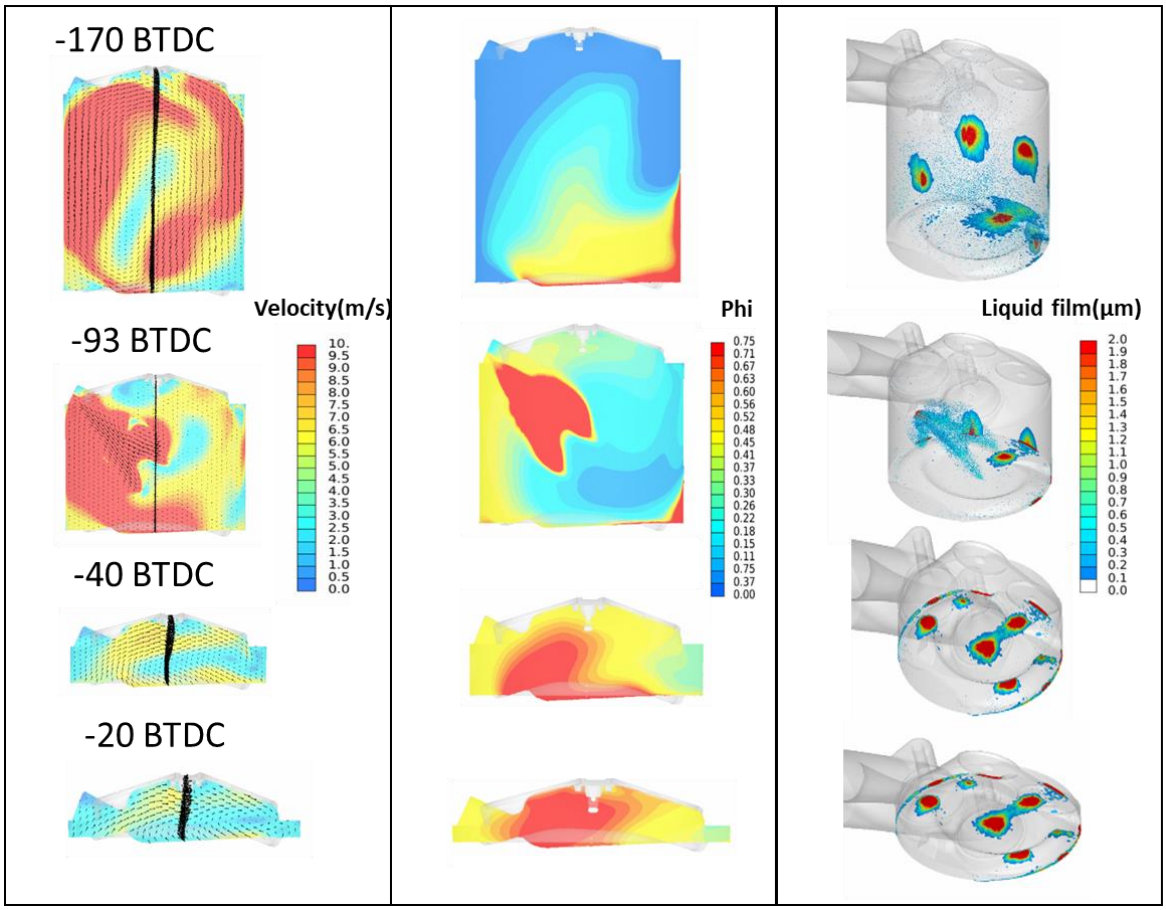

Figure 5.2.4: Velocity, equivalence ratio and wall wetting in air-guided system.

Wall wetting expressed as the mass fraction of total injected fuel is shown in Figure 5.2.5. The wall wetting with the air-guided system is less than half of the wall-guided at the firing TDC. The slopes of the curves represent the evaporation rates of fuel film. Charge motion and

wetted surface area are the two factors which have significant influence on fuel film evaporation. The fuel film formed from the first injection evaporates faster than that from the second injection due to the presence of strong charge motion. Because the air-guided strategy has stronger charge motion, the evaporation is faster, as shown in Figure 5.2.5. Fuel film formed from second injection evaporates relatively slowly due to rapidly decreased charge motion and higher in-cylinder pressure (decreasing the saturation mass fraction of the liquid film which is proportional to the ratio of the saturation pressure and local charge pressure). The wall wetting in other parts of the engine cylinder were negligible and hence not shown in this plot.

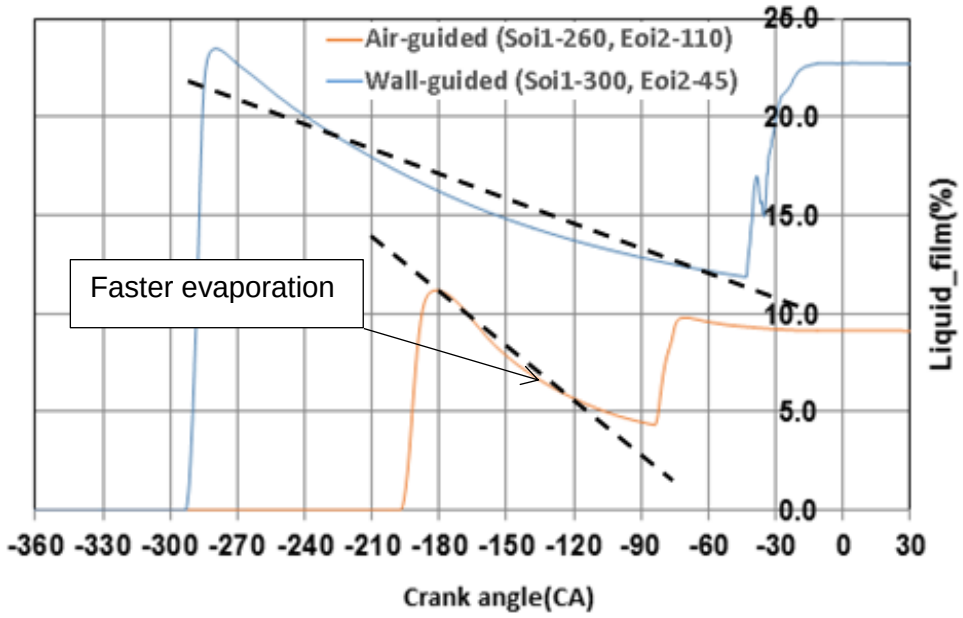

Figure 5.2.5: Total liquid film on walls in air-guided and wall-guided systems.

The cylinder averaged turbulent kinetic energy (TKE) is shown in Figure 5.2.6. Fuel injection increases TKE as there is a rise of TKE corresponding to each injection. Difference in TKE between the two strategies diminishes when approaching the firing TDC. There is little difference in TKE at the spark timing 15° ATDC, which may suggest that the combustion difference between the two strategies is mainly due to the difference in mixture strength.

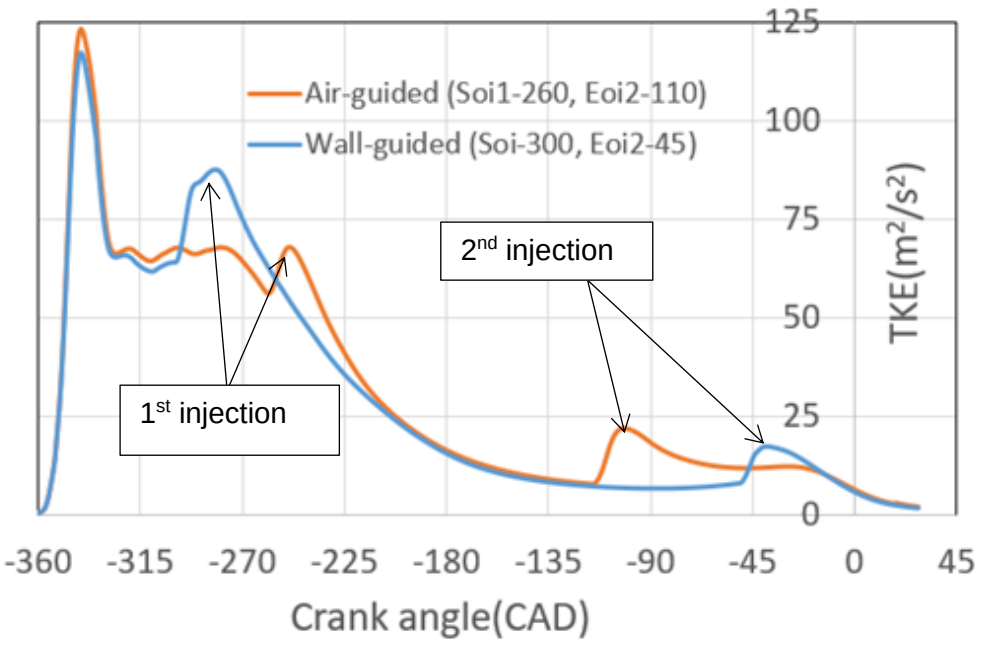

Figure 5.2.6: Cylinder averaged turbulent kinetic energy.

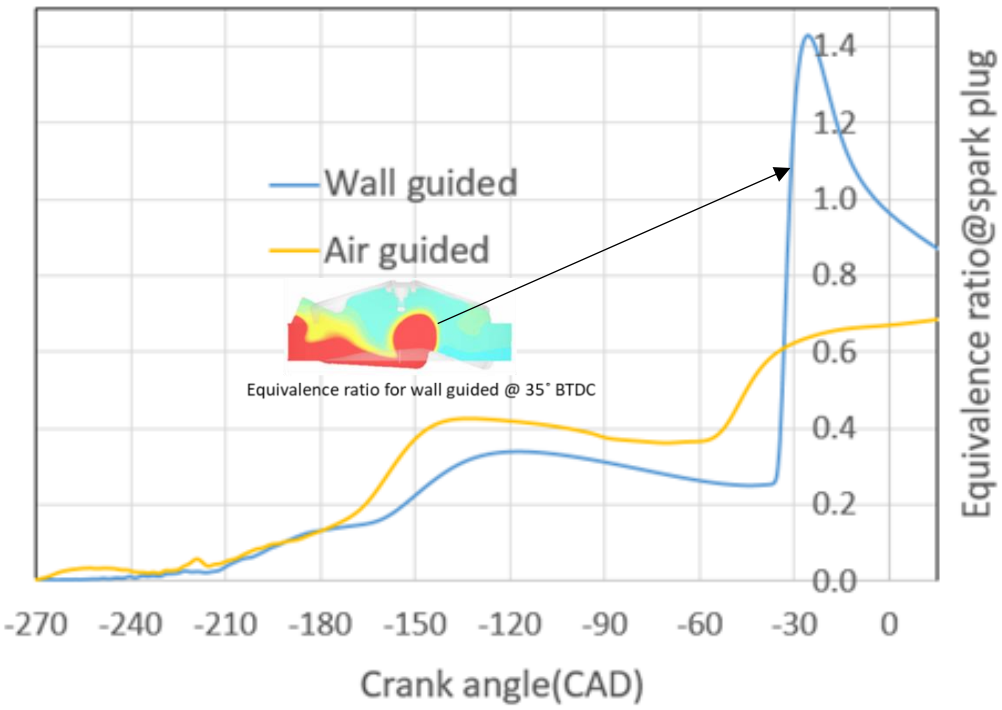

Figure 5.2.7: Equivalence ratio near spark plug.

A significant difference in equivalence ratio near the spark plug is shown in Figure 5.2.7. The equivalence ratio is averaged over the spherical volume of 3 mm radius around the spark plug. It is evident that the second injection of the wall-guided strategy gives a sudden rise of equivalence ratio.

Figure 5.2.8 to Figure 5.2.11 show the engine test results under the catalyst heating operation, i.e., 1200 RPM, 3 bar IMEP, 40°C coolant temperature (Yuan, Hu and Zhang, 2017). Twin injection strategy is used with the fuel split ratio of 6:4. The first injection timing is kept constant, i.e., SOI1=280° BTDC, and the second injection timing is swept with EOI2=49° BTDC for wall-guided and 113° for the air-guided. In the tests, standard deviation of IMEP, which represents combustion stability, is kept near the target value of 0.3 bar.

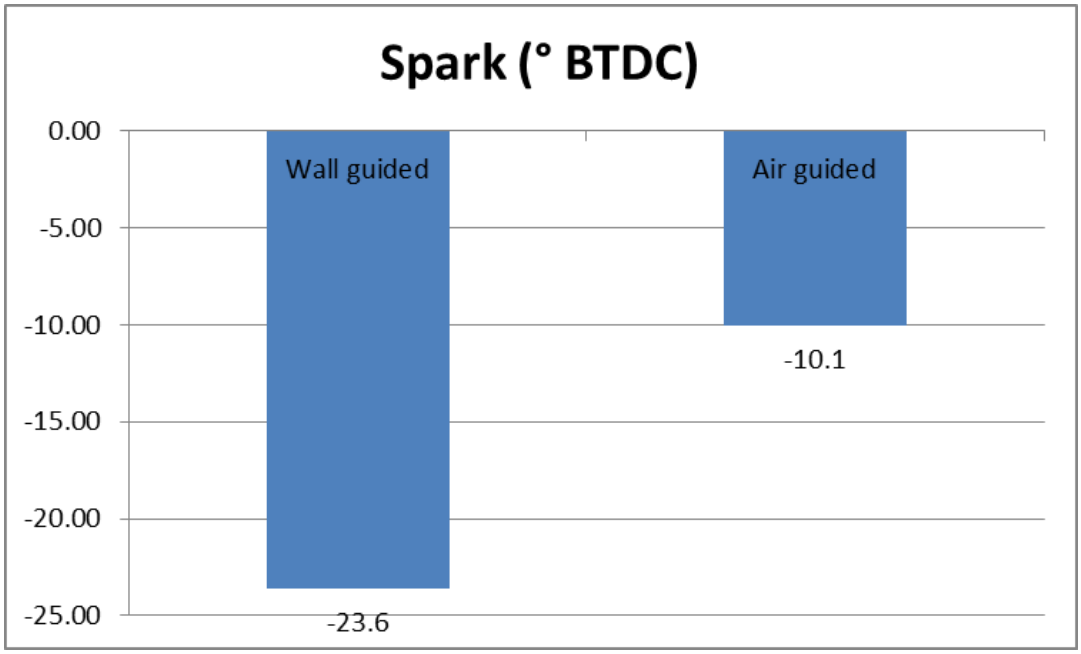

Figure 5.2.8: Spark timing comparison between the wall-guided and air-guided (Taken from Yuan et al., 2017).

As shown in Figure 5.2.8, the spark timing of the wall-guided system is more retarded than the air-guided due to the rich mixture formed in the spark plug region. As a result, the corresponding heat flux is 74% higher than the air-guided (Figure 5.2.9).

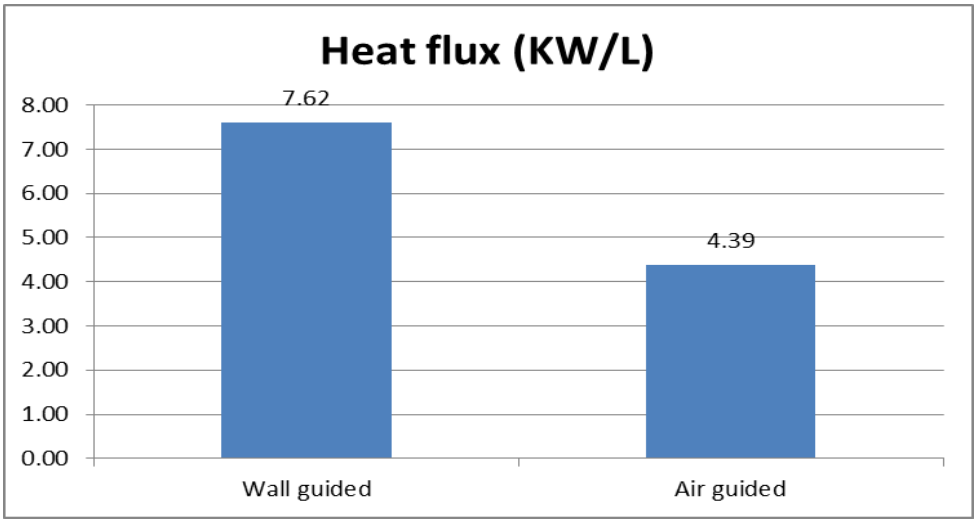

Figure 5.2.9: Heat flux comparison between the wall-guided (Data taken from Yuan et al., 2017) and air-guided operation.

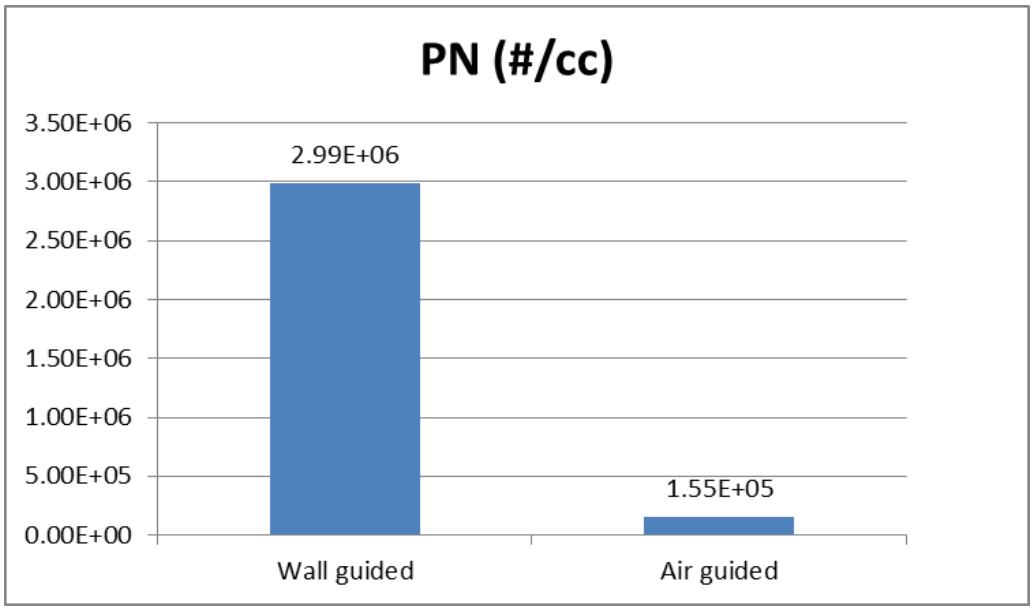

Figure 5.2.10: PN comparison between wall-guided and air-guided strategies (Taken from Yuan, Hu and Zhang, 2017).

The PN of the wall-guided is higher than the air-guided by an order of magnitude (Figure 5.2.10) due to the rich mixture and high piston wetting. Meeting the PN emission standard of the China 6 (b), the Euro 6 equivalent, is the most challenging and this high level of PN is considered unacceptable. Therefore, the air-guided strategy is finally chosen for the catalyst heating operation and all the emission standards can be met over the WLTC driving cycle.

Figure 5.2.11 shows comparison of combustion stability between the two strategies. The standard deviation of IMEP is slightly lower with the wall-guided despite more retarded spark. This shows that the air-guided strategy as demonstrated by the simulation, there is a reduction in PN emission by a factor of 19 without loss of combustion stability criteria. As noticed in the simulation, the charge motion is enhanced by the injection quantity and timing. To further understand the underlying process, studies are extended to quantify the effect of injection timing and the injection quantity with the Injector-C, configuration. The details of the simulation are shown in Section 5.3.

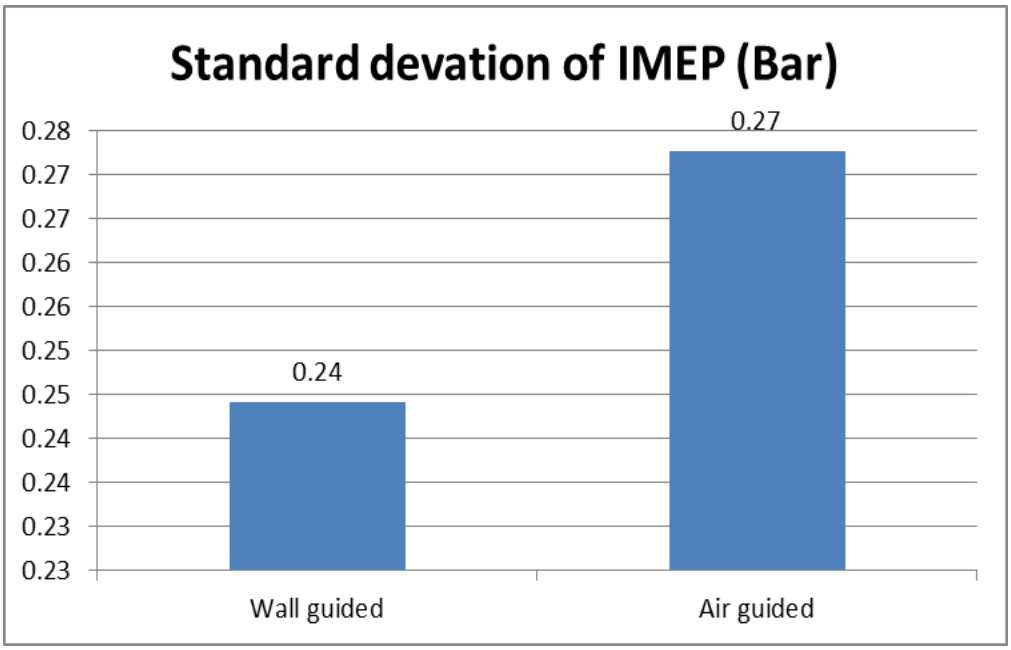

Figure 5.2.11: Combustion stability comparison between wall-guided and air-guided strategies (Taken from Yuan et al., 2017).

5.3 Effect of spray on charge motion and mixture preparation:

Figure 5.3.1 depicts the typical spray orientation in an engine cylinder arrangement. The crank angle relative to the piston fire TDC and the corresponding piston displacement are also shown. In this, the mass centre of the charge is located at the origin “O”. In the three-dimensional flow field, the mass centre is not necessary to be the volume centre of the

cylinder. During the piston motion, the centre of mass moves according to the tumble structure governed by the piston speed, the intake port design, CAM profile and CAM timing. It is evident from the description that the higher the spray plume relative position with respect to the mass centre “O”, the higher the angular moment of inertia of the spray. If net resultant angular moment synchronises with the angular moment of inertia of air-fuel charge mixture during the intake or compression stroke, the moments add up and increase the charge motion, which enhances the fuel-air mixing. This benefits turbulent mixing, combustion efficiency and lowering the burn duration. Angular momentum of the spray can be increased by injection timing, the quantity of injected fuel or by orienting the spray more outwards relative to the mass centre. As the overall engine λ is fixed to ~1, the quantity of the injected fuel from the injector is also fixed for a defined intake charge pressure. To achieve fuel stratification, delayed injection near TDC is required, which can cause increased piston wetting. In order to enhance the charge motion and lower the piston wetting, triple injections were adopted with the delayed split injections near the TDC.

5.3.1 Effect of injection timing and injection quantity:

Simulation is carried out for engine specification-B. The details of the engine are given in Table 5.3.1. The catalyst heating operating conditions are listed in Table 5.3.2 and the piston geometry used for the simulation is shown in Figure 5.3.2. This is a shallow bowl piston designed to obtain a compression ratio of 12.0. The spark plug location relative to the piston is also shown. In this simulation, the effect of injection quantity on charge motion and the fuel stratification are quantified by the equivalence ratio around the spark plug (3 mm around the spark plug) and in-cylinder tumble ratio. The injection timing and the fuel split used in the simulation are shown in Table 5.3.3. The case names are identified as Case-1 to Case-5. SOI2 and EOI3 are based on earlier analysis and test data. However, the SOI1-200 is chosen close to the BDC to study the charge motion effects from the spray, where a maximum angular momentum can be delivered to the charge (spray plume axis has the maximum offset from the cylinder charge mass centre).

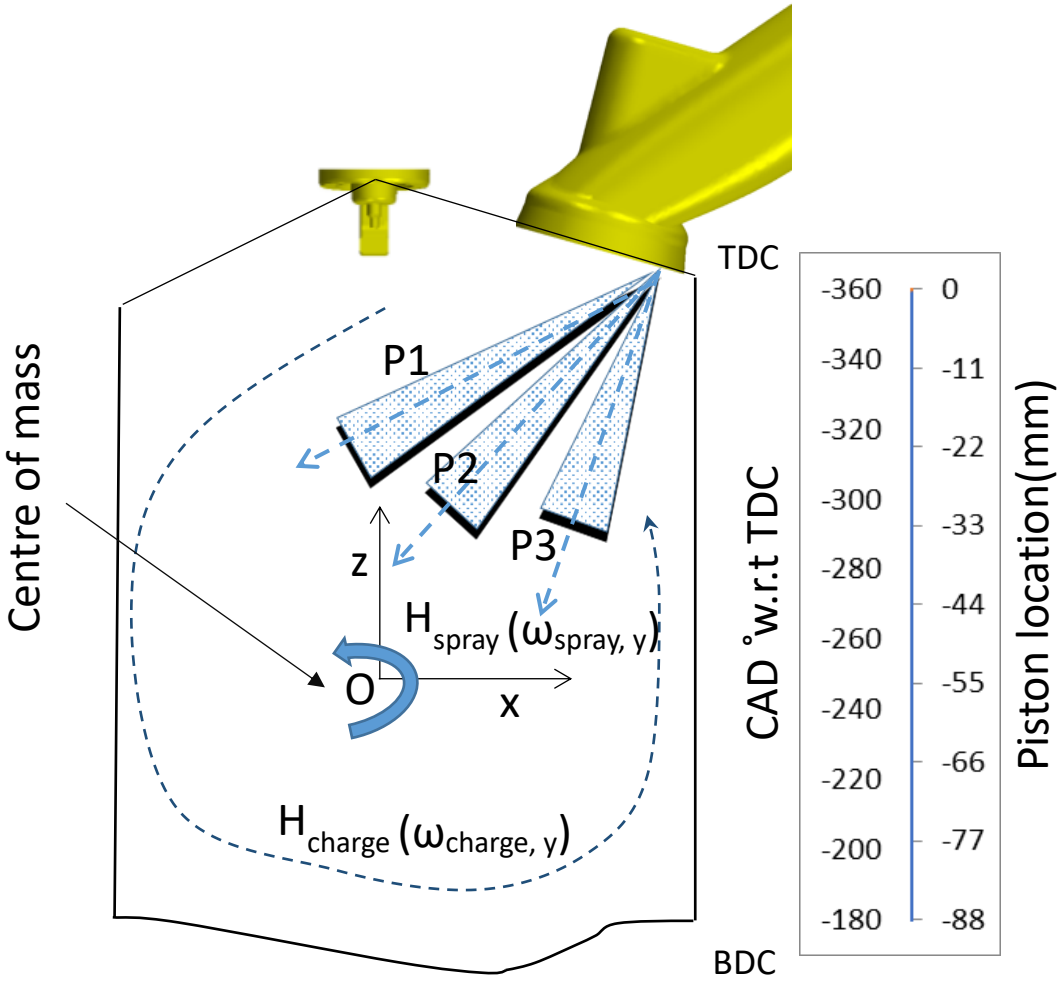

Figure 5.3.1: Illustration of angular momentum exchange of spray with the charge motion. P1, P2 and P3 are the different plumes defined by injector spray pattern. H and ω are the angular moment of inertia and angular velocity, respectively, for the spray and the charge air-fuel mixture. -360 CAD is the intake TDC position.

Table 5.3.1: Engine specification-B.

Engine displacement	1.5 L
Bore	73.5
Stroke	88
Compression ratio	12
Number of cylinders	4
Injection system	DI
Injector (Injector-C)	6-hole
Injector position	Side-mounted

Table 5.3.2: Catalyst heating condition-B.

Strategy	**Air-guided**
Engine speed	1200 RPM
IMEP	3 bar
Intake pressure	0.723 bar
Intake temperature	28˚C
Total fuel injected/cycle/cylinder	20.2 mg
Fuel pressure	280 bar
Wall temperature	27˚C
Lambda (λ)	1

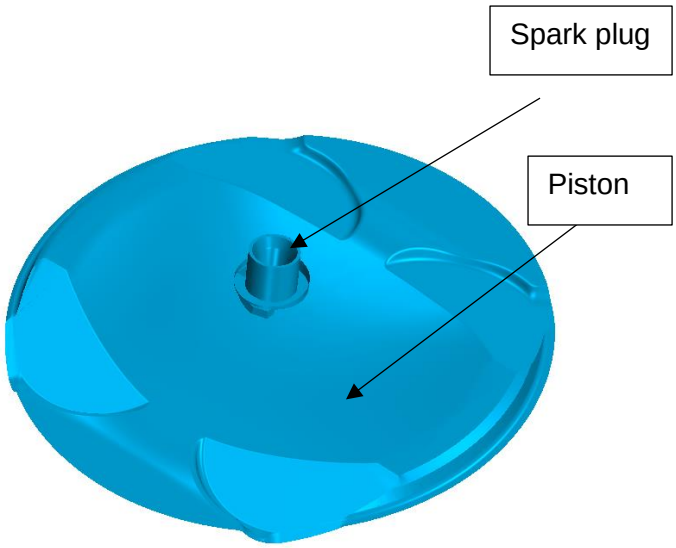

Figure 5.3.2: 12.5 CR, Engine-B piston shape placed relative to the spark plug geometry.

Table 5.3.3: List of injection timing (BTDC) and fuel split % used in the simulation.

	SOI 1	SOI 2	EOI 3	1st Injection (%)	2nd Injection (%)	3rd Injection (%)
Case-1	200˚	110˚	90˚	40	35	25
Case-2	200˚	110˚	90˚	30	35	35
Case-3	200˚	110˚	90˚	30	45	25
Case-4	200˚	100˚	90˚	65	35	-
Case-5	200˚	110˚	90˚	50	35	15

Figure 5.3.3 shows the temporal evolution of in-cylinder tumble ratios of the five different injection strategies using three injections. The injection timing is evident from the spikes noticed in the tumble ratio plot. Under the same injection timing, the larger the first injection pulse width/quantity, the higher is the charge motion. Case-4, with the maximum first injection quantity of 65%, shows the maximum charge motion build-up. This further builds up during the earlier second injection at 100˚ BTDC in generating a maximum tumble ratio second peak to ~1.7. It further continues until the TDC.

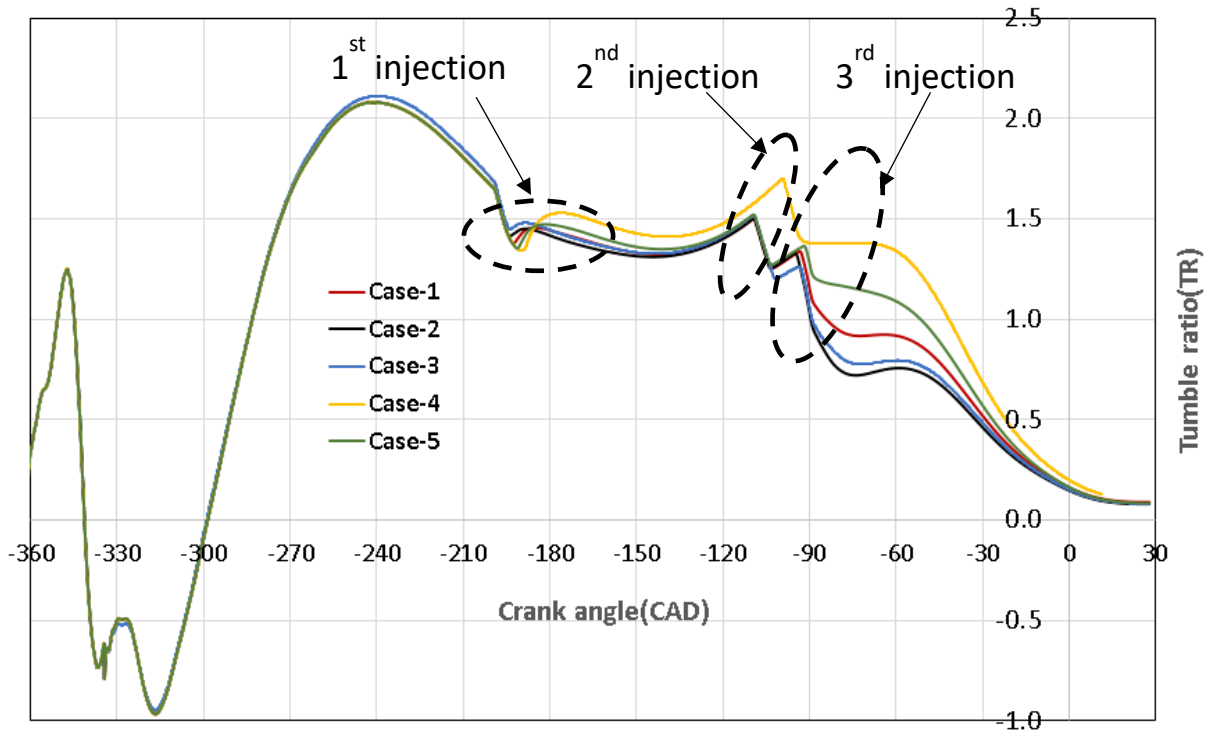

Figure 5.3.3: Crank angle resolved tumble ratio comparing the different injection strategies. The first, second and third injection events are circled in dotted lines.

As noticed in the earlier results, the delayed third injection causes the charge motion disruption. However, decreasing the third injection quantity decreases the charge motion disruption, as noticed in Case-5. The order of the flow disruption during the delayed third injection at 90˚ BTDC is proportional to the injection quantity. The total in-cylinder turbulent kinetic energy generated in the different injection strategies is shown in Figure 5.3.4. A similar trend of tumble ratio is noticed, where the higher the injection quantity, the higher is the turbulent kinetic energy generation during the first injection. The twin injection, as in Case-4, shows a maximum turbulent kinetic energy during the end of compression stroke. It should be noted that, even though the second peak is relatively (~26%) low, the TKE decay is less. This is mainly due to the continued charge motion as noticed in the tumble ratio plot (Figure 5.3.3). However, the TDC TKE for all other cases, Case-1, 2, 3 and 5, shows a similar level. The monitored TKE near the spark plug (Figure 5.3.5) for the different injection timing strategies shows a similar behaviour as that of the total TKE evolution plot (Figure 5.3.4).

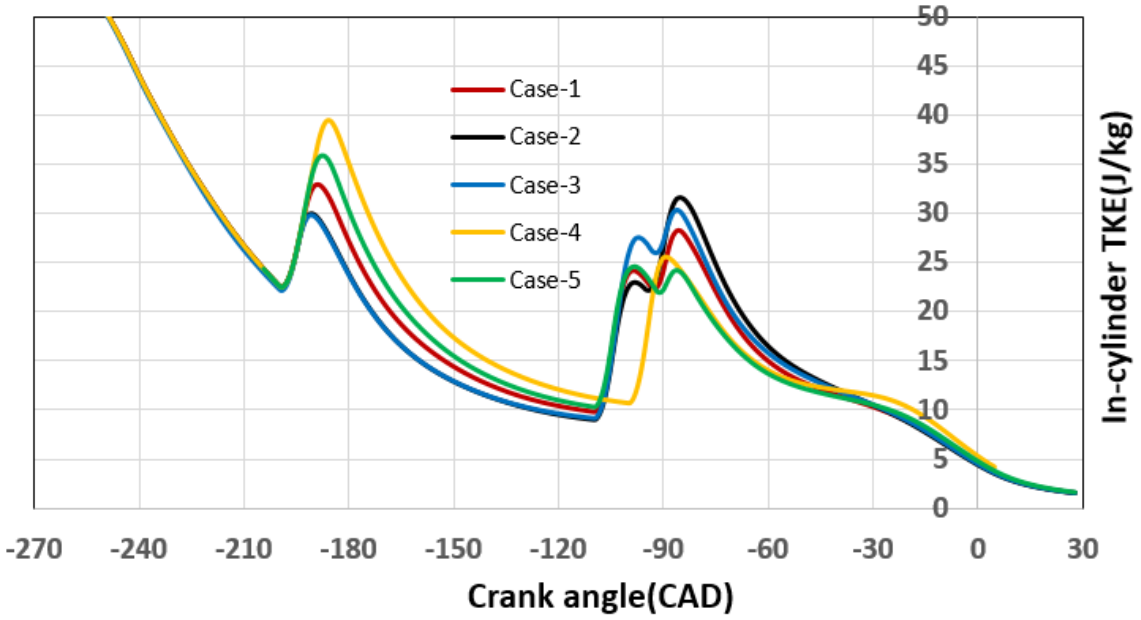

Figure 5.3.4: Crank angle resolved in-cylinder TKE, comparing the different injection strategies.

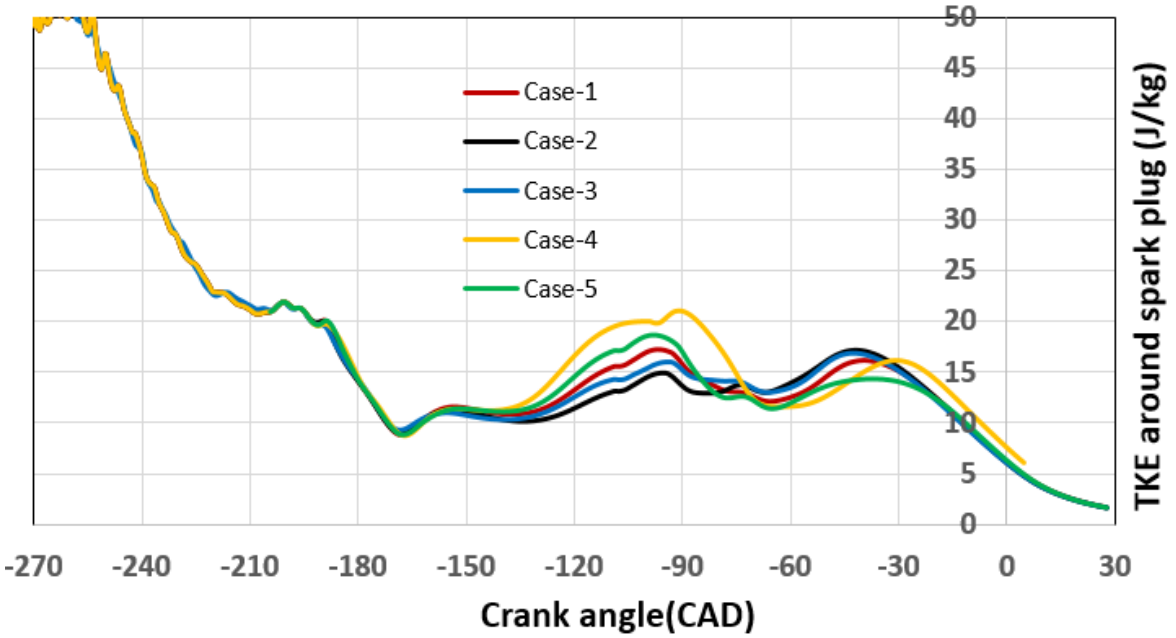

Figure 5.3.5: Crank angle resolved TKE monitored around the spark plug, comparing the different injection strategies.

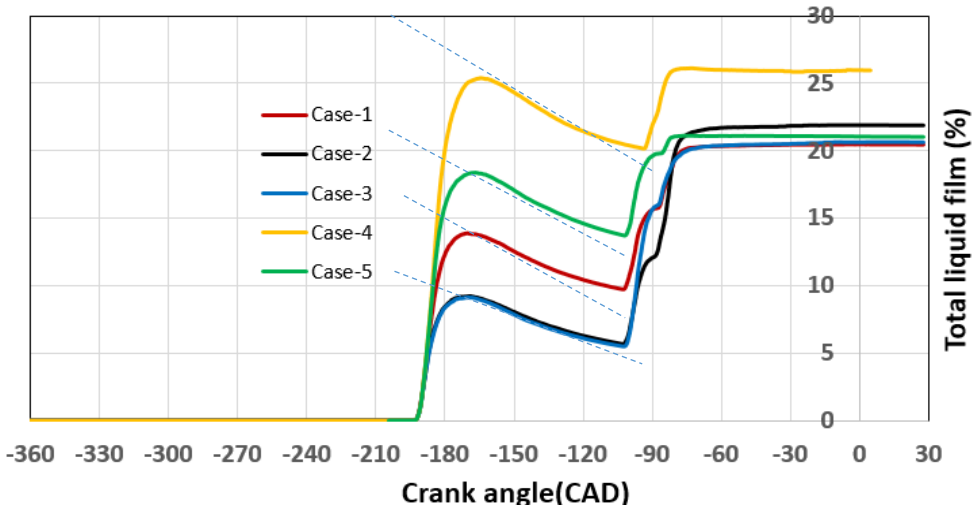

Figure 5.3.6: Crank angle resolved total liquid film on the cylinder walls, comparing different injection strategies. The liquid film mass is normalised based on the total injected fuel.

Figure 5.3.6 shows the crank angle resolved total liquid film on the engine cylinder walls. It represents the amount of liquid film formation and the evaporation characteristics from the wall. The amount of liquid film formed is proportional to the quantity of injected fuel and it can be seen from Figure 5.3.6 that the minimum liquid film remains using a shorter late injection, with a pulse width 25 to 15% of the total injected fuel. Any higher than 25%, results in higher wall wetting with Injector-C. The cylinder wall liquid film plot (Figure 5.3.7) showing a flat line at the end of third injection indicates a poor liquid film evaporation.

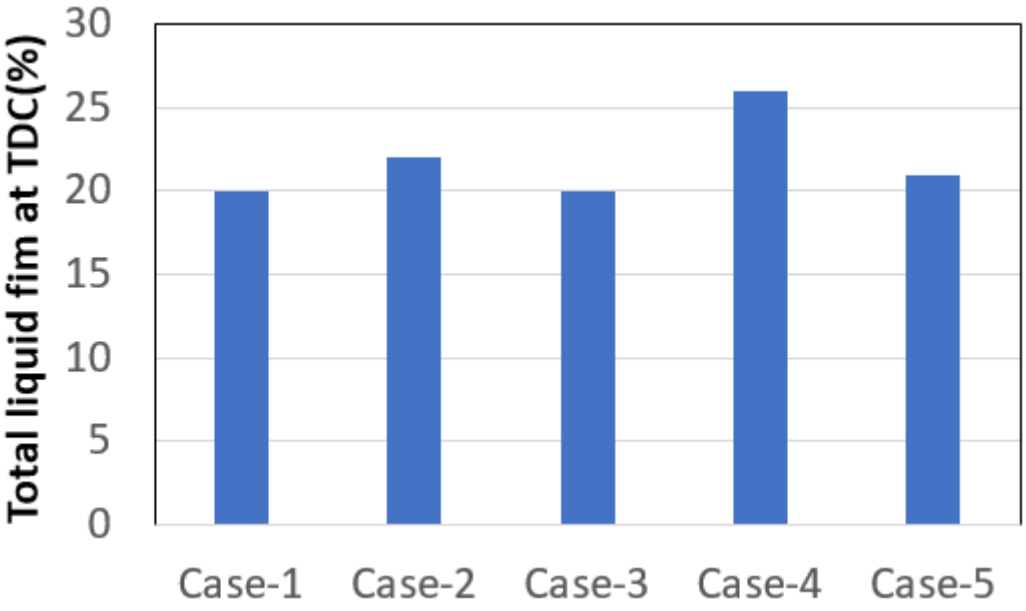

Figure 5.3.7: Comparison of total liquid film during the end of compression. Liquid film mass is normalised based on the total fuel injected.

The resultant equivalence ratio near the spark plug is shown in Figure 5.3.8. The triple injection strategy, as that of Case-5, was found to show the maximum equivalence ratio, which can best support a stable combustion by retaining the charge motion (Figure 5.3.3). This analysis has given a qualitative assessment for understanding the charge motion and injection quantity for the engine calibration directions. Hence, a lower Q_{stat} in managing a short pulse width at higher injection pressure should also be one of the injector selection criteria.

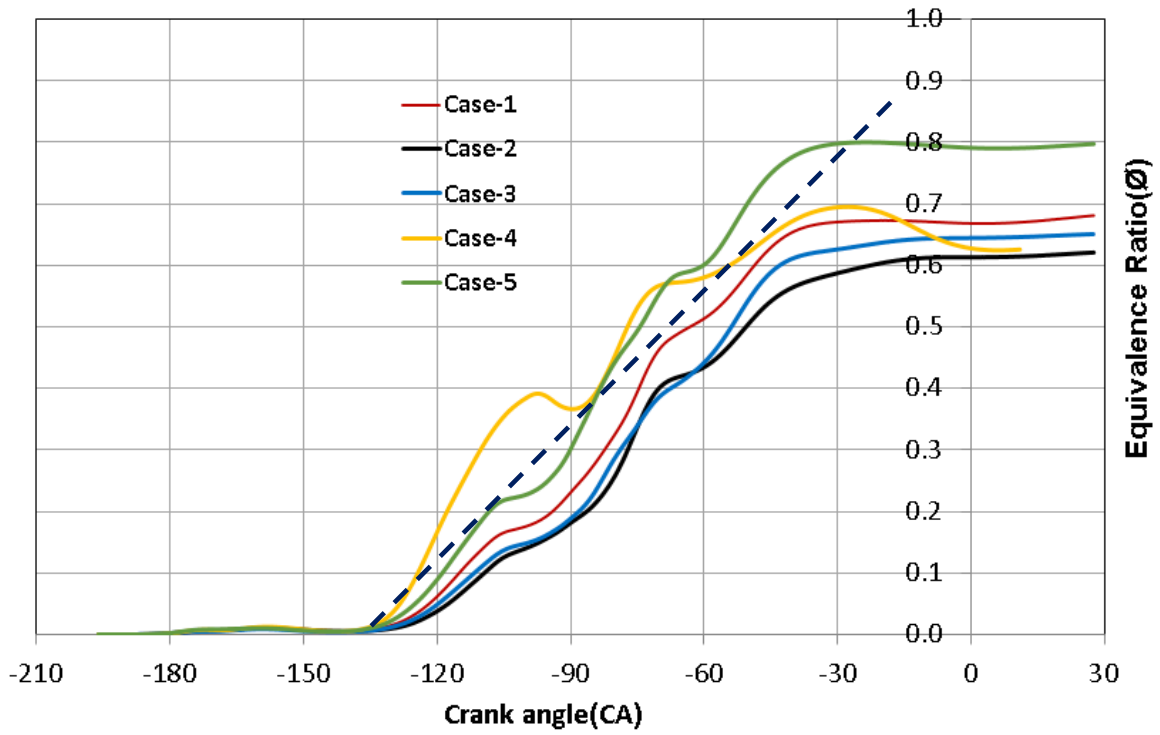

Figure 5.3.8: Crank angle resolved equivalence ratio monitored around the spark plug, comparing the different injection strategies.

5.3.2 Effect of spray pattern on charge motion:

As illustrated in Figure 5.3.1, in this section the effect of spray pattern is analysed by changing the spray angle to favour the spray-induced angular moment to support the charge motion. The details of the injectors used in the simulation are provided in Table 5.3.4. The same injection settings and the catalyst heating operating conditions as referred to in Table 5.3.2 are used in the simulation. SOI1, SOI2 and EOI3 of 200˚, 110˚ and 90˚ CAD BTDC, respectively, are used. Injection split ratios of 50%, 35% and 15%, respectively, are used for the chosen injection timing.

Table 5.3.4: Injector nozzle parameters used in the simulation are listed.

	N-hole (#)	Nozzle size (μm)
Injector-C	**6**	**123**
Inj-2	**6**	**123**
Inj-3	**5**	**137**
Inj-4	**6**	**123**
Inj-5	**6**	**123**

The injector spray pattern for the Injector-C, Inj-2, Inj-3, Inj-4 and Inj-5 are shown in Figure 5.3.9 to 5.3.13, respectively.

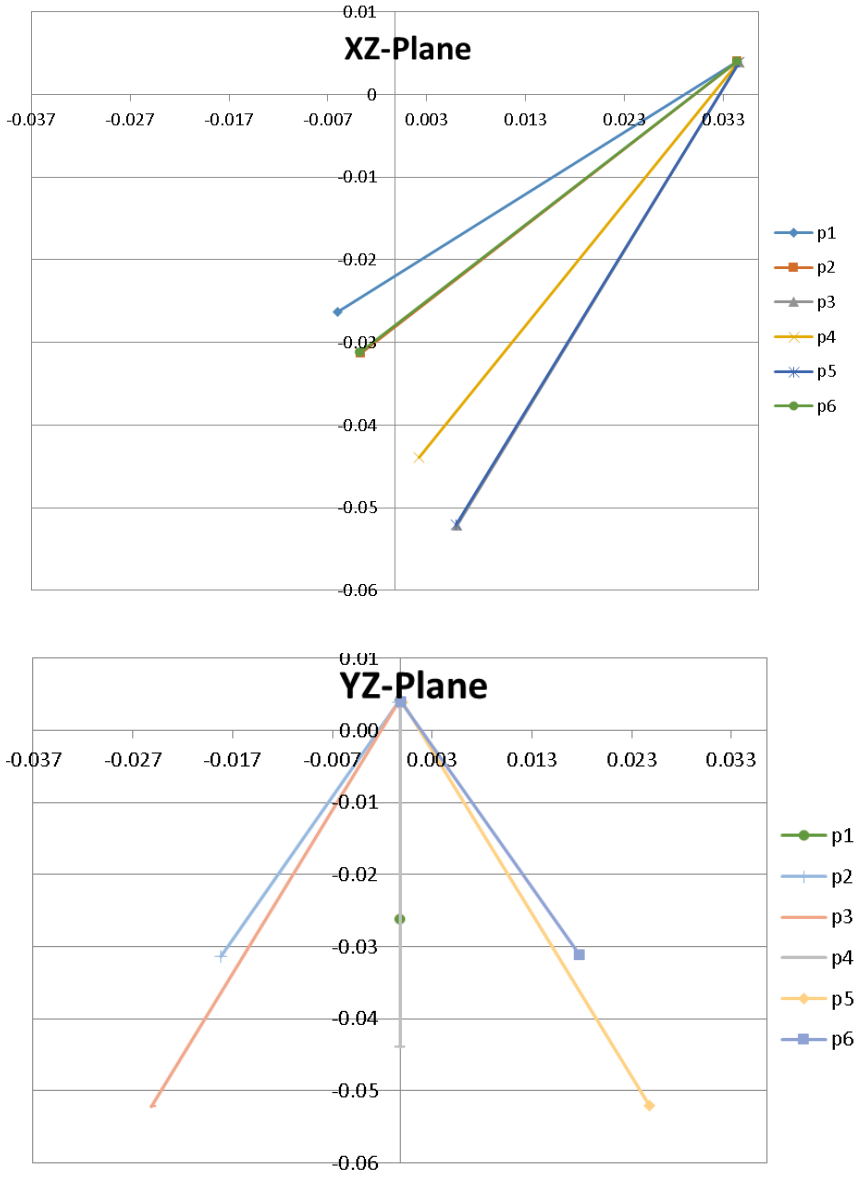

Figure 5.3.9: Injector-C, spray pattern shown in XZ and YZ plane, where p1, p2, p3, p4, p5 and p6 are the plume axes.

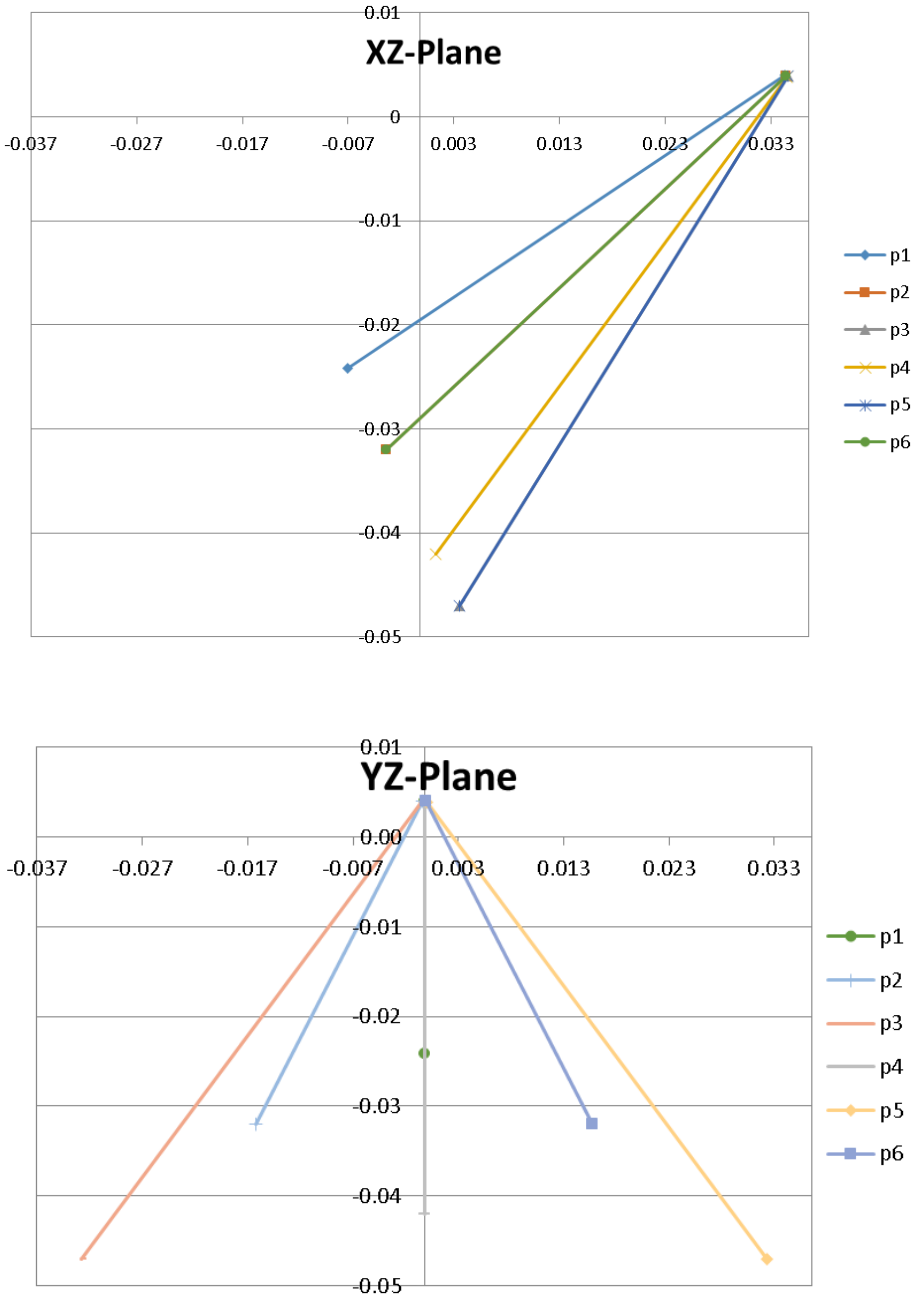

Figure 5.3.10: Inj-2, spray pattern shown in XZ and YZ plane. Where, p1, p2, p3, p4, p5 and p6 are the plume axes.

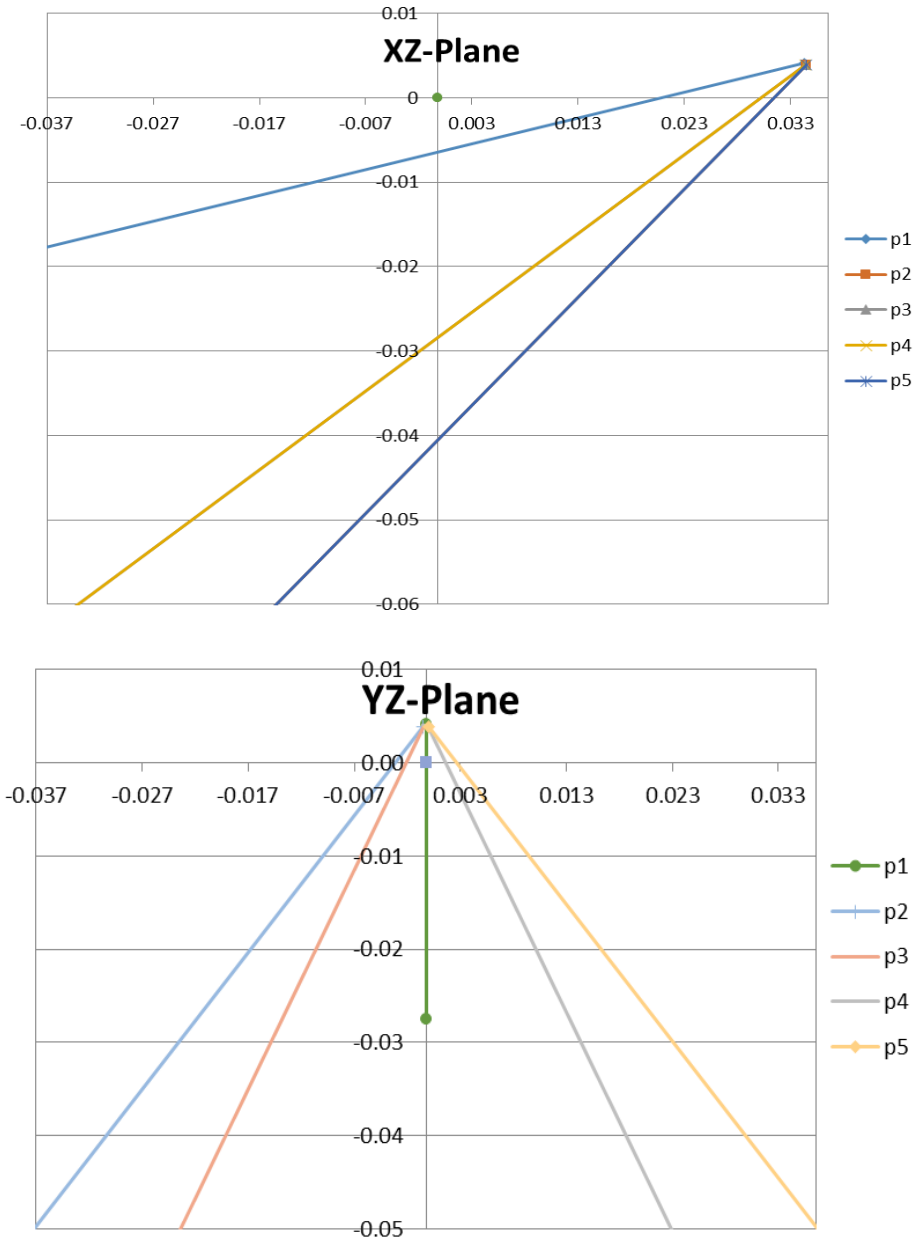

Figure 5.3.11: Inj-3, spray pattern shown in XZ and YZ plane, where p1, p2, p3, p4 and p5 are the plume axis. Spray pattern taken from “The new EA211 EVO, 2016”.

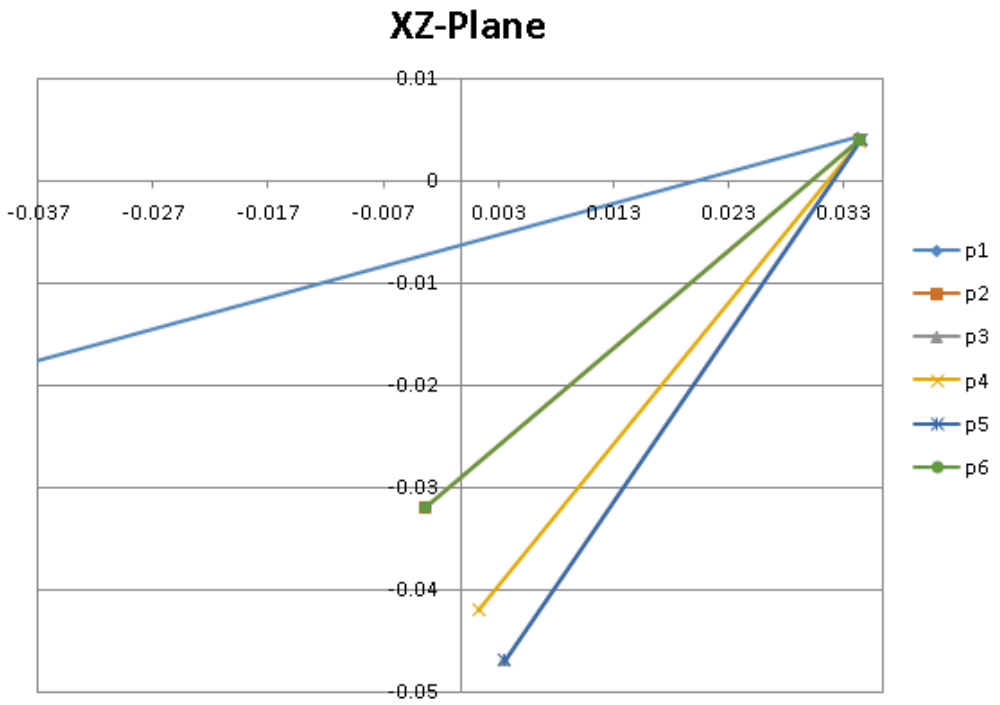

Figure 5.3.12: Inj-4, spray pattern shown in XZ plane, where p1 to p6 are the plume axes. In this, the base Inj-2 spray pattern is modified by replacing plume p1, from Inj-3.

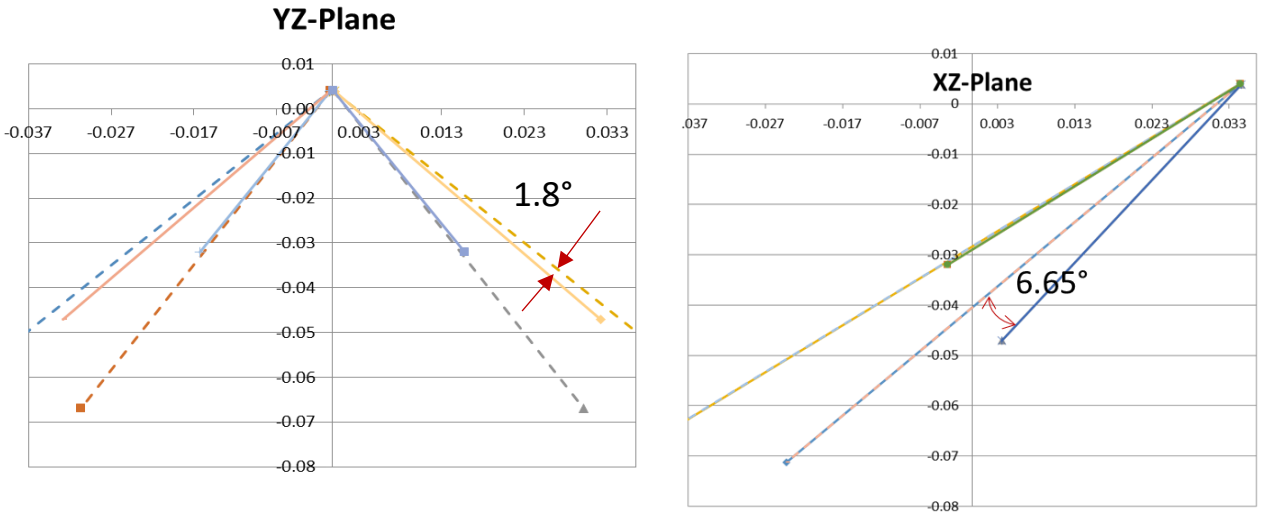

Figure 5.3.13: Modifications for spray pattern Inj-5, from spray pattern Inj-2 and Inj-3 are shown in YZ and XZ plane. Dotted lines are the plumes from Inj-3 and solid lines are from Inj-2. In injector Inj-5, the angles mentioned are the defined modifications. The rest of the plumes are maintained from Inj-2.

In comparison to 6-hole nozzle spray pattern of Injector-C, the Inj-3 has five nozzle holes with 11% larger hole size to deliver the same total injected mass. The frontal spray axis for Inj-3, shown in Figure 5.3.11, is more horizontal. As detailed in Figure 5.3.1, the horizontal spray plume is expected to deliver higher angular momentum in comparison to a spray plume with less horizontal component. In inj-4, the horizontal frontal plume from Inj-3 is added to Inj-2. In Inj-5, the two of the outward plumes from Inj-3 are added to Inj-2 by replacing the two of the side plumes, as shown in Figure 5.3.12. The results of the simulations are discussed in this section.

Figure 5.3.14 shows the tumble ratio comparison for different spray patterns. In comparison to all the spray pattern cases, the 5-hole Inj-3 spray pattern shows the maximum tumble ratio. Even though the injection timings for all the simulations are the same, the most outward direction spray pattern with larger nozzle size, i.e., Inj-3, shows the maximum tumble ratio. This is mainly due to the larger droplet size associated with larger nozzle size and due to higher angular moments generated by the outward directing spray pattern of Inj-3. It should be noted from Figure 5.3.14 that the first tumble ratio peak is mainly due to the intake port, piston speed and CAM timings. The second peak is due to the piston speed and the moments generated by the injector spray pattern.

To understand the spray pattern influences, in this discussion, the focus is given to the second peak in the tumble ratio plot (Figure 5.3.14). Figure 5.3.15 shows the relative comparison of tumble ratio benefits comparing different spray patterns w.r.t. the baseline injector, Injector-C. Inj-3 and Inj-5, with the introduction of the outward spray pattern, benefit the tumble ratio by 87% and 75%, respectively.

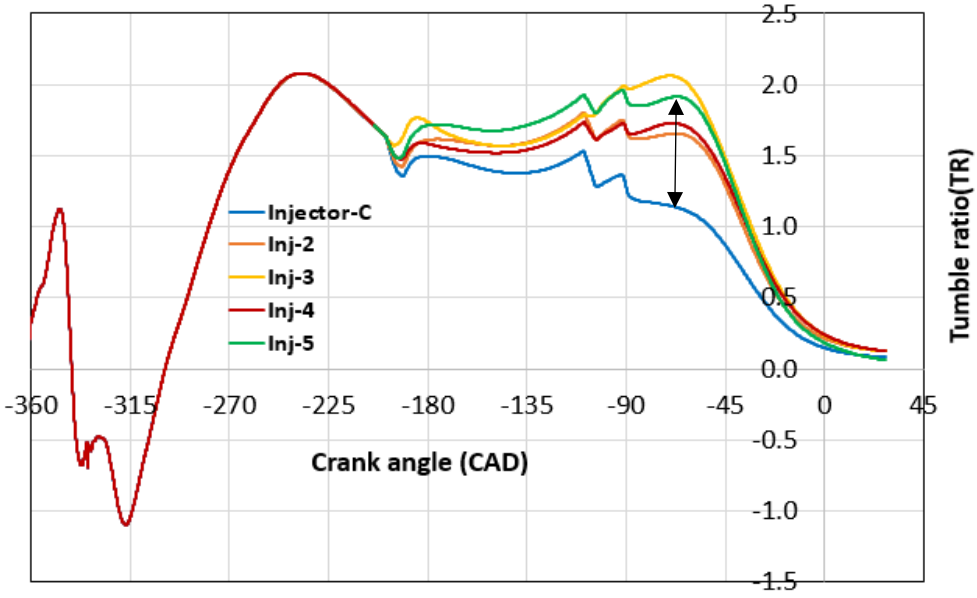

Figure 5.3.14: In-cylinder tumble ratio, comparing different spray patterns taken for the study.

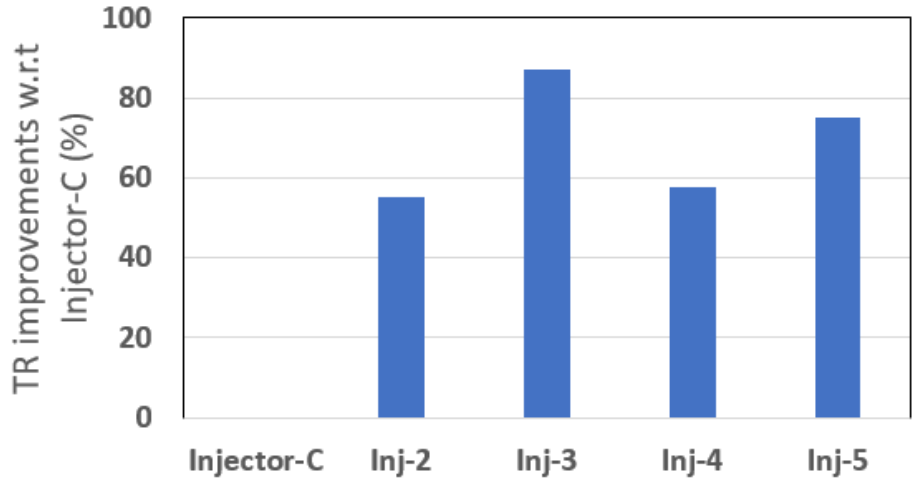

Figure 5.3.15: In-cylinder second peak tumble ratio improvement, comparing different spray patterns w.r.t. the baseline, Injector-C.

Figure 5.3.16 shows the comparison of the generated in-cylinder turbulent kinetic energy (TKE) for the chosen spray patterns. The individual spikes in the TKE evolution coincide with the injection, showing the spray interaction with the charge motion. As noticed in the tumble ratio comparison, a similar trend is noticed with the TKE evolution.

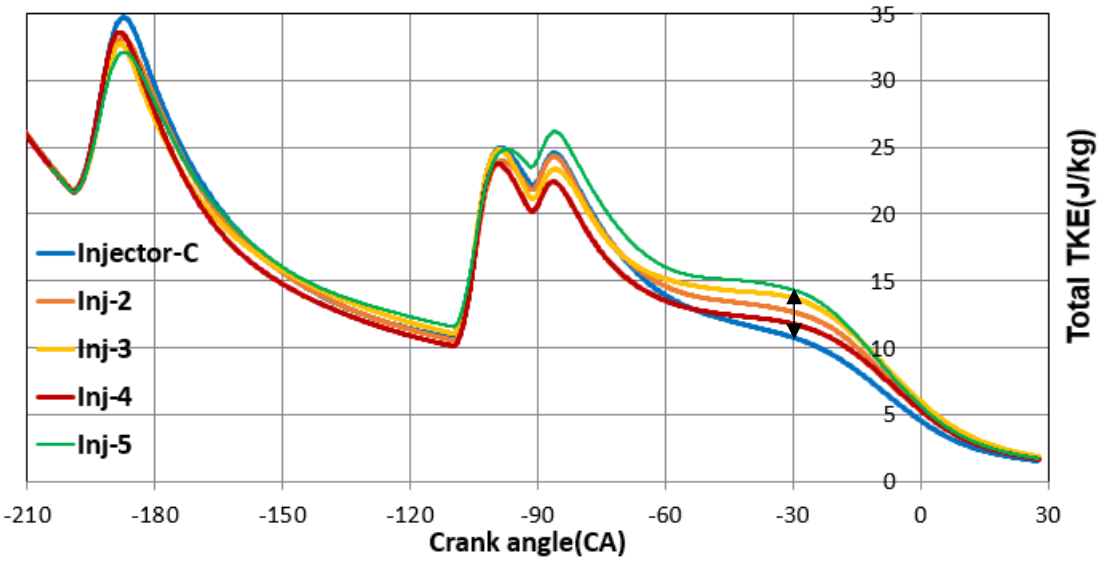

Figure 5.3.16: In-cylinder total TKE, comparing different spray patterns taken for the study.

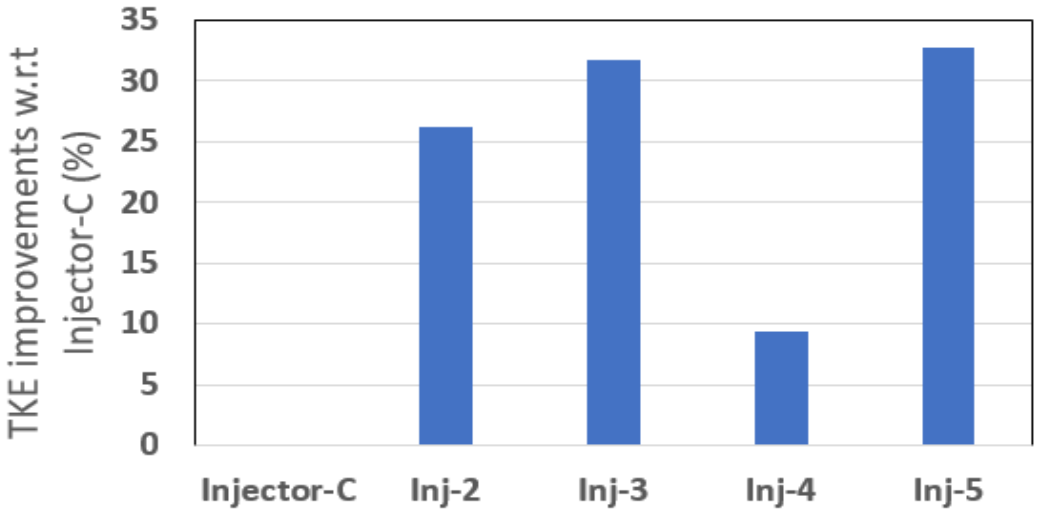

Figure 5.3.17: In-cylinder second peak TKE improvement, comparing different spray patterns w.r.t. the baseline, Injector-C.

Figure 5.3.17 shows relative comparison of the second peak TKE improvement w.r.t. the baseline, Injector-C spray pattern. It is evident that the injector spray patterns in Inj-3 and inj-5 are shown to have 31 to 32% improvement with Injector-C.

Figure 5.3.18 shows the crank angle resolved equivalence ratio development around the spark

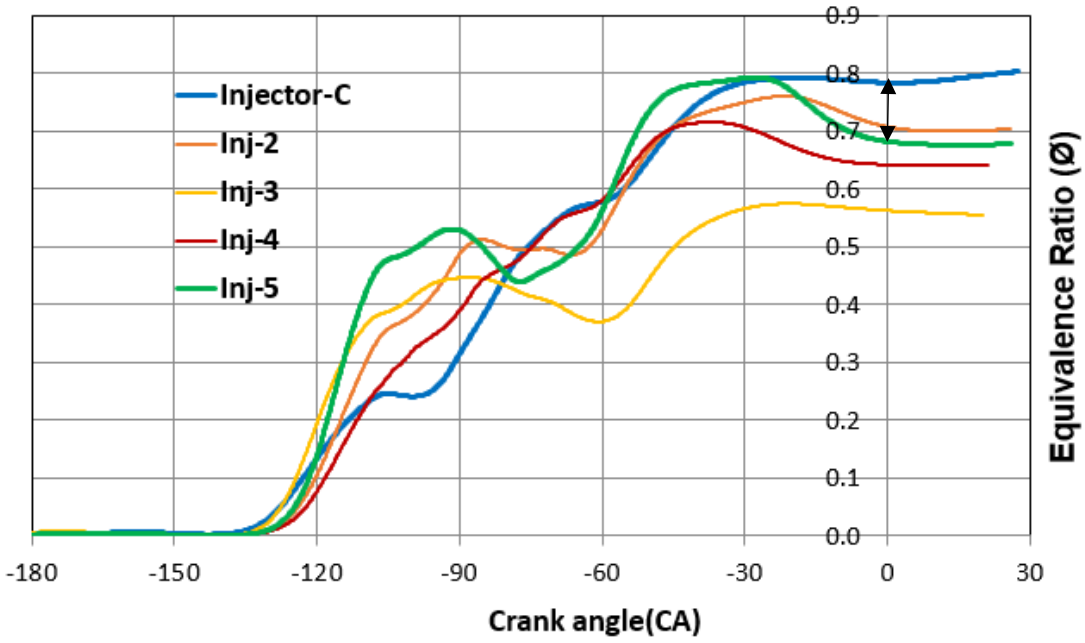

Figure 5.3.18: Monitored local equivalence ratio around the spark plug, comparing different spray patterns taken for the study.

plug (3 mm radius). In this plot, the baseline, Injector-C, shows the best stratification showing a maximum equivalence ratio of 0.8 for the chosen injection timing. Figure 5.3.19 shows the relative comparison of the equivalence ratio near 3 mm radius around the spark plug at the time of compression TDC. In comparison to the baseline, Injector-C spray pattern, all the outward-oriented spray patterns show a lower stratification. However, Inj-2 and Inj-5, spray patterns show 9.5 to 12.7% decrease in equivalence ratio with a benefit of 26 to 32% improvement in turbulent kinetic energy.

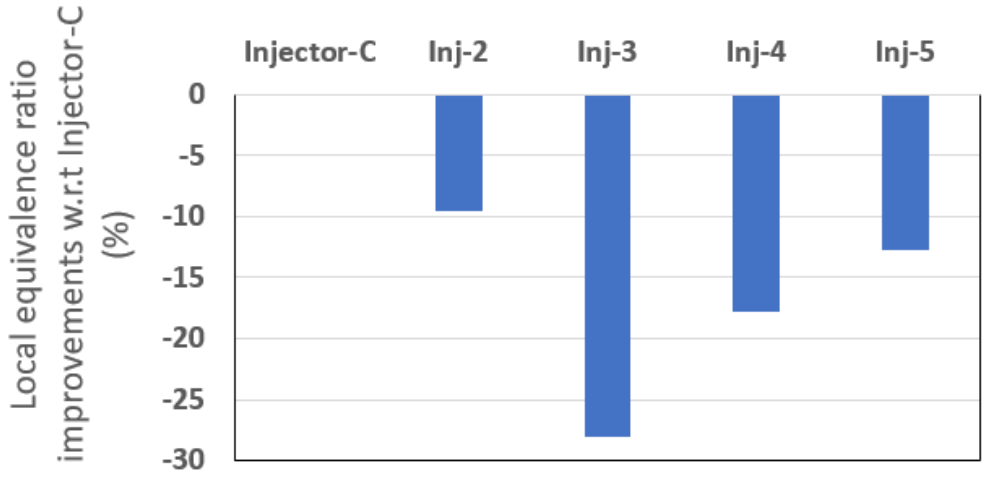

Figure 5.3.19: Monitored local equivalence ratio improvement near TDC, comparing different spray patterns w.r.t. the baseline, Injector-C.

Figure 5.3.20 shows the liquid film mass predicted on the surface of in-cylinder wall due to the wall impingement of the injector spray. In this, the liquid films formed in the walls are categorised as liner and piston. Moreover, the total liquid film formed on all the surfaces, including the liner and piston, are also provided. The liner and piston wetting shows the spray pattern influence due to liquid spray penetration, influenced by spray targeting. Inj-3, spray pattern shows the maximum liquid film due to the larger nozzle size and most outward facing plume.

The most horizontal spray impinges the liner directly and results in higher liner wetting. Similarly, the most vertical spray pattern influences the piston wetting. The liquid film formation also depends on the size of the droplets impinging on the cylinder walls. As the 5-hole spray pattern (Inj-3) has a larger nozzle diameter, it is expected to form a higher liquid film mass. Hence, the developed spray methodology was applied in the in-cylinder simulation to capture the underlying physics qualitatively. It should also be noted that the actual crevices gaps are not fully modelled in the simulation and, hence, scraped fuel in the crevices region between the piston and the liner is inaccurate.

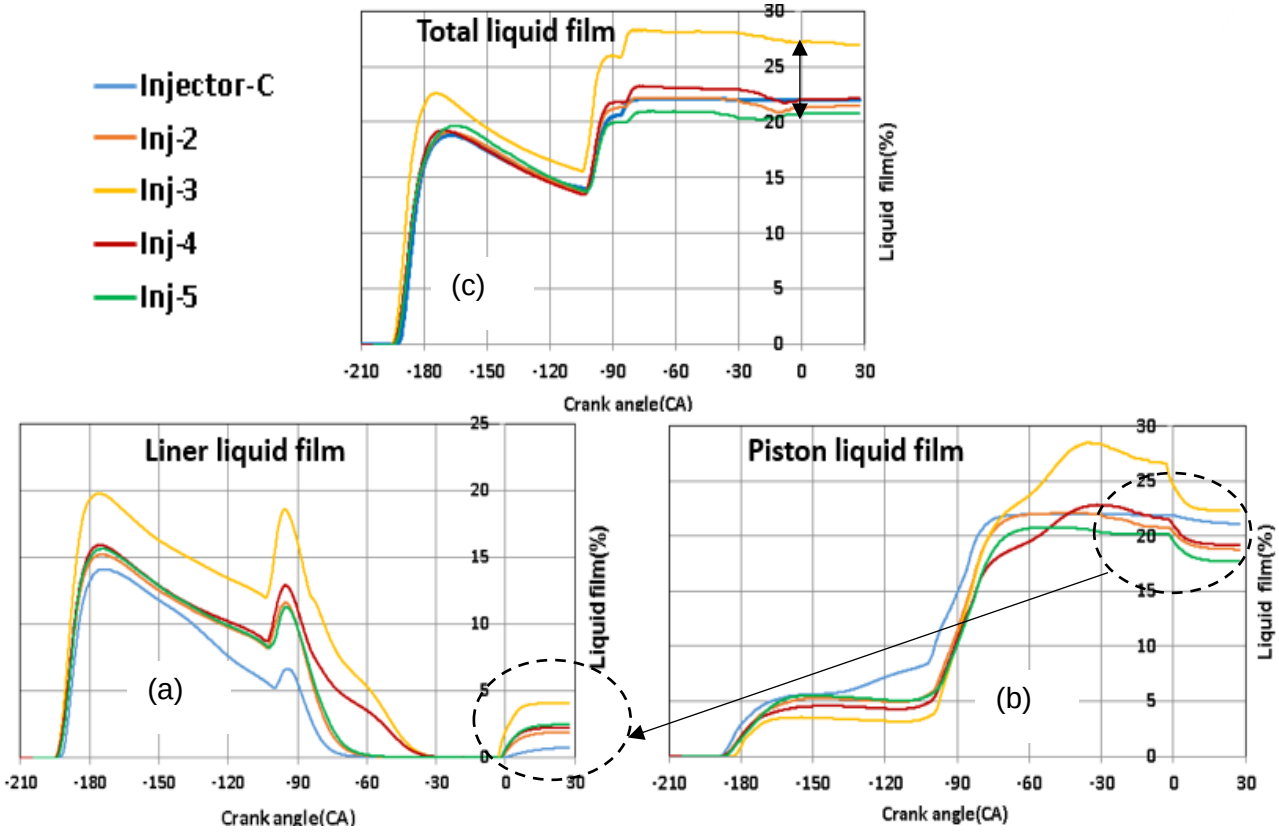

Figure 5.3.20: Crank angle resolved total liquid film on the cylinder walls, comparing different injector spray pattern. The liquid film mass normalised based on the total injected fuel. In this (a), (b) and (c) are the normalised liquid film evolution on liner, piston and total film, respectively. The dotted circle shows the liquid film exchange near the piston and liner crevices region.

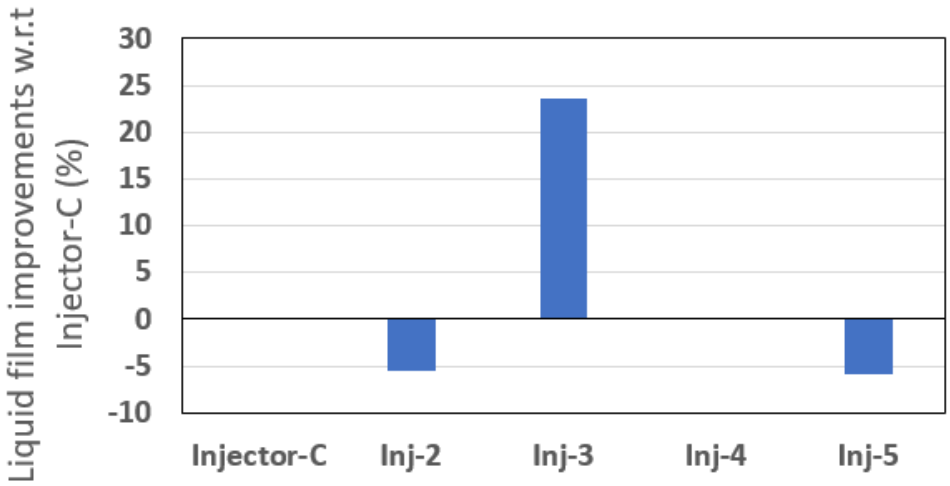

Figure 5.3.21: The total liquid film improvement near TDC, comparing different spray patterns w.r.t. the baseline, Injector-C.

Figure 5.3.21 shows the relative comparison of the total liquid film formed by the wall impingement of the chosen spray patterns. The Inj-2 and Inj-5 spray patterns respectively show 5% relative decrease in the total liquid film in comparison to the baseline spray pattern, Injector-C.

The result of the spray pattern analysis shows that the spray plume axis orientation affects the in-cylinder charge motion significantly. The most horizontal/outward facing spray pattern was found to impart larger angular momentum to the charge motion, but, however, at the expense of liner wetting, as well as obtaining 75 to 87% improvement in tumble ratio and 32% improvement in the TKE. However, with Inj-5, it shows relatively 5% decrease in total liquid film with a sacrifice in fuel stratification. The fuel stratification can be further improved by changing the SOI1 earlier.

5.4 Summary and conclusion

The validated spray model has been applied to investigate wall-guided and air-guided strategy for the catalyst heating simulation. The detailed mechanisms of the piston interaction with the charge motion and the region of liquid film formation were analysed. This helped to identify that an air-guided strategy can help decrease the PN/PM emission by a factor of 19, without the loss of combustion stability criteria of Std NMEP <0.3 bar BMEP. Therefore, the air-guided strategy has been chosen for the catalyst heating operation to meet the emission standards over the WLTC driving cycle.

A detailed study was then carried out to improve the in-cylinder charge motion using the side-mounted multi-hole injector configuration. The study shows that the first injection near BDC helps improve the charge motion with the additional angular momentum gained from the offset of the injector spray axis from the charge motion mass centre. The use of a smaller and delayed third injection is shown to keep the charge motion active with lower liquid film formation near TDC. This helps directing the choice of low Q_{stat} requirements to accommodate the smaller injection quantity with higher injection pressure.

The study of spray plume axis orientation of a side-mounted injector shows that, with the help of the outward facing plume axis, additional angular momentum gain can be achieved. This helps to improve the tumble ratio by 75% along with a TKE improvement of 32% relative to the baseline injector spray pattern, Injector-C. Furthermore, the effect of number of nozzle holes and their hole sizes (5 vs 6-hole injectors) on the spray and mixture formation was investigated.

Chapter 6. Effects of Intake Cam Designs on In-cylinder Charge Motion

6.1 Introduction

Thermal efficiency of an engine (Heywood, 1989, pp.184-186) can be improved by increasing the geometric compression ratio (CR) and further by increasing the ratio of volumetric expansion ratio (r_e) to volumetric compression ratio(r_c). A pressure-volume diagram of a typical over-expanded cycle is illustrated in Figure 6.1. The ratio $r=r_e/r_c$, is increased by either decreasing the effective volumetric compression ratio (r_c) of the engine relative to the volumetric expansion ratio (r_e) or increasing the volumetric expansion ratio (r_e) relative to the volumetric compression ratio (r_c). These are referred to as over-expanded engine cycles ($r_e/r_c > 1$). In a case where a complete expansion happens within the engine cylinder nearly to the exhaust pressure, this is referred to as Atkinson cycle (Figure 6.1, cycle representing 1235*61). The thermal efficiency improvement by decreasing the effective volumetric compression ratio (r_c) is generally referred to as Miller's cycle (Figure 6.1, cycle representing 1234561).

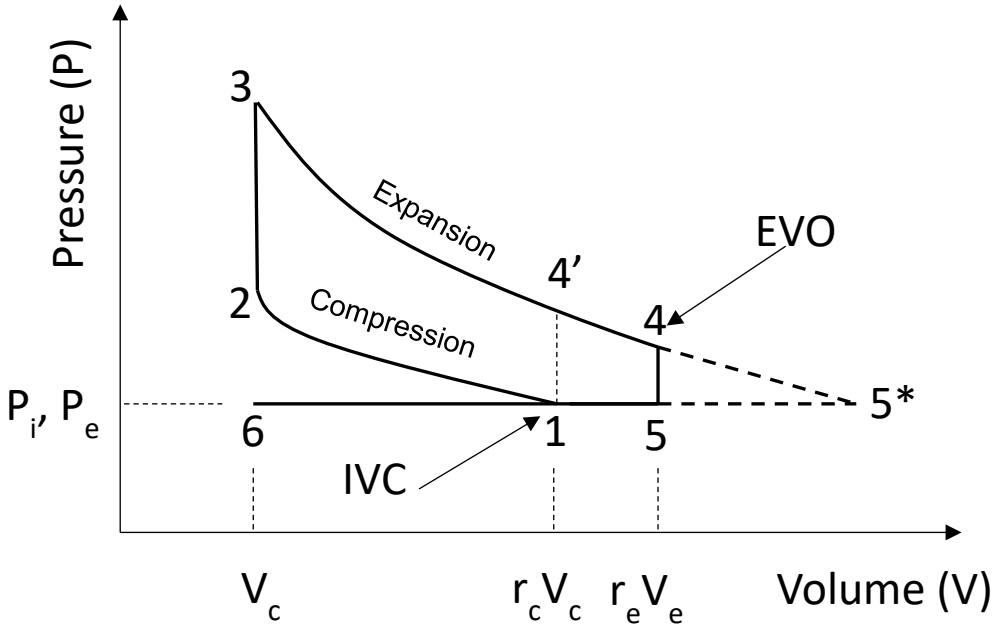

Figure 6.1: Typical pressure vs volume diagram for the over-expanded cycle is depicted. The events, such as intake valve closing (IVC), compression, expansion and exhaust valve opening (EVO), are located. V_c, r_c, r_e, P_i and P_e are the clearance volume, compression ratio, expansion ratio, intake pressure and exhaust pressure, respectively.

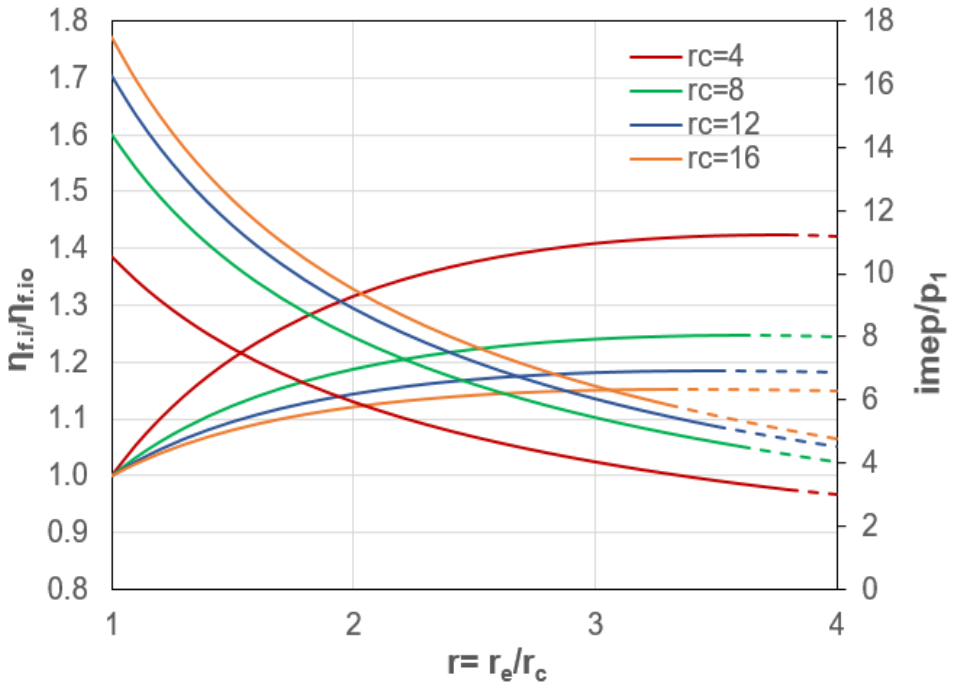

Figure 6.2: Indicated fuel conversion efficiency and mean effective pressure for over expanded engine cycle as a function of r_e/r_c. Efficiencies given relative to $r_e=r_c$ (Otto cycle) value $\eta_{f,\,io}$. γ=1.3, Q*/ (C_v T_1) =9.3 (r_c-1)/r_c. Solid to dashed line transition marks the complete expansion point (Atkinson cycle). Plotted using the thermodynamic equations from Heywood (1989, p. 184).

Typical efficiency benefits calculated for iso-octane fuel from the thermodynamic relations are shown in Figure 6.2. The effective compression ratio can be decreased either by closing the intake valve early or late with respect to the piston bottom dead centre (BDC).

At high loads, higher compression ratio increases the knock tendency. Miller's cycle approach helps decreasing the effective compression ratio and mitigates knock by lowering the charge temperature at the end of compression. Miller's cycle engine uses a short duration intake CAM to close the intake valve much before the piston, bottom dead centre (BDC). This approach is generally referred to as early intake valve closing (EIVC). Alternatively, a long duration intake CAM is used to close the intake valve by delaying the start of compression, late after the piston BDC. This approach is normally referred to as late intake valve closing approach (LIVC). Even though, thermodynamically, there is no difference in the theoretical efficiency calculation, there are some advantages and disadvantages to using LIVC or EIVC approach in a real engine. Several detailed single cylinders engine studies were carried out to understand the thermodynamics of LIVC and EIVC strategies (Li et al., 2015; Osborne et al., 2017).

In EIVC operation, the short duration (120 to 160 CAD) and low lift CAMs (6 mm to 8 mm) are used. During short duration and low lift intake valve operation, the in-cylinder charge motion builds up rapidly, but starts decaying once the valve closes. As the charge motion decreases, the large-scale flow structure weakens, which results in rapid decaying of turbulent kinetic energy. As the flame speed is proportional to the level of TKE during the ignition phase, the burn rates are affected significantly. This demands high tumble intake port for improving the fuel mixing and TKE. In LIVC operation. which generally operated with a longer duration CAM (220 to 260 CAD) and higher valve lifts, this results in higher charge motion, resulting in sustainable high TKE during the ignition phase. This provides faster burn and optimised combustion phasing using the MBT spark timing. A detailed analysis showing the difference between the LIVC and EIVC CAMs is reported in the literature (Luo et al., 2017; Ketterer, Gautier and Keating, 2018). However, the influence of injection on the charge motion and underlying physics from injections were not visualised. As detailed in Chapter 4 and 5, the benefit of multiple injection with a side-mounted injector can be realised to improve the charge motion and help in improving minimum BSFC of the engine.

In this chapter, the simulation results are provided in three sections. In the first two sections, the results of the air flow simulation comparing the LIVC and EIVC strategy for 1500 RPM WOT and 2000 RPM 2 bar BMEP condition, respectively, are given. In the third section, the charge motion enhancements and combustion benefits with multiple injection are presented for the low speed high load condition.

6.2 EIVC and LIVC setups

In this study, the in-cylinder charge motions of the EIVC and LIVC approach are compared for low speed high load (1500 RPM WOT) and medium speed part load (2000 RPM, 2 bar BMEP) operation using 1.5 litre turbocharged GDI engine conditions.

The engine configuration used in the simulation is shown in Table 6.1. The in-cylinder geometry model used for this study is shown in Figure 6.3. It should be noted that, during the different intake valve lift CAM simulations, the inlet boost pressure is adjusted to maintain the same amount of charge mass (measured in O_2) flowing through the intake valves. This is to ensure quantitatively similar engine conditions for comparing two different engine operations (EIVC or LIVC). In both cases, the same exhaust CAM lifts and CAM timings are used.

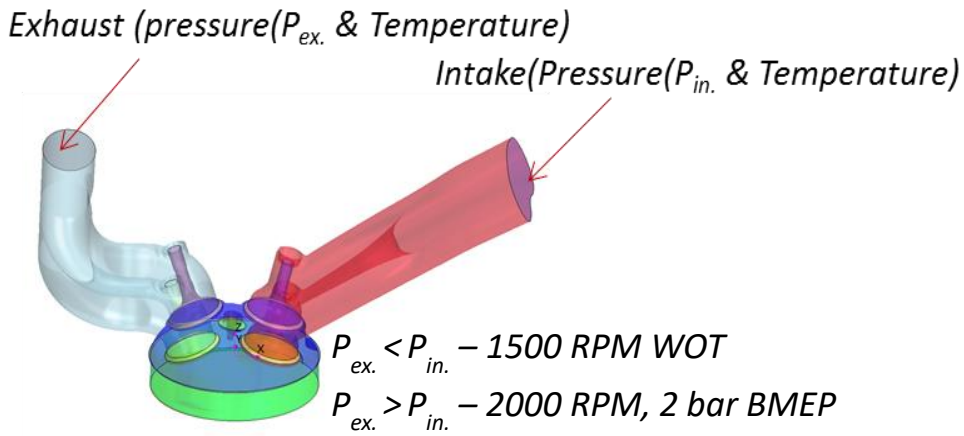

Figure 6.3: In-cylinder model showing the intake and exhaust ports. Reference intake and exhaust pressure conditions are shown. The exhaust manifold is asymmetric relative to the intake ports.

Table 6.1: Engine specification-C.

Engine displacement	1.5 L
Bore (mm)	73.5
Stroke (mm)	88
Geometric compression ratio	12.5
Number of cylinders	4
Injection system	DI
Effective compression ratio calculated at 50 CAD before or after BDC.	11

The different EIVC and LIVC CAM profiles chosen for the study are shown in Figure 6.4 and Figure 6.5, respectively. In both EIVC and LIVC settings, the same exhaust CAM profile is used. The relative valve lift heights can be visualised by referencing the maximum exhaust valve lift (Figure 6.4, thin dotted line). In the EIVC CAMs shown in Figure 6.4, E3 is the shortest of all with 130 CAD duration. Similarly, in the LIVC CAMs, L2 is the longest CAM of 240 CAD duration. In comparison to the EIVC cases, the LIVC CAM are taller (>48%). Events such as maximum piston speed, BDC position and the IVC points are presented in Figure 6.4 and 6.5.

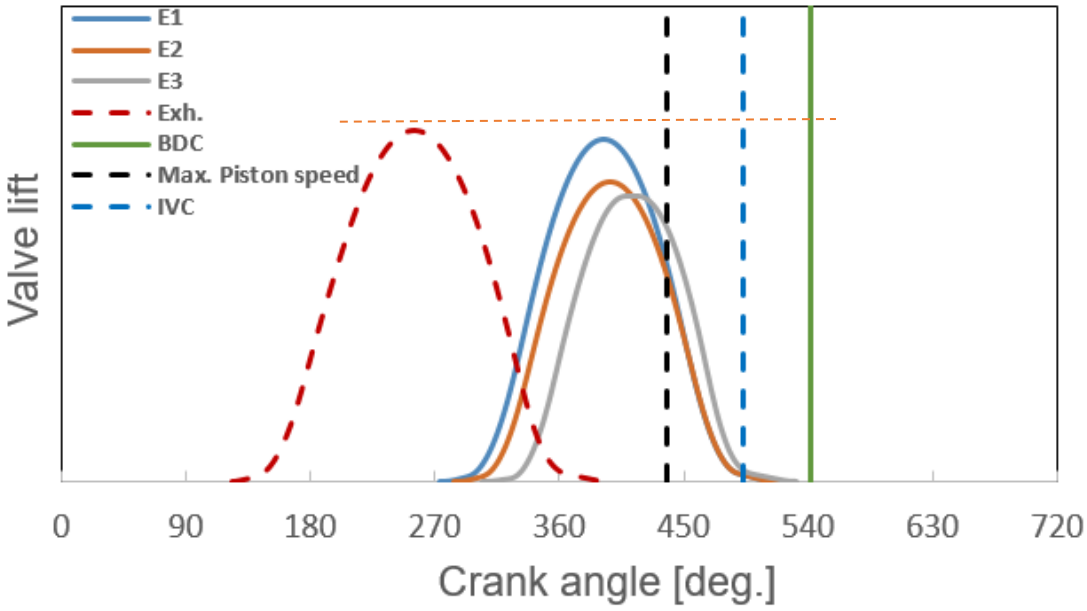

Figure 6.4: EIVC CAMs chosen for the study are shown. E1, E2 and E3 are the intake CAMs and Exh. is the exhaust CAM. The maximum piston speed location, intake valve closing (IVC) position and piston bottom dead centre (BDC) are referenced in 720-degree cycle.

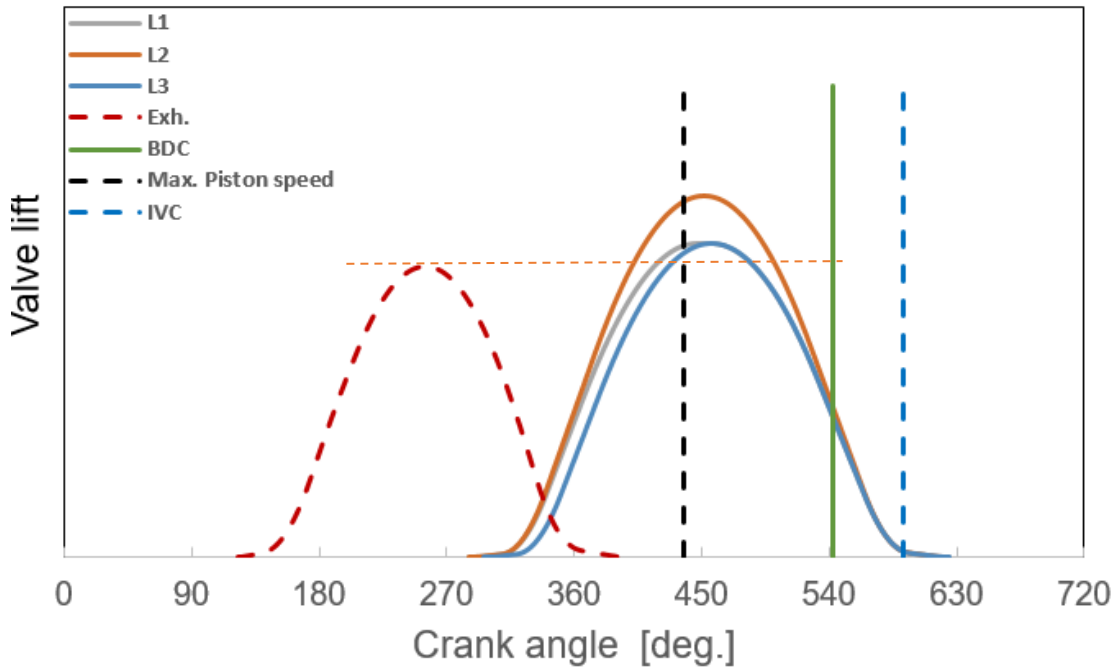

Figure 6.5: LIVC CAMs chosen for the study are shown. L1, L2 and L3 are the intake CAMs and Exh. is the exhaust CAM. The maximum piston speed location, intake valve closing (IVC) position and piston bottom dead centre (BDC) are referenced.

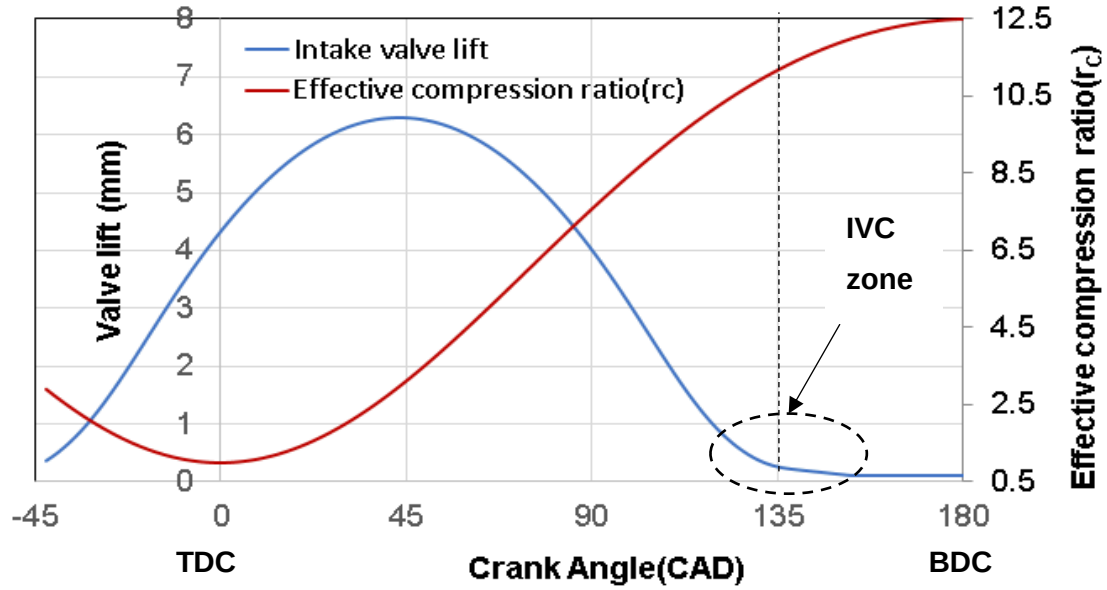

Figure 6.6: Intake valve lift profile and relation to the series of effective compression ratios are shown. TDC and BDC positions are marked below the plot.

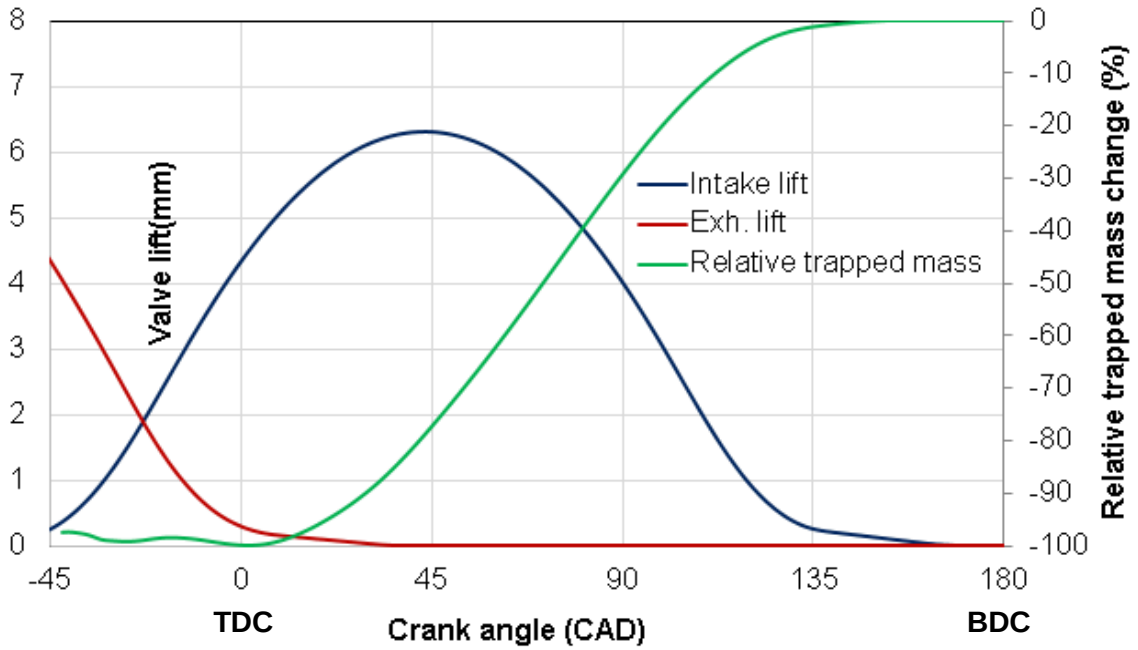

Figure 6.7: Intake lift profile and the relative trapped mass change (%). In this chart, 0% and -100% refer to the relative trapped mass % condition equivalent to 100% filled and empty cylinder trapped mass, respectively.

6.2.1 Intake valve closing lift position definition

As illustrated in Figure 6.1, the intake valve closing point, "1" defines the effective compression ratio "r_c". The value of "r_c" at TDC is equal to "1" and reaches the geometric compression ratio at BDC. The calculated effective compression ratio for the engine parameters from Table 6.1 is shown in Figure 6.6. In this case, the typical EIVC CAM is overlaid showing the intake valve closing zone.

In the CFD simulation, intake port, exhaust port and the cylinder volume are considered as different regions. During the intake or the exhaust valve closing event, the regions are disconnected accordingly (intake or exhaust or both disconnected from the cylinder region) with a closing cell thickness corresponding to the minimum valve lift specification. In the thermodynamic consideration, this closing lift signifies the start of effective compression ratio. An initial simulation was performed to understand the effective mass exchange during the valve closing event. A very fine time step equivalent of 0.05 CAD (3.703µs) at 2250 RPM, 14 bar BMEP condition (1.66 bar, boost pressure) was chosen to study the charge mass filling the cylinder during the intake stroke. The result of the simulation is shown in Figure 6.7. The charge mass filling the cylinder is normalised by the percentage with respect to the in-cylinder charge mass near BDC.

In this case, the TDC charge mass is subtracted from the BDC charge mass to show net incremental change in charge mass %. The relative trapped mass change (%) equivalent to zero indicates the cylinder is 100% filled. Similarly, -100% indicates the cylinder is relatively empty. Figure 6.8 shows the detailed charge mass change during the intake valve closing zone (110 CAD to 180 CAD). It is evident, that a relative trapped mass change of 6% is noticed from 1 mm valve lift to 0.1 mm valve lift. This shows the significance of the closing lift specification. It can be noticed that, at an intake valve lift of 0.2 to 0.15 mm valve lift, there is less than 1% change in charge mass and this is taken as a criterion for the closing lift position specification. However, the CAM designer normally refers to the CAM duration equivalent to the crank angle separation equivalent to 1 mm valve lift. In this chapter, all the CAM duration references are w.r.t. the 1 mm lift and in the CFD simulation the closing lift point is at 0.15 mm lift.

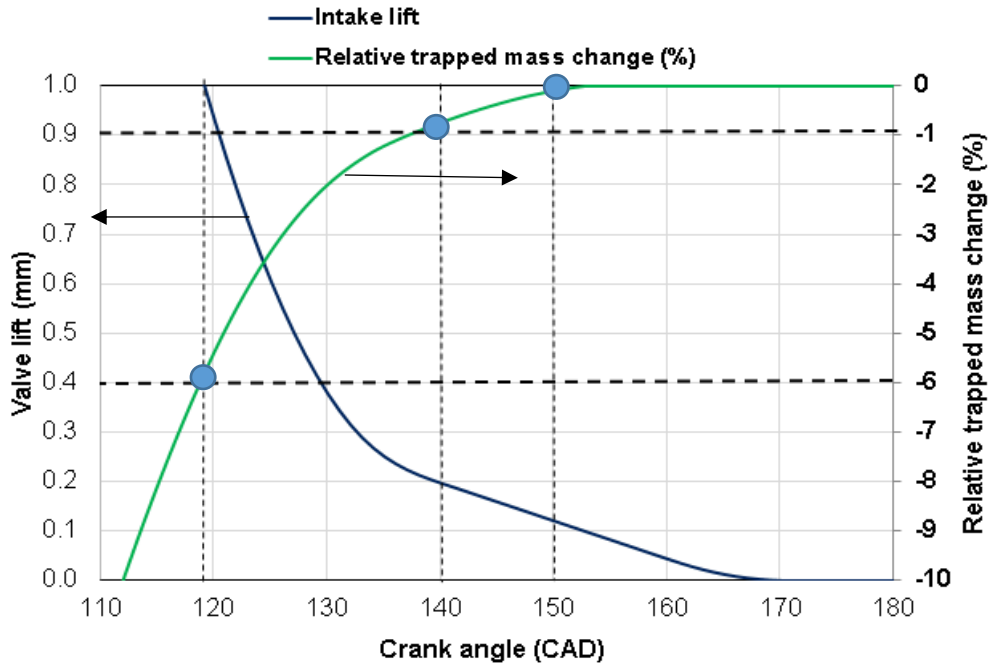

Figure 6.8: Intake lift profile and the relative trapped mass change (%). In this chart, 0% and -10% refer to the relative trapped mass % condition equivalent to 100% filled and 90% filled cylinder trapped mass, respectively. The trapped mass change % at 1 mm, 0.2 mm and 0.1 mm, respectively, are marked in this plot.

6.2.2Charge motion study at low speed high load condition: 1500 RPM, WOT

E3 CAM is the shortest duration and its maximum lift position (MOP) for this case is much closer to the maximum piston speed crank angle location (Figure 6.4). Similarly, L3 CAM is the shortest LIVC CAM with 230 CAD, showing MOP closer to the maximum piston speed crank angle location (Figure 6.5). Flow fields in the cylinder for EIVC CAMs are compared with LIVC CAM, L3. The instantaneous sectional flow field for E1, E2, E3 and L3 CAMs at 272, 178, 138 and 20 CAD before compression TDC are shown in Figure 6.9, 6.10, 6.11 and 6.12, respectively. In the initial charge motion build-up phase (Figure 6.6), both EIVC and LIVC CAMs show similar flow structure. As the intake valve closes much before BDC for EIVC CAMs, the charge motion starts to decay (Figure 6.9). In Figure 6.10, the LIVC CAM, L3, shows the clean air pushed back into the intake port, as the intake valves remains open after BDC, whereby the piston starts to move up. In a case with fuel injection, the clean air leaving the intake port during the charge push back will carry the fuel mixture into the port. Based on the length of the intake runner, the fuel either mixes into the manifold or redistributes into the other cylinders. Figure 6.12 shows the charge motion comparison of EIVC CAMs with LIVC CAMs at 20 CAD BTDC. It is evident that the LIVC CAM shows much stronger charge motion in comparison to the other EIVC CAMs, which is favourable for combustion.

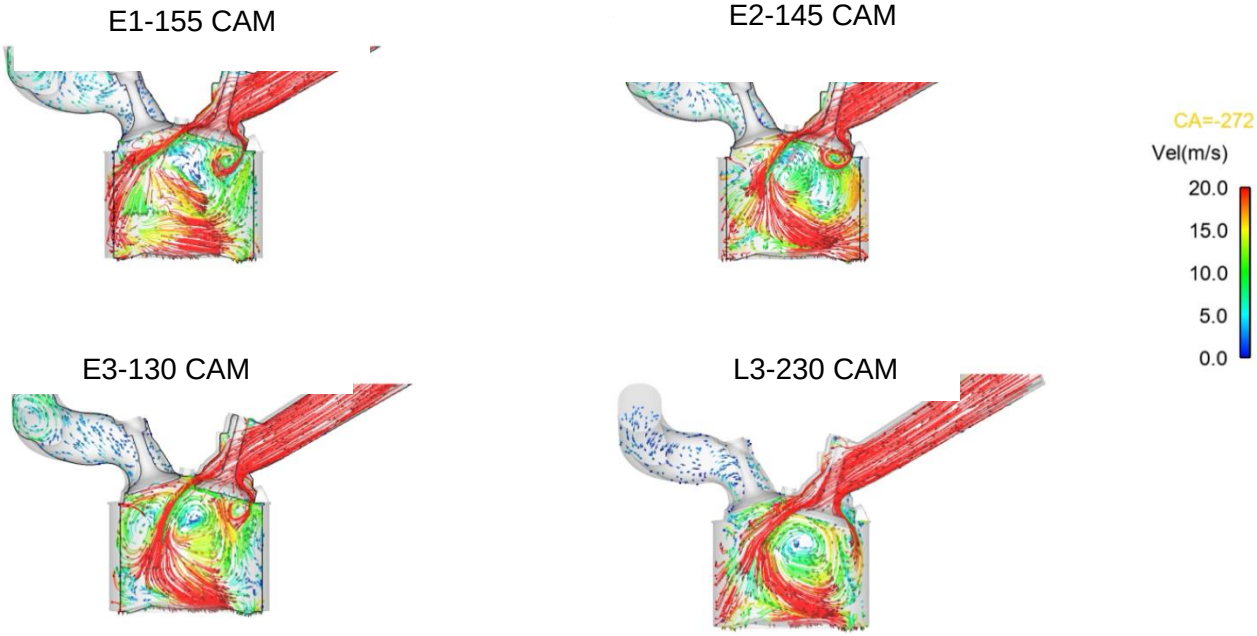

Figure 6.9: Comparison of the charge motion at 272 CAD before fire TDC@1500RPM WOT condition. The path-lines are coloured by velocity magnitude. E1, E2 and E3 are the simulation with EIVC CAMs and L3 is the simulation with LIVC CAM.

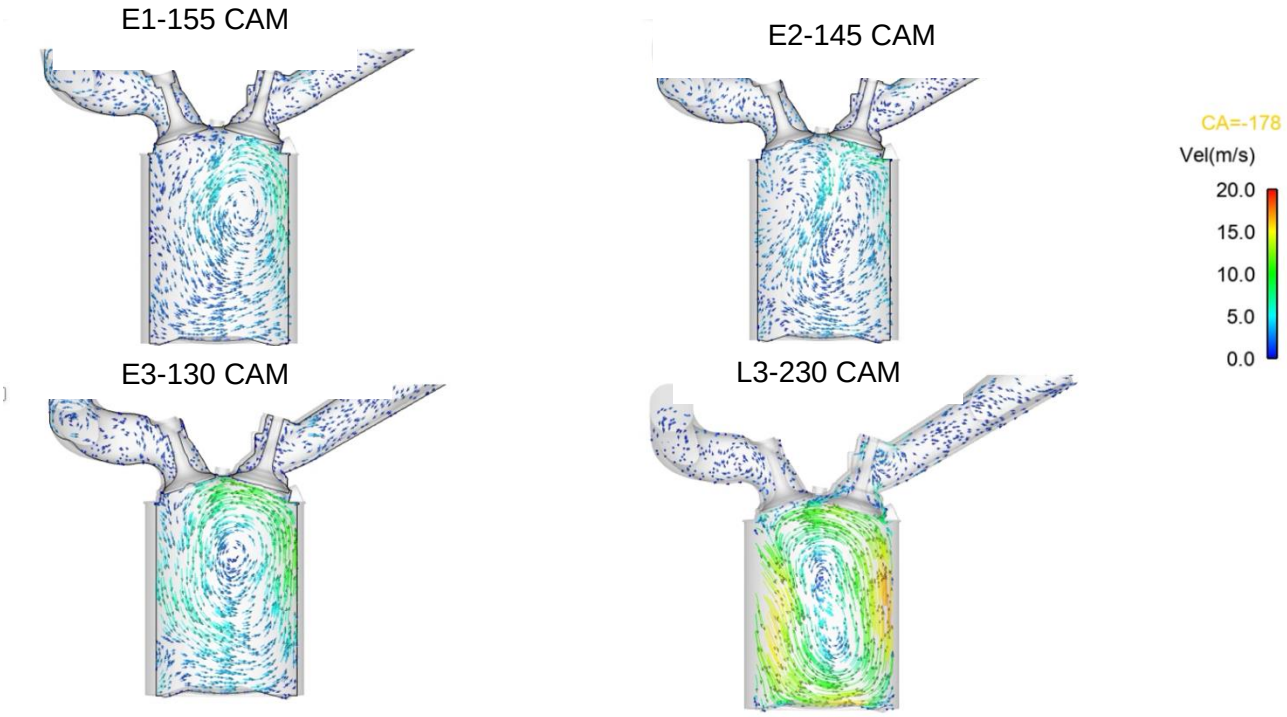

Figure 6.10: Comparison of the charge motion at 178 CAD before fire TDC@1500RPM WOT condition. The path-lines are coloured by velocity magnitude. E1, E2 and E3 are the simulation with EIVC CAMs and L3 is the simulation with LIVC CAM.

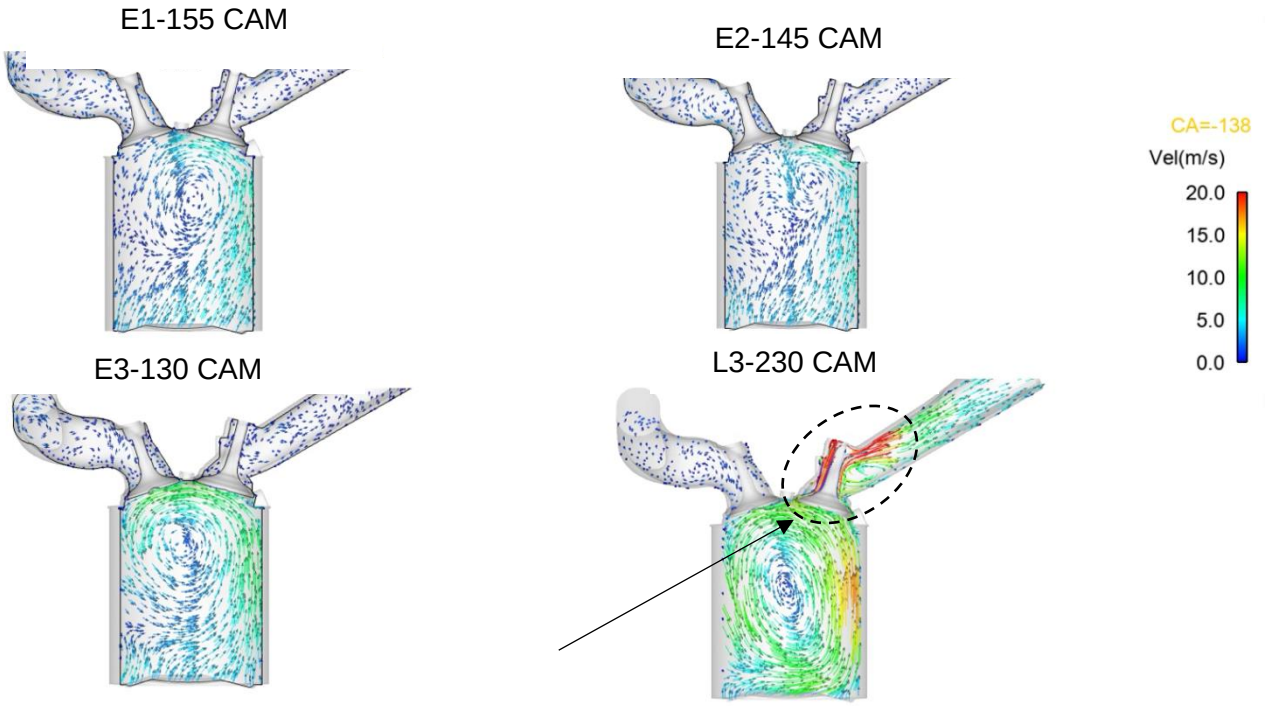

Figure 6.11: Comparison of the charge motion at 138 CAD before fire TDC@1500RPM WOT condition. The path-lines are coloured by velocity magnitude. E1, E2 and E3 are the simulation with EIVC CAMs and L3 is the simulation with LIVC CAM.

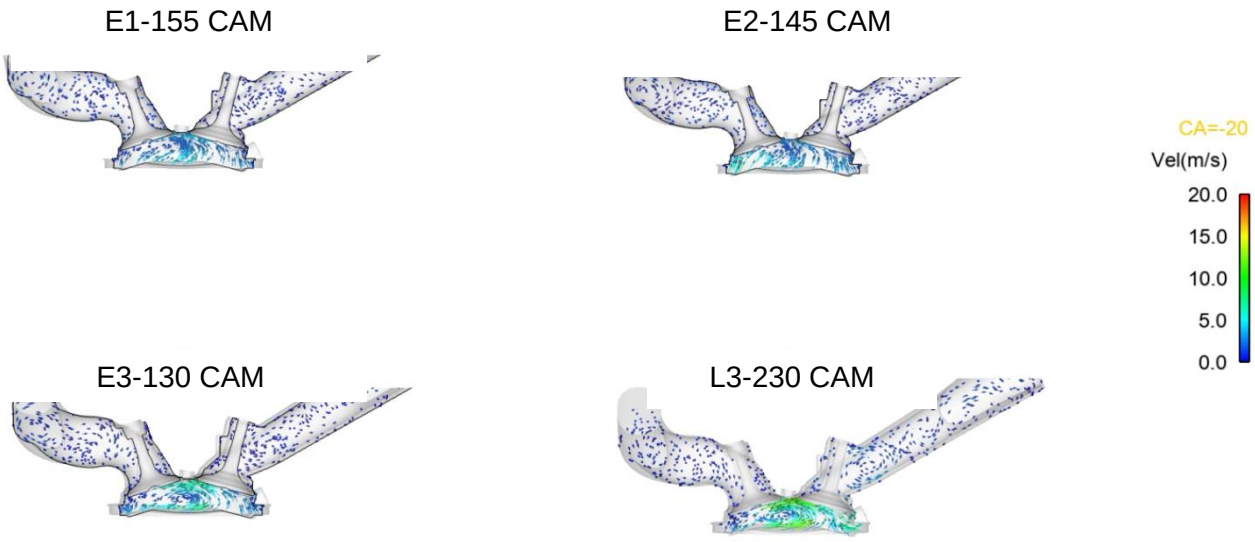

Figure 6.12: comparison of the charge motion at 20 CAD before fire TDC@1500 RPM WOT condition. The path-lines are coloured by velocity magnitude. E1, E2 and E3 are the simulation with EIVC CAMs and L3 is the simulation with LIVC CAM.

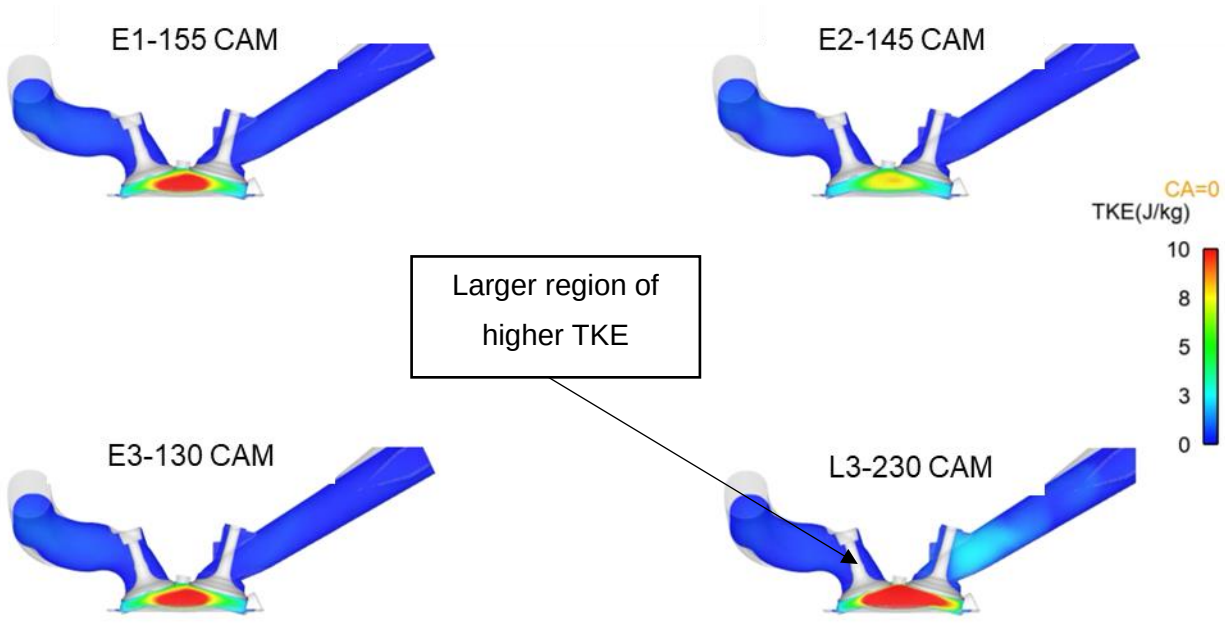

Figure 6.13: Comparison of turbulent kinetic energy distribution at a section through intake and exhaust valve of the cylinder. E1, E2 and E3 are the simulation with EIVC CAMs and L3 is the simulation with LIVC CAM.

The resultant in-cylinder TKE distribution near the compression TDC, comparing EIVC CAMs with the L3 is shown in Figure 6.13. It is evident from the distribution that LIVC CAM, L3, shows relatively larger region of higher TKE in comparison to EIVC CAMs.

Crank angle resolved in-cylinder tumble ratios, during the intake and compression stroke, are shown in Figure 6.14. In comparison to the EIVC CAMs (E1 and E2), E3 shows maximum tumble ratio. As shown in Figure 6.4, for the same intake valve closing position, the shortest duration was E3 CAM, with MOP aligned closer to the maximum piston speed. The maximum piston speed is related to the rate of cylinder volume displacement. The higher the piston speed, the faster the volume displacement, and, hence, the volume rate of intake flow. If the manifold charge mass (reference density) is accessible through the intake valve with less resistance during this period, a maximum charge mass can enter. The restriction through the valve is related to the valve lifts. The higher the valve lift, the lower the resistance for the same charge mass entry. Thus, the combination of higher valve lift and alignment of maximum piston speed for E3 CAM increases the initial charge motion for the short duration CAMs. Hence, tumble ratio first peak for E3 CAM shows to be higher in comparison to CAMs, E1 and E2. However, in comparing the tumble ratio of the EIVC CAMs with LIVC CAMs, the tumble ratios

of EIVC CAMs are 40 to 50% lower. This is mainly due to higher restrictions in valve curtains with the low lift CAMs relative to the high lift, LIVC CAMs (i.e., the chosen LIVC CAMs have 48% higher valve lift in comparison to the EIVC CAMs).

Figure 6.15 shows the crank angle resolved total TKE generated in the cylinder comparing both LIVC and EIVC CAMs. The EIVC CAMs initially generate higher TKE than LIVC CAMs due to high shear/strain (mean strain rate tensor, $S_{ij} = \frac{1}{2}\left(\frac{\partial \widetilde{u_i}}{\partial x_j} + \frac{\partial \widetilde{u_j}}{\partial x_i}\right)$) for the same trapped mass in a much shorter duration. However, with a lower kinetic energy associated from higher loss through the low lift valve curtain, the TKE is not maintained, hence, it decays faster. In

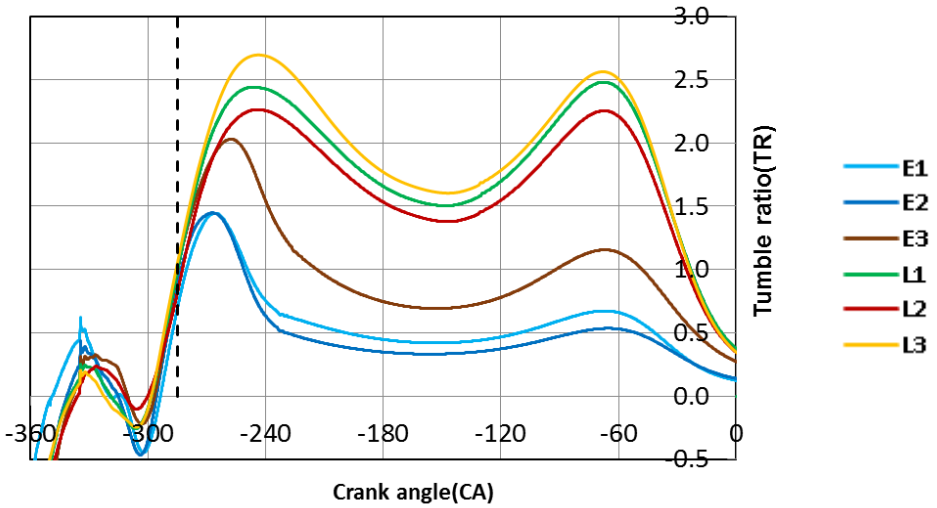

Figure 6.14: Comparison of transient tumble ratio during the intake stroke to the end of compression stroke for 1500 RPM WOT condition. E1, E2 and E3 are the EIVC CAMs. Similarly, L1, L2 and L3 are the LIVC CAMs.

the case of LIVC CAMs, even though the piston decelerates near the BDC, the intake valve is kept open till the early part of the compression stroke. During this period, a continuous stream of charge exchange through the valve replenishes the dissipated TKE and results in high TKE restoration. Hence, LIVC CAMs show higher (> 60%) TKE in comparison to EIVC CAMs near TDC (Figure 6.13).

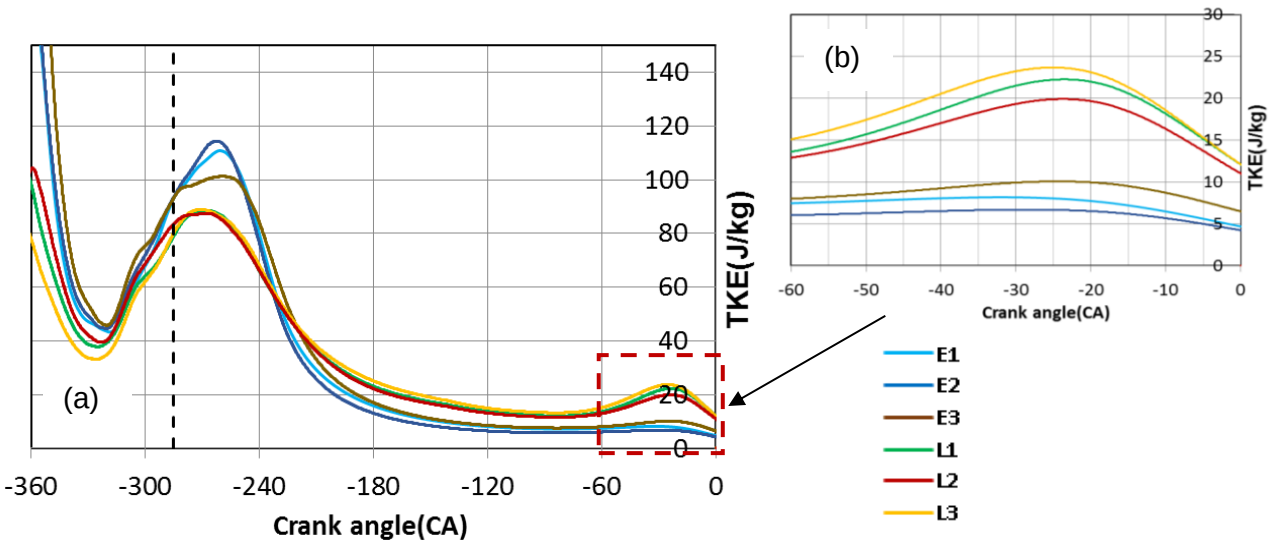

Figure 6.15: (a) Comparison of transient TKE evolution during the intake to the end of compression stroke for 1500 RPM WOT condition. (b) Shows the TKE from near 60 CAD BTDC to TDC. E1, E2 and E3 are the EIVC CAMs. Similarly, L1, L2 and L3 are the LIVC CAMs.

A comparison of TDC TKE of all the CAMs relative to L3 is shown in Figure 6.16. In all cases, the LIVC CAMs show higher TKE near the TDC reflecting higher burn rate. Figure 6.17 shows the RGF % noticed near TDC comparing the LIVC and EIVC CAMs. The EIVC CAMs show negligible RGFs in comparison to the LIVC CAMs. In general, the RGFs are considered to

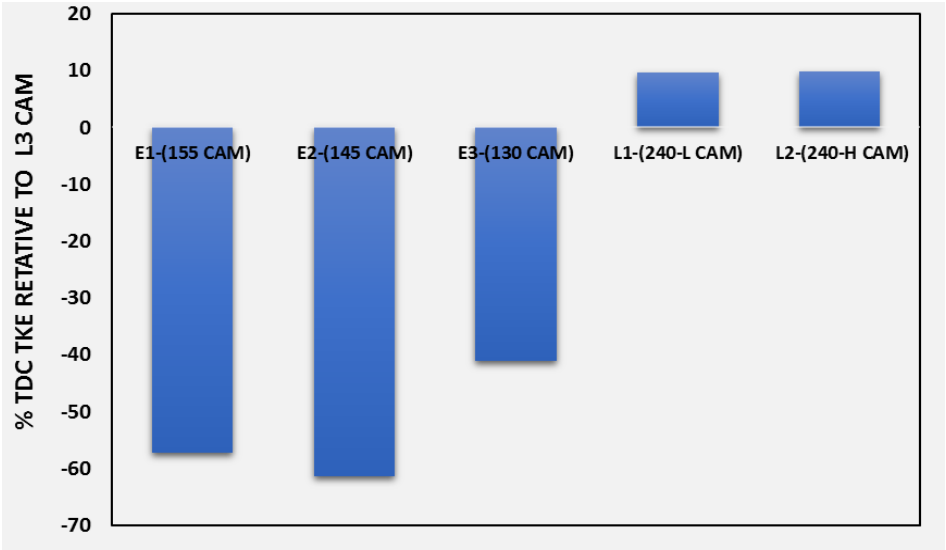

Figure 6.16: Comparison of TKE at the end of compression TDC. In this, L and H are added to differentiate L1 and L2 as low lift and high lift LIVC CAMs.

increase the charge temperature and reactivity of the charge. Under certain conditions, it increases the cycle-to-cycle variation and increases the knock tendency (Westin et al., 2000). In this simulation, as the exhaust air flow was fixed for all the conditions, the short duration CAMs require higher boost pressure in comparison to the LIVC CAMs. This results in larger clean air scavenging through the exhaust valves. Intake and exhaust valve overlap is shown in Figure 6.3 and 6.4. Higher amount of scavenging results in lower level of RGFs for the EIVC CAMs. This demands more EGR to suppress knocking.

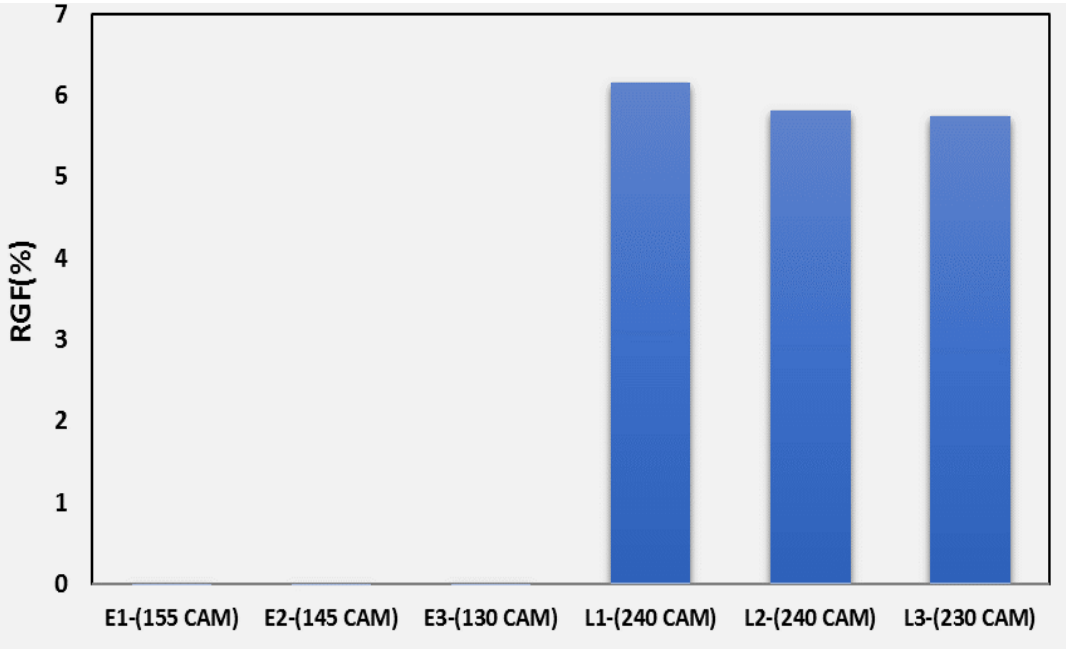

Figure 6.17: Comparison of end residual gas fraction (RGF %) at the end of compression TDC.

6.2.3 Charge motion study at low speed medium load condition: 2000 RPM, 2 bar BMEP

Simulation results for 2000 RPM, 2 bar BMEP conditions are summarised in this section. As detailed earlier, in low speed low load cases, the exhaust pressure is normally higher than the intake pressure. This results in exhaust gas re-entering the cylinder and the intake port. Once the flow builds up, a regular charge motion develops in the cylinder, as shown from Figure 6.18 to Figure 6.20. Figure 6.20 shows the charge motion comparison of EIVC CAMs with L3, LIVC CAM at 10 CAD before TDC. As observed earlier, the LIVC CAM, L3 shows a higher charge motion near the compression TDC.

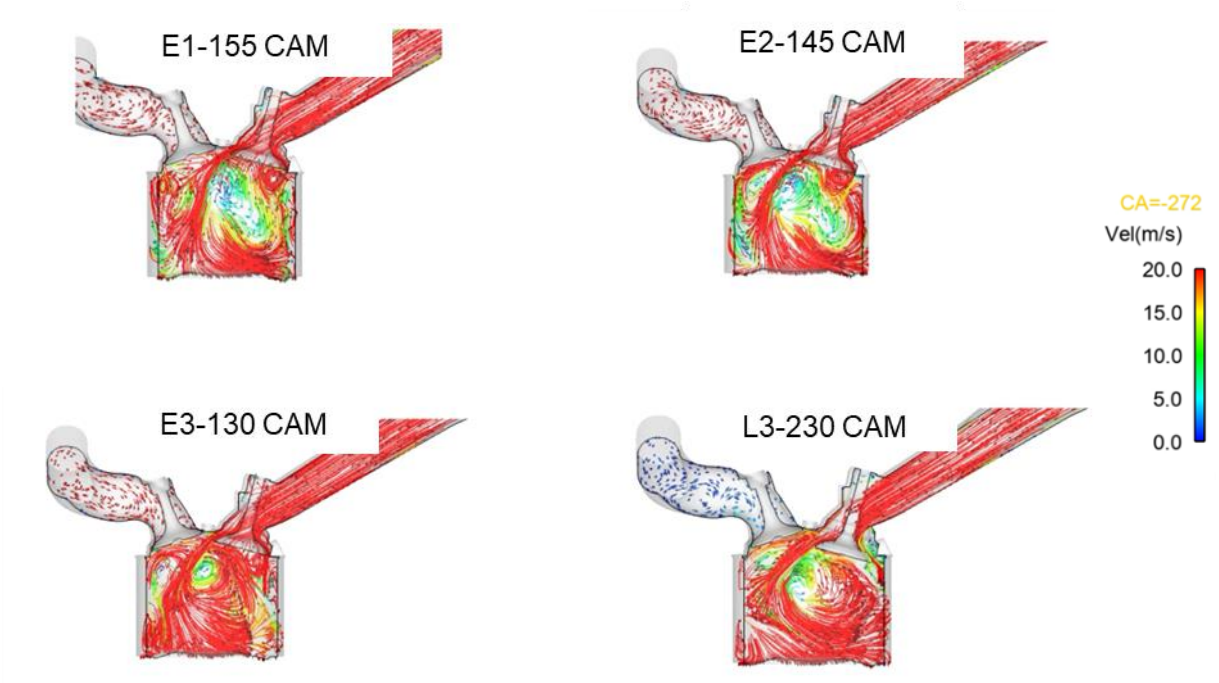

Figure 6.18: Comparison of the charge motion at 272 CAD BTDC for 2000 RPM 2 bar BMEP condition. The path-lines are coloured by velocity magnitude. E1, E2 and E3 are the simulation with EIVC CAMs and L3 is the simulation with LIVC CAM.

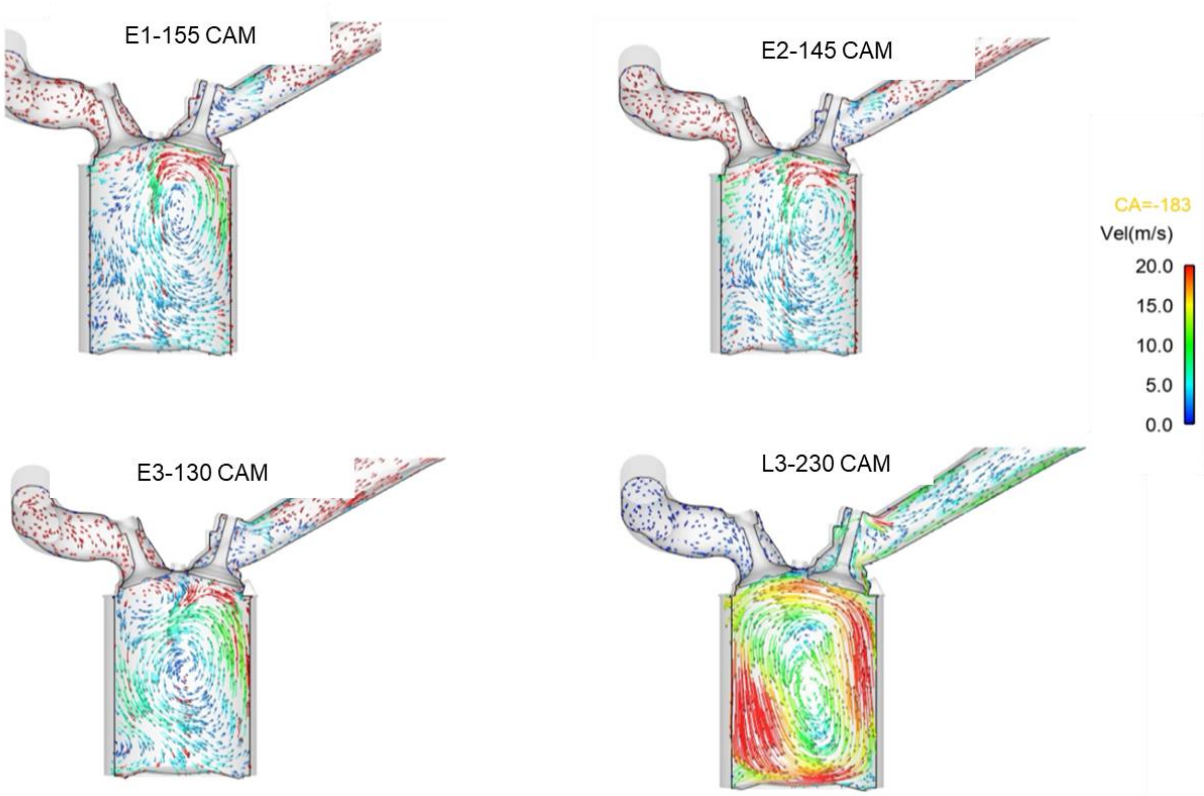

Figure 6.19: Comparison of the charge motion at 183 CAD BTDC for 2000RPM 2 Bar BMEP condition. The path-lines are coloured by velocity magnitude. E1, E2, E3 are the simulation with EIVC CAM's and L3 is the simulation with LIVC CAM.

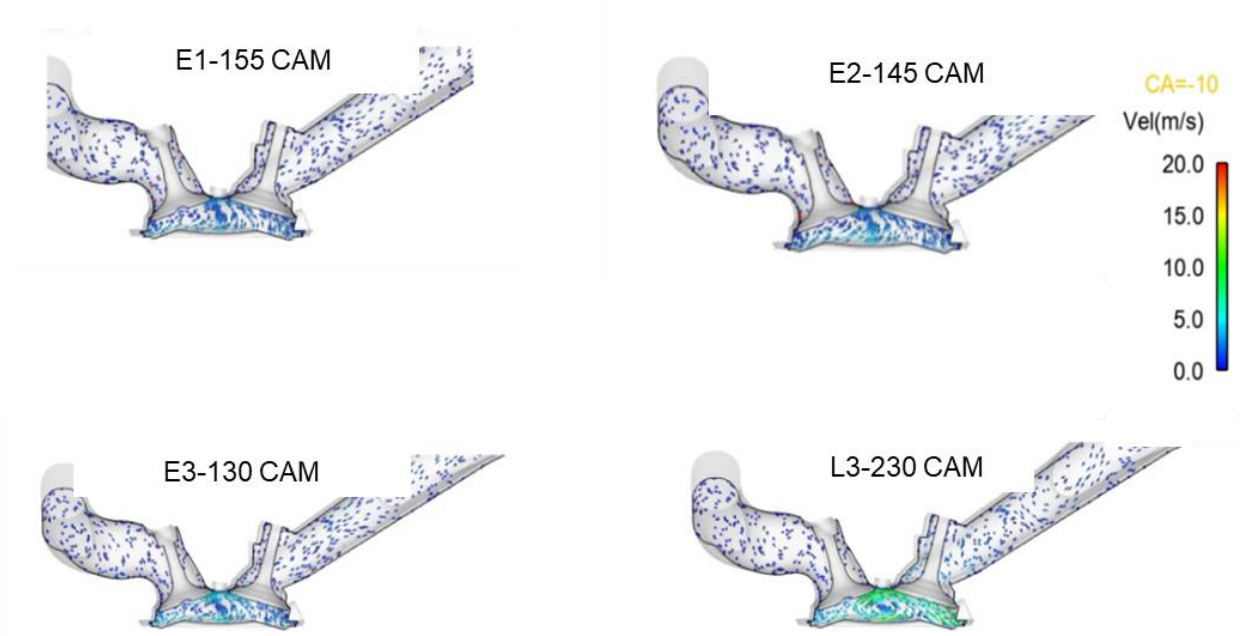

Figure 6.20: Comparison of the charge motion at 10 CAD BTDC for 2000 RPM, 2 bar BMEP condition. The path-lines are coloured by velocity magnitude. E1, E2 and E3 are the simulation with EIVC CAMs and L3 is the simulation with LIVC CAM.

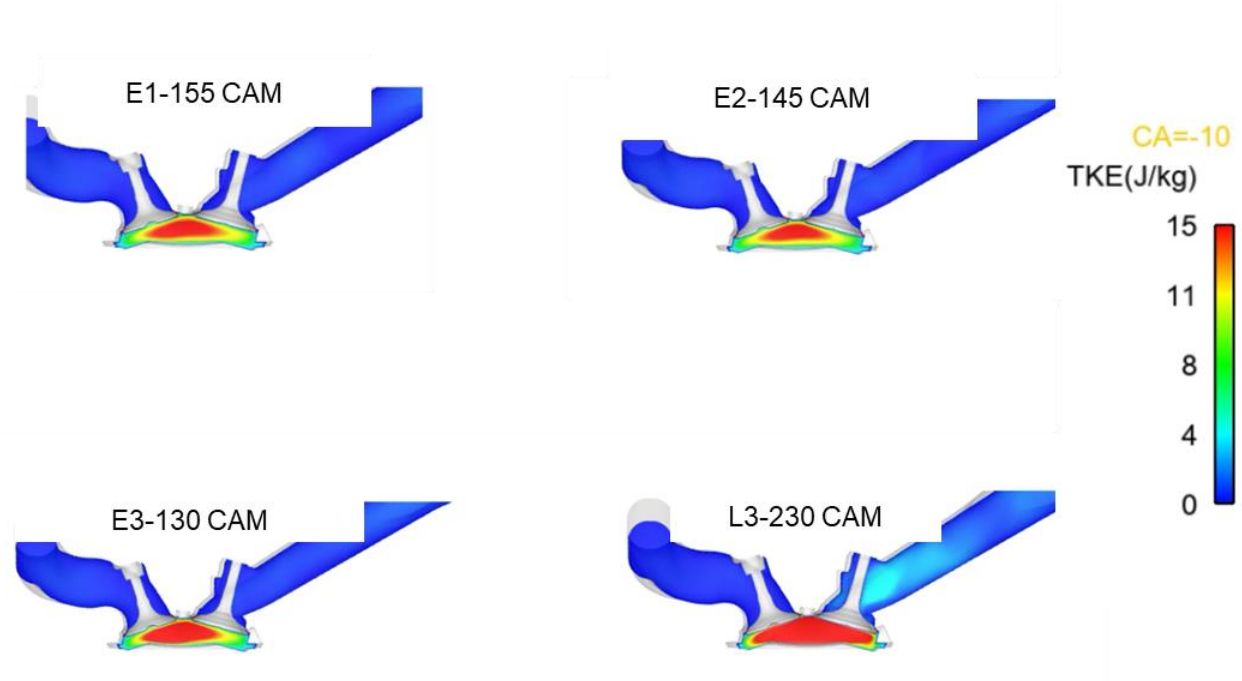

Figure 6.21: Comparison of turbulent kinetic energy distribution at a section passing through intake and exhaust valve of the cylinder.

TKE distribution of EIVC and LIVC CAMs near the compression TDC (10 CAD BTDC) are shown in Figure 6.21. As observed earlier, for the low speed high load case, LIVC, L3 CAM, shows relatively higher region of high TKE.

Figure 6.22 compares the crank angle resolved tumble ratios for EIVC and LIVC CAMs during the intake and compression strokes. All LIVC CAMs show a delay in the tumble development near the peak piston speed. This is mainly due to the ramming effect of the charge on the piston, resulting in increase in charge pressure and temperature. However, this is not noticed in the EIVC CAMs. A similar observation of higher tumble ratio was noticed for LIVC CAMs in comparison to EIVC CAMs. Figure 6.23 shows the crank angle-resolved in-cylinder turbulent kinetic energy during the intake and compression stroke comparing the LIVC and EIVC CAMs. It can be seen that there is no significant change in the TDC TKE for all three EIVC CAMs. The relative (normalised with L3) comparison of the net TKE near TDC is shown in Figure 6.24. E1 CAM shows 60% lower TKE than L3 CAM. In the 2000 RPM, 2 bar BMEP condition, a higher level of RGFs is noticed for both EIVC and LIVC operation (Figure 6.25). However, both E3 and L3 show similar level of RGFs (25%). This significantly increases the charge gas temperatures and increases knock tendency.

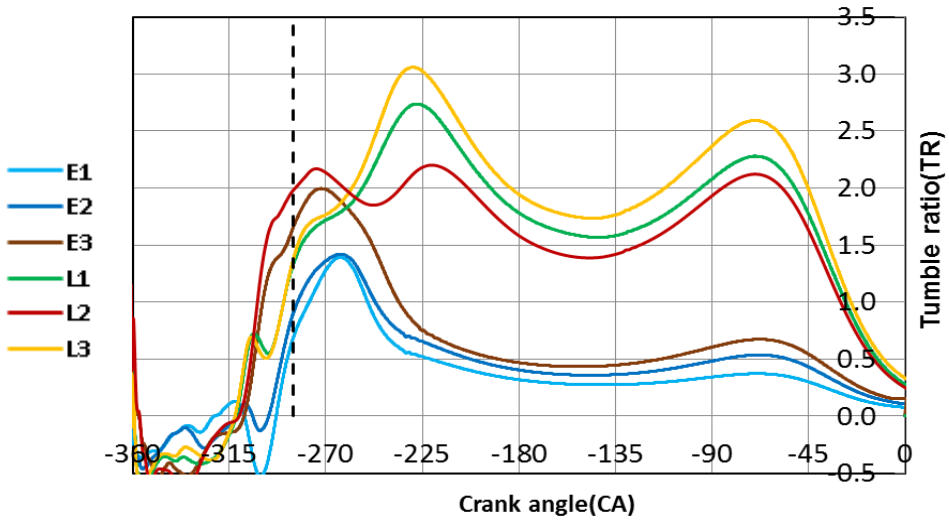

Figure 6.22: Comparison of transient tumble ratio during the intake stroke to the end of compression stroke for 2000 RPM 2 bar BMEP condition. E1, E2 and E3 are the EIVC CAMs. L1, L2 and L3 are the LIVC CAMs.

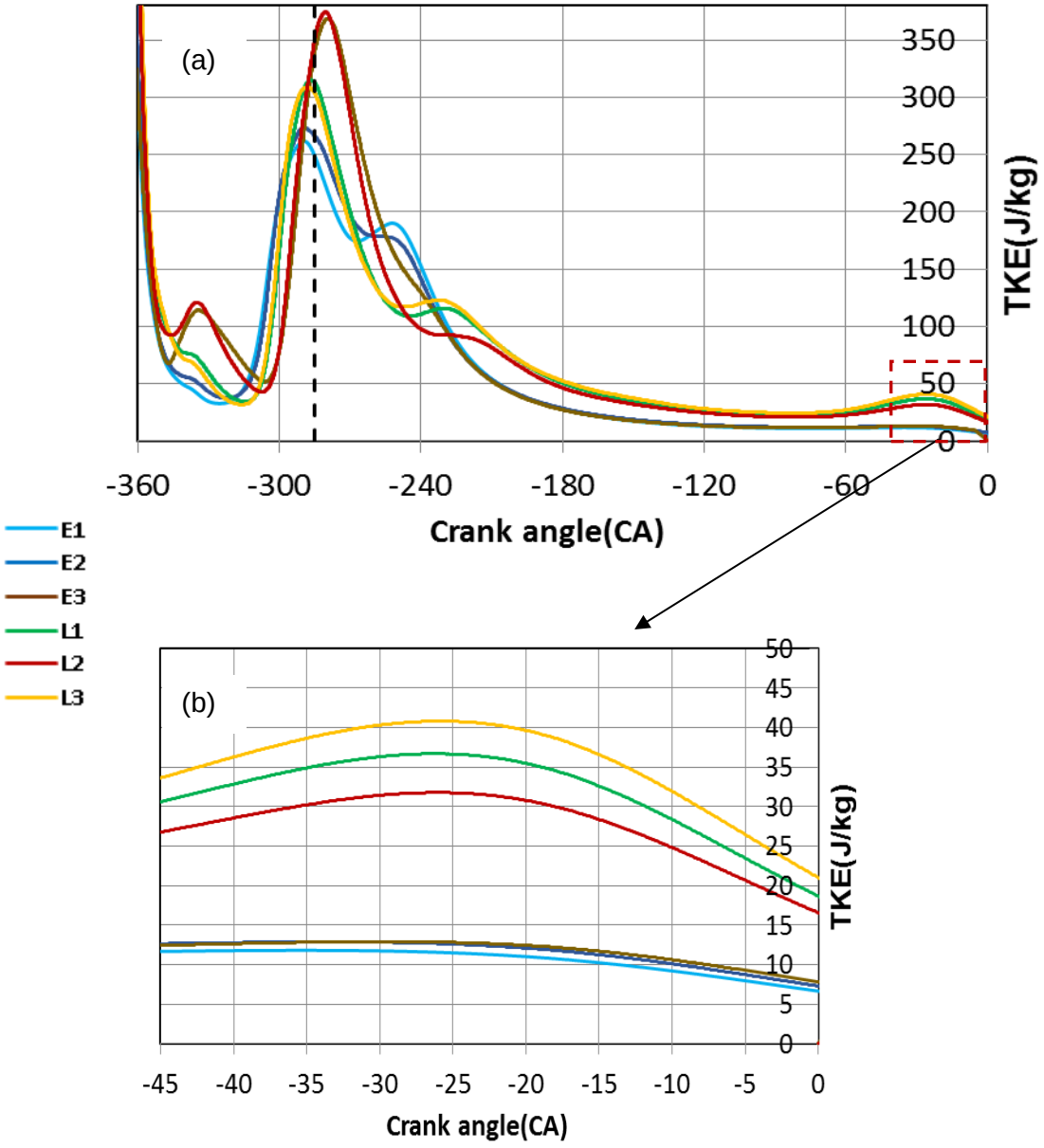

Figure 6.23: (a) Comparison of angle resolved in cylinder TKE evolution during the intake to the end of compression stroke for 2000 RPM 2 bar BMEP condition. (b) Shows the TKE from near 60 CAD BTDC to TDC. E1, E2 and E3 are the EIVC CAMs. L1, L2 and L3 are the LIVC CAMs.

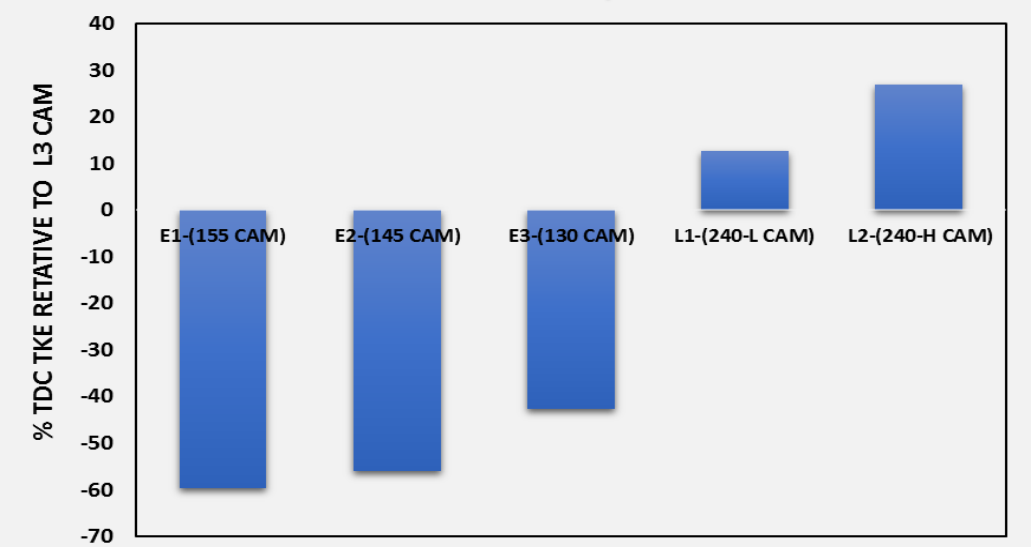

Figure 6.24: Comparison of in-cylinder TKE with different CAMs at the end of compression TDC. In this, L and H are added to LIVC CAMs L1 and L2 to differentiate low lift and high lift within LIVC CAMs.

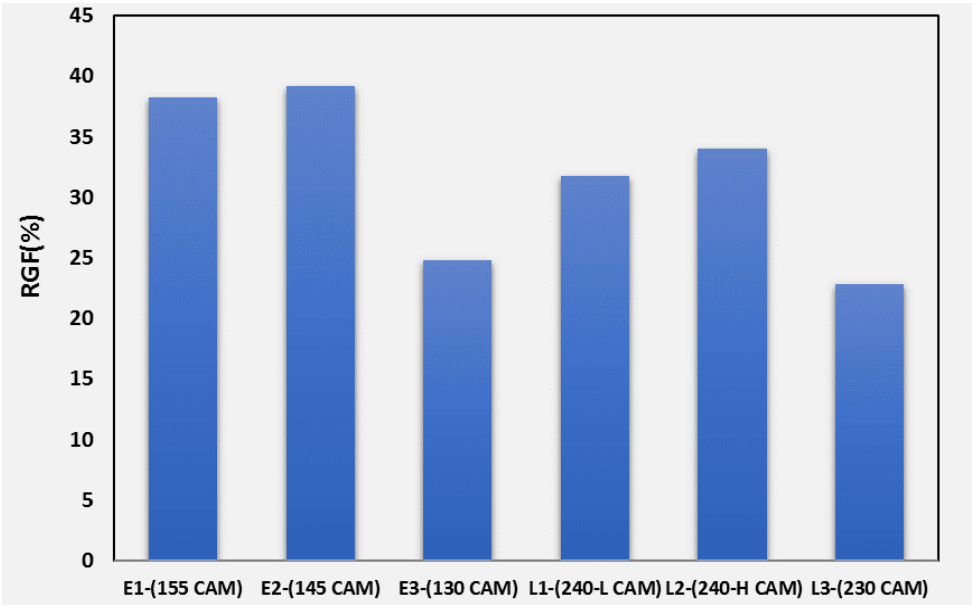

Figure 6.25: Comparison of residual gas fraction (RGF %) for different CAMs at the end of compression TDC. In this, L and H are added to LIVC CAMs L1 and L2 to differentiate as low lift and high lift within LIVC CAMs

In summary, EIVC CAMs show a poor charge motion and lower level of TKE near fire TDC and this is expected to decrease an overall burn rate. On the other hand, the LIVC CAMs show stronger charge motion and TKE than the EIVC CAMs, which will increase combustion speed. However, considering charge/fuel push back and the resulting effects on the cylinder-to-cylinder fuel-air variation, EIVC CAMs are preferred. As detailed in the earlier part of the study (Section 5.3.1 and 5.3.2), the spray pattern and injection strategy have shown significant influence on the charge motion under low speed low load condition. In Section 6.5, based on the results discussed in Chapter 5, the benefit shown by the injection strategy is applied to improve the charge motion for the EIVC CAM application.

6.3 Effect of multiple injection on charge motion and combustion at 1500 RPM WOT condition.

In this study, combustion simulations (STAR-CD, ECFM-3Z model) are carried out with 1500 RPM WOT condition with the EIVC, E1 CAM. Under low speed high load condition, the injection quantity and pulse widths are significantly larger than those at the low load condition. Hence, the impact of spray on charge motion is expected to be more significant under this condition than the high-speed high load condition. As both EIVC and LIVC CAMs are expected to have better charge motion during high speed high load condition, split injection strategies may not be required.

Injector-C referred to in Section 5.3.2 is used in this simulation along with the developed spray model assumptions discussed in Chapter 3. Figure 5.3.9 shows the spray pattern of Injector-C. Figure 6.26 shows the single and multiple injection timing chosen relative to the intake and exhaust valve timing. Based on the EIVC CAM timing study (Figure 6.14), to have best spray charge air interaction, the first injection is timed close to the maximum piston speed and aligned close to intake MOP. Moreover, to avoid piston wetting, in the single injection case an SOI of -293(100%) is used. In triple injection strategy, a fuel split ratio of 40% (SOI1-293) 35% (SOI2-234) and 25% (EOI3-115) was used. In this strategy, the first two injections are adopted to generate the background fuel with less liquid penetration and the third injection is chosen to enhance the charge motion, as discussed in Section 5.3.1. Table 6.2 shows the overall engine settings used in the single and triple injection simulation cases. All the simulation settings are kept the same except for the injection settings, as mentioned in Table 6.2.

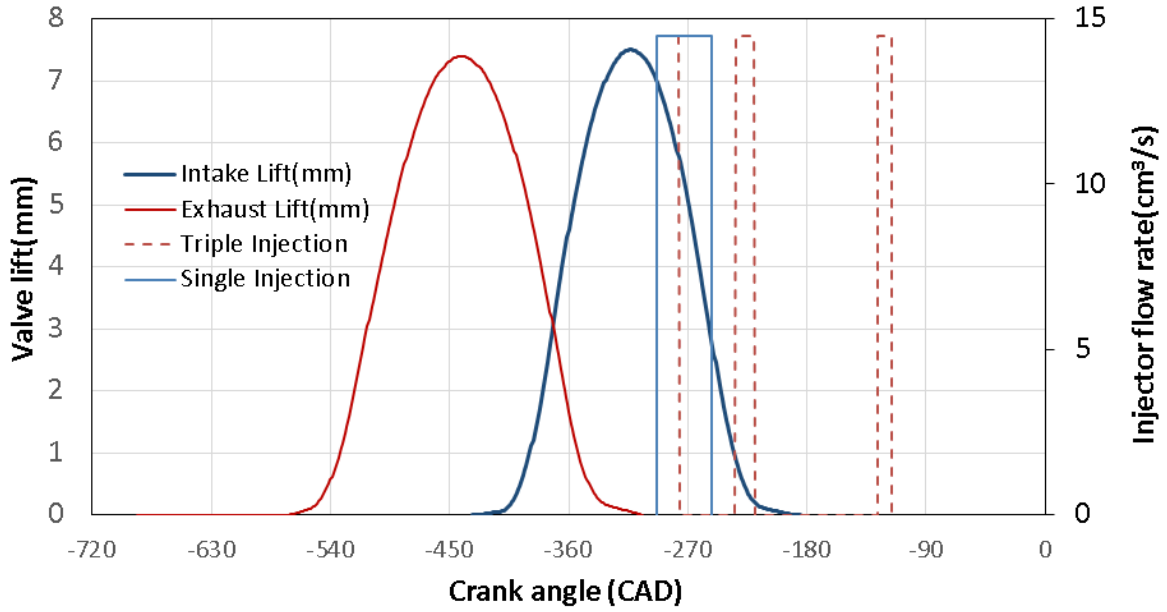

Figure 6.26: Shows the injection timing for single and multiple injection relative to the valve timing. The Q_{stat} is calculated with an injection pressure of 310 bar.

Table 6.2: Injection and ignition settings for 1500 RPM WOT condition for Engine specification-C.

Injection strategy	Single injection	Triple injection
Engine speed	1500 RPM	1500 RPM
Indicated power	32.98 kW	32.98 kW
Intake pressure	1.704 bar	1.704 bar
Intake temperature	41.85˚C	41.85˚C
Exhaust pressure	1.59 bar	1.59 bar
Exhaust gas temperature	689.27˚C	689.27˚C
Fuel split ratio	100%	40% : 35% : 25%
Total fuel injected/cycle/cylinder	48.76 mg	48.76 mg
SOI1	293.26˚ BTDC	293.26˚ BTDC
SOI2	-	234˚ BTDC
EOI3	-	115˚ BTDC
Fuel pressure (8.26 cc/s @100 Bar)	310 bar	310 bar
Spark (80mJ)	0 CAD BTDC	0 CAD BTDC
Lambda (λ)	1	1

6.3.1 Charge motion comparison: Single vs triple injection

The charge motion comparison during the injection events is shown in Figures 6.27, 6.28 and 6.29, respectively. The velocity field and the wall wetting on the engine cylinder are also shown

in the figures. During the first injection (Figure 6.27), the spray imparts high momentum to the charge air, resulting in local rise in charge velocity. In comparison to the earlier flow field data for EIVC and LIVC CAM (Section 6.4) simulation, the injection was found to impart higher charge motion. The injection shows significant change in the flow pattern aligning the injector

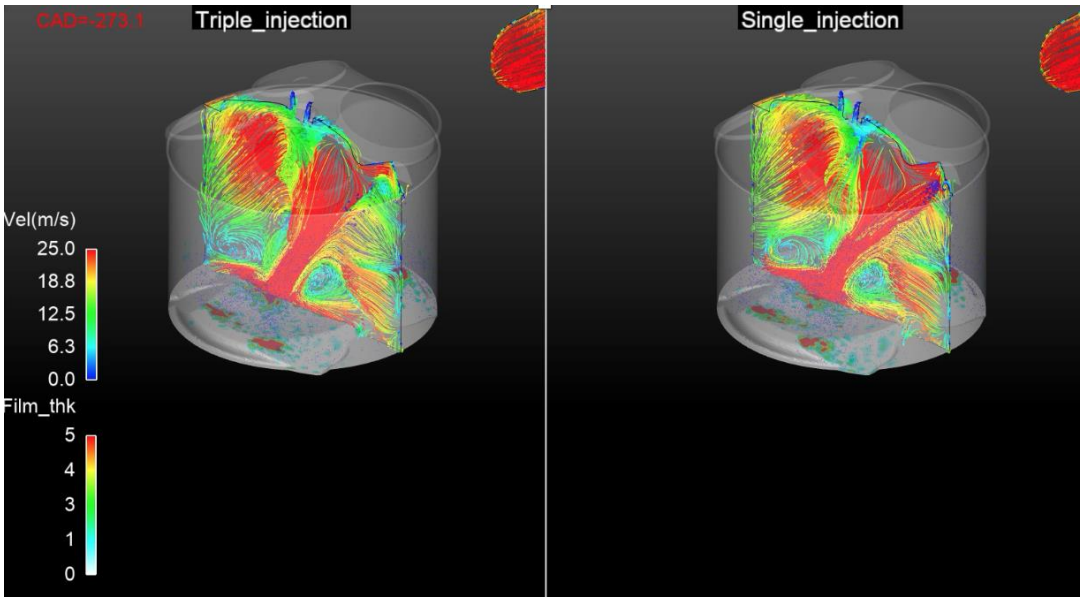

Figure 6.27: Instantaneous sectional flow field comparison during the first injection for single and triple injection case. The section is taken at 273 CAD BTDC. The path-lines are coloured by velocity and cylinder walls coloured by liquid film thickness (µm).

spray plume direction. The piston wall wetting can also be noticed, showing spots of liquid film coloured by film thicknesses. Figure 6.27 shows the comparison of sectional flow field between the single and triple injection cases. The single injection flow field starts to decay after the end of only the first injection. However, in the triple injection case, the second injection before BDC imparts additional charge motion and keeps the flow structure active (Figure 6.28). Local high velocity core of the plume during the injection increases the mean strains rate (S_{ij}), thereby, increasing TKE during this phase. A similar effect is also noticed during the third injection (Figure 6.29). In summary, even with the low velocity EIVC CAM, E1, the charge motion is significantly improved using the multiple injection strategy. Figure 6.30 shows the net charge motion in the cylinder near TDC. It can be seen that the single injection case shows a very weak charge motion in comparison to the triple injection case. This is evident to show the underlying charge motion differences in the low lift EIVC CAM for single and triple injection strategy.

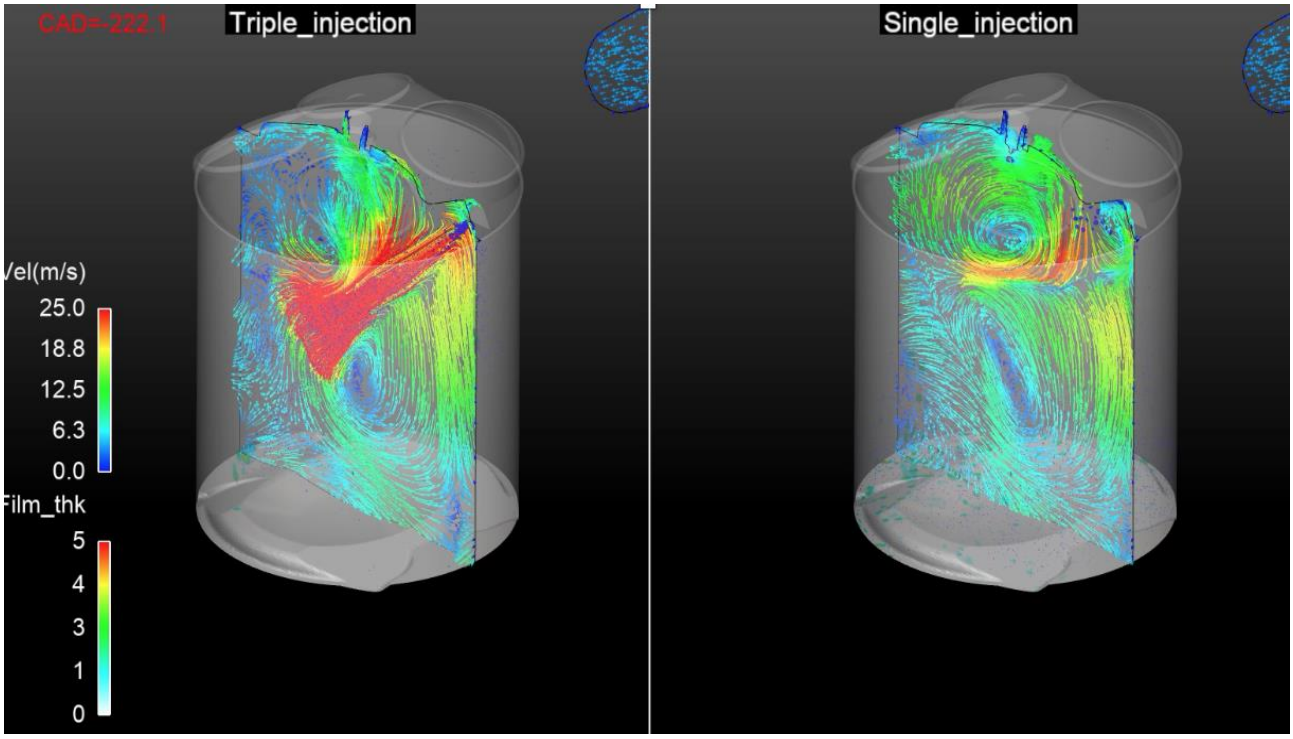

Figure 6.28: Instantaneous sectional flow field comparison during the second injection for triple injection and single injection case. The section is taken at 222 CAD BTDC. The path-lines are coloured by velocity and cylinder walls coloured by liquid film thickness (µm).

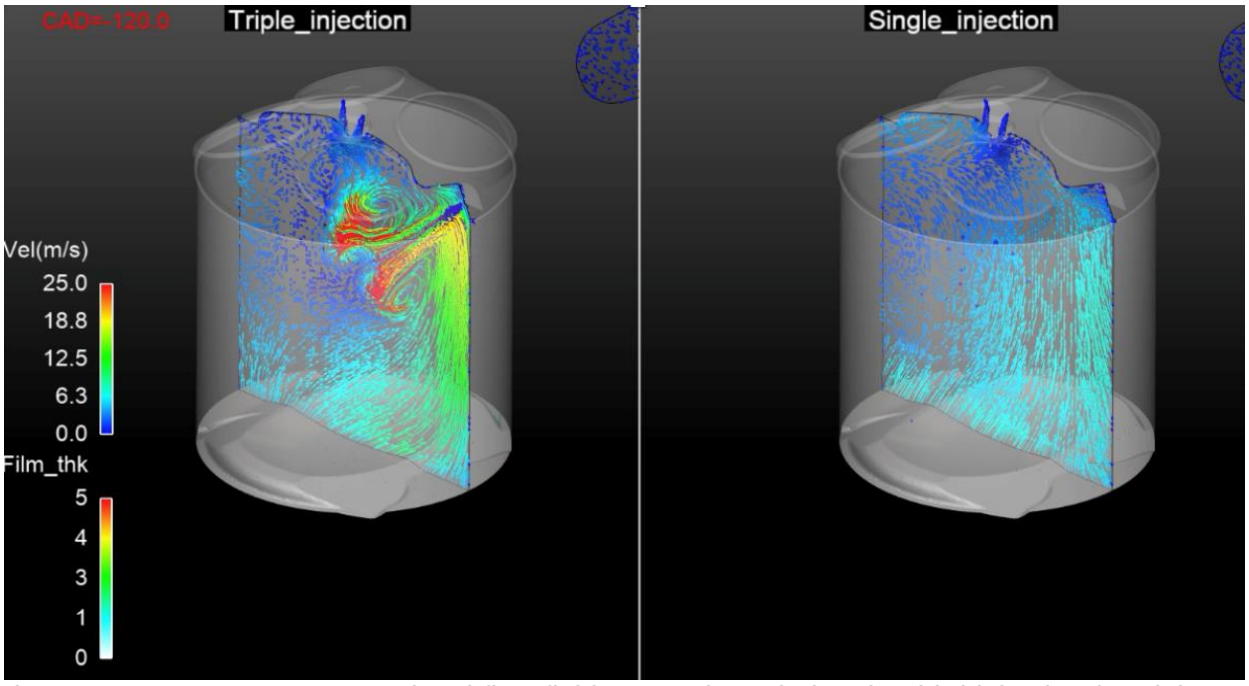

Figure 6.29: Instantaneous sectional flow field comparison during the third injection for triple injection case and single injection case. The section is taken at 120 CAD BTDC. The path-lines are coloured by velocity and cylinder walls coloured by liquid film thickness (µm).

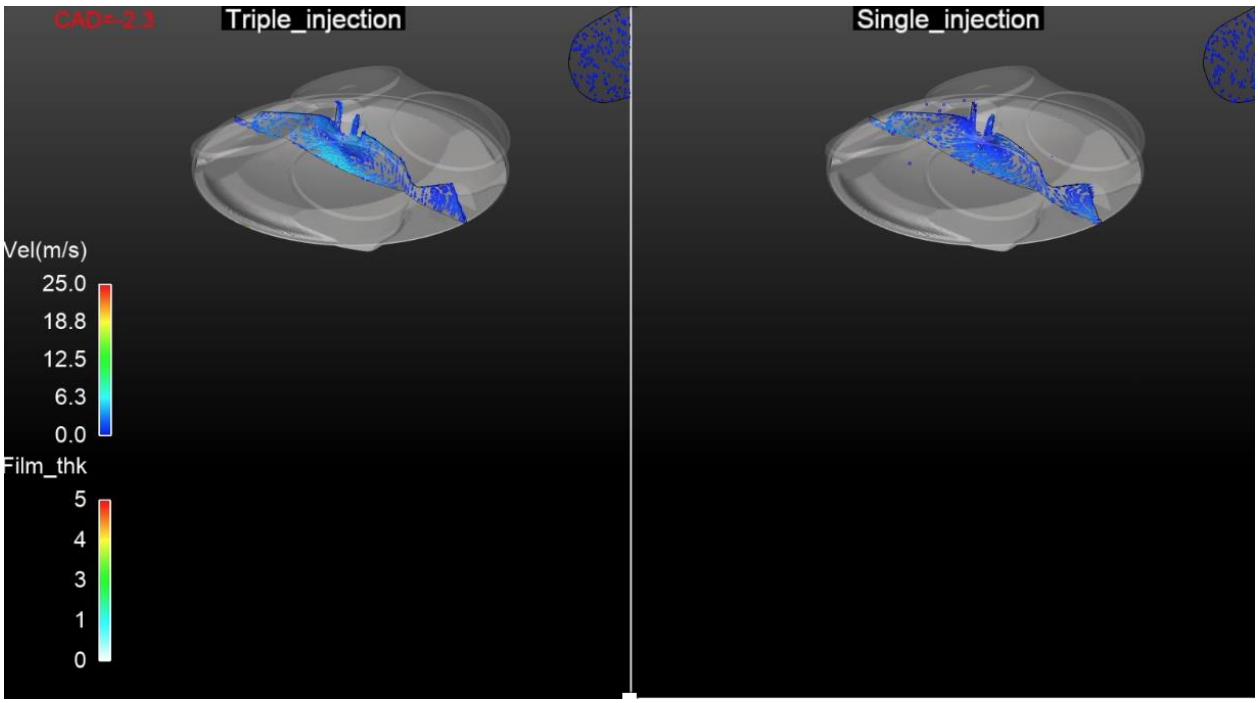

Figure 6.30: Instantaneous sectional flow field comparison during the first injection for single and triple injection case. The section is taken at -2.3 CAD BTDC. The path-lines are coloured by velocity and cylinder walls coloured by liquid film thickness (µm).

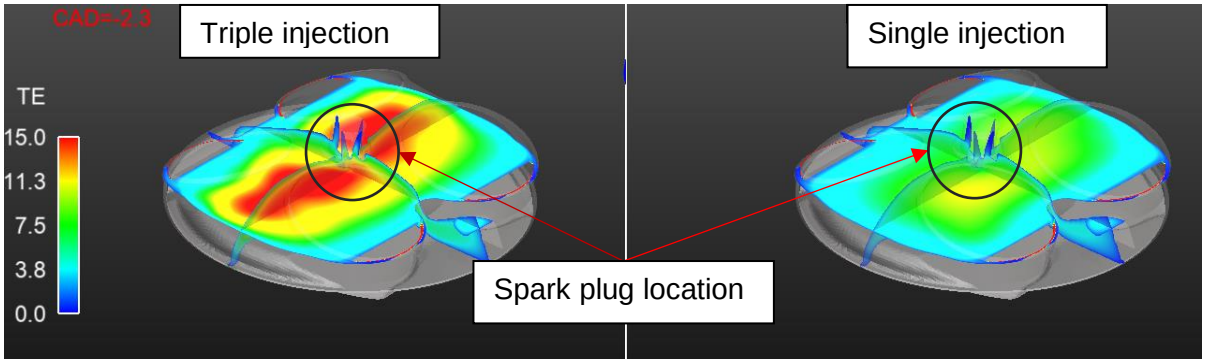

Figure 6.31: Comparison of TKE distribution near the spark plug and other areas of the cylinder for single injection and triple injection case.

Typical TKE distributions near TDC are shown in Figure 6.31. The single injection case shows significantly lower TKE near the spark plug region.

Figure 6.32 shows the evolution of in-cylinder tumble ratio for both single and triple injection cases. The local dip in the tumble ratio plot shows the injection timing and how the first injection

with a 40% injected mass (triple injection case) preserves the charge motion against the single injection at the same timing with 100% injected mass. It can be seen that the triple injection case generates 50% higher tumble ratio than the single injection strategy. It is evident that a small quantity in the third injection (Figure 6.33) 115 CAD before TDC enhances the TKE significantly.

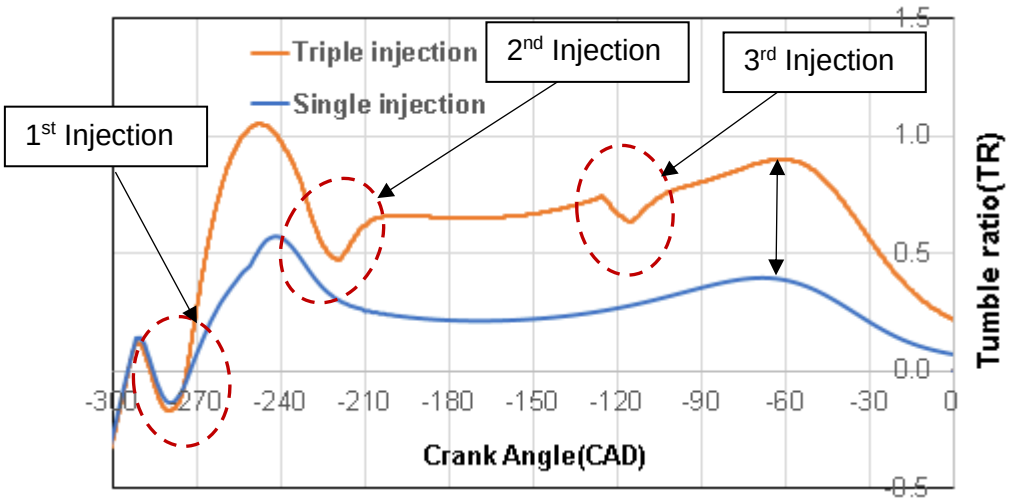

Figure 6.32: Comparison of crank angle resolved tumble ratio during the intake to the end of compression stroke with single and triple injection. The tumble ratio influences from the injections are circled in dotted lines.

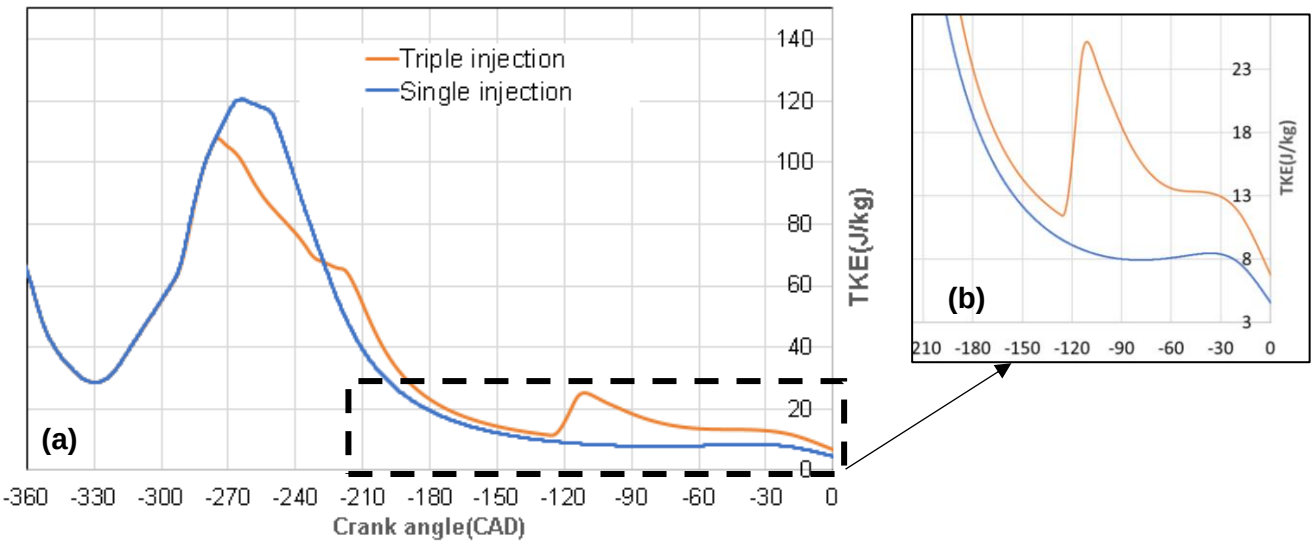

Figure 6.33: (a) Comparison of transient TKE during the intake to the end of compression stroke at 1500 RPM WOT condition. (b) Shows the TKE variation near 210 CAD to TDC.

Figure 6.34 shows the equivalence ratio distribution near the spark plug comparing single and triple injection cases. The single injection case also shows non-homogeneous charge mixing and asymmetrically placed due the weaker charge motion and from the initial flow development from the asymmetric exhaust port (Figure 6.3). Thus, the multiple injection not only increases the TDC TKE, it also improves the mixing, even with a weaker initial charge flow setup by the low lift short duration EIVC CAMs.

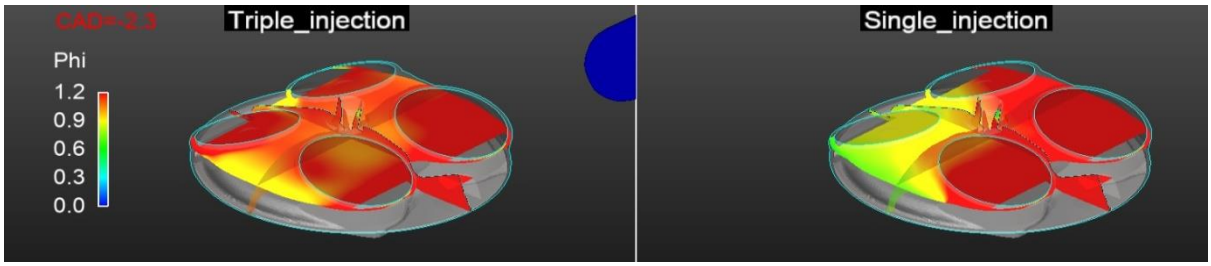

Figure 6.34: Equivalence ratio distribution comparing single and multiple injection case.

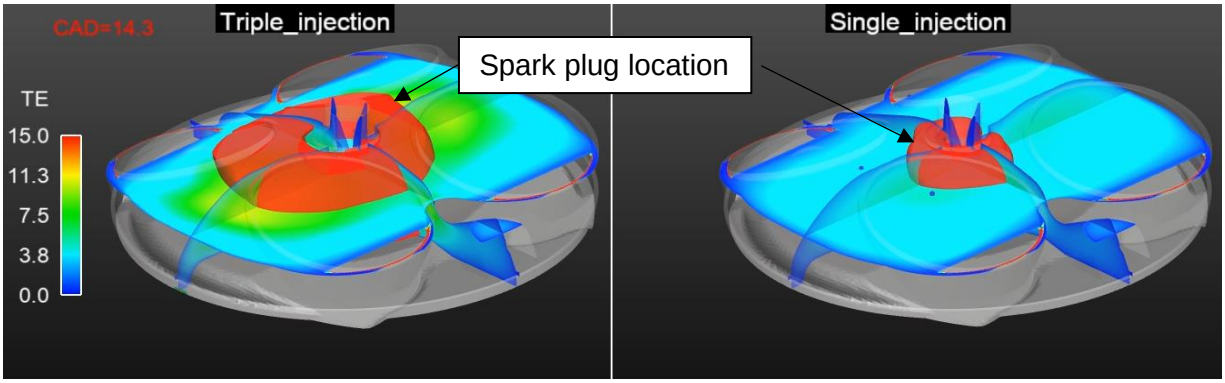

Figure 6.35: Comparison of flame front represented by red isosurface generated with the flame surface density (∑) calculated using ECFM-3Z model. The sectional view shows the contours of TKE.

The initial flame kernel simulated from the ECFM-3Z model tracked by the isosurface of the flame surface density (∑) is shown in Figure 6.35. It is very evident that, for the same crank angle, the combustion simulation shows that, in triple injection strategy, the flame kernel covered a larger area (30 to 40%) in comparison to the single injection strategy. The computed heat release curve is shown in Figure 6.36. In this, the shift in the 10%, 50% and 90% heat release points are specified. The resultant pressure traces obtained from the simulations are shown in Figure 6.37.

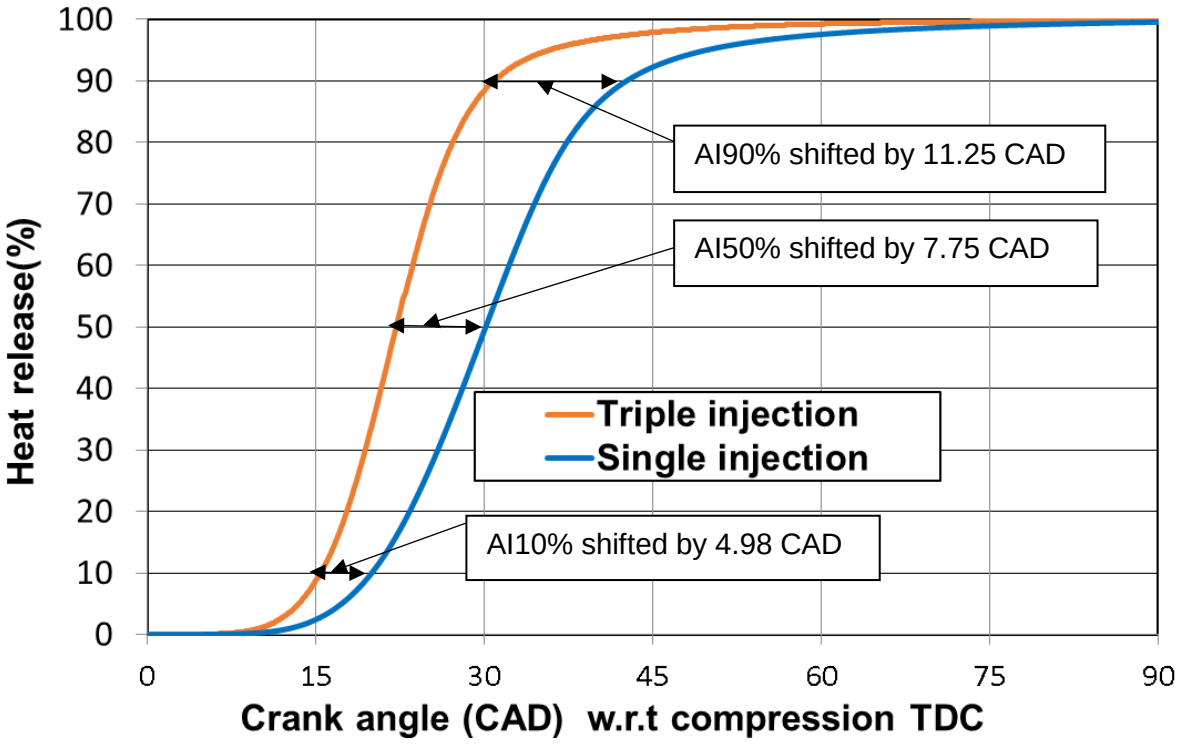

Figure 6.36: The comparison of the fraction release computed from the simulation for single and triple injection. The shift in 50% heat release point is also shown for the same spark timing (0 CAD BTDC).

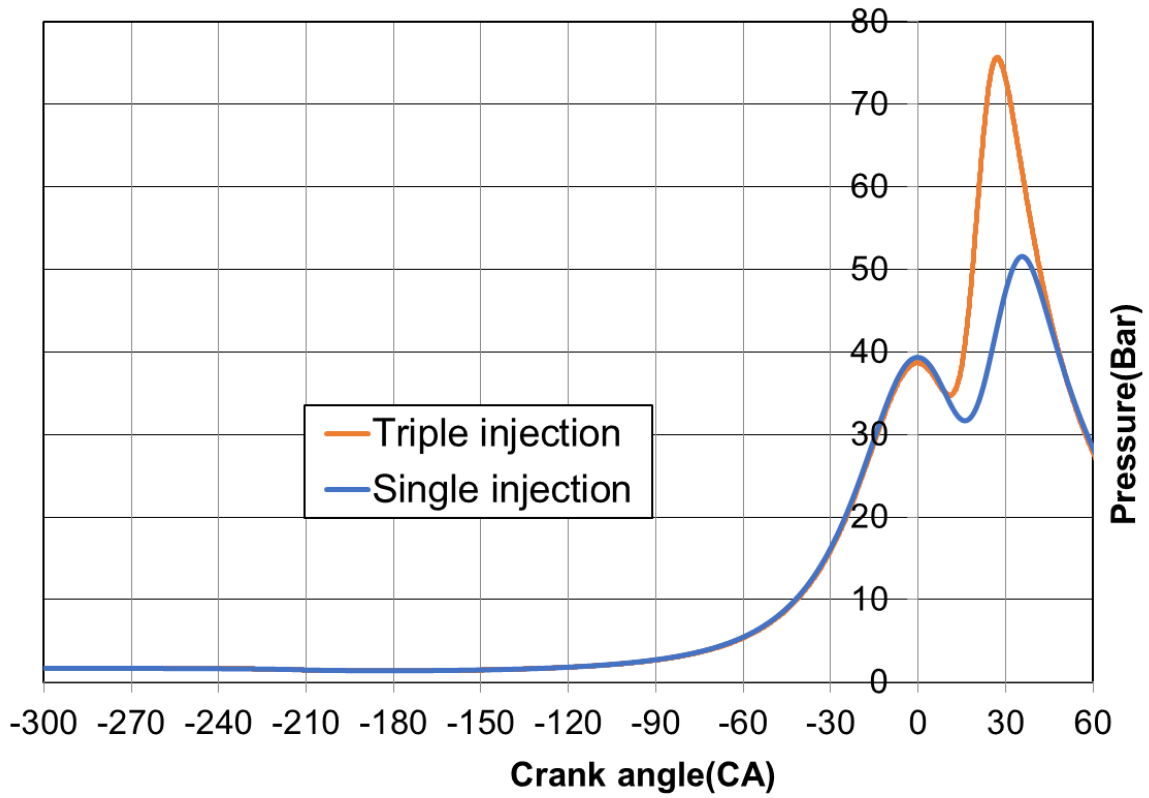

Figure 6.37: The comparison of the in-cylinder pressure traces computed from the simulation for single and triple injection strategies.

6.4 Summary and conclusion

The details of the over-expanded engine cycle adopted for the improvement of higher thermal efficiency were illustrated. Even though the thermodynamic relations did not show the difference in the calculated relative efficiencies ($\eta_{f.i}/\eta_{f.io}$) for EIVC and LIVC strategy, actual CAM features adopted (low lift short duration and high lift long duration) showed a significant impact on the charge motion. In both low speed, high load (1500 RPM WOT) and medium speed part load condition (2000 RPM 2 bar BMEP), the charge motion is stronger with the

LIVC CAMs. LIVC CAMs show 50 to 60% increase in the TKE near TDC in comparison to the EIVC CAMs.

For the chosen CAM timing, the LIVC CAMs show a maximum of 6% RGF at 1500 RPM WOT condition. However, the short duration EIVC CAMs do not show RGFs, and, hence, are expected to be knock resilient in this perspective. In the case of the chosen CAM timing at 2000 RPM 2 bar BMEP with both LIVC and EIVC CAM profiles, significantly higher RGFs (25 to 40%) were noticed due to relatively higher back pressure. By altering the CAM duration, as in the case of E3, the RGFs can be decreased significantly (25%). The presence of RGF is expected to increase the intake charge temperature and result in increasing knock tendency.

In this work, the benefits in multiple injections and the possible improvements in charge motions for EIVC CAMs were studied. It was demonstrated that, under low speed high load operation with EIVC CAMs, the side-mounted injectors with the multiple injections strategy have an injection in the compression stroke closer to the BDC, which benefits the charge motion. The combustion simulation shows that the triple injection strategy decreased the burn duration (AI0-90) by 36% with respect to the early single injection strategy. Based on the spray pattern study demonstrated in Chapter 5, the charge motion can further be improved with a more outward spray plume modification. As the ECFM-3Z combustion model used in simulation does not consider the detailed chemistry/detailed reaction mechanism, the actual benefits need to be revaluated for more accurate predictions in the future studies along with knock modelling.

Chapter 7. Conclusions and Future work

7.1 Introduction

GDI engines play a major role in improving the thermal efficiency of the internal combustion engine and reduce CO_2 and pollutant emissions. They need to be optimised to minimise emission and increase thermal efficiency for different operating conditions, including: cold start, idle, low speed medium load, minimum brake specific fuel consumption point and high speed high load points. Different injection strategy needs to be adopted for the individual operating conditions. Computational fluid dynamics (CFD) simulation is an effective tool to help the design of a modern GDI engine by providing the detailed analysis of the spray and mixture formation, as well as the in-cylinder flow and turbulence of different combustion systems. In this study, a simplified spray model has been developed and validated for the CFD simulation of the GDI engine. The CFD simulation was then carried out to investigate the optimised mixture formation process for different engine operations as well as the effect of fuel injection on the in-cylinder charge motion. The main conclusions are summarised in the following sections.

7.2 Simplified spray model

A detailed literature review was presented to describe the fundamentals of turbulence, spray atomisation and different phenomenological models. In this work, the computational modelling of spray using Lagrangian-multiphase model was adopted. In this approach, the droplets emanating from the nozzle after undergoing the primary breakup were defined using the Rosin-Rammler distribution with high-resolution droplet size bins. The nozzle hole diameter was used as the initial SMD of droplets to calculate the input parameters for defining the Rosin-Rammler distribution. The velocity of the primary droplets was based on the mean velocity calculated from the injector static flow rate and the nozzle diameter. This simplistic approach allowed it to be used for a wide range of multi-hole injectors with minimum information from the injector supplier.

Both Reitz-Diwakar model and KHRT spray models were considered. The effect of modelling parameters or constants for calibrating the spray were analysed. A detailed sensitivity study was carried out on the secondary breakup model constants. In the spray calibration process, measured spray images and the liquid penetration depths of three injectors were used to validate the spray model for injection pressures of 150 bar, 200 bar, 300 bar and 350 bar. The

Reitz-Diwakar model constants obtained from the calibration process were found to be less sensitive to injection pressures. This helped in modelling the injectors for the in-cylinder simulation for a wider range of injection pressures. In comparison, the KH-RT model constants were more sensitive to injection pressures. The calibrated spray model could predict accurately the spray shape and penetration over a wider range of injection pressure and injection duration. This ensured that the secondary breakup mechanisms were captured with air entrainment processes along with droplet momentum. However, the droplet SMD obtained from the simulation at 45 mm or 50 mm from the injector tip was over-estimated by 3 to 4 µm.

7.3 Catalyst light-off PN/PM reduction

The calibrated spray model was applied to investigate the mixture formation and combustion strategy for the catalyst heating/light-off during the cold-start operation. In the spray model development, detailed Fortran user routines were modified to calculate and provide the primary droplet spray model input parameters for the engine simulation. In this, a twin injection condition was used for qualitative assessment of the engine simulation with the available engine stability data (Std. NMEP). The fuel-air mixture distribution, the final fuel rich mixture available near the spark plug and the turbulent kinetic energy correlated with the engine stability.

Detailed study was carried out to understand the air-guided and wall-guided pistons for the modern low PN/PM emission engine development. Analysis demonstrated that, with the air-guided piston design (lower curved piston bowl shape) with the twin injection strategies, it can improve mixing, liquid film vaporisation and decrease the piston wetting for the catalyst light-off condition. The air-guided piston approach was found to decrease the PN/PM (#/ccm) emission by an order of magnitude and was used to support the engine development to meet the WLTC engine cycle emission test.

7.4 Charge motion improvements with injection strategy

The effect of multiple injections on the total in-cylinder tumble ratio, fuel stratification and TKE available near the spark plug were studied. It could be seen that a smaller quantity of injection is required in the compression stroke to avoid wall wetting and retain the charge motion at the time of spark event. The injection near the bottom dead centre (~100 to 200 BTDC) enhances the charge motion, TKE and better mixing. It also helped to decrease the piston and liner wetting significantly to avoid fuel rich combustion near the wall and the resulting emission. This analysis has led to the decision to adopt a low static flow injector to make it possible to inject a controlled small injection at light engine load in the production engine by ChangAn.

Different spray patterns were analysed starting from a 6-hole injector to a 5-hole injector with the simplified spray model. The benefits of the side-mounted injector on tumble ratio and mixing were demonstrated. It could be seen that, with the outward directed spray pattern with delayed injection having the charge motion mass centre of the cylinder below the spray plume it increases the charge tumble ratio. It should be noted that the 5-hole injector with the more horizontal spray plume increases the tumble ratio along with a significant increase in the liquid film. This shows the necessity for the spray optimisation to balance the liquid film, mixing and charge motion benefit.

7.5 Charge motion improvements for CAM strategy

In the modern engine, the thermal efficiencies are further improved using the over-expanded engine cycles such as Atkinson or Miller's cycle. One of the enabling parameters for achieving over-expanded cycle is an EIVC or LIVC approach. Even though the theoretical thermal efficiencies calculated using the EIVC or LIVC are the same, in reality, there is a fundamental difference in charge motion and the resulting combustion. The charge motion benefits and disadvantages of the two different CAMs strategies were analysed for the low speed high load and medium speed low load conditions. The simulation results show that the EIVC CAMs have poor charge motion compared to the LIVC CAMs. Moreover, the turbulent kinetic energy near the TDC with EIVC CAMs are 50 to 60% lower than the LIVC CAMs for the both the conditions. However, the residual gas fractions (RGFs) obtained from the LIVC CAMs are higher at the low speed high load condition, which could result in higher knocking tendency. Having the advantage of a lower RGFs and no fuel push back into the intake port, there is a need to improve charge motion for the EIVC CAMs. It was shown that the low lift CAM charge motion can be improved by triple injections and the burn duration can be reduced by 36% compared to a single injection case. Further improvement may be achieved by modifying the reference spray pattern with outward facing spray plumes.

7.6 Future work and model improvement recommendations

7.6.1 Spray modelling improvements

Von Kuensberg Sarre, Kong and Reitz (1999) studied the effect of injector nozzle geometry on fuel atomisation effects using a phenomenological model considering the cavitation regimes. In this, the nozzles were characterised as turbulent flow, onset of cavitation, super cavitation, hydraulic flip and partly reattached flow. Considering the confidentiality of the injector geometry details from the supplier, a more general simplified approach is described in this section.

Initial velocity corrections based on flow cavitation

Generally, the static flow rate of injector, i.e., the flow rate at 10 MPa fuel pressure, is known and the discharge coefficient C_d can be calculated.

$$C_d = \frac{Q_{static}}{Q_{ideal}} = \frac{Q_{static}}{\rho_l A_{hole}\sqrt{\frac{2\Delta p}{\rho_l}}} = \frac{Q_{static}}{A_{hole}\sqrt{\rho_l (2\Delta p)}} \qquad (7.1)$$

where

ρ_l is density of liquid fuel

Δp is the static pressure 10MPa

A_{hole} is the total area of nozzle holes.

At a given engine operating condition, mean velocity in nozzle hole, u_{mean}, can be calculated from C_d and the pressure difference between fuel rail and combustion chamber.

$$u_{mean} = C_d\sqrt{\frac{2\Delta P}{\rho_l}} \qquad (7.2)$$

where

$$u_{Bernoulli} = \sqrt{\frac{2\Delta P}{\rho_l}}$$

where ΔP is the pressure difference between fuel rail and combustion chamber at the given engine operating condition.

During the main injection phase, the flow is usually cavitating Figure 7.1 and there is a vena contracta where flow area reaches its minimum, A_{vena}. C_c, the area ratio of A_{vena}/A_{hole} is less than 1 and can be calculated using Nurick's (1976) expression in the absence of more accurate value. More accurate C_c may be obtained from 3-D CFD simulation, which may not be feasible as detailed geometry of injectors is not always available.

.

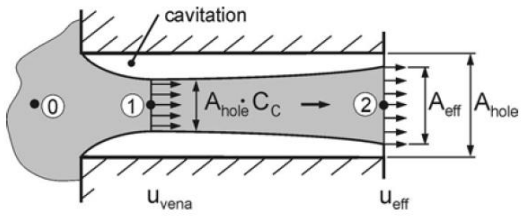

Figure 7.1: Cavitating nozzle hole flow (Baumgarten, 2006).

$$C_c = \left[\left(\frac{1}{C_{c0}}\right)^2 - 11.4\frac{r}{D}\right]^{-0.5} \qquad (7.3)$$

where

C_{c0}=0.61

r is radius of nozzle entry fillet

d is nozzle hole diameter

r/D=0.03-0.07 for sharp edged nozzle hole.

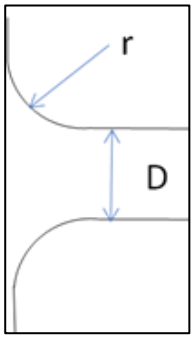

Figure 7.2: Typical simplified nozzle structure showing the round edge radius (r) for a nozzle diameter of D.

$$u_{vena} = \frac{u_{mean}}{C_c} = \frac{C_d\sqrt{\frac{2(\Delta P)}{\rho_l}}}{C_c} = \frac{C_d}{C_c}\sqrt{\frac{2(\Delta P)}{\rho_l}} \qquad (7.4)$$

Using Bernoulli's equation for nozzle flow from position 0 to position 1 gives

$$p_0 - p_{loss} = p_1 + \frac{1}{2}\rho_l u_{vena}^2 \qquad (7.5)$$

p_0 is the total pressure just before the nozzle entry and p_{loss} is the pressure loss at nozzle entry. For the cavitating flow during main injection, p_1 is equal to the saturation vapour pressure, p_{vap}.

$$p_0 - p_{loss} = p_{vap} + \frac{1}{2}\rho_l u_{vena}^2 \qquad (7.6)$$

$$u_{vena} = \sqrt{\frac{2(p_0 - p_{vap} - p_{loss})}{\rho_l}} \qquad (7.7)$$

Substituting Eq. 7.4 into Eq. 7.7 yields

$$\frac{C_d}{C_c}\sqrt{\frac{2(\Delta P)}{\rho_l}} = \sqrt{\frac{2(p_0 - p_{vap} - p_{loss})}{\rho_l}} \qquad (7.8)$$

$$\frac{C_d}{C_c} = \sqrt{\frac{p_0 - (p_{vap} + p_{loss})}{\Delta P}} = \sqrt{\frac{p_0 - (p_{vap} + p_{loss})}{p_{inj} - p_2}} \qquad (7.9)$$

$$= \sqrt{\frac{\frac{p_0}{p_{inj}} - \frac{p_{vap} + p_{loss}}{p_{inj}}}{1 - \frac{p_2}{p_{inj}}}} \qquad (7.10)$$

When p_{inj} is sufficiently high, (p_{vap} + p_{loss}) and p_2 are lower than p_{inj} by two-order of magnitude; therefore, $\frac{p_{vap}+p_{loss}}{p_{inj}}$ and $\frac{p_2}{p_{inj}}$ $are\ negligible$. We may have

$$\frac{C_d}{C_c} = \sqrt{\frac{\frac{p_0}{p_{inj}} - \frac{p_{vap}}{p_{inj}}}{1 - \frac{p_2}{p_{inj}}}} \cong \sqrt{\frac{p_0}{p_{inj}}} < 1 \qquad (7.11)$$

Therefore

$C_c > C_d$

P_0 is the total pressure before the entry of nozzle hole and is lower than p_{inj} due to the significant pressure loss at needle valve. Therefore, p_0/p_{inj} is less than 1 and C_c is greater than C_d. From Equation 7.4, we have:

$$\frac{u_{vena}}{\sqrt{\frac{2(\Delta P)}{\rho_l}}} = \frac{C_d}{C_c} \qquad (7.12)$$

As u_{vena} is less than the Bernoulli velocity $\sqrt{\frac{2(\Delta P)}{\rho_l}}$ and, therefore, $C_d/C_c<1$, i.e., $C_c>C_d$. $C_d<C_c<1$ means the vena velocity is always between the Bernoulli velocity and the mean velocity. C_c is constant in turbulent flow regime for the nozzle, independent of cylinder pressure. Therefore, $C_d<C_c<1$ is also valid for the late injection in compression stroke where the cylinder pressure is high. If the C_c calculated from the Nurick's expression is less than C_d, correction needs to be made, and $C_c=(C_d+1)/2$ can be used as an approximation.

As the ratio of hole length/hole diameter (L/D) of GDI injector is small, e.g. L/D=1.1, the friction loss in the hole may be ignored. Applying Bernoulli's equation yields

$$\frac{1}{2}\rho_l u_{eff}^2 + p_2 = \frac{1}{2}\rho_l u_{vena}^2 + p_{vap} \qquad (7.13)$$

$$u_{eff} = \sqrt{\frac{2(p_{vap} - P_2)}{\rho_l} + u_{vena}^2} \quad (7.14)$$

$$A_{eff} = \frac{A_{hole} u_{mean}}{u_{eff}} \quad (7.15)$$

$$D_{eff} = \sqrt{\frac{4A_{eff}}{\pi}} \quad (7.16)$$

where

p_{vap} is saturation vapour pressure of fuel

p_2 is combustion chamber pressure

ρ_l is density of liquid fuel

As p_{vap} is usually lower than p_2, u_{eff} is lower than u_{vena}. This effect becomes more significant for late injection in compression stroke where p_2 is high. The SMD at nozzle exit is assumed to be equal to the effective diameter D_{eff} and the exit velocity is equal to the effective velocity u_{eff}. It is noticed that u_{eff} is significantly higher than u_{mean}. The SMD and velocity at nozzle exit, the Rosin-Rammler droplet distribution and the spray cone angle of 20° describe the droplet condition from primary breakup to form a complete set of input data for secondary breakup model. Simulation with the above recommended approach can be applied for the future spray and in-cylinder simulation. This is expected to decrease the droplet SMD predictions which was overestimated with the lower initial droplet velocity assumption without nozzle flow contraction (Section 3.1.4.4).

7.6.2 Modelling improvements for catalyst heating simulation

For the qualitative assessment of the combustion system development, the current cold flow simulation methodology adopted in this work should be adequate. However, for the combustion simulation, the model requires further improvements. Firstly, in the catalyst light-off cold flow simulation, the colder engine cylinder wall results in 20 to 25% of the injected fuel as a liquid film at the end of compression stroke. Due to the relative motion of the piston on the liner, the liquid film formed on the liner is scraped back on to the piston during the compression stroke. However, the crevices volume around the piston is expected to entrain the fuel rather than the film movement on to the surface of the piston. Hence, in the combustion simulation, the crevices volume needs to be included in the engine simulation especially for the catalyst light-off condition to account for the emission-related predictions. Moreover, in this simulation, a single component fuel assumption was used. This does not include the effects of differential evaporation from the fuel blend containing the heavier and lighter components. Combustion simulation requires the multi-component fuel model to predict the burn duration

and the exhaust heat flux. It is also required to consider the multi-component fuel effects for engine cold-start simulation (-30°C) even for cold flow simulation.

7.6.3 Requirement of combustion simulation

In general, for the engine development process, cold flow simulations are used to assess the catalyst light-off condition with the equivalence ratio distribution, tumble ratio and TKE. However, these are not the concluding parameters in the actual combustion performance. The detailed chemistry considering the timescales for different chemical reactions and flow (Damköhler number, Da) are required to be considered for more realistic predictions. This is currently under progress using Converge (SAGE, model) CFD tool to evaluate different injection strategy and injector designs.

7.6.4 Thermal efficiency improvements with advanced combustion system.

Further understanding on spray with the very high pressure injector (> 500 bar to 1000 bar) is required to control charge motion and end-gas mixture cooling to decrease knock tendency and achieve MBT under low speed high load condition. Moreover, this simplified in-cylinder modelling approach along with the detailed chemistry can be used further to understand the advanced combustion system, such as the high-energy ignition coil, active or passive pre-chamber and corona discharge to improve the engine combustion and help in improving the engine efficiencies further to meet the future stringent emissions. Using these technologies Changan is in the process of building a 45% BTE engine to mitigate global warming.

References

Abani, N., Bakshi, S. and Ravikrishna, R. V. (2001) *'Modelling of Spray and In-cylinder Air Flow Interaction in Direct-Injection Engines*', SAE Paper, 2001-28-0071.

Abianeh, O. S. and Chen, C. P. (2011) *'A turbulence model of bi-component fuel droplet for atomizing sprays*', Proceedings of the ASME-JSME-KSM, 2011, AJK Joint Fluids Engineering Conference, 2011-10038.

Abraham, J., Williams, F. A. and Bracco, F.V. (1985) *'A Discussion of Turbulent Flame Structure in Premixed Charges*', SAE Transactions 1986 - Fuels and Lubricants, 94 (7), pp. 128-143.

Abramzon, B. and Sirignano, W. A. (1989) *'Droplet vaporization model for spray combustion calculations*', *International Journal of Heat Mass Transfer*, 32 (9), pp. 1605-1618.

Amsden, A. A., O'Rourke, P. J., Butler, T. D. (1989) '*KIVA-II: A Computer Program for Chemically Reactive Flows with Sprays*', Los Alamos National Laboratory, Report LA-11560-MS

Amsden, A. A., Ramshaw, J. D., O'Rourke, P. J. and Dukowicz, J. K. (1985) *'KIVA: A computer Program for Two and three-Dimensional Fluid Flows with Chemical reactions and Fuel Sprays*', Los Alamos report No. LA-10245-MS.

An, F. and Santini, D. (2004) *'Mass Impacts on Fuel Economies of Conventional vs. Hybrid Electric Vehicles*', SAE Technical Paper, 2004-01-0572.

An, F., Stodolsky, F. and Santini, D. (1999) '*Hybrid Options for Light-Duty Vehicles*', SAE Technical Paper, 1999-01-2929.

Angleberger, C., Poinsot, T. and Delhay, B. (1997) *'Improving Near-Wall Combustion and Wall Heat Transfer Modelling in SI Engine Computations*', SAE Technical Paper, 972881.

Bai, C. and Gosman, A. (1995) *'Development of Methodology for Spray Impingement Simulation*', SAE Technical Paper, 950283.

Baumgarten, C. (2006) *'Mixture Formation in Internal Combustion Engines*', Germany: Springer-Verlag Berlin Heidelberg.

Befrui, B., Corbinelli, G., D'Onofrio, M. and Varble, D. (2011) *'GDI Multi-Hole Injector Internal Flow and Spray Analysis*', SAE Technical Paper, 2011-01-1211.

Blazek, J. (2001), '*Computational Fluid Dynamics: Principles and Applications*', First ed. Elsevier Science Ltd. Amsterdam, London, New York, Oxford, Paris, Shannon, Tokyo.

Boussinesq, J. (1877) '*Essai sur la theorie des eaux courantes*', Mem. Pres. Acad. Sci., XXIII, 46, Paris.

Boussinesq, J. (1896) '*Theorie de l' e'coulement tourbillonant et tumubteur des liquides dans les lits rectiligues',* Comptes Rendus de l' Acad. des Sciences, CXXII (1896), p. 1293.

Brulatout, J., Garnier, F., Mounaïm–Rousselle, R. and Seers, P. (2015) 'Calibration strategy of diesel-fuel spray atomization models using a design of experiment method', *International Journal of Engine Research*, 17 (3), pp. 713-731.

Chen, X., Fu, H., Smith, S. and Sandford, M. (2009) *'Investigation of Combustion Robustness in Catalyst Heating Operation on a Spray-guided DISI Engine*', SAE Technical Paper, 2009-01-1489.

Cheng, W., Hamrin, D., Heywood, J., Hochgreb, S., Min, K. and Norris. M. (1993) *'An Overview of Hydrocarbon Emissions Mechanisms in Spark-Ignition Engines*', SAE Technical Paper, 932708.

Cimarello, A., Grimaldi, C., Mariani, F., Battistoni, M. and Dal Re, M. (2017) '*Analysis of RF Corona Ignition in Lean Operating Conditions Using an Optical Access Engine*', SAE Technical Paper, 2017-01-0673.

Converge CFD Manual Series, V3.0, © 2020 Convergent Science.

Cook, A. W. and Riley, J. J. (1996) 'Direct Numerical Simulation of a Turbulent Reactive Plume on a Parallel Computer', J. Computational Physics, 129, pp. 263-283.

Cooper, A. and Bassett, M. (2020) *'A Compact Pre-chamber Ignition System for High-efficiency Gasoline Engines*', RSR, MAHLE powertrain [online], Available at: https://mobex.io/webinars/a-compact-pre-chamber-ignition-system-for-high-efficiency-gasoline-engines/ (Accessed: :27 Feb 2021).

Cotterman, R. L., Bender, R. and Prausnitz, J. M. (1985) 'Phase equilibria for mixtures containing very many components: Development and application of continuous thermodynamics for chemical process design', *Industrial and Engineering Chemistry Process Design and Development*, 24, pp. 194-203.

d'Adamo, A., Breda, S., Fontanesi, S., and Cantore, G. (2015) '*LES Modelling of Spark-Ignition Cycle-to-Cycle Variability on a Highly Downsized DISI Engine'*, SAE Int. J. Engines 8(5), 2015-24-2403, pp. 2029-2041.

Daif, A., Bouaziz, M., Chesneau, X. and Ali Cherif, A. (1999) 'Comparison of multicomponent fuel droplet vaporization', *Experimental Thermal and Fluid Science*, 18, pp. 282-290.

Dhanji, M. and Zhao, H. (2019) '*Effect of a split-injections strategy on the atomisation rate for charge stratification using a high-pressure gasoline multi-hole injector*', SAE Technical Paper, 2019-01-2248.

Dhanji, M. P. (2020) '*Optical Studies of Gasoline Sprays and In-cylinder Mixture Formation using a High Pressure Multi-Hole Injector*', PhD. thesis, Department of Mechanical and Aerospace Engineering, Brunel University London.

Dhanji, M. P. and Zhao, H. (2020) '*Effect of a split-injection strategy on the atomisation rate using a high-pressure gasoline DI Injector*', SAE Technical Paper, 2020-01-0322.

Drake, M. C., Fansler, T. D., Solomon, A. S. and Szekely, G. A. (2003) '*Piston fuel films as a source of smoke and hydrocarbon emissions from a wall-controlled spark-ignited direct-injection engine*'. SAE Technical Paper, 2003-01-0547.

Dukowicz, J. K. (1980) 'A particle–fluid numerical model for liquid sprays'. Journal of Computational Physics, 35 (2), pp. 229–253.

Dumouchel, C. (2008) 'On the experimental investigation on primary atomization of liquid streams', Experiments in Fluids, 45, pp. 371–422.

Faeth, G. M. (1983) 'Evaporation and combustion of sprays', *Progress in Energy and Combustion Science*, 9 (1-2), pp. 1-76.

Faville, J. (2018), *'Injector data for NE1 engine development-2*', Delphi Technologies, TCR Spray lab: JS.

Faville, J. and Moore, K. (2015), *'Injector data for NE1 engine development*', Delphi Technologies, TCR Spray lab.

Favre, A. (1965), '*Equations des gaz turbulents compressibles', part 1: formes ge'ne'rales. Journal de Me'canique* 4, pp. 361-390.

Fu, H. and Peethambaram, M. R. (2017) '*Piston design and analysis for NE1 1.2 A phase engine*', Changan UK internal report, CAUK00231CAE.

Guildenbecher, D. R., Lopez-Rivera, C. and Sojka, P. E. (2009) 'Secondary atomization', *Experiments in Fluids*, 46 (3), pp. 371-402.

Hakariya, M., Toda, T. and Sakai, M. (2017) '*The New Toyota Inline 4-Cylinder 2.5L Gasoline Engine*', SAE Technical Paper, 2017-01-1021.

Han, Z. and Reitz, R. D. (1995) 'Turbulent modeling of internal combustion engines using RNG k-e', *Combustion Science and Technology*, 10 (4-6), pp. 267–295.

Han, Z., Parrish, S., Farrel, P. V. and Reitz, R. D. (1997) 'Modelling atomization process of pressure swirl hollow-cone fuel sprays', *Atomization and Sprays*, 7 (6), pp. 663-684.

Han, Z., Yi, J. and Trigui, N. (2002) *'Stratified mixture formation and piston surface wetting in a DISI engine*', SAE Technical Paper, 2002-01-2655.

Heywood, J. B. (1989) *Internal Combustion Fundamentals*. London: McGraw-Hill.

Hiroyasu, H. and Kadota, T. (1974) '*Fuel Droplet Size Distribution in Diesel Combustion Chamber*', SAE Technical Paper, 740715.

Hsiang, L. P. and Faeth, G. M. (1992) 'Near-Limit drop deformation and secondary breakup', *International Journal of Multiphase Flow*, 18 (5), pp. 635-652.

Hung, D., Harrington, D., Gandhi, A., Markle, L.E., Parrish, S.E., Shakal, J.S., Sayar, H., Cummings, S.D. and Kramer, J.L. (2009) 'Gasoline Fuel Injector Spray Measurement and Characterization - A New SAE J2715 Recommended Practice', *SAE International Journal of Fuels and Lubricants*, 1 (1), pp. 534-548.

Huu, P. Trinh, Chen, C. P. and Balasubramanyam, M. S. (2007) 'Numerical simulation of Liquid Jet Atomization Including Turbulence Effects', *Journal of Engineering for Gas Turbines and Power*, 129 (4), pp. 920-928.

Hwang, K., Hwang, I., Lee, H., Park, H., Choi, H., Lee, K., Kim, W., Kim, H., Han, B., Lee, J., Shin, B. and Chae, D. (2016) '*Development of New High-Efficiency Kappa 1.6L GDI Engine*', SAE Technical Paper, 2016-01-0667.

Jiao, Q. and Reitz, R.D. (2015) *'*Modeling soot emissions from wall films in a direct-injection spark-ignition engine', *International Journal of Engine Research*, 16(8), 994-1013.

Joshi, A. (2020) '*Review of Vehicle Engine Efficiency and Emissions*', SAE Technical Paper, 2020-01-0352.

Kargul, J., Stuhldreher, M., Barba, D., Schenk, C., Bohac, S., McDonald, J., Dekraker, P. and Alden, J. (2019) 'Benchmarking a 2018 Toyota Camry 2.5-Liter Atkinson Cycle Engine with Cooled-EGR', SAE *International Journal of Advanced and Current Practices in Mobility*, 1(2), pp. 601-638.

Ketterer, J., Gautier, E. and Keating, E. (2018) '*The Development and Evaluation of Robust Combustion Systems for Miller Cycle Engines*', SAE Technical Paper, 2018-01-1416.

King, J., Barker, L., Turner, J. and Martin, J. (2016) '*SuperGen - A Novel Low Costs Electro-Mechanical Mild Hybrid and Boosting System for Engine Efficiency Enhancements*', SAE Technical Paper, 2016-01-0682.

Krzeczkowski, S. A. (1980) ‘Measurements of liquid droplets disintegration mechanism', *International Journal of Multiphase Flow*, 6 (3), pp. 227-239.

Kuwahara, K., Ueda, K. and Ando, H. (1998) ‘*Mixing Control Strategy for Engine Performance Improvement in a Gasoline Direct Injection Engine*', SAE Technical Paper, 980158.

Launder, B. E. (1991), '*Current Capabilities for Modeling Turbulence in Industrial Flows*', J. Applied Scientific Research, 48, 247

Launder, B.E. and Spalding, D. B. (1974) '*The Numerical Computation of Turbulent Flows*'. Computational Methods Appl. Mech. Eng., 3, pp. 269-289

Lee, B., Oh, H., Han, S., Woo, S. and Son, J.W. (2017) ‘*Development of High Efficiency Gasoline Engine with Thermal Efficiency over 42%*', SAE Technical Paper, 2017-01-2229.

Lefebver, A. H. (1989) *Atomization and Sprays*. Purdue University: Taylor and Francis Group.

Lesieur, M., Yaglom, A. M. and David, F., (2000) '*New trends in turbulence. Turbulence: nouveaux aspects*', Les Houches Session LXXIV, Springer, Heidelberg, New York

Li, T., Hiroyasu, H., Zhang, Y. and Nishida, K. (2003) *'Characterization of Mixture Formation Processes in DI Gasoline Engine Sprays with Split Injection Strategy via Laser Absorption and Scattering (LAS) Technique*', SAE Technical Paper, 2003-01-3161.

Li, T., Nishida, K., Zhang, Y., Yamakawa, M. and Hiroyasu, H. (2004) '*An Insight into Effect of Split Injection on Mixture Formation and Combustion of DI Gasoline Engines*', SAE Technical Paper, 2004-01-1949.

Li, Y., Zhao, H., Stansfield, P. and Freeland, P. (2015) ‘*Synergy between Boost and Valve Timings in a Highly Boosted Direct Injection Gasoline Engine Operating with Miller Cycle*', SAE Technical Paper, 2015-01-1262.

Liang, L and Reitz, R. D. (2006) '*Spark Ignition Engine Combustion Modeling Using a Level Set Method with Detailed Chemistry*', SAE Technical Paper, 2006-01-0243.

Liu, C., and Liu, Z. (1993) '*Multigrid Methods and High Order Finite Difference for Flow in Transition*', AIAA Paper 93-3354

Liu, Y. and Reitz, R. D. (1998) *'Modeling of heat conduction within chamber walls for multidimensional internal combustion simulations'*, *International Journal of Heat and Mass Transfer*, 41 (6–7), pp. 859–869.

Liu, Z. and Reitz, R. D. (1997) ‘An analysis of the distortion and breakup mechanisms of high speed liquid drops', *International Journal of Multiphase Flow*, 23 (4), pp. 631–650.

Lumley, J.L. (1970) '*Toward a Turbulent Constitutive Equation*', J. Fluid Mechanics, 41, pp. 413-434

Lumley, J.L. (1978) '*Computational Modeling of Turbulent Flows*', Advances in Applied Mechanics, 18, pp. 123-176

Luo, X., Teng, H., Lin, Y., Li, B., Zeng, X., Hu, T., Huang, X. and Yuan, X. (2017) '*A Comparative Study on Influence of EIVC and LIVC on Fuel Economy of a TGDI Engine Part II: Influences of Intake Event and Intake Valve Closing Timing on the Cylinder Charge Motion*', SAE Technical Paper, 2017-01-2246.

Melaika, M., Mamikoglu, S. and Dahlander, P. (2019) '*48V Mild-Hybrid Architecture Types, Fuels and Power Levels Needed to Achieve 75g CO2/km*', SAE Technical Paper, 2019-01-0366.

Metghalchi, M. and Keck, J. C. (1982) 'Burning Velocities of Mixtures of Air with Methanol, Isooctane, and Indolene at High Pressures and Temperatures', *Combustion and Flame*, 48, pp. 191-210.

Miller, R. (1956). *High Expansion, Spark Ignited, Gas Burning, Internal Combustion Engines*, U.S. Patent Office. No. 2773490. [online] Available at: https://patents.google.com/patent/US2773490A/en (Accessed: 27 Feb 2021).

Miller, R. (1957). *Supercharged engine*, U.S. Patent Office. no. 2817322. [online] Available at: https://patents.google.com/patent/US2817322A/en (Accessed: 27 Feb. 2021).

Mock, P., (2019) '*EU Regulations: CO2 Emission Standards for Passenger Cars and Light-Commercial Vehicles in the European Union*'' [online]. Available at: https://theicct.org/publications/ldv-co2-stds-eu-2030-update-jan2019 (Accessed: 27 Feb 2021).

Nagaoka, M. and Kawamura, K. (2001) '*A deforming droplet model for fuel spray in direct-injection gasoline engines*', SAE Technical Paper, 2001-01-1225.

Nagaoka, M., Kawazoe, H. and Nomura, N. (1994) '*Modeling Fuel Spray Impingement on a Hot Wall for Gasoline Engines*', SAE Technical Paper, 940525.

Nakata, K., Nogawa, S., Takahashi, D., Yoshihara, Y., Kumagai, A. and Suzukim, T. (2016) ‘Engine Technologies for Achieving 45% Thermal Efficiency of S.I. Engine', *SAE International Journal of Engines*, 9 (1), pp. 179-192.

Nauwerck, A., Pfeil, J., Velji, A., Spicher, U. and Richter, B. (2005) '*A Basic Experimental Study of Gasoline Direct Injection at Significantly High Injection Pressures*', SAE Technical Paper, 2005-01-0098.

Nurick, W. H. (1976) 'Orifice Cavitation and Its Effect on Spray Mixing', *Journal of Fluids Engineering*, 98 (4), pp. 681-687.

O'Rourke P. J. and Amsden A. A. (2000) '*A spray/wall interaction submodel for the KIVA-3 wall film model*', SAE paper, 2000-01-0271.

O'Rourke, P. J. and Amsden, A. A. (1996) '*A Particle Numerical Model for Wall Film Dynamics in Port-Injected Engines*', SAE Technical Paper, 961961.

Ortmann, R., Arndt, S., Raimann, J., Grzeszik, R. and Würfel, G. (2001) '*Methods and Analysis of Fuel Injection, Mixture Preparation and Charge Stratification in Different Direct Injected SI Engines*', SAE Technical Paper, 2001-01-0970.

Osborne, R., Downes, T., O'Brien, S., Pendlebury, K. and Christie, M. (2017) 'A Miller Cycle Engine without Compromise - The Magma Concept', *SAE International Journal of Engines*, 10 (3), pp. 846-857.

Patil, D., Wang, Y., Liang, L., Puduppakkam, K. et al., (2018), "*Large-Eddy Simulation and Analysis of Turbulent Flows in a Motored Spark-Ignition Engine*," SAE Technical Paper 2018-01-0202.

Patterson, M. and Reitz, R. (1998) '*Modeling the Effects of Fuel Spray Characteristics on Diesel Engine Combustion and Emission*', SAE Technical Paper, 980131.

Peethambaram, M. R. and Fu, H. (2016) '*A generic method of spray modelling for GDI engines*', Changan UK internal report, CAUK00205CAE.

Pilch, M. and Erdman, C. A. (1987) 'Use of breakup time data and velocity history data to predict the maximum size of stable fragments for acceleration-induced breakup of a liquid drop', *International Journal of Multiphase Flow*, 13 (6), pp. 741-757.

Piock, W., Befrui, B., Berndorfer, A. and Hoffmann, G. (2015) *'Fuel Pressure and Charge Motion Effects on GDi Engine Particulate Emissions', SAE International Journal of Engines*, 8 (2), pp.464-473.

Pitsch. H. (2006) '*Large-Eddy Simulation of Turbulent Combustion*', Annual Review of Fluid Mechanics, Vol. 38, pp 453-482.

Pope, S. B., (2000) '*Turbulent Flows*', Cambridge University Press, Cornell University, New York

Prandtl, L. (1925) '*Dber die ausgebildete Turbulenz*', ZAMM, Vol. 5, pp. 136-139

Ra, Y. and Reitz, R. D. (2009) *'A vaporization model for discrete multi-component fuel sprays', International Journal of Multiphase Flow*, 35 (2), pp.101–117.

Ra, Y. and Reitz, R. D. (2011) 'A combustion model for IC engine combustion simulations with multi-component fuels', *Combustion and Flame*, 158 (1), pp. 69–90.

Reitz, R. and Diwakar, R. (1986) '*Effect of Drop Breakup on Fuel Sprays*', SAE Technical Paper, 860469.

Reitz, R. and Diwakar, R. (1987) '*Structure of High-Pressure Fuel Sprays*', SAE Technical Paper, 870598.

Reynolds, O. (1874) '*On the Extent and Action of the Heating Surface for Steam Boilers*', Proc. Manchester Lit. Phil. Soc., Vol. 14, pp. 7-12

Reynolds, O. (1895) '*On the Dynamical Theory of Incompressible Viscous Fluids and the Determination of the Criterion*', Phil. Trans. Roy. SOC., London, Series A 186, pp. 123-164

Ritter, M., Malbec, L. M. and Laget, O. (2021) '*Assessment and Validation of Internal Aerodynamics and Mixture Preparation in Spark-Ignition Engine Using LES Approach*', SAE Int. J. Advances and Curr. Prac. in Mobility 3(1): 95-112

Rotondi, R. and Bella, G. (2006) 'Gasoline direct injection spray simulation', *International Journal of Thermal Sciences*, 45 (2), pp. 168-179.

Sandquist, H., Lindgren, R. and Denbratt, I. (2000) '*Sources of Hydrocarbon Emissions from a Direct Injection Stratified Charge Spark Ignition Engine*', SAE Technical Paper, 2000-01-1906.

Schlichting, H. and Gersten K., (2000) '*Boundary Layer Theory'*, 8th ed. London: Springer Edn-Verlag Berlin Heidelberg.

Senecal, P. K., Richards, K. J., Pomraning, E., Yang, T., Dai, M. Z., McDavid, R. M., Patterson, M. A., Hou, S. and Shethaji, T. (2007) '*A New Parallel Cut-Cell Cartesian CFD Code for Rapid Grid Generation Applied to In-Cylinder Diesel Engine Simulations*', SAE Technical Paper, 2007-01-0159.

Senecal, P.K., Schmidt, D.P., Nouar, I., Rutland, C.J., Reitz, R.D. and Corradini, M.L. (1999) 'Modeling high-speed viscous liquid sheet atomization', *International Journal of Multiphase Flow*, 25 (6-7), pp. 1073-1097.

Serrano, D., Zaccardi, J., Müller, C., Libert, C. and Habermann, K., (2019) 'Ultra-Lean Pre-Chamber Gasoline Engine for Future Hybrid Powertrains', *SAE International Journal of Advances and Current Practices in Mobility*, 2 (2), pp. 607-622.

Shih, T.H., Liou, W. W., Shabbir, A., Yang, Z. and Zhu, J. (1994) 'A new k-ε eddy viscosity model for high Reynolds number turbulent flows - Model development and validation', NASA TM-106721.

Shin, Y., Cheng, W. K. and Heywood J. B. (1994) '*Liquid gasoline behavior in the engine cylinder of an SI engines*', SAE paper, 941872.

Sims, R., Schaeffer, R., Creutzig, F., Cruz-Núñez, X., D'Agosto, M., Dimitriu, D., Figueroa Meza, M. J., Fulton, L., Kobayashi, S., Lah, O., McKinnon, A., Newman, P., Ouyang, M., Schauer, J. J., Sperling, D. and Tiwari, G. (2014) '*Transport.* In: Edenhofer, O., Pichs-Madruga, R., Sokona, Y., Farahani, E., Kadner, S., Seyboth, K., Adler, A., Baum, I., Brunner, S., Eickemeier, P., Kriemann, K., Savolainen, J., Schlömer, S. von Stechow, C., Zwickel, T. and Minx, J. C. eds., *Climate Change 2014: Mitigation of Climate Change. Contribution of Working Group III to the Fifth Assessment Report of the Intergovernmental Panel on Climate Change*', Cambridge: Cambridge University Press.

Smagorinsky, J. (1963) '*General Circulation Experiments with the Primitive Equations*', Monthly Weather Review, 91, pp. 99-165.

Smith, J., Szekely Jr, G., Solomon, A. and Parrish, S., (2011) 'A Comparison of Spray-Guided Stratified-Charge Combustion Performance with Outwardly-Opening Piezo and Multi-Hole Solenoid Injectors', *SAE International Journal of Engines*, 4 (1), pp. 1481-1497

Smith, L. M. and Reynolds, W. C. (1992) '*On the Yakhot-O~szag Renormalization Group Method for Deriving Turbulence Statistics and Models*', Phys. Fluid A, 4, 364.

Smith, O. I. (1980) 'Fundamentals of soot formation in flames with Application to diesel engine particulate emissions', *Progress in Energy and Combustion Science*, 7 (4), pp 275-291.

STAR-CD Methodology 4.30 Manual, Siemens (2018).

Stevens, E. and Steeper, R. (2001) '*Piston Wetting in an Optical DISI Engine: Fuel Films, Pool Fires, and Soot Generation*', SAE Technical Paper, 2001-01-1203.

Su, T., Farrell, P. and Nagarajan, R., (1995) '*Nozzle Effect on High Pressure Diesel Injection*', SAE Technical Paper, 950083.

Tagishi, R., Ikeya, K., Takazawa, M. and Yamada, T. (2015) 'Technology for Realization of Gasoline Engine Brake Thermal Efficiency of 45%', *Honda R&D Technical Review*, 27 (2), pp.1-10.

Takahashi, D., Nakata, K., Yoshihara, Y., Ohta, Y. and Nishiura, H. (2015) '*Combustion Development to Achieve Engine Thermal Efficiency of 40% for Hybrid Vehicles*', SAE Technical Paper, 2015-01-1254.

Tennekes, H., and Lumley, J. L. (1972) '*A First Course in Turbulence',* Cambridge, Massachusetts, and London, England: The MIT Press.

Tietge, U. Mock, P. and Dornoff, J. (2019) '*CO2 emissions from new passenger cars in Europe: Car manufacturers performance in 2019*' [online]. International Council on Clean Transportation(ICCT), Available at: https://theicct.org/sites/default/files/publications/CO2-EU-update-aug2020.pdf (Accessed: 27 Feb 2021).

Tietge, U., Díaz, S., Yang, Z. and Mock, P. (2017) '*A comparison of official and real-world fuel consumption and CO2 values for passenger cars in Europe, The United States, China and Japan*', White paper, ICCT (The international Council on Clean Transportation) [online], Available at: https://theicct.org/sites/default/files/publications/Lab-to-road-intl_ICCT-white-paper_06112017_vF.pdf (Accessed: 27 Feb 2021).

Tongroon, M. and Zhao, H. (2015) 'Thermal and chemical effects of fuel direct injection on kinetically controlled combustion of alcohol and gasoline fuels', *International Journal of Engine Research*, 16 (8), pp. 982–993.

Torres, D. J., O'Rourke, P. J. and Amsden, A. A. (2003) 'Efficient multicomponent fuel algorithm', *Combustion Theory and Modelling*, 7 (1), pp. 66-86.

Toulson, E., Schock, H. and Attard, W. (2010) '*A Review of Pre-Chamber Initiated Jet Ignition Combustion Systems*', SAE Technical Paper, 2010-01-2263.

Tuner, M. (2016) '*Review and Benchmarking of Alternative Fuels in Conventional and Advanced Engine Concepts with Emphasis on Efficiency, CO2, and Regulated Emissions*', SAE Technical Paper, 2016-01-0882.

Turner, J., Popplewell, A., Patel, R., Johnson, T.R., Richardson, D.S., Bredda, S.W., Tudor, R.J., Bithell, C.I., Jackson, R., Remmert, S. M., Cracknell, R.F., Fernandes, J.X., Lewis, A.G.J., Akehurst, S., Brace, C.J., Copeland, C., Martinez-Botas, R., Romagnoli, A. and Burluka, A.A. (2014) 'Ultra Boost for Economy: Extending the Limits of Extreme Engine Downsizing', *SAE International Journal of Engines*, 7 (1), pp. 387-417.

Turns, S. R. (2000) '*An Introduction to Combustion: Concepts and Applications*'. 2nd ed. New York: McGraw Hill.

Volkswagen (2016) '*The New EA211 TSI® evo*', Internationales Wiener Motorensymposium, 37.

Von Kuensberg Sarre, C., Kong, S.-C. and Reitz, R.D. (1999) '*Modeling the Effects of Injector Nozzle Geometry on Diesel Sprays*', SAE Paper, 1999-01-0912.

Wang, D. Y. and Lee. C. F. (2005) '*Continuous multicomponent fuel film vaporization model for multidimensional engine modeling*', SAE Technical Paper, 2005-01-0209.

Wang, X., Xie, H. and Zhao, H. (2015) 'Computational study of the influence of in-cylinder flow on spark ignition controlled auto-ignition hybrid combustion in a gasoline engine', *International Journal of Engine Research*, 16 (6), pp. 795–809.

Waters, B. and McGhee, M. (2019) *'Catalyst heating operation, engine operation', Engine development, Internal report*, Changan UK Ltd.

Watkins, A. P. (1977) '*Flow and Heat Transfer in Piston/Cylinder Assemblies*', PhD. thesis, Mechanical Engineering Department, Imperial College of Science and Technology, London.

Westin, F., Grandin, B. and Ångström, H. (2000) *'The Influence of Residual Gases on Knock in Turbocharged SI-Engines*', SAE Technical Paper 2000-01-2840.

Wilcox, D. C. (1988) '*Reassessment of the Scale Determining Equation for Advanced Turbulence Models'*, AIAA Journal, Vol. 26, No. 11, pp. 1299-1310.

Wilcox, D.C. (2006) '*Turbulence Modeling for CFD*', Published by DCW Industries, Inc., La Cafiada, California, USA.

Xu, Z., Yi, J., Curtis, E. and Wooldridge, S. (2009) *'Applications of CFD Modeling in GDI Engine Piston Optimization*', SAE Technical Paper, 2009-01-1936.

Yakhot, V. and Orszag, S. A. (1986) '*Renormalization Group Analysis of Turbulence: 1. Basic Theory*', Journal of Scientific Computing, Vol. 1, pp. 3-51.

Yamada, T., Adachi, S., Nakata, K., Kurauchi, T. and Takagi, I. (2014) *'Economy with Superior Thermal Efficient Combustion (ESTEC)',* SAE Technical Paper, 2014-01-1192.

Yamamoto, S., Tanaka, D., Takemura, J., Nakayama, O. and Ando, H. (2001) '*Mixing Control and Combustion in Gasoline Direct Injection Engines for Reducing Cold-Start Emissions*', SAE Technical Paper, 2001-01-0550.

Yang, H. Q. (1990) '*Asymmetric Instability of a liquid jet*', Physics of Fluid, 4 (4), pp. 681-689.

Yang, S. and Reitz, R. D. (2009) '*Integration of a Continuous Multi-Component Fuel Evaporation Model with an Improved G-Equation Combustion and Detailed Chemical Kinetics Model with Application to GDI Engines*', SAE Technical Paper, 2009-01-0722.

Yang, Z. and Bandivadekar, A. (2017) '*Global update, Light-Duty Vehicle Greenhouse Gas and Fuel Economy Standards*', The international council on clean transportation (ICCT) [online], Available at: https://theicct.org/sites/default/files/publications/2017-Global-LDV-Standards-Update_ICCT-Report_23062017_vF.pdf (Accessed: 27 Feb 2021).

Yuan, S., Hu, T. and Zhang, X. (2017) '*Performance of the NE14TG-AA engine at catalyst heating operation*', Changan HQ internal technical report.

Zubkov, V. S., Cossali, G. E., Tonini, S., Rybdylova, O., Crua, C., Heikal, M. and Sazhin, S. S. (2017) '*Mathematical modelling of heating and evaporation of a spheroidal droplet*', International Journal of Heat and Mass Transfer, 108, pp. 2181–2190.